SUSPENSION DESIGN

GRC19

ORION MILLER

WILL HUGHES

SUSPENSION DESIGN SUMMARY **03/11/2019**

This year, major suspension configuration changes were made to establish a strong platform for new 16" tires and pursue the chosen team goals. Points of focus included the lowering, centralization, and reduction of mass, and improved standards in the areas of tire analysis, steering design, and brakes design.

Tire Evaluation/Analysis

A new Matlab tire model has been developed for force and moment analysis, with the ability to isolate for normal force, pressure, or camber as varied parameters. Heat maps of the different tire tread areas can also be generated for temperature analysis. Curve fitting is done using Pacejka 1996 or 2012 models. The tire evaluation process included consideration of the following factors:

- Normal force sensitivity
- Pressure sensitivity
- Camber sensitivity
- Temperature sensitivity
- Wear sensitivity

These factors were used to inform the design process, while also considering the limitations of the model as well as the effects of differing wheel weights on overall vehicle performance.

This process concluded with the selection of Hoosier 16x7.5-10 LCO tires in favor of the previous Hoosier 20.5x7.0-13 R25B's. These new tires provide major opportunity for performance gains by reduction of CG, unsprung mass, yaw inertia, rotating inertia in the wheel, as well as overall vehicle weight. The use of slightly wider tires allows for the apparent decreases in grip associated with smaller diameter and contact patch to be reduced. These tires also exhibit desirable camber sensitivity qualities.

Suspension Design

The car uses a conventional double wishbone setup, with pullrod suspension in the front end and pushrod suspension in the rear. The camber progression is designed to provide ideal compensation in roll rather than through pitching and heave motions, based on sensitivity analysis of lateral and longitudinal grip. The front geometry is designed to provide a more gradual curve than the rear as a consideration for steer-camber effects, as well as a lower roll center to provide a roll axis inclination with suitable alignment to the theoretical center of mass axis.

In order of priority, the main factors considered when developing the suspension configuration were:

- Ability to provide appropriate response to system inputs
- Packaging and mounting
- Effect on CG
- Effect on drag
- Orientation of suspension planes

The suspension planes are tilted inwards from the top view to centralize weight, and are oriented vertically to minimize the generation of out-of-plane forces throughout travel. The shocks are oriented as coincident to the frame mount tubes and each other as possible; this acts to decrease bending stress at the mount tubes and provide force cancellation between the shocks during bump loadings. The Ohlins TTX25 shocks have been tested on a custom damper dynamometer to investigate operating behavior and validate the manufacturer-provided data.

Front and rear anti-roll bars are also being implemented for the first time. After considering previous performance issues, it was determined that the ability to tune ride and roll rates independently justifies the increase in components and weight. These use a simple but functional design and are mounted below the bottom of the frame to minimize CG.

All components were designed using load cases generated from tire test data. The uprights, hubs, and bellcranks are CNC machined 6061-T6.

Steering Design

The steering system is configured with a "bottom-front" mounted rack and a double u-joint steering column. The column is supported by three needle bearing pillow blocks.

Adams Car was used to determine the required overall wheel travels and Ackermann angles. The Ackermann progression is designed to most closely approximate the ideal angle needed throughout the expected ranges of turn radii and wheel slip angles.

Estimation of forces throughout all system components were made using a steady-state cornering model to provide component design loads and ensure drivability.

FZ COMPARISON – FZVAR P12 C0

TIRE 1 – HOOSIER 16.0x7.5-10 LCO, **TIRE 2** – HOOSIER 16.0x7.5-10 R25B, **TIRE 3** – HOOSIER 20.5x7.0-13 R25B

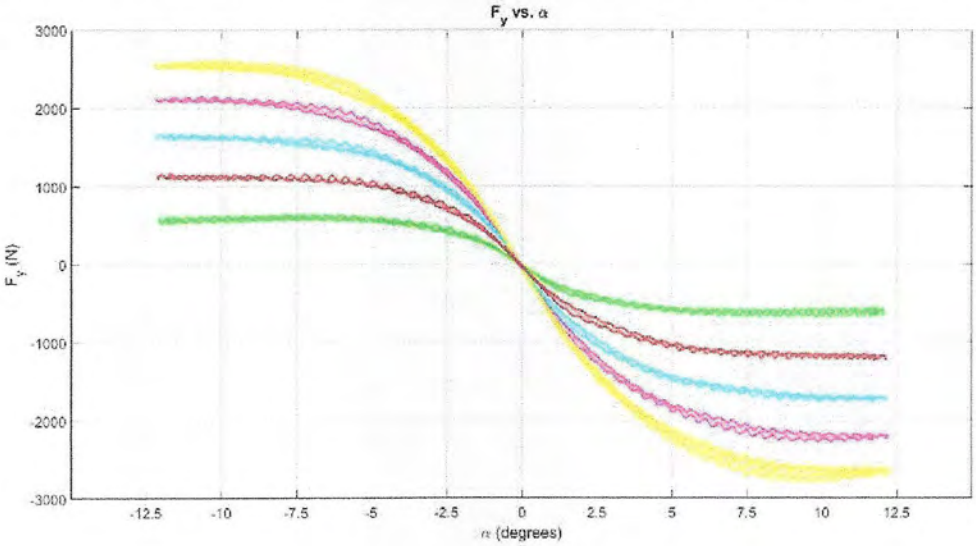

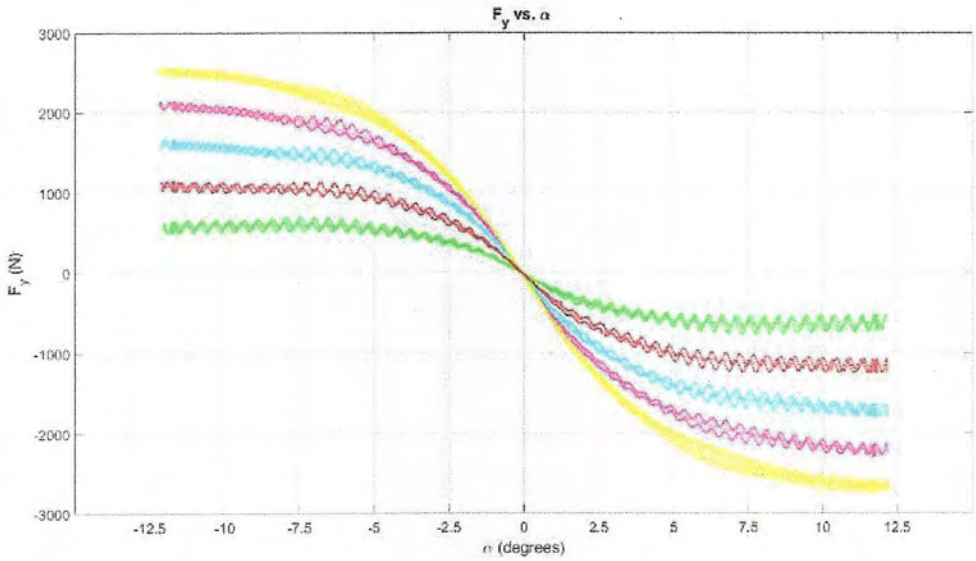

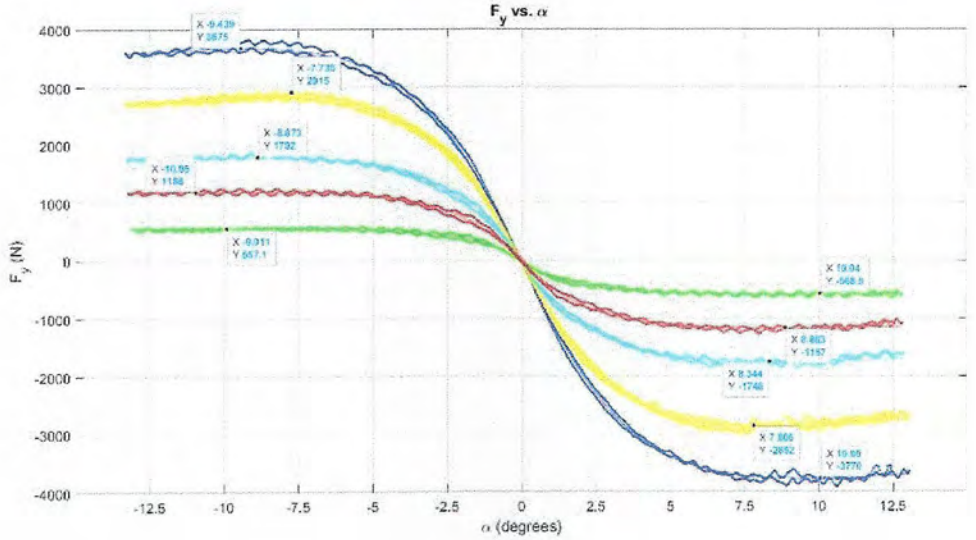

FZ COMPARISON – FZ660 PVAR C0

TIRE 1 – HOOSIER 16.0x7.5-10 LCO, **TIRE 2** – HOOSIER 16.0x7.5-10 R25B, **TIRE 3** – HOOSIER 20.5x7.0-13 R25B

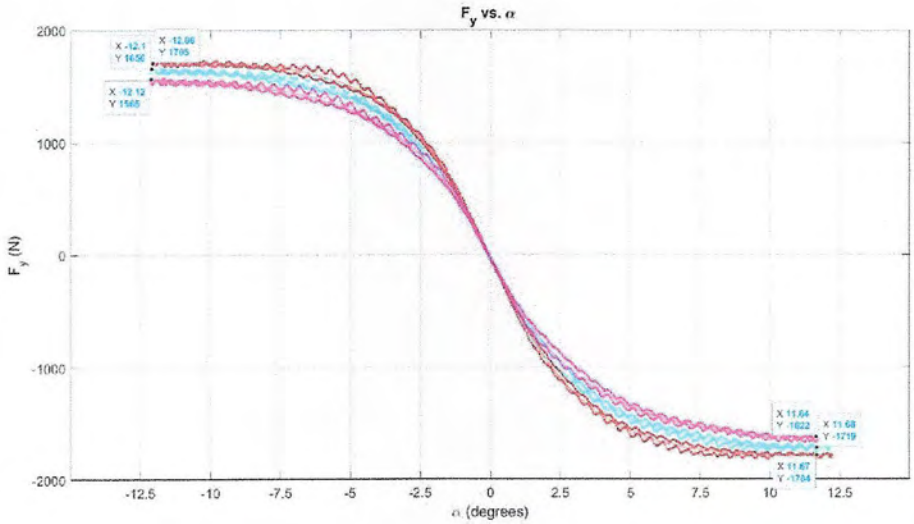

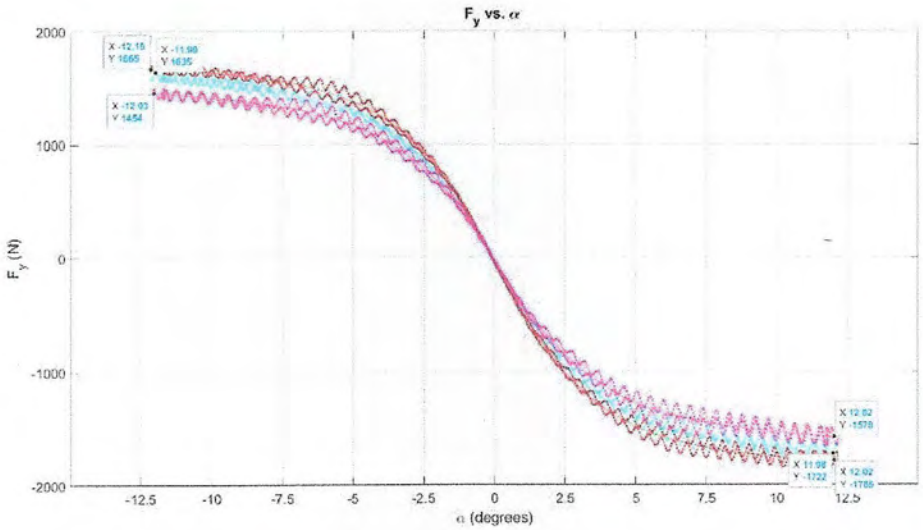

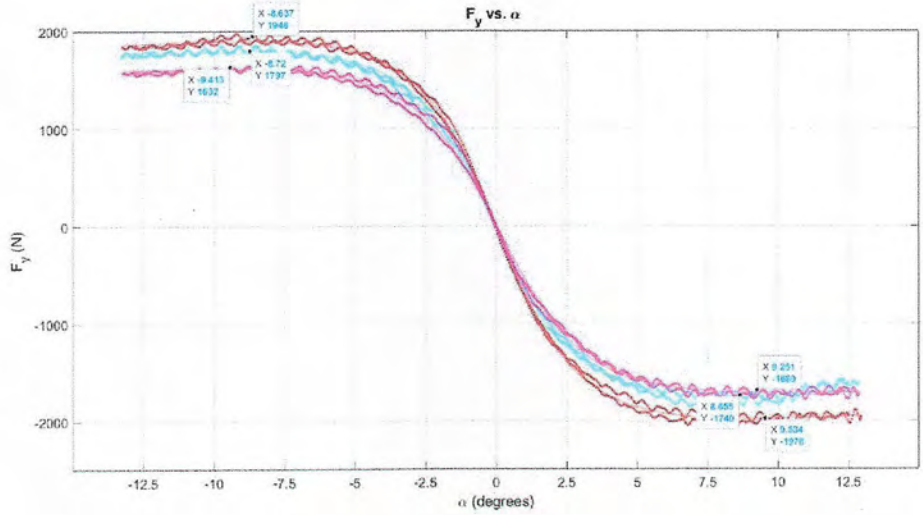

MZ COMPARISON – FZVAR P12 C0

TIRE 1 – HOOSIER 16.0x7.5-10 LCO, **TIRE 2** – HOOSIER 16.0x7.5-10 R25B, **TIRE 3** – HOOSIER 20.5x7.0-13 R25B

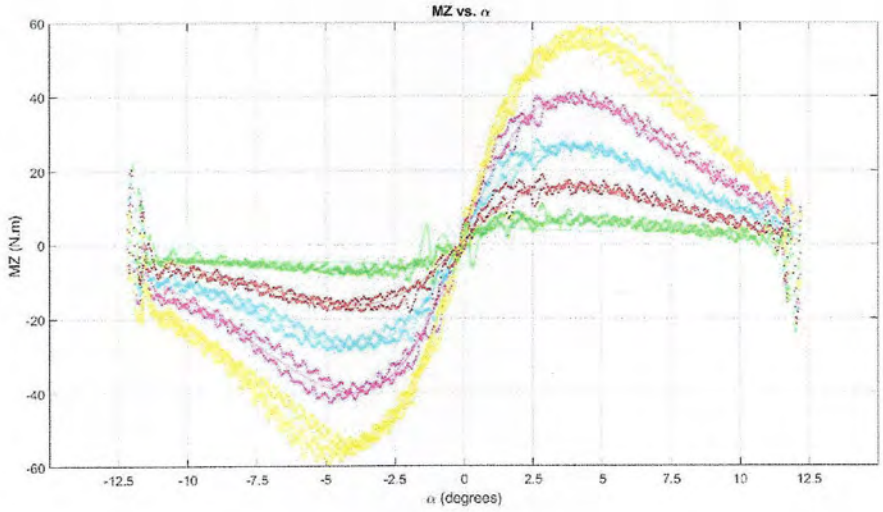

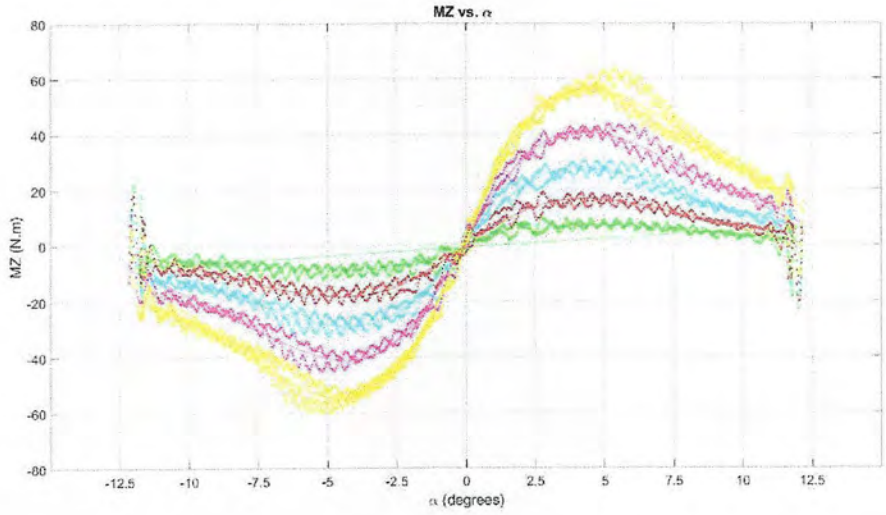

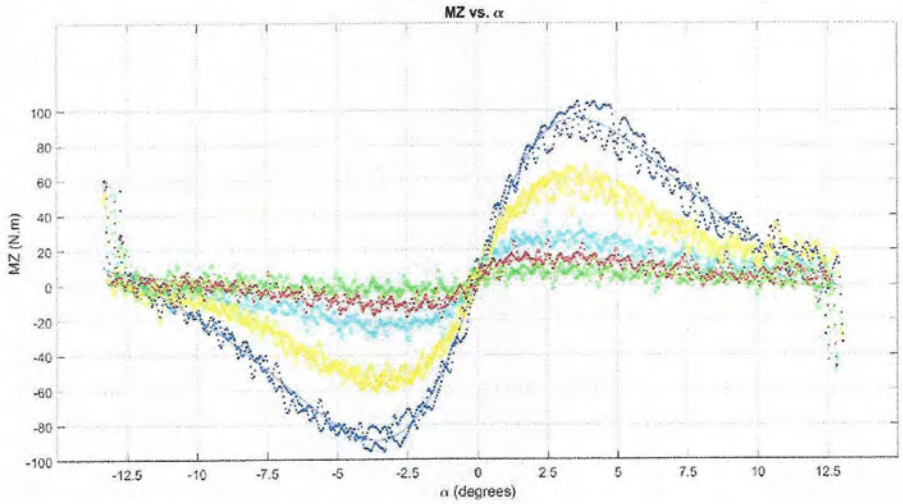

TREAD TEMPS – FZVAR P12 C0-C4

TIRE 1 – HOOSIER 16.0x7.5-10 LCO, **TIRE 2** – HOOSIER 16.0x7.5-10 R25B, **TIRE 3** – HOOSIER 20.5x7.0-13 R25B

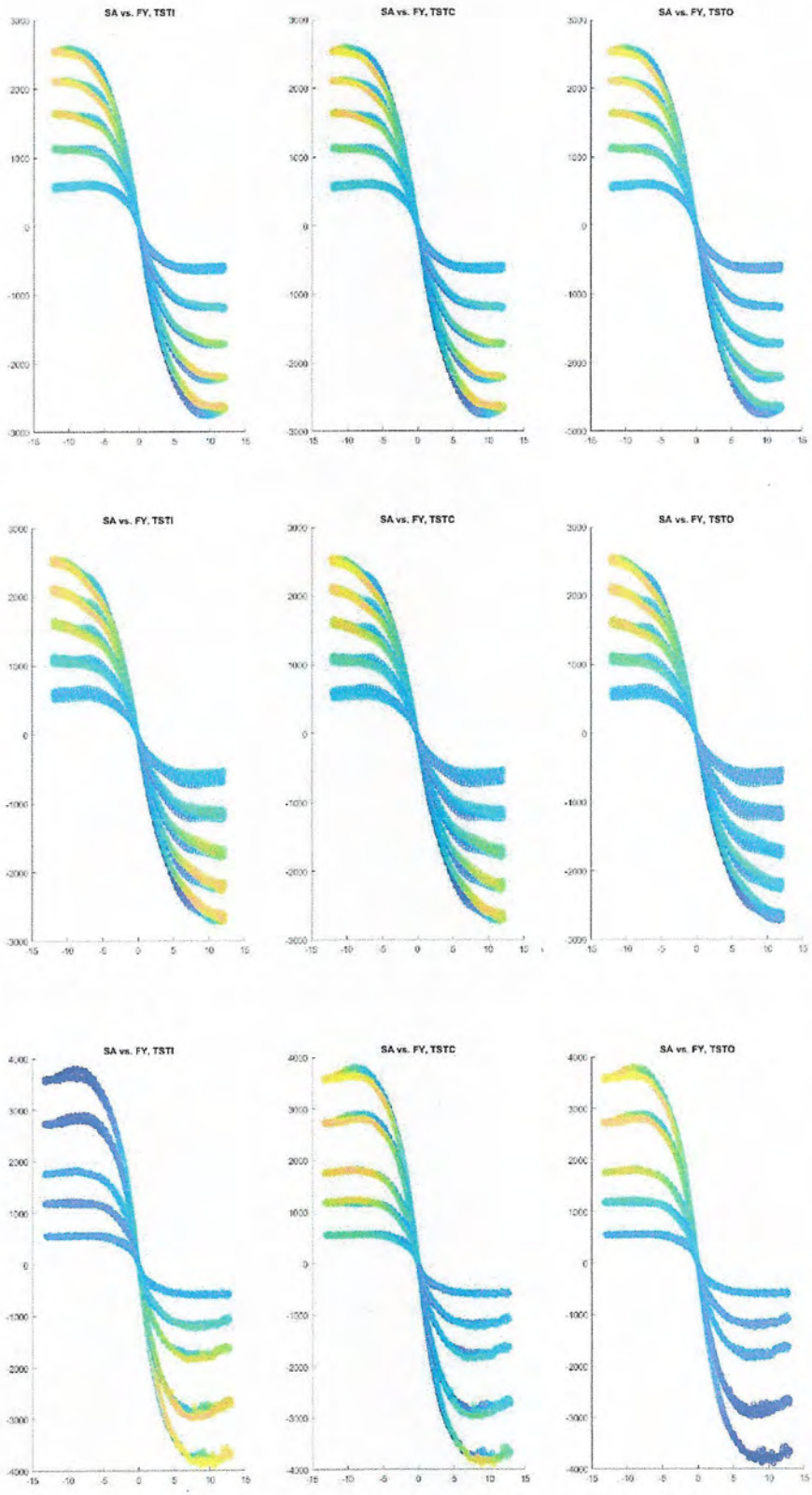

TEMPERATURES

TIRE 1 – HOOSIER 16.0x7.5-10 LCO, **TIRE 2** – HOOSIER 16.0x7.5-10 R25B, **TIRE 3** – HOOSIER 20.5x7.0-13 R25B

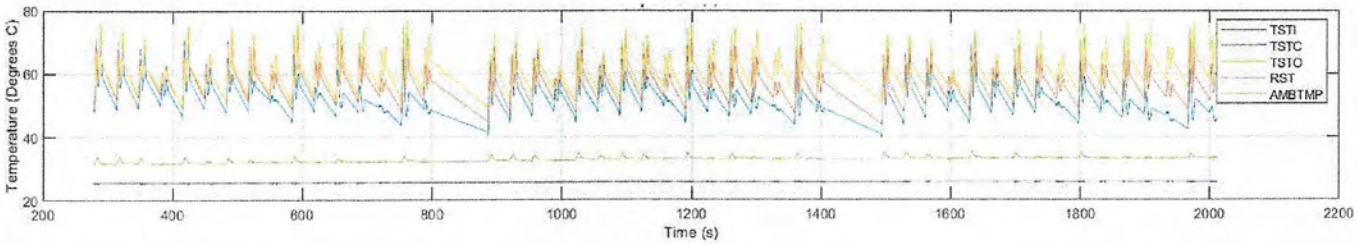

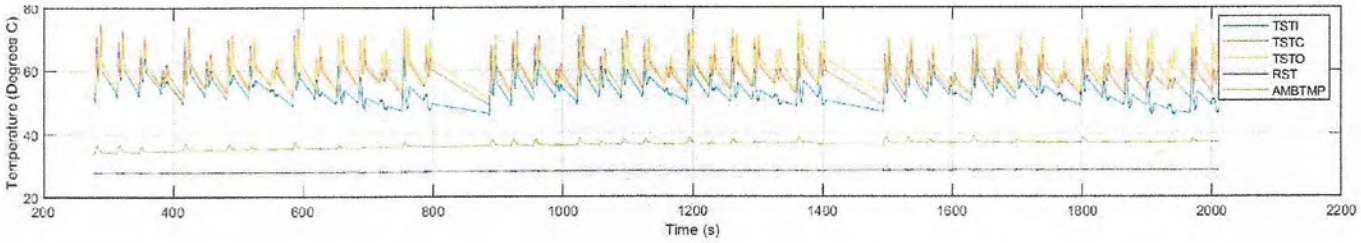

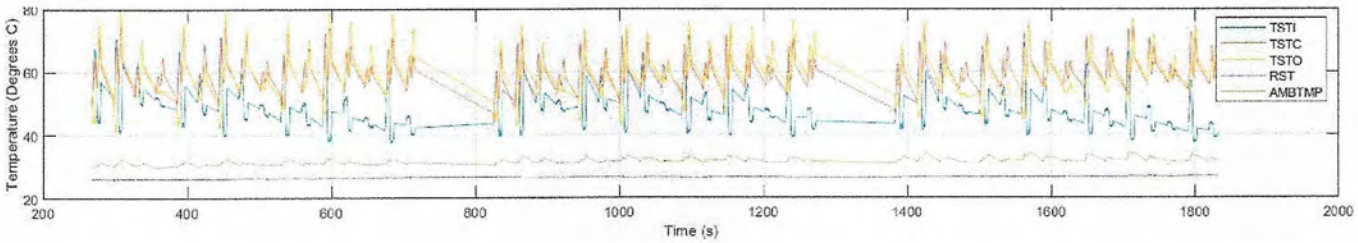

Tire	Fz Sensitivity	P Sensitivity	IA Sensitivity
Hoosier 16.0x7.5-10 LCO, 7" Rim	2.50E-01	4.02E-01	4.60E-01
Hoosier 16.0x7.5-10 LCO, 8" Rim	2.40E-01	4.00E-01	4.56E-01
Hoosier 16x6.0-10 LCO, 6" Rim	2.59E-01	3.96E-01	4.52E-01
Continental 205/470R13 43329, 7" Rim	5.10E-01	3.96E-01	4.09E-01
Goodyear 20x7-13 D2704, 7"Rim	3.97E-01	3.93E-01	4.13E-01
Avon 7.0/16.0-10, 7" Rim	2.25E-01	3.91E-01	4.80E-01
Avon 7.2/20.0-13, 7" Rim	2.43E-01	3.91E-01	4.68E-01
Hoosier 20.5 x 7.0 13 R25B A2500. 7" Rim	2.23E-01	3.99E-01	4.60E-01
Hoosier 18.0 x 7.5 10 R25B, 7" Rim	2.34E-01	3.93E-01	4.81E-01
Continental 205/510R13, 7" Rim	2.58E-01	3.80E-01	4.39E-01
Hoosier 6.0 / 18.0 - 10 LCO, 6" Rim	2.30E-01	3.24E-01	4.37E-01
Hoosier 18.0 x 6.0 - 10 R25B, 6" Rim	2.12E-01	3.18E-01	4.42E-01
Hoosier 18.0 x 6.0 - 10 R25B, 7" Rim	1.90E-01	3.27E-01	4.66E-01

TIRE WEAR SENSITIVITY – HOOSIER 16.0X7.5-10 LCO

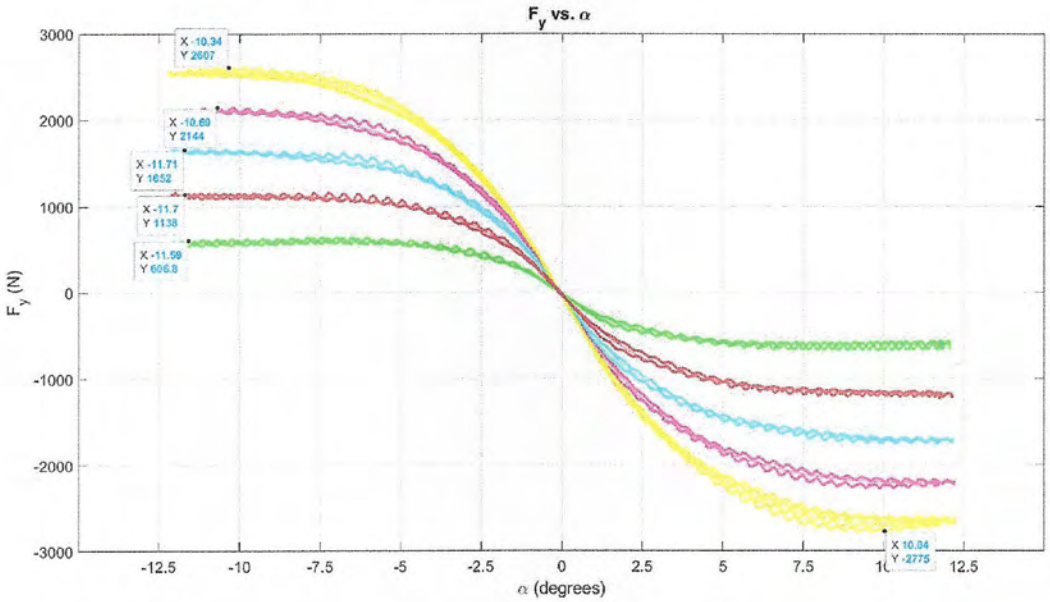

INITIAL - 12 PSI

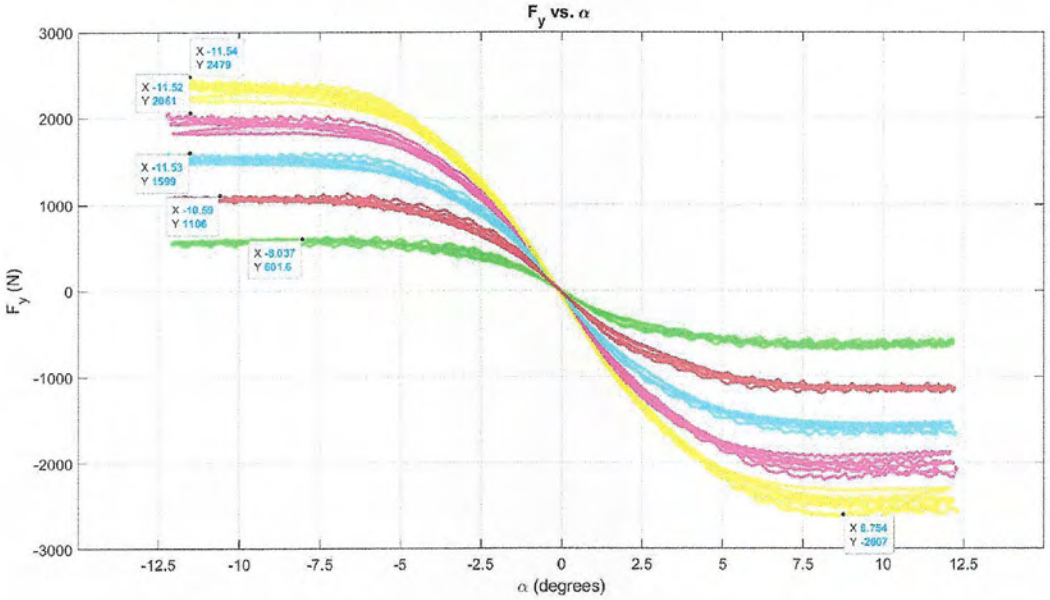

FINAL - 12 PSI

```
%%%%%%%%%%%%%%%%%%%%%%%%%%%%%%%%%%%%%%%%%%%%%%%%%%%%%%%%%%%%%%%%%%%%%%%%%%%%%%%%
% Orion Miller        Simple Traction Circle Calculator        12/30/2018.
%%%%%%%%%%%%%%%%%%%%%%%%%%%%%%%%%%%%%%%%%%%%%%%%%%%%%%%%%%%%%%%%%%%%%%%%%%%%%%%%

T_MAX = 1.5; % Max Accels
A_MAX = 1.6;
B_MAX = 1.8;

a = ['Maximum Lateral Acceleration (g): ', num2str(T_MAX)]; %Shows max accels to user
disp(a);
b = ['Maximum Longitudinal Acceleration (g): ', num2str(A_MAX)];
disp(b);
c = ['Maximum Braking Acceleration (g): ', num2str(B_MAX)];
disp(c);

while(1)
NEW_INPUT = input('Define new maximum accelerations? Enter 1 for yes, 2 for no: ');

if NEW_INPUT == 1
T_MAX = input('Define Maximum Lateral Acceleration: ');
A_MAX = input('Define Maximum Longitudinal Acceleration: ');
B_MAX = input('Define Maximum Braking Acceleration: ');
break
        else
        break
    end
end %Collects new max accels if desired


Choice = input('What acceleration are you specifying? Enter 1 for longitudinal, 2 for lateral:
'); %This code lets the user pick whether to specify lateral and calc. long. or give long. and
get lat.
if Choice ==1
   LONG_ACCEL = input('Longitudinal Accel. (in g, negative for braking): ');

   if LONG_ACCEL > A_MAX || LONG_ACCEL < -B_MAX
       disp('Invalid Input');

   else if LONG_ACCEL >= 0
       A = LONG_ACCEL;
       T = T_MAX*(1-(A./A_MAX)^2)^0.5;
       GA = (A.^2+T.^2).^0.5;

       d = ['Available Lateral Acceleration (g): ', num2str(T)];
       disp(d);
       e = ['Total Traction Capacity (g): ', num2str(GA)];
       disp(e);

   else
       B = -LONG_ACCEL;
       T = T_MAX*(1-(B./B_MAX)^2)^0.5;
       GB = (B.^2+T.^2).^0.5;

       d = ['Available Lateral Acceleration (g): ', num2str(T)];
       disp(d);
       e = ['Total Traction Capacity (g): ', num2str(GB)];
       disp(e);
       end
   end

else if Choice == 2
        T = input('Lateral Accel. (g): ');
        if T>T_MAX || T<0
            disp('Invalid Input');

        else
        A = A_MAX*(1-(T./T_MAX)^2)^0.5;
        B = B_MAX*(1-(T./T_MAX)^2)^0.5;
        GA = (A.^2+T.^2).^0.5;
        GB = (B.^2+T.^2).^0.5;
```

```
        d = ['Available Longitudinal Acceleration (g): ', num2str(A)];
        disp(d);
        e = ['Total Traction Capacity (in g, Accel.): ', num2str(GA)];
        disp(e);
        f = ['Available Longitudinal Deceleration (g): ', num2str(B)];
        disp(f);
        g = ['Total Traction Capacity (in g, Decel.): ', num2str(GB)];
        disp(g);
         end
    end
end

% q = @(x,y) (x.^2/T_MAX.^2)+(y.^2/A_MAX.^2),[-3 3 -3 0];
% fcontour(q)
% hold on
% w = @(x,y) (x.^2/T_MAX.^2)+(y.^2/B_MAX.^2),[-3 3 0 3];
% fcontour(w)
% hold off
% grid on

% fplot(@(y) (x.^2/T_MAX.^2)+(y.^2/A_MAX.^2)==1,[-3 0],'b')
% hold on
% fplot(@(y) (x.^2/T_MAX.^2)+(y.^2/B_MAX.^2)==1,[0 3],'b')
% hold off
% grid on

ezplot('x.^2/2.25+y.^2/2.56=1',[-2,2,-2,0]) %This plots the traction circle, not the best method
axis equal;
hold on
ezplot('x.^2/2.25+y.^2/3.24=1',[-2,2,0.00001,2]) %Y should be dividing by A_MAX^2 and B_MAX^2
rather than the raw value so this could update with changes, not working though
title('Hoosier 43075 Traction Circle for 1100 N Vertical Force','FontSize',16);
xlabel('Lateral Acceleration (g)','Fontsize',12);
ylabel('Longitudinal Acceleration (g)','Fontsize',12);
grid on
```

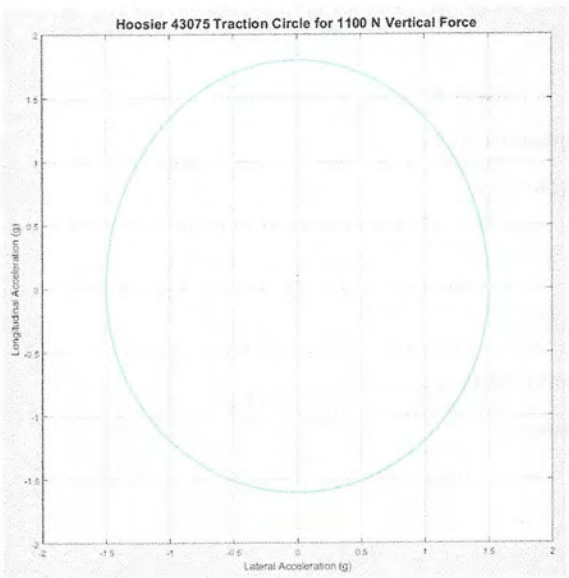

Test Data – Skidpad Practice

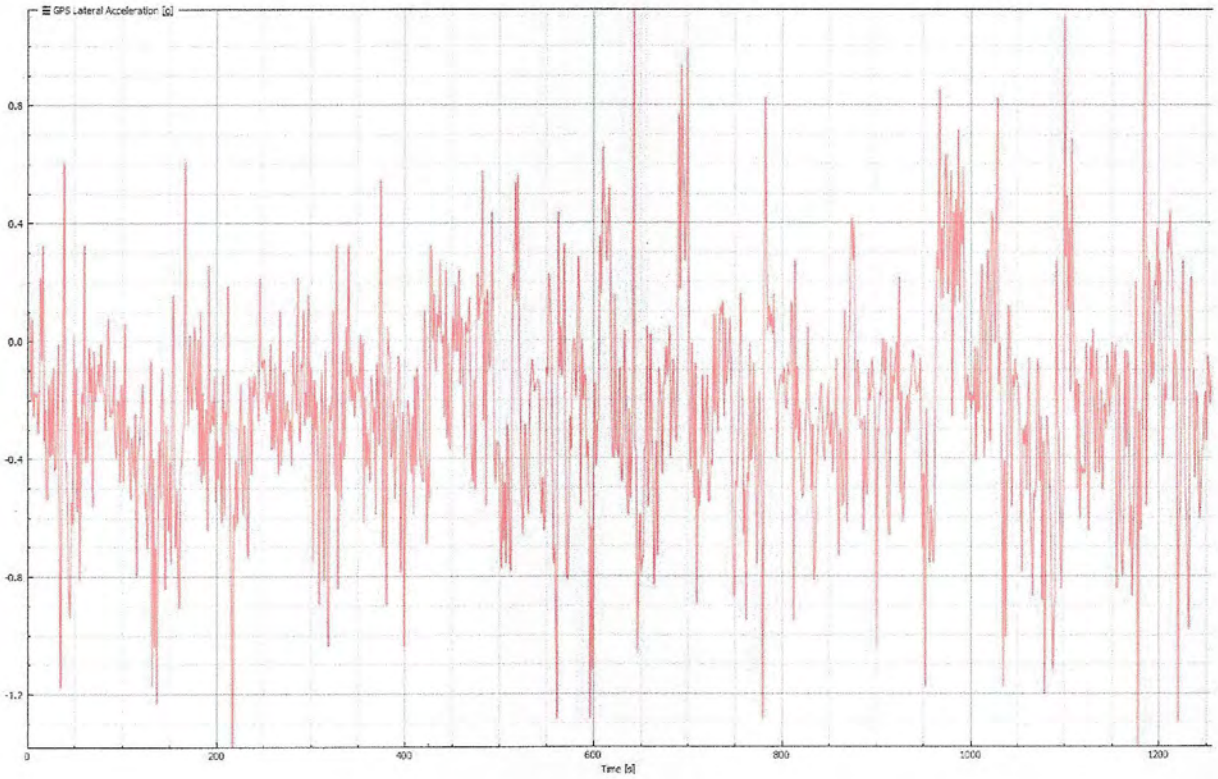

Lateral Accel vs Time

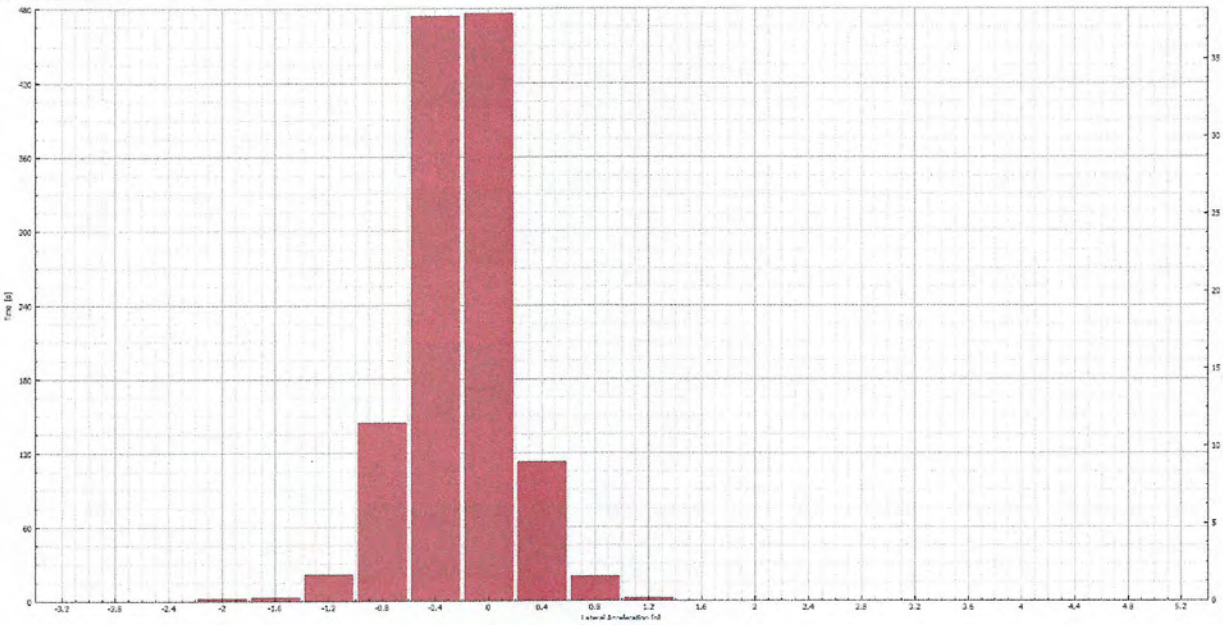

Lateral Accel Histogram

FRONT END

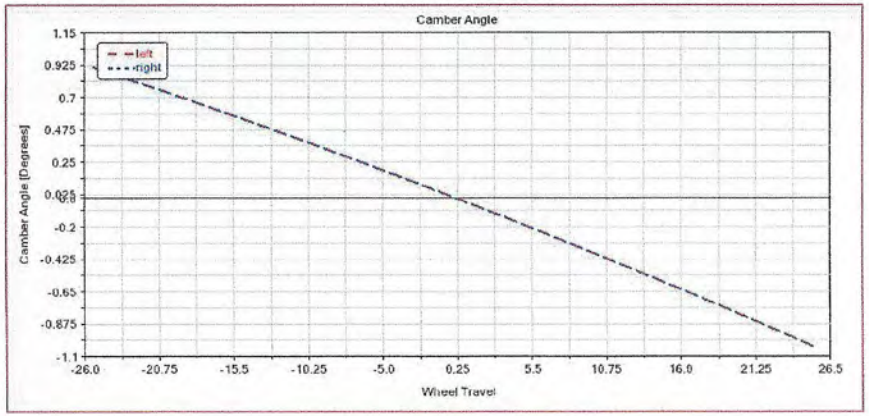

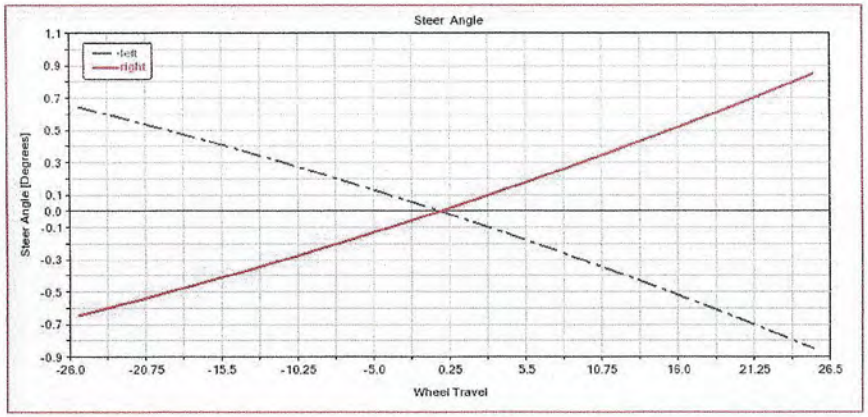

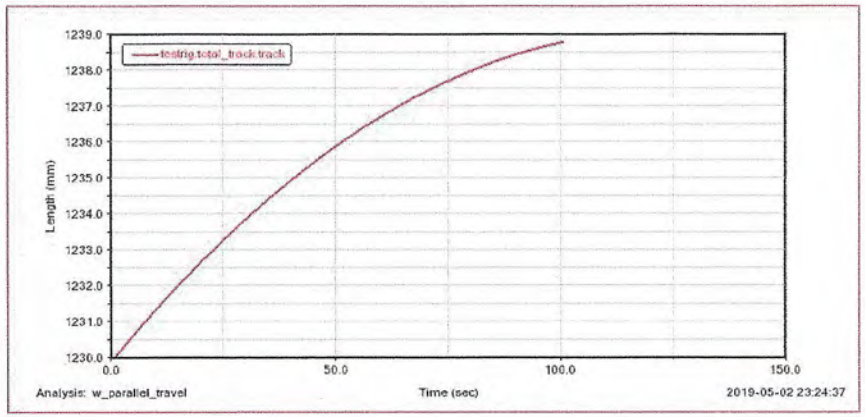

REAR END

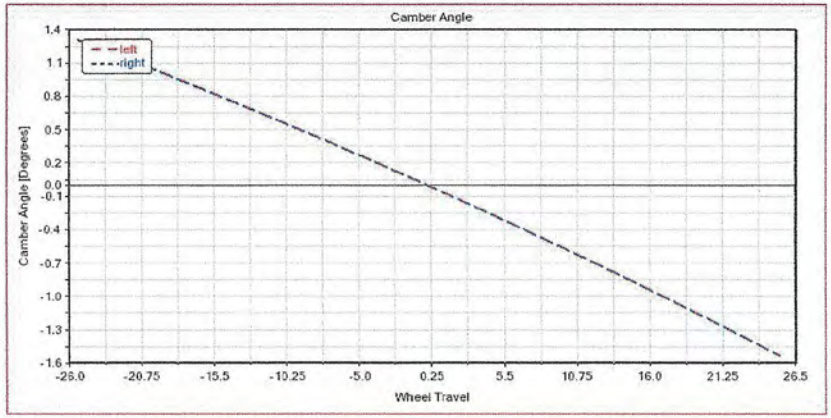

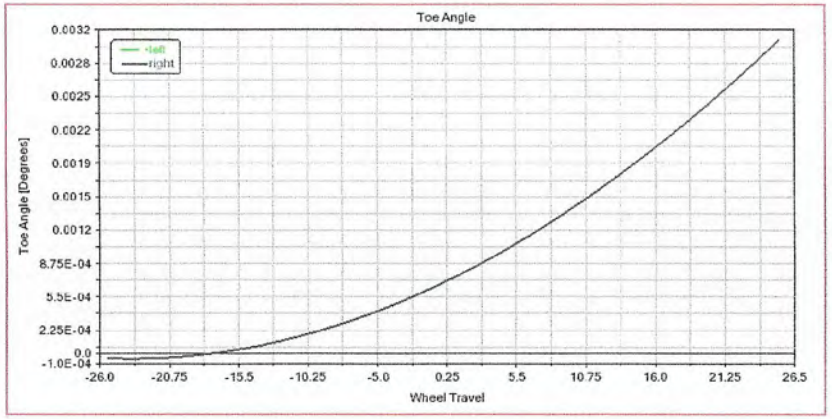

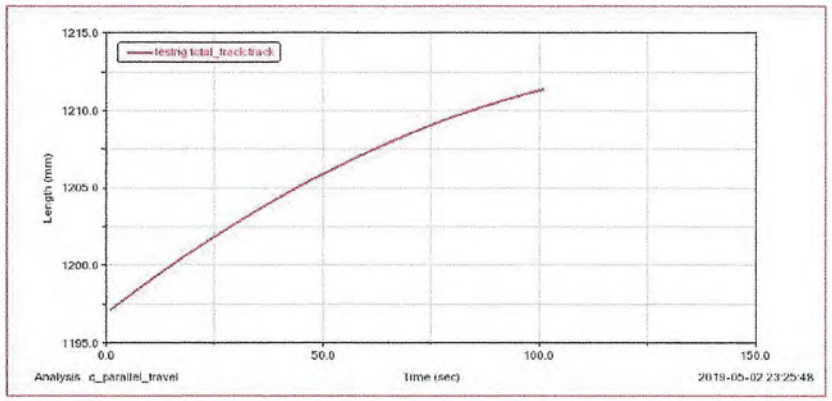

PARALLEL TRAVEL ANALYSIS

FRONT END

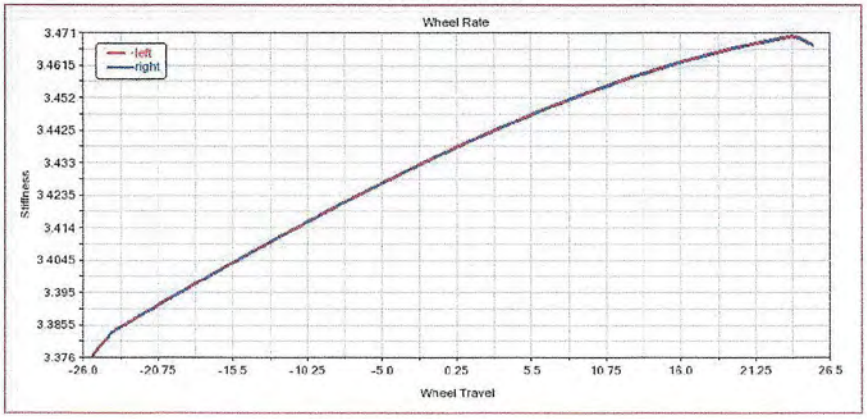

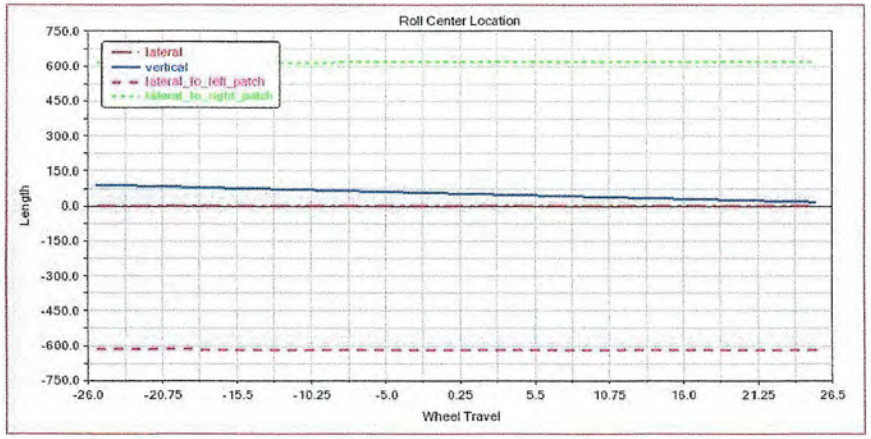

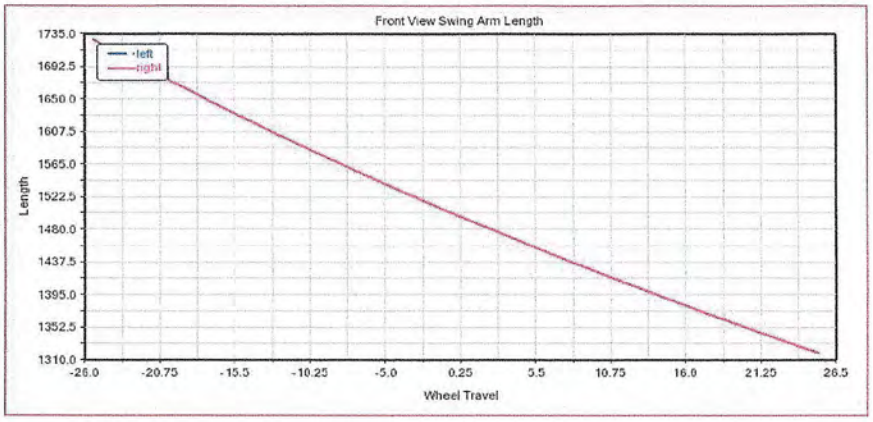

REAR END

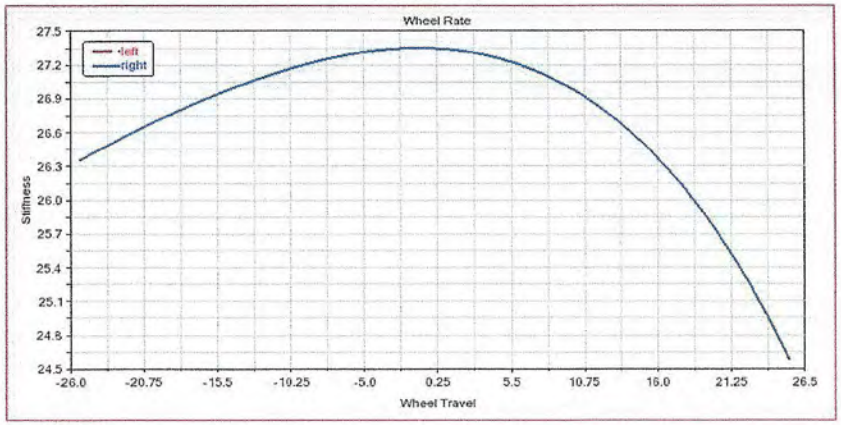

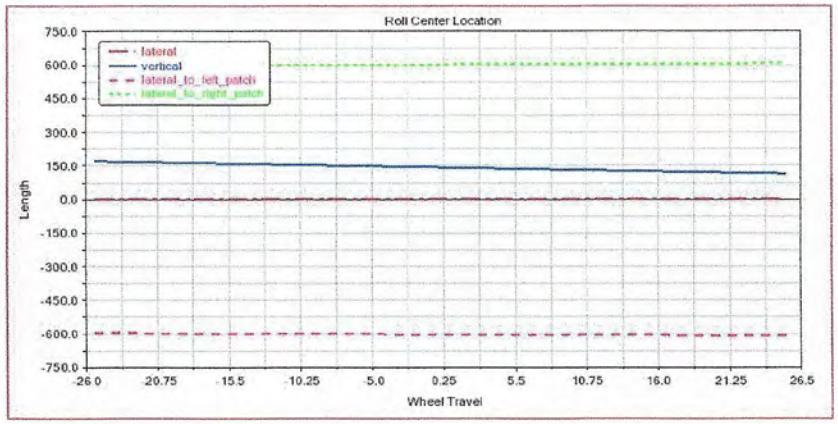

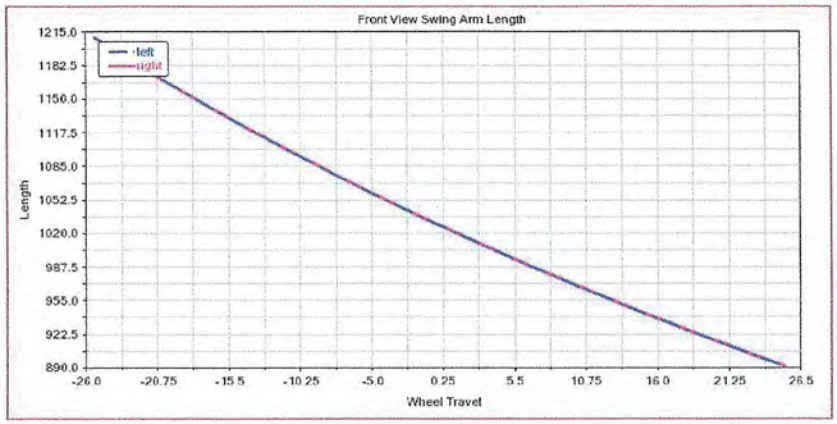

PARALLEL TRAVEL ANALYSIS

FRONT END

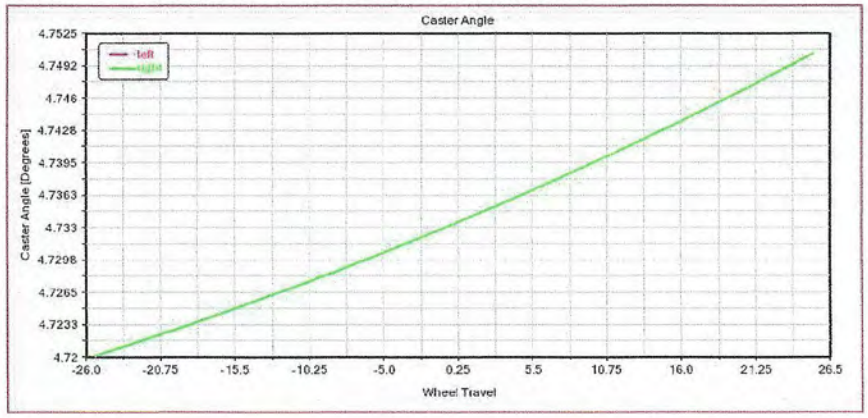

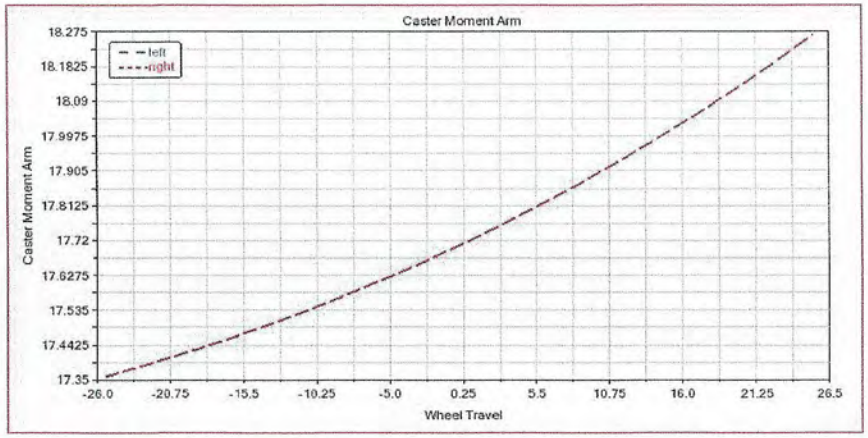

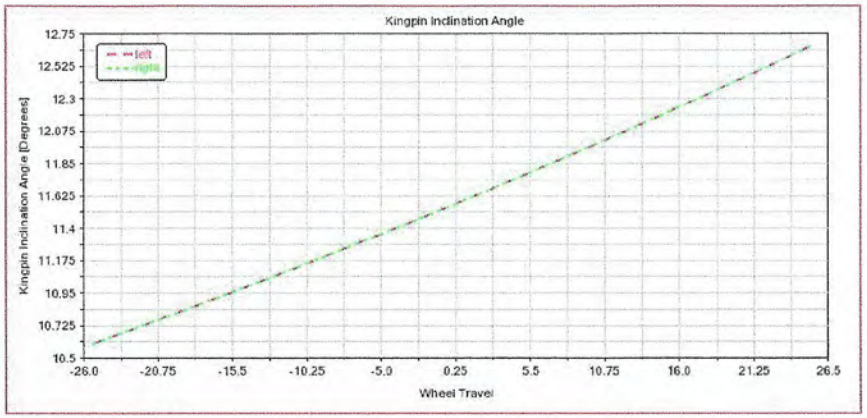

REAR END

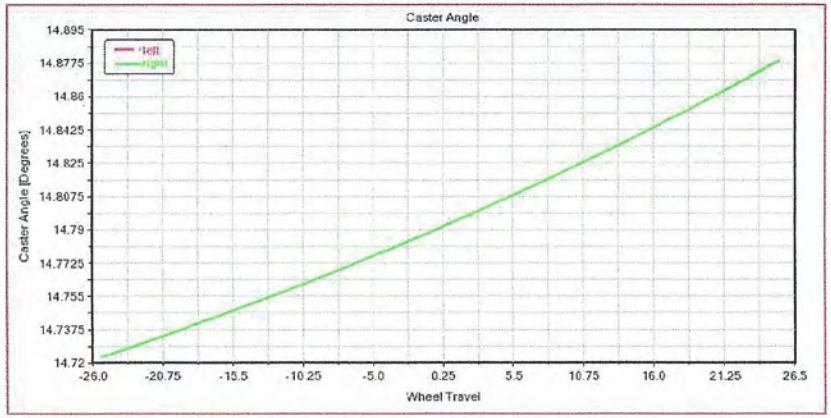

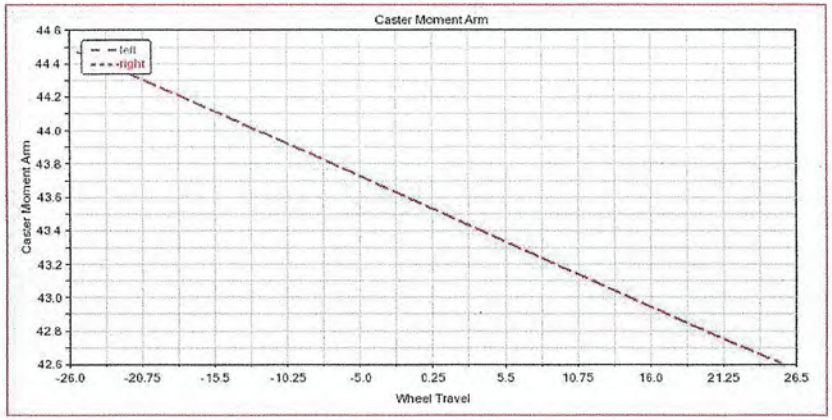

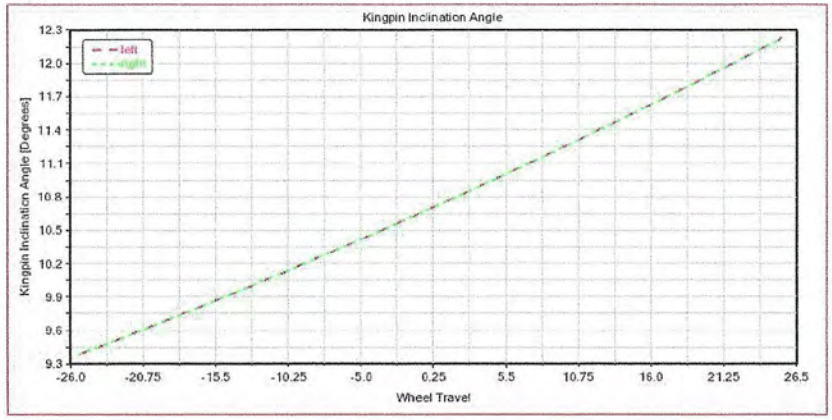

PARALLEL TRAVEL ANALYSIS

FRONT END

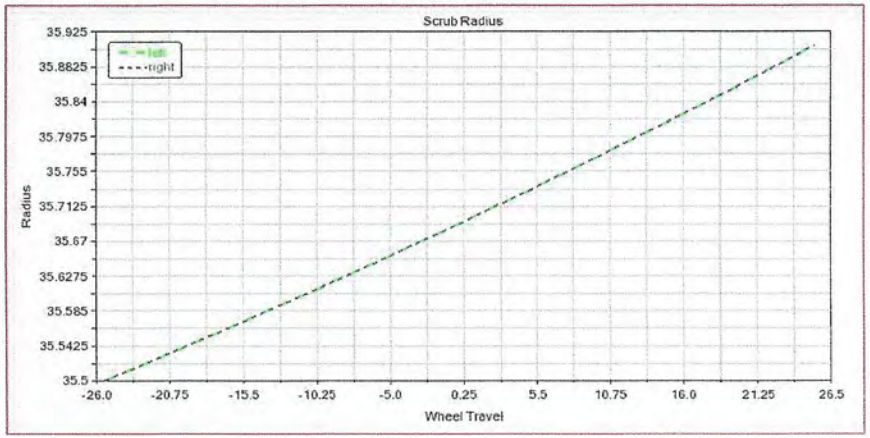

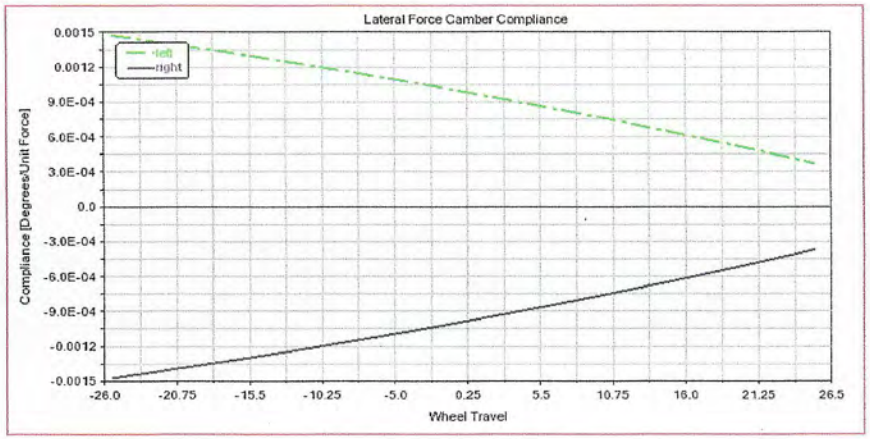

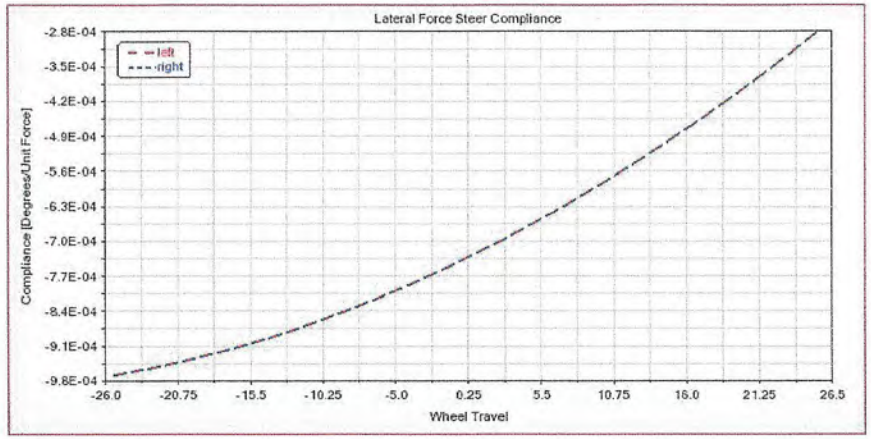

REAR END

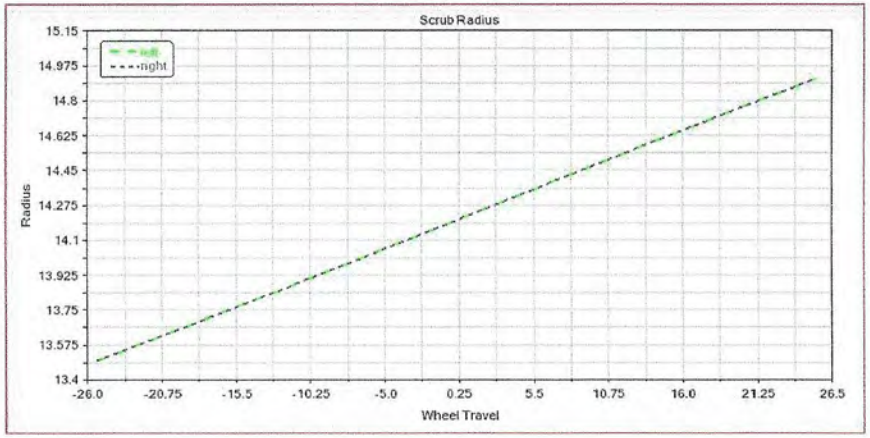

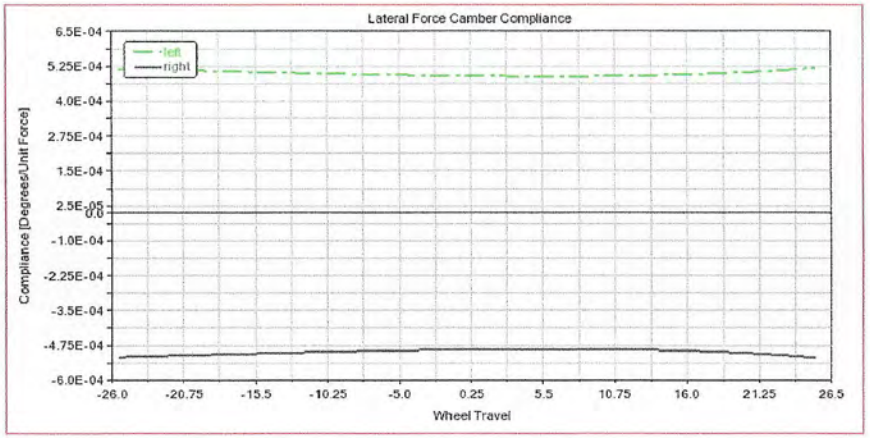

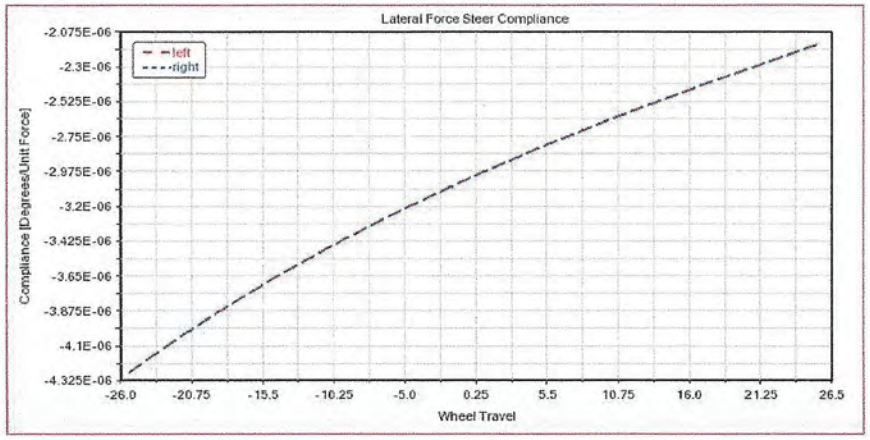

PARALLEL TRAVEL ANALYSIS

FRONT END

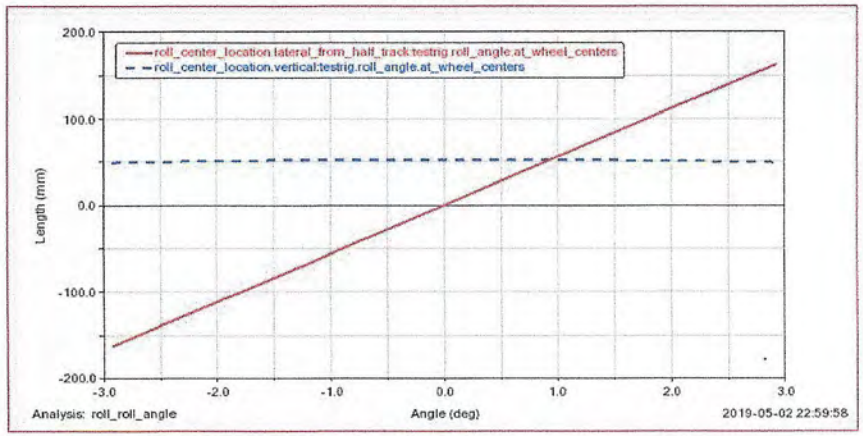

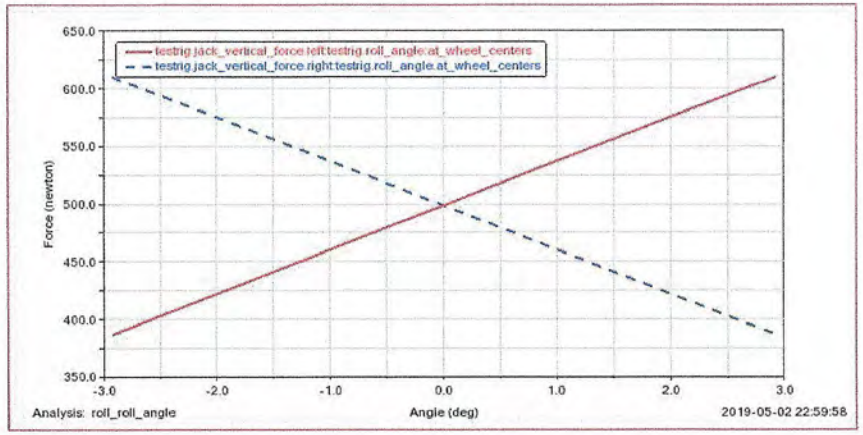

REAR END

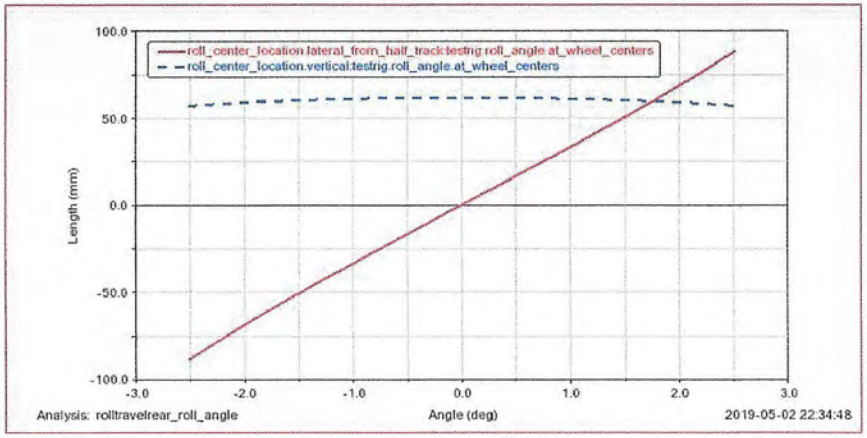

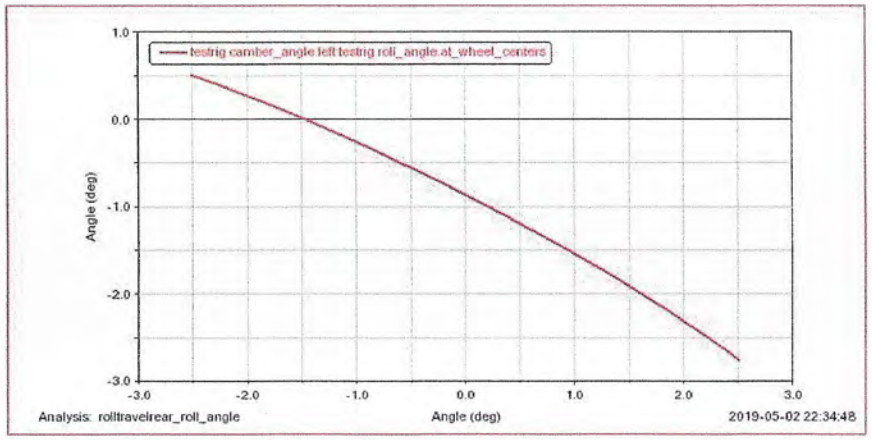

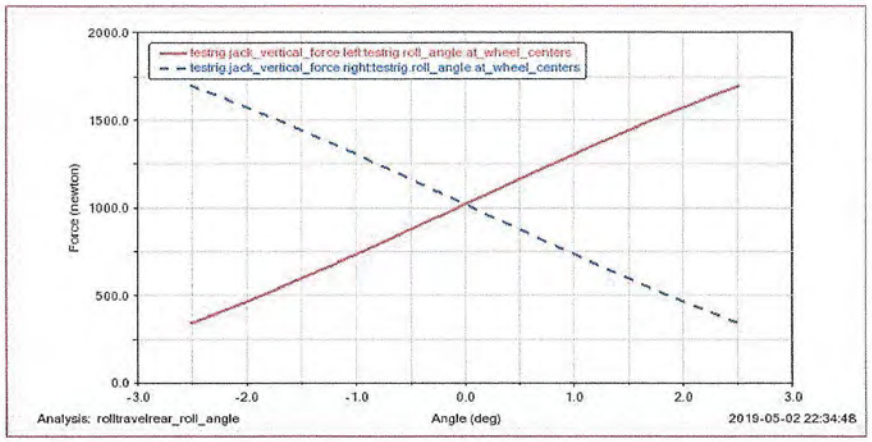

ROLL TRAVEL ANALYSIS

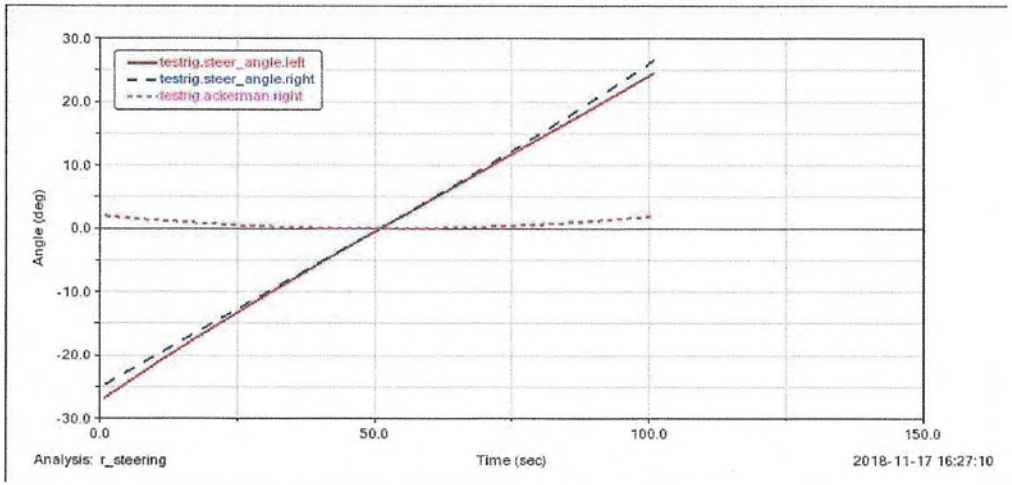

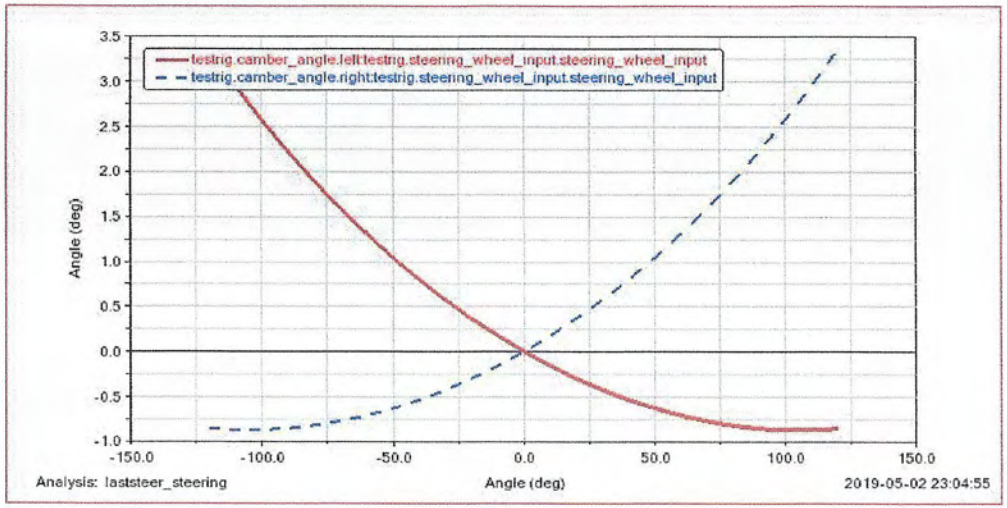

STEERING TRAVEL ANALYSIS

FSAE Design Spec Sheet

2019

Competitors: Please read the Instructions-Tips (tab below) prior to the completion and submission of this sheet.

Car No.	67
School	UNIVERSITY OF GUELPH

Dimensions	Units						
Overall Dimensions	mm	Length:	2670	Width:	1460	Height:	1072
Wheelbase & Track	mm	Wheelbase:	1550	Front Track:	1221	Rear Track:	1181
Center of Gravity Design Height	mm	CG Height:	260.0	Confirmed Via:	Unconfirmed (Solidworks Only)		
Mass without driver	kg	Front:	97.5	Rear:	97.5	Total:	195.0
Weight Distribution with 68kg driver		% Front:	50.0	% Left:	50.0		

Suspension Parameters	Units	Front			Rear		
Tire Size, Compound and Make		16x7.5-10	LCO	Hoosier	16x7.5-10	LCO	Hoosier
Wheels (diameter, width, material)	inch	Diamter (col D): Width (col E):	10.0	7.0	Diameter (col G): Width (col H):	10.0	7.0
Wheel material and construction		3 Piece Aluminum			3 Piece Aluminum		
Suspension Type		Double Wishbone Pullrod Actuated w/ ARB			Double Wishbone Pushrod Actuated w/ ARB		
Suspension design travel	mm	Jounce (col D): Rebound (col E):	25.4	25.4	Jounce (col G): Rebound (col H):	25.4	25.4
Wheel rate (chassis to wheel center)	N/mm	81			97		
Roll rate (chassis to wheel center)	Nm/deg	340			328		
Sprung mass natural frequency	Hz	4.50			4.81		
Jounce Damping	% critical	35-50	at __ mm/sec:	125	35-50	at __ mm/sec:	125
Rebound Damping	% critical	35-45	at __ mm/sec:	125	35-45	at __ mm/sec:	125
Motion ratio	_.__:1	0.87	Type:	Linear	0.79	Type:	Linear
Ride Camber (Rate of Camber Change)	deg/m	35.0			43.5		
Roll Camber	deg/deg	0.6			0.73		
Static Toe (- out, + in)	deg	0.50			0.00		
Static camber	deg	-1.00			-1.00		
Static camber adjustment method		Shimable frame mounts and upright			Shimable frame mounts		
Anti dive / Anti Squat	%	0			0		
Roll center height above ground, static	mm	41.5			86.4		
Roll center position at 1g lateral acc	mm	Height (col D): Lateral (col E):	38.9	63.8	Height (col G): Lateral (col H):	82.2	43.0
Front Caster, Trail, and Scrub Radius		Caster (deg):	5.0	Kin Trail (mm):	14.4	Scrub Rad (mm)	**19.7**
Front Kingpin Axis		Inclination (deg):	11.5	Offset (mm):	66.7		
Static Ackermann	%	0	Adjustable?	No			
Suspension Adjustment Methods		Adjustable suspension link lengths, shock preloads, ARB stiffnesses					
Steer Ratio, C-Factor, Steer Arm Length		Steer Ratio (x:1)	4.4	c-factor (mm)	88.9	Steer Arm Length	56 mm

Brake System / Hub & Axle	Units	Front			Rear		
Rotors		Floating 200.5mm OD x 4.54mm, drilled 1018			Floating 190.5mm OD x 4.54mm, drilled 1018		
Master Cylinder		Tilton 76-Series 1.0" Bore			Tilton 76-Series 1.0" Bore		
Calipers		Wilwood GP200 1.25" double piston			Wilwood PS-1 1.0" double piston		
Brake Pad/Lining Material		Wilwood BP-20			Wilwood Sintered Metallic		
Force and Pressures @ 1g Deceleration		Front Pres. (bar):	21.0	Rear Pres. (bar):	8.7	Pedal Force (kN)	215*10^-3
Upright Assembly		Billet 6061-T6 Machined			Billet 6061-T6 Machined		
Hub Bearings		Floating 6206-2RS, deep groove, 30x62x16			Floating 61814-2RZ, deep groove thin section, 70x90x10		
Axle type, size, and material		Billet 6061-T6Machined, Type III Anodize			Billet 6061-T6Machined, Type III Anodize		

Purpose: To estimate anticipated weight of new car based on proje

ITEM	POSITIVE	NEGATIVE
GRC18 Weight	453	
UNSPRUNG MASS CHANGES		
Tires		11.6
Rims		14
Hubs	2	
Uprights		0
Rotors		0
Calipers		
Linkages (x0.5)		
Half Shafts (x0.5)		
SPRUNG MASS CHANGES		
Frame	7	
Engine		
Cooling	2	
Intake		
Exhaust		
Tanks + Fluids		4
Fuel Delivery		
Shifting		
Driveline		1
Pedal Assembly	1.5	
Steering Assembly		1.5
Shocks + Bellcranks		2.5
Aero		
Linkages (x0.5)		
Half Shafts (x0.5)		
GRC19 WEIGHT:	430.9	
N.S.M. CHANGE:	-23.6	
S.M. CHANGE:	1.5	

Car Properties Inputs

GRC 2019

Dim.	Wheel Base			1550.00	mm
	Front Track			1220.70	
	Rear Track			1180.60	
Suspension Geometry Input		X	Y	Z	
Front	Lower	Chassis Aft	624.00	-243.82	110.70	mm
		Chassis Fore	887.10	-228.82	110.70	
		Upright	792.40	-559.56	111.40	
	Upper	Chassis Aft	625.00	-283.82	260.70	mm
		Chassis Fore	887.10	-268.83	260.70	
		Upright	779.65	-522.80	291.40	
	Pullrod Susp.	Bellcrank Chassis Pivot	711.57	-244.04	114.85	mm
		Bellcrank Pivot Axis	697.10	-248.08	114.85	
		Shock Bellcrank Mount	706.38	-225.48	176.93	
		Shock Chassis	649.00	-20.00	110.70	
		Pullrod Bellcrank Mount	720.33	-275.43	76.93	
		Pullrod Upright	779.65	-487.81	266.42	
	Steering	Tierod Upright	847.00	-559.60	144.00	mm
		Tierod Rack	820.00	-220.98	145.70	
		Rack Center	820.00	0.00	145.70	
	Wheel	Longitudinal Offset (X Dist.)	842.10			mm
		Half Track (Y Dist.)	-610.35			
		Rim Offset	12.70			
		Rim dia.	254.00			
		Tire Dia.	406.40			
		Tire Width	190.50			
		Static Camber	1.0			deg
		Static Toe	0.0			
Rear	Lower	Chassis Aft	-884.90	-248.82	127.70	mm
		Chassis Fore	-660.00	-248.82	127.70	
		Upright	-760.90	-548.70	118.70	
	Upper	Chassis Aft	-884.90	-303.53	245.00	mm
		Chassis Fore	-660.00	-303.53	245.00	
		Upright	-720.00	-519.45	273.70	
	Pushrod Susp.	Bellcrank Chassis Pivot	-707.60	-246.46	299.80	mm
		Bellcrank Pivot Axis	-729.26	-242.20	299.80	
		Shock Bellcrank Mount	-707.00	-243.20	364.70	
		Shock Chassis	-663.00	-20.00	353.00	
		Pushrod Bellcrank Mount	-714.20	-279.70	336.50	
		Pushrod Upright	-750.13	-462.08	178.00	
	Toe Link	Toe Link Upright	-825.40	-519.45	273.70	mm
		Toe Link Frame	-884.90	-303.53	245.00	
	Wheel	Longitudinal Offset (X Dist.)	-734.28			mm
		Half Track (Y Dist.)	-598.00			
		Rim Offset	12.7			
		Rim dia.	254.00			
		Tire Dia.	406.40			
		Tire Width	190.50			
		Static Camber	1.0			deg
		Static Toe	0.0			

Rim Specs 2019	Front	Rear	Comment
Width(in.)	7	7	
Diameter(in.)	10	10	
Offset(mm)	12.7	12.7	
PCD(in.) ((Diameter))	4.5	4.5	
Lug Diameter (in)	0.4375	0.4375	
Mounting Holes	5	5	
Center Hole Diam(In.)	3.5	3.5	

*** Analysing Right Components ***
i.e Y values should be Negative

Output Kinematic Properties Front

	Kinematic Outputs	X	Y	Z	
Front	Lower Chassis 2D Mount	842.10	-231.39	110.70	mm
	Lower Balljoint (Upright)	842.10	-559.56	111.40	
	Upper Chassis 2D Mount	842.10	-271.40	260.70	mm
	Upper Balljoint (Upright)	842.10	-522.80	291.40	
	Tire Centerline (Ground)	842.10	-610.35	203.20	mm
	Wheel Center	842.10	-606.80	203.20	
	Front View Instant Center	842.10	978.062	108.120	mm
	Roll Center	842.10	0.00	41.545	
	Fvsa Length		-1588.41		
	Fvsa Angle		3.43		deg
	King Pin Angle		-11.542		
	Scrub Radius		0.000		mm
	Side View Instant Center	#DIV/0!	-610.35	#DIV/0!	mm
	Svsa Length		#DIV/0!		
	Svsa Angle		#DIV/0!		deg
	Caster Angle		35.300		
	Mechanical Trail		-41.809		mm

Output Kinematic Properties Rear

	Kinematic Outputs	X	Y	Z	
Rear	Lower Chassis 2D Mount	-734.28	-248.82	127.70	mm
	Lower Balljoint (Upright)	-734.28	-548.70	118.70	
	Upper Chassis 2D Mount	-734.28	-303.53	245.00	mm
	Upper Balljoint (Upright)	-734.28	-519.45	273.70	
	Tire Centerline (Ground)	-734.28	-598.00	203.20	mm
	Wheel Center	-734.28	-594.45	203.20	
	Front View Instant Center	-734.28	426.500	147.968	mm
	Roll Center	-734.28	0.00	86.369	
	Fvsa Length		-1024.50		
	Fvsa Angle		3.09		deg
	Side View Instant Center	#DIV/0!	-598.00	#DIV/0!	mm
	Svsa Length		#DIV/0!		
	Svsa Angle		#DIV/0!		deg
	Caster Angle		-11.451		
	Mechanical Trail		-57.941		mm
	Toe Link Frame				mm

Output Link Lengths

	Link Geometry Output	Length	Unit
Front	Lower Aft Link	357.84	mm
	Lower Fore Link	344.03	
	Upper Aft Link	286.30	mm
	Upper Fore Link	277.47	
	Pullrod Link	290.74	mm
	Tierod Link	339.70	
Rear	Lower Aft Link	324.64	mm
	Lower Fore Link	316.53	
	Upper Aft Link	273.20	mm
	Upper Fore Link	225.94	
	Pullrod Link	244.29	mm
	Toe Link	225.80	

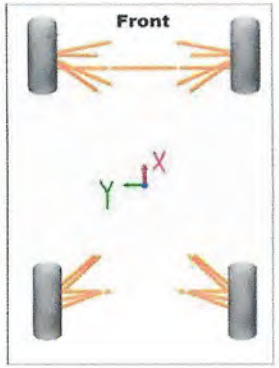

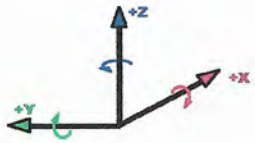

2019 Weights

	Item	Weight
	201p Total Mass (With Driver)	271.500
	2019 Mass	218.000
	2019 Sprung Mass	219.656
Rear	Rear Unsprung Assembly	13.219
	Rear Caliper + Pads	0.592
	Toe link + Auroras	0.196
	Pullrod + Auroras	0.220
	Upper A Arm	0.360
	Lower A Arm	0.410
	Rear Upright (incl bolts)	1.566
Front	Front Unsprung Assembly	12.703

*** Analysing Right Components ***
On Left Hand Turn

Car Properties Inputs

GBC 2018

Dim.	Wheel Base			1550.00	mm
	Front Track			1220.70	
	Rear Track			1190.60	
	Car Mass (With Driver)			271.50	kg
	Mass Distribution (Front)			50.00	%
	CG Z			260.00	mm
	CG Y			0.00	
Suspension Geometry (Inc.)		X	Y	Z	
Front – Lower	Chassis Aft	624.00	-243.82	110.70	mm
	Chassis Fore	887.10	-228.82	110.70	
	Upright	792.40	-559.56	111.40	
Front – Upper	Chassis Aft	625.00	-283.82	260.70	mm
	Chassis Fore	887.10	-263.83	260.70	
	Upright	779.65	-522.80	291.40	
Front – Pullrod Susp.	Bellcrank Chassis Pivot	711.57	-244.04	114.85	mm
	Bellcrank Pivot Axis	697.10	-248.08	114.85	
	Shock Bellcrank Mount	706.38	-225.48	176.93	
	Shock Chassis	649.00	-20.00	110.70	
	Pullrod Bellcrank Mount	720.33	-275.43	76.93	
	Pullrod Upright	779.65	-487.81	266.42	
Front – Steering	Tierod Upright	847.00	-559.60	144.00	mm
	Tierod Rack	820.00	-220.98	145.70	
	Rack Center	820.00	0.00	145.70	
Front – Wheel	Tire Dia.		520.70		mm
	Tire Width		206.00		
	Wheel Center	894.00	-852.90	261.01	
	Contact Patch	894.00	-810.35	0.00	
	Upright Orgin	894.00	-607.64	259.56	
	Wheel Bearing Effective Dist.	894.00	-564.64	228.56	
Rear – Lower	Chassis Aft	-884.90	-248.82	127.70	mm
	Chassis Fore	-660.00	-248.82	127.70	
	Upright	-760.90	-548.70	118.70	
Rear – Upper	Chassis Aft	-884.90	-303.53	245.00	mm
	Chassis Fore	-660.00	-303.53	245.00	
	Upright	-720.00	-519.45	273.70	
Rear – Pullrod Susp.	Bellcrank Chassis Pivot	-707.60	-246.46	299.80	mm
	Bellcrank Pivot Axis	-729.26	-242.20	299.80	
	Shock Bellcrank Mount	-707.00	-243.20	364.70	
	Shock Chassis	-663.00	-20.00	353.00	
	Pullrod Bellcrank Mount	-714.20	-279.70	336.50	
	Pullrod Upright	-750.13	-462.08	178.00	
Rear – Toe Link	Toe Link Upright	-825.40	-519.45	273.70	mm
	Toe Link Frame	-684.90	-303.53	245.00	
Rear – Wheel	Tire Dia.		520.70		mm
	Tire Width		206.00		
	Wheel Center	-734.24	-616.80	261.01	
	Contact Patch	-734.27	-590.30	0.00	
	Upright Orgin	-734.27	-593.80	260.72	
	Wheel Bearing Effective Dist.	-734.27	-581.30	226.72	

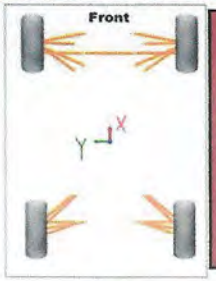

Keep your coordinates in mind!!

Braking

		Front	Rear	Units
Dim.	Braking G's	2.0		Accel.
	Friction Coeff.	2.000	2.000	
	Long. Mass Transfer (One Wheel)	**45.542**	**-45.542**	kg
	Long. Total Mass of (One Wheel)	113.417	22.333	
	Long. Verticle Load (One Wheel Z)	1112.62	219.09	N
	Friction Force at Tire (X)	-2225.24	-438.17	
	My about Wheel From Braking	-579.34	-114.08	Nm
	Caliper Radius	108.090	91.800	m
	Braking Force on Upright	-5315.55	-1242.69	N

Lateral Force

		Front	Rear	Units
Dim.	Lateral G's	2.0		Accel.
	Friction Coeff.	2.000	2.000	
	Lateral Mass Transfer (One Wheel)	**57.827**	**59.792**	kg
	Lateral Mass (One Wheel)	125.702	127.667	
	Lateral Verticle Load (One Wheel Z)	1233.341	1252.410	N
	Friction Force At Tire (Y)	2466.283	2504.819	
	Mx about Wheel From Lateral	642.097	652.130	Nm

Bump Condition

		Front	Rear	Units
Dim.	Bump G's	3.0		Accel.
	Lateral Verticlal Load (One Wheel Z)	1997.561	1997.561	N

Combined Loads

		Front	Rear	Units
Dim.	Total Mass (One Wheel)	**171.244**	**82.125**	kg
	Combined Vertical Load (One Wheel Z)	**1678.908**	**805.643**	N
	Friction Force At Tire (Y)	**3359.815**	**1611.287**	
	Friction Force at Tire (X)	**-3359.82**	**-1611.29**	

Output A Arm Axial Force Front (Right Front)

Lower Aft Link	5098.98	N	Compression
Lower Fore Link	4180.61		Tension
Upper Aft Link	5413.08		Compression
Upper Fore Link	5065.14		Compression
Tierod Link	3700.14		Compression
Pullrod Link	6862.93		Tension

Output A Arm Axial Force Rear (Right Rear)

Lower Aft Link	8017.22	N	Compression
Lower Fore Link	-5014.76		Tension
Upper Aft Link	584.98		Tension
Upper Fore Link	604.32		Compression
Toe Link	323.86		Compression
Pullrod Link	6362.73		Compression

Reaction Force Components (Right Front)

	X	Y	Z	Units
Upper A Arm Reaction	1421.39	-3646.90	466.61	N
Lower A Arm Reaction	3530.72	472.51	3.45	
Tie Rod	-204.09	-3588.34	-18.53	
Pullrod	1298.23	-6647.97	4147.02	
Braking Force on Upright		475.00		Nm

Reaction Force Components (Right Rear)

	X	Y	Z	Units
Upper A Arm Reaction	-747.62	698.74	8.27	N
Lower A Arm Reaction	-2947.63	1001.94	-41.00	
Toe Link	98.48	314.13	-28.20	
Pullrod	647.38	3255.31	-2829.35	
Braking Force on Upright		475.00		Nm

Upright Wheel Bearing Forces (Right Front)

	X	Y	Z	Units
Inboard Bearing	3905.77	0.00	15339.81	N
Outboard Bearing	-3905.77	0.00	-15339.81	
Magnitude		15831.97		

Upright Wheel Bearing Forces (Right Rear)

	X	Y	Z	Units
Inboard Bearing	1484.32	0.00	14224.64	N
Outboard Bearing	-1484.32	0.00	-14224.64	
Magnitude		14303.97		

Front Unit Vectors

	X	Y	Z
Lower Aft	-0.421	0.882	-0.002
Lower Fore	0.275	0.961	-0.002
Upper Aft	-0.540	0.835	-0.107
Upper Fore	0.387	0.915	-0.111
Tierod	0.079	0.997	0.005
Pullrod	-0.204	0.730	-0.652

Front "A" Matrix

						"B"		
-0.471	0.275	-0.540	0.387	0.079	-0.204	-3359.815	Fx	Forces acting at the contact patch, Moment about car origin
0.882	0.961	0.835	0.915	0.997	0.730	3359.815	Fy	
-0.002	-0.002	-0.107	-0.111	0.005	-0.652	3627.469	Fz	
-0.097	-0.106	-0.187	-0.209	-0.146	0.123	-2244.543	Mx	
-0.051	0.032	-0.074	0.199	0.007	0.454	-3287.657	My	
0.436	0.916	0.368	0.916	0.889	0.470	953.012	Mz	

Output Front Link Lengths

	Link Geometry Output	Length	Units
Front	**Lower Aft Link**	**357.842**	mm
	Lower Fore Link	**344.031**	
	Upper Aft Link	**286.305**	mm
	Upper Fore Link	**277.472**	
	Tierod Link	**339.699**	mm
	Pullrod Link	**290.741**	

Force Components (Right Front)

	X	Y	Z	
Lower Aft Link	-2281.42	3872.67	-8.92	N
Lower Fore Link	-3140.53	-4000.06	3.47	
Upper Aft Link	-1643.59	2616.40	765.98	
Upper Fore Link	922.17	988.06	-420.64	
Toe Link	290.50	3028.38	18.52	
Pullrod Link	1298.23	-6647.97	4147.02	

Rear Unit Vectors

	X	Y	Z
Lower Aft	-0.382	0.924	0.028
Lower Fore	0.919	0.947	0.028
Upper Aft	-0.604	0.790	-0.105
Upper Fore	0.266	0.956	-0.127
Toe Link	-0.264	-0.936	0.127
Pullrod	0.147	0.747	0.649

Rear "A" Matrix

						"B"		
-0.382	0.319	-0.604	0.266	-0.264	0.147	-1611.287	Fx	Forces acting at the contact patch, Moment about car origin
0.924	0.947	0.790	0.956	-0.956	0.747	1611.287	Fy	
0.028	0.028	-0.105	-0.127	0.127	0.649	2803.205	Fz	
-0.125	-0.128	-0.162	-0.196	0.196	-0.433	-1854.732	Mx	
-0.024	0.039	-0.241	-0.019	0.033	0.513	2058.309	My	
-0.912	-0.546	-0.883	-0.550	0.652	-0.492	-2134.262	Mz	

Output Link Lengths

	Link Geometry Output	Length	Units
Rear	**Lower Aft Link**	**324.635**	mm
	Lower Fore Link	**316.528**	
	Angle		deg
	Upper Aft Link	**273.202**	mm
	Upper Fore Link	**225.936**	
	Angle		deg
	Toe Link	**225.804**	mm
	Pullrod Link	**244.286**	mm

Force Components (Right Rear)

	X	Y	Z	
Lower Aft Link	-1441.46	3248.07	87.52	N
Lower Fore Link	-1599.56	-4751.03	142.59	
Upper Aft Link	594.32	694.47	92.96	
Upper Fore Link	215.72	769.11	-102.23	
Toe Link	-98.48	-212.13	28.20	
Pullrod Link	647.38	3255.31	-2829.35	

Moments About Upright Origin (Right Front)

Mx	205.63	Nm
My	Bearing	Nm
Mz	-152.07	Nm

Front Bearing Force Specs

Mx	**Fy Moment Arm**	259.560	mm
	Fz Moment Arm	45.260	
Mz	**Fx Moment Arm**	45.260	
	Fy Moment Arm	0.000	
Bearing Spacing		46.000	

Moments About Upright Origin (Right Rear)

Mx	355.02	Nm
My	Bearing	Nm
Mz	-97.11	Nm

Rear Bearing Force Specs

Mx	**Fy Moment Arm**	260.720	mm
	Fz Moment Arm	23.000	
Mz	**Fx Moment Arm**	23.000	
	Fy Moment Arm	-0.030	
Bearing Spacing		25.000	

Input

Dim.	Wheel base		1550.00	mm
	Front Track		1220.6	
	Rear track		1180.6	
Mass and Inertia	Total mass		271.50	kg
	Total Mass distribution		50.00	% Fr
	Front non suspended mass (per wheel)		12.70	kg
	Rear non suspended mass (per wheel)		13.47	kg
	Non suspended mass weight distribution		50.00	% Fr
	Total mass CG height		260	mm
	Front non suspended mass CG height		195	
	Rear non suspended mass CG height		210	
	Suspended Mass		219.16	kg
	Suspended mass weight distribution		50.00	% Fr
	Suspended mass CG coordinates	X	775.00	mm
		Y	0.00	
		Z	280.00	
	Suspended mass roll inertia (ref SM CG) - I_{xx}		200.00	kg.m²
Spring ARB Tire	Front spring stiffness		70.00	N/mm
	Rear spring stiffness		70.00	
	Front ARB stiffness		120.50	N/mm
	Rear ARB stiffness		119.60	
	Front tire stiffness		115.00	N/mm
	Rear tire stiffness		115.00	
M.R.	Front spring motion ratio		1.210	mm/mm
	Rear spring motion ratio		1.300	
	Front anti roll bar motion ratio		1.500	mm/mm
	Rear anti roll bar motion ratio		1.500	
Roll	**Front** roll center height		41.5454	mm
	Rear roll center height		86.400	

Aero	Down Force Coefficient	0	-
	Down Force Distribution	0	% Fr
	Air Density	1.2255	kg/m³
	Frontal Area	0.85	m²
	Speed	187.2	km/h
	Total Down Force	0.00	Kg

Case to simulate		
Lat G	2.00	G

Error message box

Results

Roll	Suspended mass roll stiffness	0.83	°/g
	Roll angle	1.66	°Roll
Frequency & Damping	Front **NSM** frequency	15.14	Hz
	Rear **NSM** frequency	14.71	Hz
	Front **NSM** Critical damping	2.42	N/(mm/s)
	Rear **NSM** Critical damping	2.49	N/(mm/s)
	Front **SM** frequency	4.70	Hz
	Rear **SM** frequency	4.38	Hz
	Front **SM** critical damping	3.24	N/(mm/s)
	Rear **SM** critical damping	3.01	N/(mm/s)
	70% Front **SM** crit. Damp. @ Wheel	2.27	N/(mm/s)
	70% Rear **SM** crit. Damp. @ Wheel	2.11	N/(mm/s)
	70% Front **SM** crit. Damp. @ Damper	2.7417	N/(mm/s)
	70% Rear **SM** crit. Damp. @ Damper	2.7417	N/(mm/s)
	Roll natural frequency of **SM**	5.13	Hz
M.N.	1st magic number	52.85	N.m/N.m
	2nd magic number	[redacted]	
	3rd magic number	52.18	
	1st magic number	52.02	kg/kg
	2nd magic number	47.14	
	3rd magic number	46.70	

No Tire Coupling	
Dynamic Load (Kg)	
11.3	124.4
4.4	131.3

Tire Coupling	
Dynamic Load (Kg)	
11.8	123.9
3.9	131.9

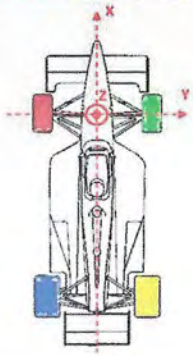

No Tires coupling

Roll

Roll angle due to lat G		0.24	°
Roll moment		928.9	N.m
Roll Gradient		0.12	°/g
Anti-roll moment total		3811.5	N.m/°
A-R moment coming from	Front springs	621.7	N.m/°
	Rear springs	503.9	N.m/°
	Total	1125.5	N.m/°
A-R moment coming from	Front ARB	1392.7	N.m/°
	Rear ARB	1293.2	N.m/°
	Total	2686.0	N.m/°

Weight Transfer

Total W.T.	**Front**		
	Lateral	56.6	kg
	Rear		
	Lateral	63.4	kg
NSM - W.T.	**Front**		
	Lateral	8.1	kg
	Rear		
	Lateral	9.6	kg
El. W.T.	**Front**		
	Lateral	41.0	kg
	Rear		
	Lateral	37.8	kg
Geo. W.T.	**Front**		
	Lateral	7.5	kg
	Rear		
	Lateral	16.0	kg

Additional values

Front wheel rate	47.811	N/mm
Rear wheel rate	41.420	N/mm
Z Distance from SM CG to **front** roll axis	238	mm
Z Distance from SM CG to **rear** roll axis	194	mm
Z Distance from SM CG to roll axis **@ SM CG**	216.03	mm
Suspended mass inertia in roll - I_{roll}	210.2	kg.m²

Spring Stiffness	
K (lb/in)	K (N/mm)
600	105.08
550	96.32
500	87.56
450	78.81
400	70.05
350	61.29
300	52.54
250	43.78
200	35.03
150	26.27
100	17.51
50	8.76
0	0.00

Tires coupling

Roll

Roll angle due to lat G		0.56	°
Roll moment		928.9	N.m
Roll Gradient		0.28	°/g
Anti-roll moment total		1644.8	N.m/°
A-R moment coming from	Front springs	621.7	N.m/°
	Rear springs	503.9	N.m/°
	Total	1125.5	N.m/°
A-R moment coming from	Front ARB	1392.7	N.m/°
	Rear ARB	1293.2	N.m/°
	Total	2686.0	N.m/°
A-R moment coming from	Front Tires	1495.3	N.m/°
	Rear Tires	1398.9	N.m/°
	Total	2894.3	N.m/°
A-R in Series with tires	Front Axle	858.2	N.m/°
	Rear Axle	786.6	N.m/°
	Total	1644.8	N.m/°

Weight Transfer

Total W.T.	**Front**		
	Lateral	56.1	kg
	Rear		
	Lateral	64.0	kg
NSM - W.T.	**Front**		
	Lateral	8.1	kg
	Rear		
	Lateral	9.6	kg
El. W.T.	**Front**		
	Lateral	40.5	kg
	Rear		
	Lateral	38.4	kg
Geo. W.T.	**Front**		
	Lateral	7.5	kg
	Rear		
	Lateral	16.0	kg

Additional values

Front wheel rate (in series with tire)	33.77	N/mm
Rear wheel rate (in series with tire)	30.45	N/mm

VARIABLE	OUTSIDE TIRE	INSIDE TIRE	UNITS
Mz	68	68	N.m
Pneumatic Trail	0.03	0.03	m
Mechanical Trail	0.04	0.04	m
Steering Pickup Length	0.055		m
Steer Angle (δ)	22.3	24.5	deg.
Tie-Rod Length	0.316		m
Tie-Rod Angle (θ)	18	14	deg.
Pinion Gear Pitch Radius	0.012		m
Steering Wheel Width	0.12		m
SYSTEM FORCES			
Resultant Lateral Force on Tire	971.43	971.43	N
Force on Upright Pickup	1236.36	1236.36	N
Tie-Rod Force	1239.85	1579.80	N
Axial Force at Rack Clevis	1179.17	1532.87	N
Transverse Force at Rack Clevis	383.14	382.19	N
Axial Force Reacted By Pinion	2712.04		N
Force at Steering Wheel	271.20		N

Sources of Inaccuracy
How are Mz's and pneumatic trail determined?

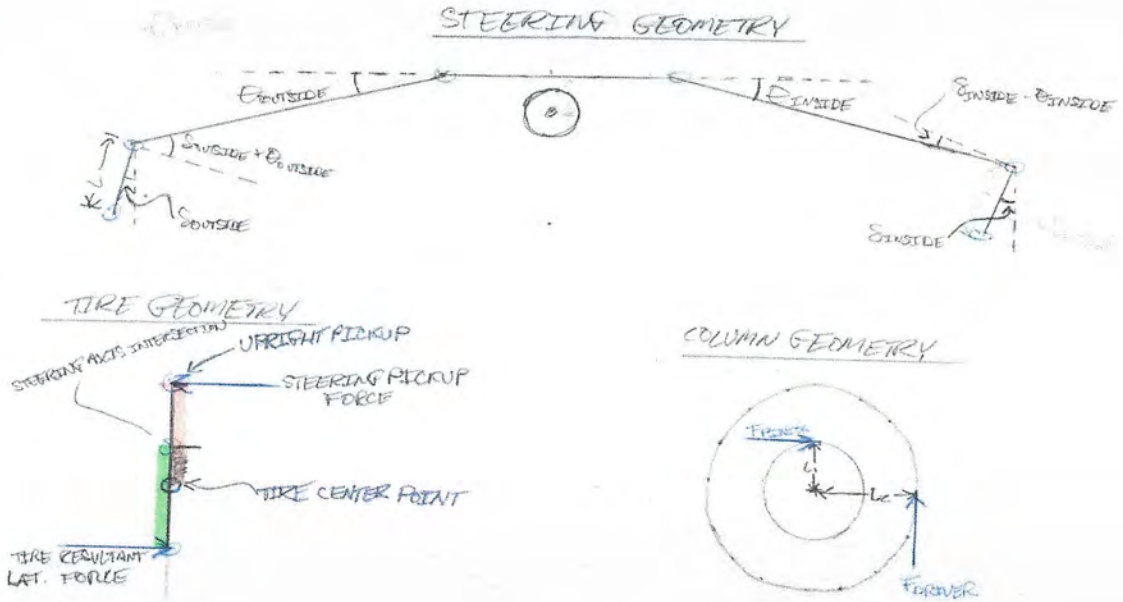

VARIABLE		UNITS
Wheelbase	1.55	m
Rear Track	1.18	m
Front Track	1.196	m
Rear Inside Slip Angle	3.4	deg.
Rear Outside Slip Angle	4.2	deg.
Front Inside Slip Angle	7.3	deg.
Front Outside Slip Angle	8.1	deg.
Turn Radius	4	m
REQUIRED GEOMETRY		
Inside Steering Angle	24.63	deg.
Outside Steering Angle	21.59	deg.
Ackermann Angle	3.05	deg.

Sources of Inaccuracy
What slip angles should be used?

VARIABLE		UNITS
CG X-Location	0.8	m
CG Y-Location	0	m
Rear Inside Fx	1000	N
Rear Inside Fy	1200	N
Rear Inside Mz	50	N.m
Rear Outside Fx	1500	N
Rear Outside Fy	2000	N
Rear Outside Mz	50	N.m
Front Inside Fx	1000	N
Front Inside Fy	1400	N
Front Inside Mz	50	N.m
Front Outside Fx	1300	N
Front Outside Fy	1700	N
Front Outside Mz	50	N.m
Aerodynamic Mz	100	N.m
Yaw Moment	8035.4	N.m

Counterclockwise Rotation is Positive
CG X-Location is distance from back of car to CG
Positive CG Y is towards the outside of the car

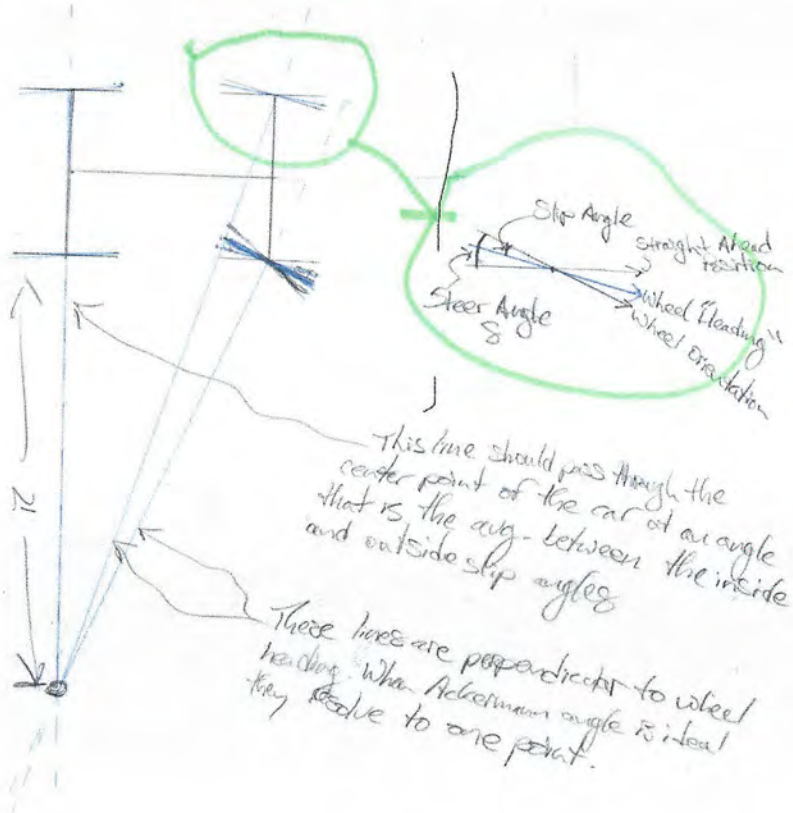

Steering Column Nonlinearity

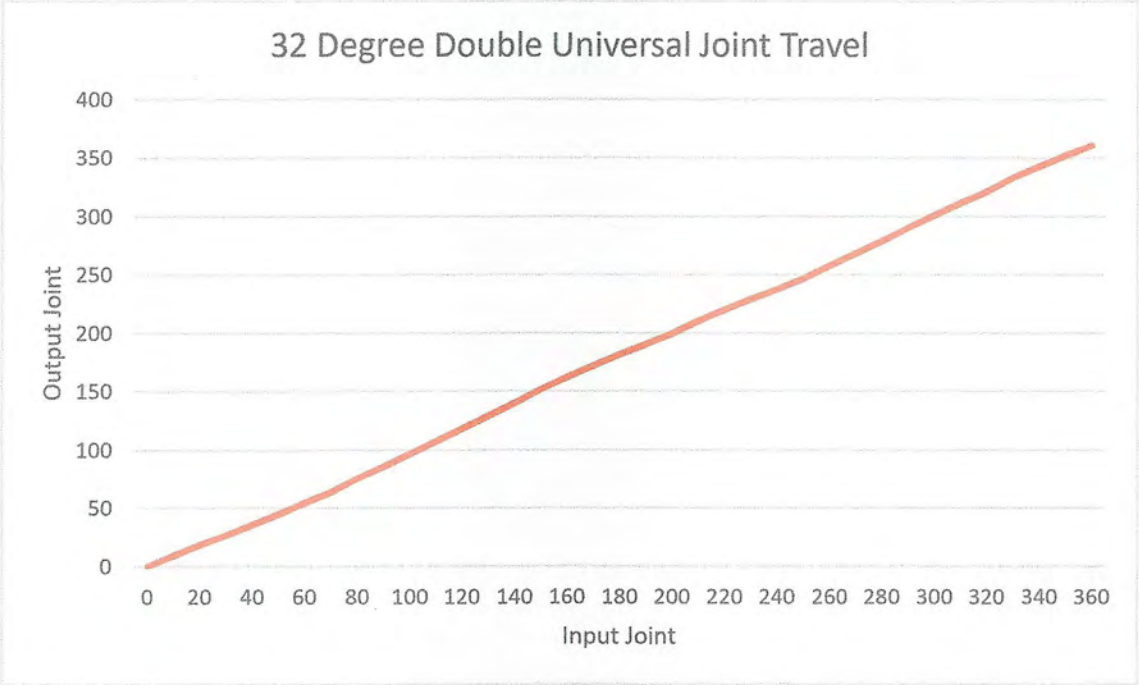

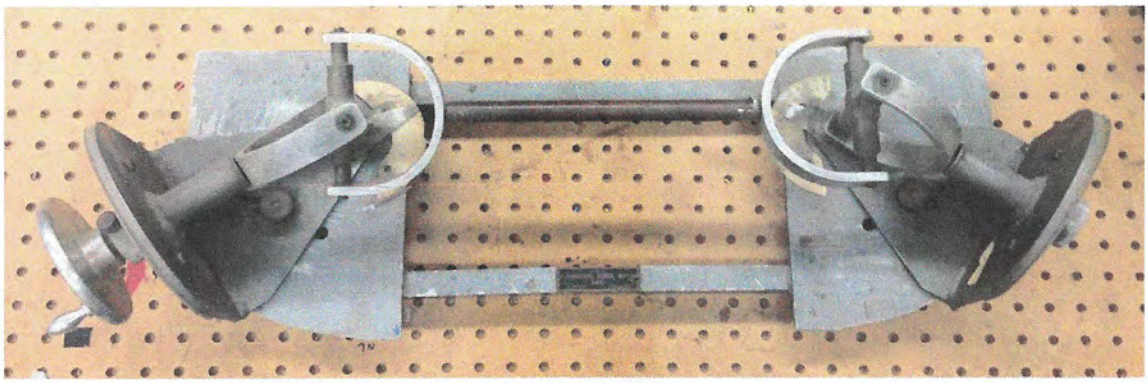

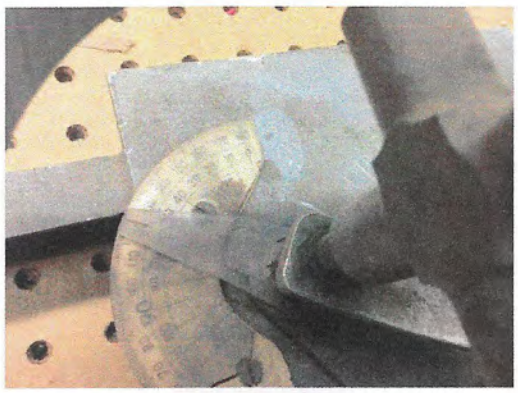

Test Apparatus

Spring Rate Verification

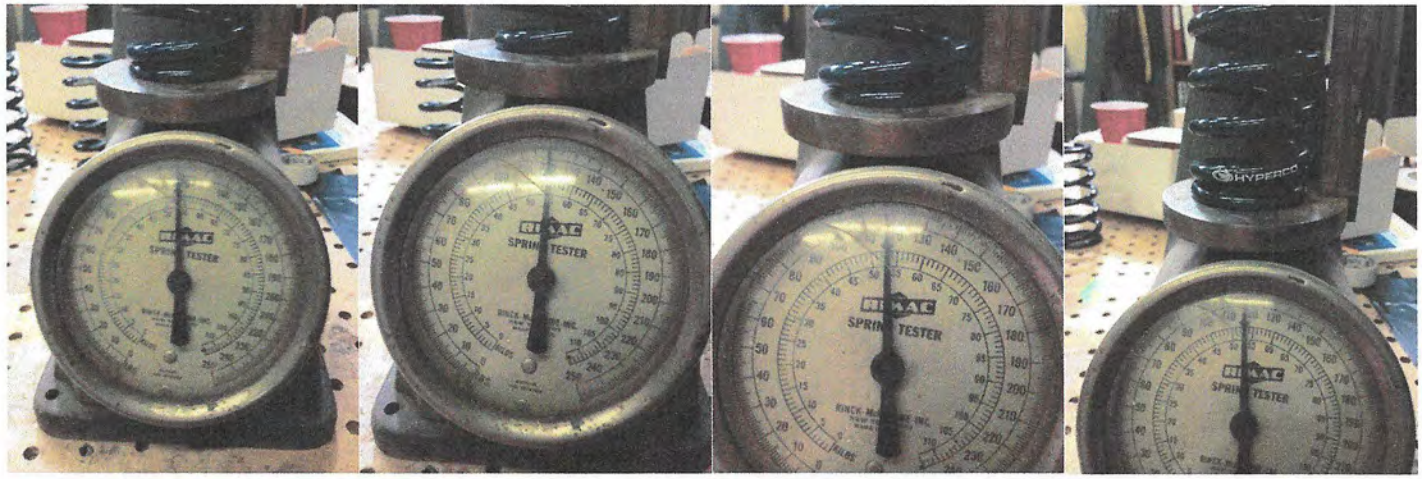

Spring Compression of Approx 0.4" from Contact

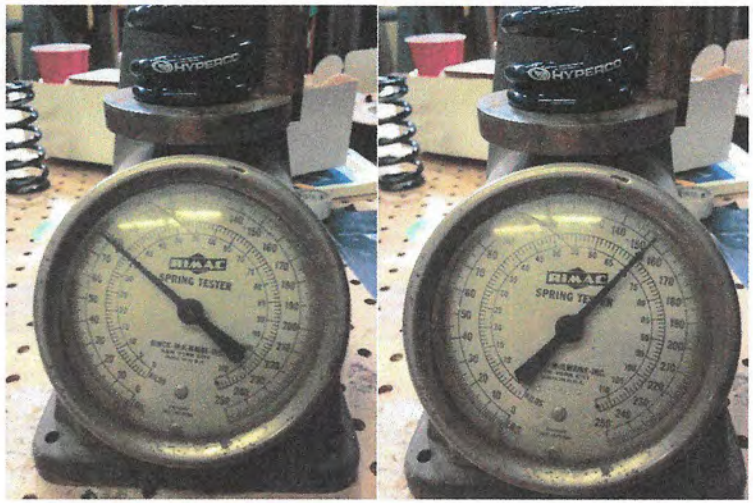

Spring Compression with 0.25" Difference

Modeling and Testing of a Shock Dynamometer

ENGG 4220

Interdisciplinary Mechanical Engineering Design

Winter 2019

Hari Simha PhD, PEng

Lindsay Burton - 0882880

Orion Miller - 0939412

Ben Tory-Pratt - 0897555

Austin Van Rossum - 0710438

Table of Contents

1 Introduction & Background

1.1 Introduction 1

1.2 Background Theory and Concept 1

2 Detailed Design

2.1 Apparatus Design And Programming 4

2.2 Mechanical Design 5

2.3 Structural Analysis 6

2.4 Electrical Design 9

3 Modeling Details

3.1 MATLAB Model and Test Results 11

4 Testing and Design Evaluation

4.1 Discussion 14

4.2 Future Changes and Recommendations 16

4.3 Conclusion and Closing Comments 16

5 Appendices

5.1 Appendix A – Drawings 17

5.2 Appendix B – Bill of Materials 19

5.3 Appendix C – Matlab Code 20

1- Introduction & Background

1.1 - Introduction

The following report details the design, methods of testing and results of a non-linear dampener testing apparatus. This testing apparatus was inherited from the work of a previous student group and it has been refined and improved through this project. The apparatus as seen consists of a dampener connected to a velocity input. The velocity input consists of a scotch-yoke mechanism driven by a 12 Volt motor. The scotch-yoke mechanism provides a sinusoidal velocity input which will give the varying velocity input that is required to test the responsiveness of the non-linear dampening mechanism. The motor and sensors are controlled through a motor controller and Arduinos, while the data collected through the sensors is catalogued real-time through computers connected to the Arduinos.

The changes that were made from the original apparatus consist of a new base, new strain gauge and some refinements to existing components. The new base was manufactured so as to provide a sound structure for the upright tubing to connect into. The base will also provide a foundation to absorb vibration and prevent any secondary movement caused by the operation of the motor. The new strain gauge was selected as it provided a more suitable weight range and thus would provide more accurate measurements than the strain gauge used by the previous group. Other various components were adjusted for ease of usability and accommodation of new sensors and configurations. Most notably, a plexiglass box was added to house the wiring, Arduinos, LEDs, motor controller and switches.

The apparatus incorporates two main physics concepts; the electrical control system and the mechanical inputs to the dampener. The electrical system directly controls the speed of the motor which in turn influences the velocity inputs to the dampener. The sensors then measure the force reactions and displacement. The mechanical and electrical systems are inseparable as they work together to simulate various velocity conditions that the dampener may experience when used in practical applications.

1.2 – Background Theory and Concept

The Ohlins TTX25 dampers being tested are used for shock absorption in FSAE race cars. The damping of the shock plays a significant role in tuning the response of the vehicle to expected conditions. Shown below is a diagram of a quarter car model, the standard way of modeling a suspension system.

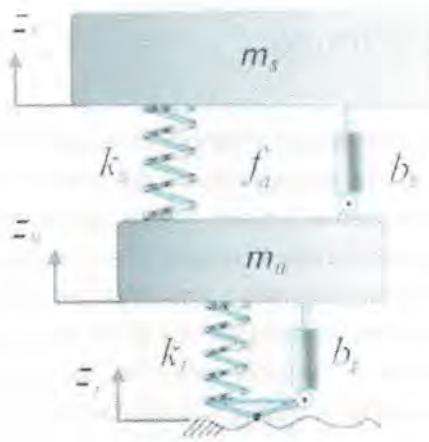

Figure 1: Quarter Car Suspension Model

The two masses seen are the sprung and unsprung masses. The sprung mass used is one quarter of all the vehicle mass which is *supported* by the suspension, i.e. the chassis, engine, driver, whereas the unsprung mass includes the mass *controlled* by the suspension, i.e. the wheel, upright, and hub. Components which connect these two masses, such as control arms, suspension linkages, and driveshafts can be treated as being partly sprung and partly unsprung. The most accurate method for doing this is to look at the center of mass of one of these components and see how much displacement it has relative to the wheel assembly during suspension travel. For example, if during an upward bump motion, the wheel has a displacement of 25 mm and the center of mass of an a-arm moves 15 mm upward, that component contributes 60 % of its mass to the unsprung mass, and the remainder to sprung mass.

The spring and damper with the "t" subscript are the stiffness and damping associated with the tire. These are dependent on factors like the tire construction and pressure. The spring and damper with the "s" subscript are the stiffness and damping of the shock. These are typically termed as the "wheel rate" and "wheel damping" respectively, as the amount of resistance provided at the wheel against normal forces in the contact patch is dependent not only on the k and b (or c) coefficients of the shock but also the motion ratio acted through. The motion ratio quantifies the amount of linear displacement that occurs in the damper for a given displacement of the wheel; this is determined by the suspension geometry and varies throughout the range of travel.

The damping coefficient of the shock absorber in this system is the main variable of interest for this project. Through conducting force vs velocity tests, some light can be shed on how to appropriately set up the dampers for given race situations. In general, the design of dampers for passenger vehicles is biased towards low damping rates, as this favours driver comfort. In race cars, damping rates are higher, usually somewhere around 50-70 % of critical, to maximize the tractive potential of the tires. However, finding the ideal balance is difficult, as the other relevant parameters of the vehicle must be carefully accounted for, as well as the driving conditions, such as whether the road is smooth or rough, hot or cold, dry or wet. There are many more considerations that can quickly complicate this process, such as whether to optimize the suspension setup for the roll motion that occurs during cornering at the expense of response during pitching motions (from longitudinal acceleration) or vice versa.

To assist in this design process, it is first necessary to have a thorough understanding of the damper's range of capability, so that the valve adjustment required for a given response is known. The two force vs. velocity plots provided from Ohlins, the manufacturer, can be used to derive a model.

The dampers are 4-way adjustable, with valves for low-speed compression, high-speed compression, low-speed rebound, and high-speed rebound. The numbers seen on each plot above indicate different adjustments used, with the numbers representing the different adjustment values, given in the same order as just stated. Low speed adjustments are taken in "clicks" from fully closed (1/6 of a revolution), meaning that higher numbers have less damping, whereas high speed adjustments are taken in turns (full revolutions) from the fully open position, so higher numbers mean more damping.

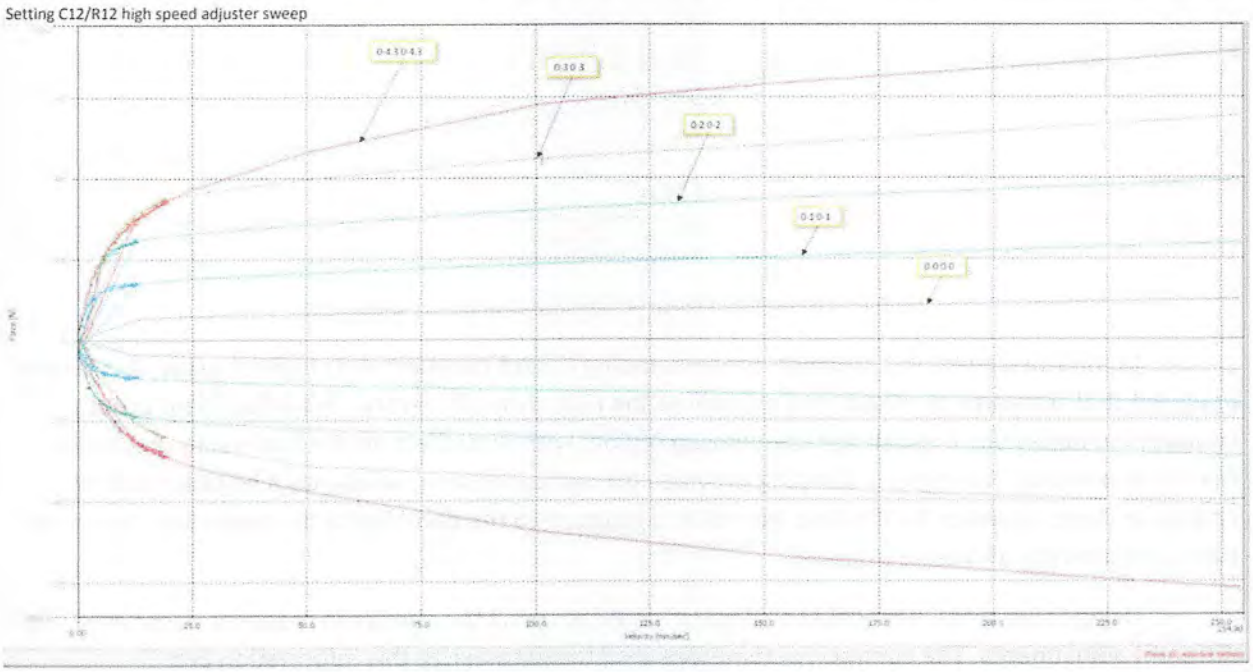

Figure 2: Ohlins TTX25 Force vs. Velocity, High Speed Adjustment

In these figures, Force is plotted on the vertical axis, with positive values for compression and negative values for rebound or extension. Velocity ranges from approximately 0 to 250 mm/s. In the high-speed adjustment plot above, the low speed damping is kept constant at its highest value. It can be seen that in general, changing the high-speed damping seems to limit the height the curve can reach, although each curve has a similar initial shape.

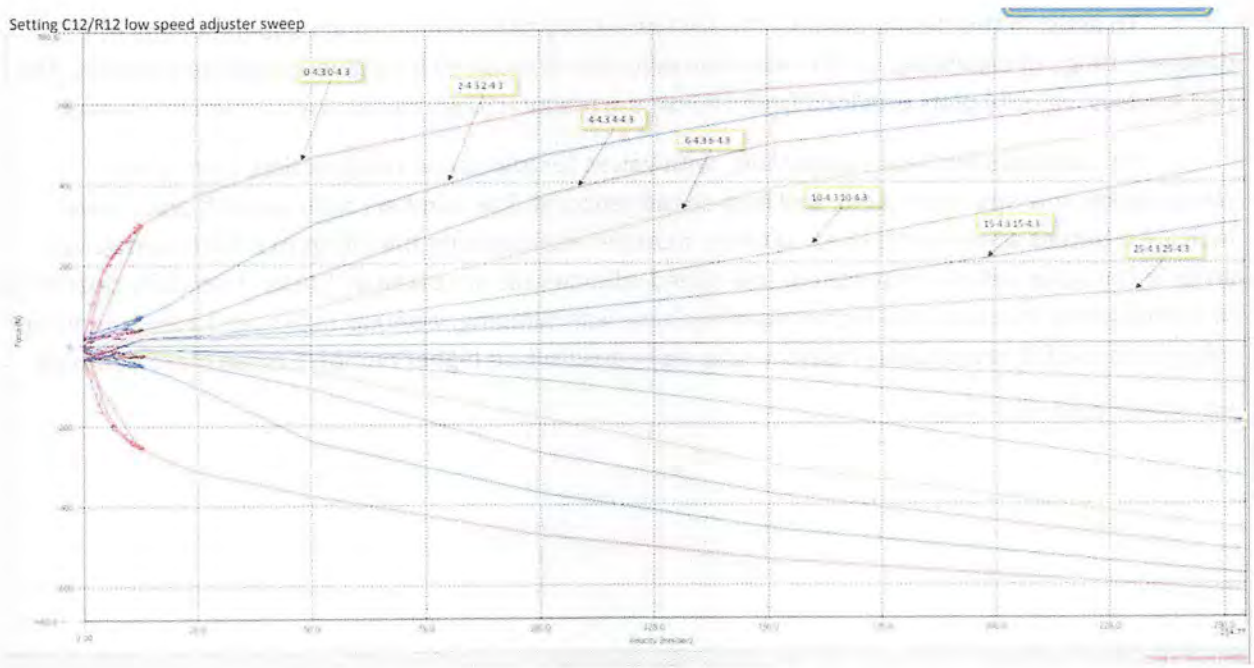

Figure 3: Ohlins TTX25 Force vs. Velocity, Low Speed Adjustment

In this low-speed plot, the high-speed damping is kept constant at its highest value. It is clearly apparent that this form of adjustment influences the response differently. This adjustment greatly changes the behaviour through the low velocity region, with less effect on the final value reached at maximum velocity. The highest damping provides the red curve seen, which has a negative rate of change in slope, however by the time the value is reduced to the damping of the green line, the curve has a positive rate of change in slope.

Using these plots, a model can be constructed to detail the change in response associated with different adjustments. The common parameters used to characterize this information are:

- R_{CE}: Ratio between compression and extension forces for a given sweep
- C_D: Damping coefficient (mean initial slope of compression and extension curves)
- λ: Non-linearity coefficient

This is a simple but effective representation of the system. Using this empirical approach will allow the model to have a high degree of accuracy, while avoiding the need to develop analysis/simulation of the physical fluid interactions from first principles, a process which would be very time intensive and require highly specialized knowledge.

2- Detailed Design

2.1 - Apparatus Design and Programming

The design of this device was composed of two main sections. The mechanical design was required to hold the damper, translate the rotational motion of the motor into linear motion on the damper, and withstand all applied stresses. The electrical system was required to control the motor input and obtain readings for the desired force and velocity outputs.

2.2 - Mechanical Design

Much of the mechanical system was previously fabricated as part of a prior project. It was comprised of a steel base plate, a scotch yoke mechanism, two vertical stainless steel tubes, a horizontal block connecting the beams, and two connection fixtures to attach the damper to the rest of the assembly. This design allowed for the effective accomplishment of the project goals, with the minimum number of required parts and machining. All components were stored, disassembled in the race team shop. After inspection of the components, and conferring with the previous designers, it was determined that some improvement were required. The base plate upon which the motor and cam are mounted was determined to be too thin based on observations from previous trial runs. Deflection in the baseplate could reduce the force recorded in the load cell at the top of the assembly. To address this issue, the base plate was replaced with a 2 ¾" thick aluminum block. The block was faced, and the required holes drilled, before it was introduced into the assembly. This component can be seen in figure 5 below.

Figure 5: Mounting Block after Being Machined

Also, the upper damper connection fixture previously had a poor tolerance on its bolt hole causing compliance in the assembly during operation. This was addressed by re-drilling out the hole to a larger diameter and pressing in a bushing. Lastly, an acrylic enclosure was built to house the circuitry. This provides a clean way of housing all the required electronic components. Following these adjustments, the device was reassembled, as shown in Figure 6 below.

Figure 4: View of Completed Device

2.3 - Structural Analysis

Structural analysis was conducted on a solid model of the apparatus in order to assess the feasibility of the structure. Since this project was inherited from a previous group, it was important to ensure the design of the structure would be able to handle and stresses exerted by the dampener. The additional modifications and additions that were completed as per the scope of this project could also be verified and justified through solid model analysis. The results of the simulations can be seen in figures 5 to 8 below.

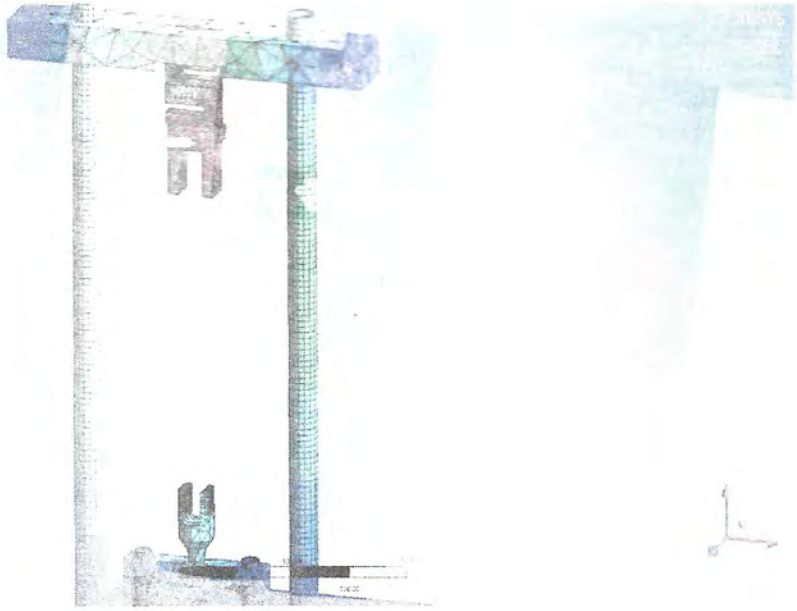

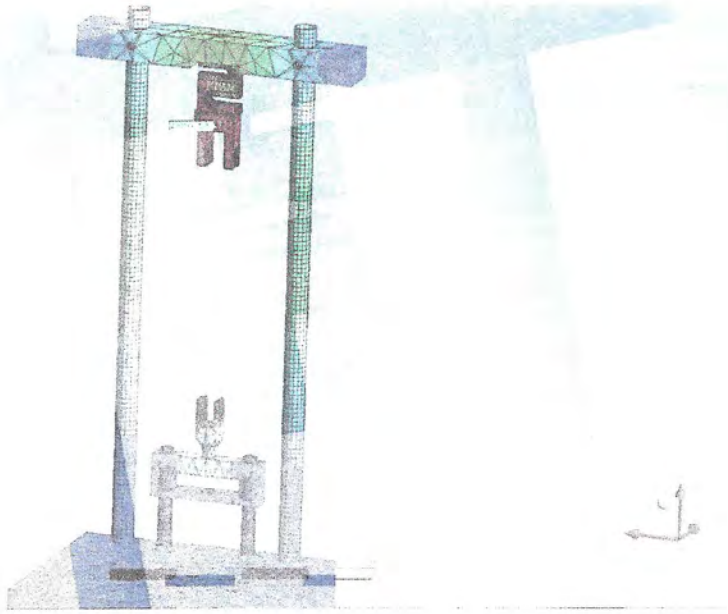

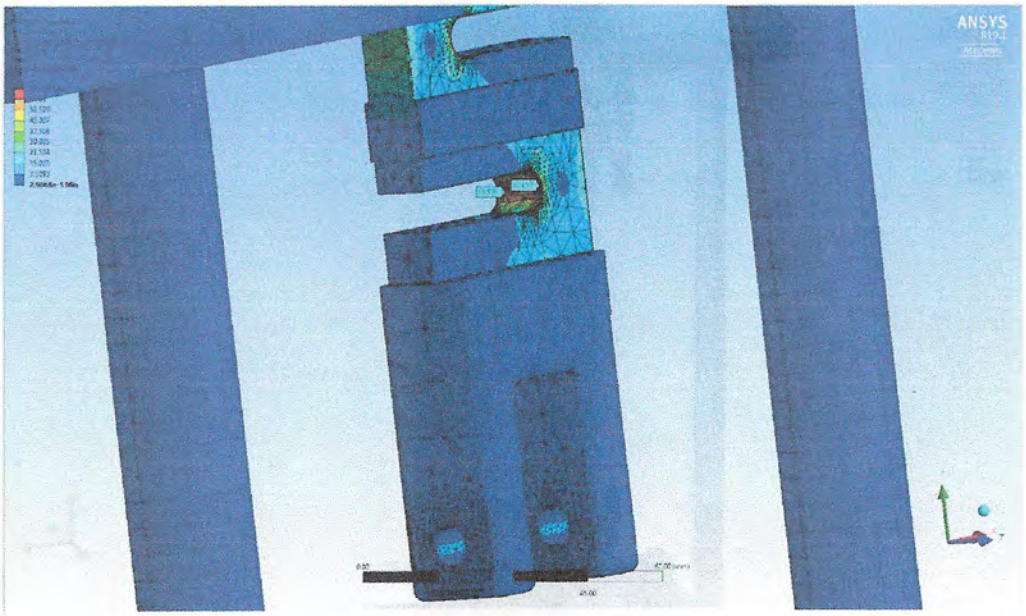

Figure 7: Equivalent Von-Mises Stress with 750N applied bearing force (compression)

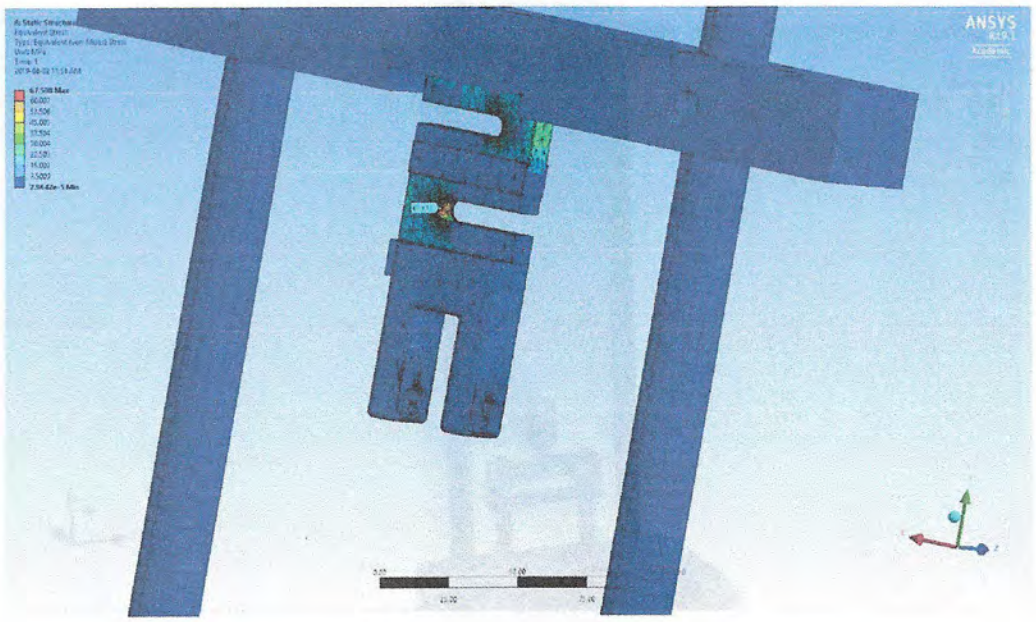

Figure 8: Equivalent Von-Misses Stress with 750N applied force (tension)

A standard mesh size was used with refinements around points of interest and stress concentrations. A maximum of 750N bearing stress was applied to the contact points between the apparatus and the dampener. Both compressive and tensile scenarios were assessed. The Deformation and Von-Mises solutions were considered as these will give the best indication of the usability of the apparatus since yield stresses should not be exceeded and any deformations in the apparatus will skew sensor results.

The preliminary structural analysis does not indicate any issues with the structural nature of the apparatus therefore the construction and modifications to the apparatus are sufficient to complete the damper testing.

2.4 - Electrical Design

In order to control the motor input and track the displacement of the cam and damping force, an electrical system was required. The main components of this system were: 2 Arduino microcontrollers, a 30 volt motor driver, a 100kg rated S-type load cell, a weight sensor module, a 100mm linear potentiometer, two switches, and four LEDs. These components were also available, disassembled, with the rest of the components from the previous project, however a circuit design and code had to be created. A complete circuit diagram of the electrical system can be seen in figure 9 below.

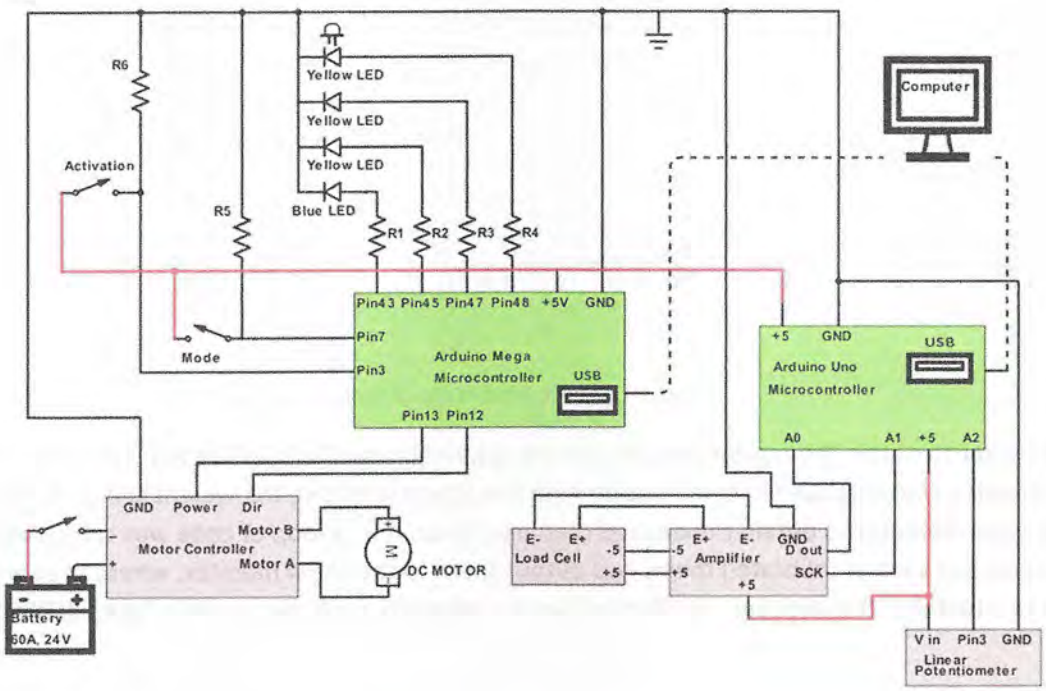

Figure 9: Circuit Diagram

The objective of the set up was to obtain load cell and potentiometer readings from the dynamometer for various motor input velocities and damper settings. To accomplish this, the Arduino mega was used in conjunction with the motor controller, switches, and LEDs to provide live manual control of the motor input speed. The set up was programmed such that the push switch had to be pushed down to begin speeding up the motor. As the motor speeds up, its speed was indicated by the LEDs displayed on top of the electrical box. If no LEDs were lit, meant the motor was stationary, one LED indicated a low speed range, two a medium low speed range, three a medium high-speed range, and four a high to maximum speed range. Once the desired speed was reached, the push button could be pressed and returned to its initial state to maintain a constant motor velocity. If a decrease in speed was desired, the push button could be pushed down, and the mode switch held down, until the desired speed was reached. The Arduino code for this motor control can be seen in figure 10 below.

```
const int Onswitch = 8;
const int Modeswitch = 9;
const int LEDpfour = 7;
const int LEDpthree = 6;
const int LEDpone = 5;
const int LEDptwo = 4;
const int pwm = 10;
const int dir = 3;

int OnSwitch = 0;
int ModeSwitch = 0;

int LEDone = 0;
int LEDtwo = 0;
int LEDthree = 0;
int LEDfour= 0;

int value = 0;

void setup() {
  Serial.begin(9600);

  pinMode(pwm, OUTPUT);
  pinMode(dir, OUTPUT);

  pinMode(Onswitch, INPUT_PULLUP);
  pinMode(Modeswitch, INPUT_PULLUP);

  pinMode(LEDpone, OUTPUT);
  pinMode(LEDptwo, OUTPUT);
  pinMode(LEDpthree, OUTPUT);
  pinMode(LEDpfour, OUTPUT);

  digitalWrite(dir, HIGH);
}
```

```
void loop() {
  OnSwitch = digitalRead(Onswitch);
  Serial.println(OnSwitch);

  if (OnSwitch == HIGH) {
    Serial.println("Altering Speed");
      delay(100);
    ModeSwitch = digitalRead(Modeswitch);

    if (ModeSwitch == 1){
      value++;
    }

      else{
        value--;
      delay(200);
      }

      if(value>255) {
        value= 255;
      }
       else if(value<0){
        value= 0;
      }
```

```
else if (value>0 && value<60){
  Serial.println("Low Speed");
  digitalWrite(LEDpone, HIGH);
  digitalWrite(LEDptwo, LOW);
  digitalWrite(LEDpthree, LOW);
  digitalWrite(LEDpfour, LOW);
}
else if (value>49 && value<120){
  Serial.println("Medium Low Speed");
  digitalWrite(LEDpone, HIGH);
  digitalWrite(LEDptwo, HIGH);
  digitalWrite(LEDpthree, LOW);
  digitalWrite(LEDpfour, LOW);
}
else if (value>99 && value<180){
  Serial.println("Medium High Speed");
  digitalWrite(LEDpone, HIGH);
  digitalWrite(LEDptwo, HIGH);
  digitalWrite(LEDpthree, HIGH);
  digitalWrite(LEDpfour, LOW);
}
else if (value>149 && value<255){
  Serial.println("High Speed Speed");
  digitalWrite(LEDpone, HIGH);
  digitalWrite(LEDptwo, HIGH);
  digitalWrite(LEDpthree, HIGH);
  digitalWrite(LEDpfour, HIGH);
}
}
  else{
    value=value;
    Serial.println("Constant Speed");
    delay(500);
  }
  analogWrite(pwm, value);
  Serial.println(value);
  delay(500);
}
```

Figure 10: Arduino Motor Control Code

In order to obtain the measurements, sensor values also had to be recorded. To do this, the Arduino Genuino Uno was used in combination with the S-type load cell, the weight sensor module, and the linear potentiometer to obtain the desired readings. To do this, a loop of code was composed that read in the sensor values, calibrated them, and output them to the serial monitor, where they were exported to a text file. The Arduino code for this sensor integration can be found in figure 10 below.

```
#include <Hx711.h>

Hx711 scale(A0, A1);
int val;
int calval;
int Potval;
void setup() {
  Serial.begin(9600);
}

void loop() {
  val = scale.getGram();

  //Serial.println (val);
  Potval = analogRead(A3);
  Serial.println((Potval-500)*0.1*100);
  //Serial.println(val);


  if (val > (.1) && val < 10){
    Serial.println(val*29.422+6.802);
  }
  else if (val < -4000) {
    calval = ( 8420- val*(-1))*29.422+6.802;
    Serial.println(calval);
  }
  else if (val > (-0.1) && val < 0.1){
    Serial.println("0");
  }
  else {
    calval = val*29.422+6.802;
    Serial.println(calval);

  }

  delay(10);



}
```

Figure 11: Sensor control Arduino Code

3- Modelling Details

3.1 - MATLAB Model and Test Results

The goal of the modelling component of this project has been to allow analysis of theoretical and tested force vs velocity curves, throughout the full range of valve adjustment. The behaviour of the damper at any of the damper settings can now be understood, while the manufacturer plots only provide data in set increments of the damper valves. The theoretical vs. tested values can also be compared to validate the accuracy of the original supplied data, with the potential to test all four dampers of the Gryphon Racing car to ensure that they are a properly "matched set" and within tolerance. To do this, first the manufacturer plots were digitized so that data sets could be imported into Matlab. The structure of the program is as follows (full code available in Appendix C):

The data sets are first imported in to the program. A series of filtering and sorting commands are done to separate out the data into appropriate compression and rebound bins for each adjustment level. These individual data sets, referred to as sweeps throughout the program, are then concatenated into a master data set. The starts and ends of each individual sweep within this set are defined, as well as each of their associated adjustment conditions. In this manner, the data can now be easily worked with using loops. A simple one-term exponential equation is fitted to each curve, using a loop which

cycles through each sweep of the data set. From these equations, the previously mentioned modeling parameters Cd, Lambda, and Rce are derived.

The test data is then imported into the program. Firstly, all the variables of the test are plotted vs. time to give a quick glimpse of what occurred during the test. This includes the displacement and velocity of the damper, as well as the damper force vs time. Damper velocity is found by taking the difference between each adjacent displacement data points and dividing by the sampling frequency specified in the Arduino code.

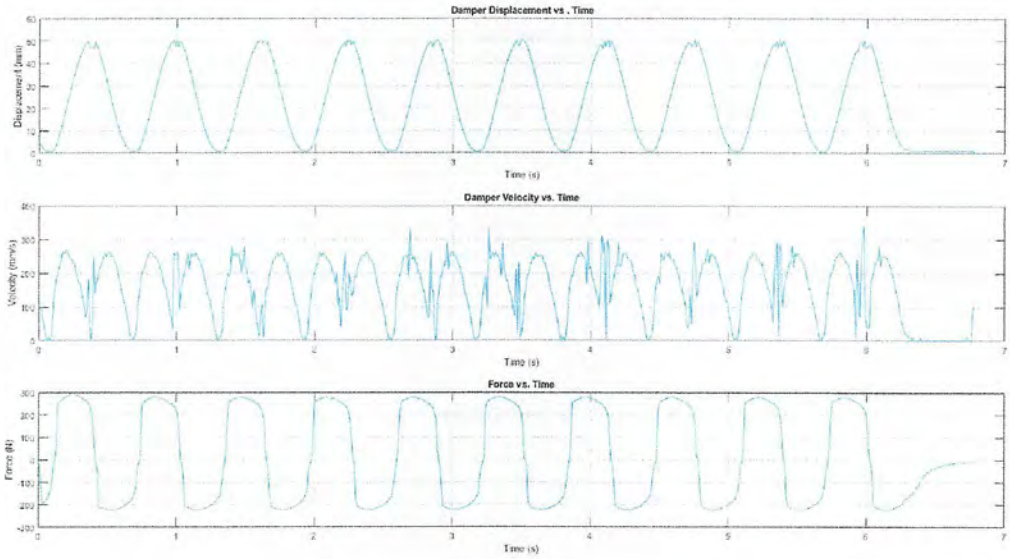

Figure 12: Displacement, Velocity and Force Plots vs. Time

The user is asked in the command line whether they would like to work with the low-speed or high-speed variation model, and what the specific damper settings of their test were. The suitable values from the theoretical model are then used to construct an expected force vs velocity response for the test data. The modeled curve and test data are then plotted together as seen below. For all following graphs, force is plotted in Newtons, and velocity is given in mm per second.

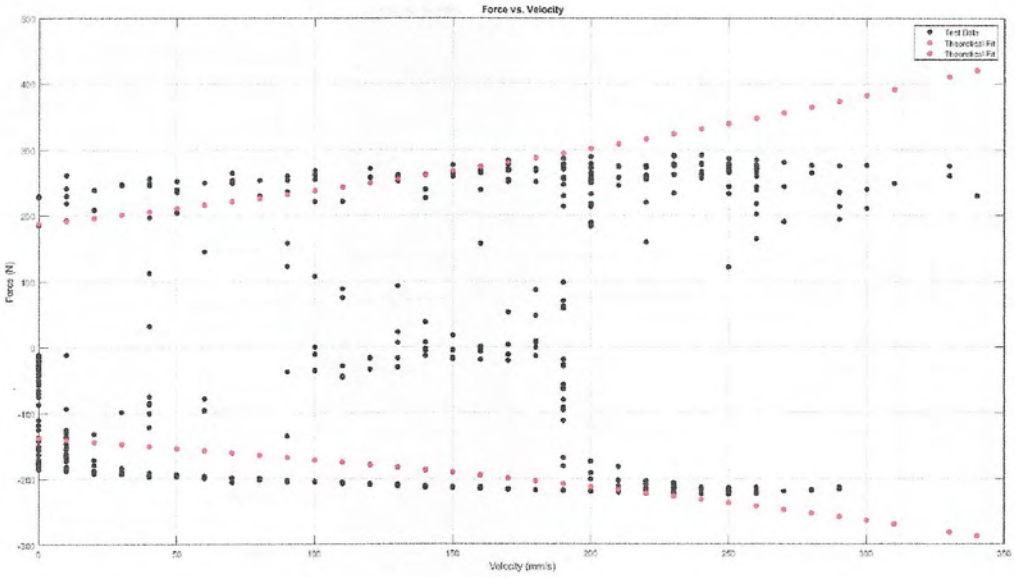

Figure 13: Experimental Data plotted with Mathematical Model

Lastly, the original OEM data is plotted. This is done with the intention that as the device continues to be used in the future, test data can be plotted against the original curves to verify whether the apparatus can reproduce them.

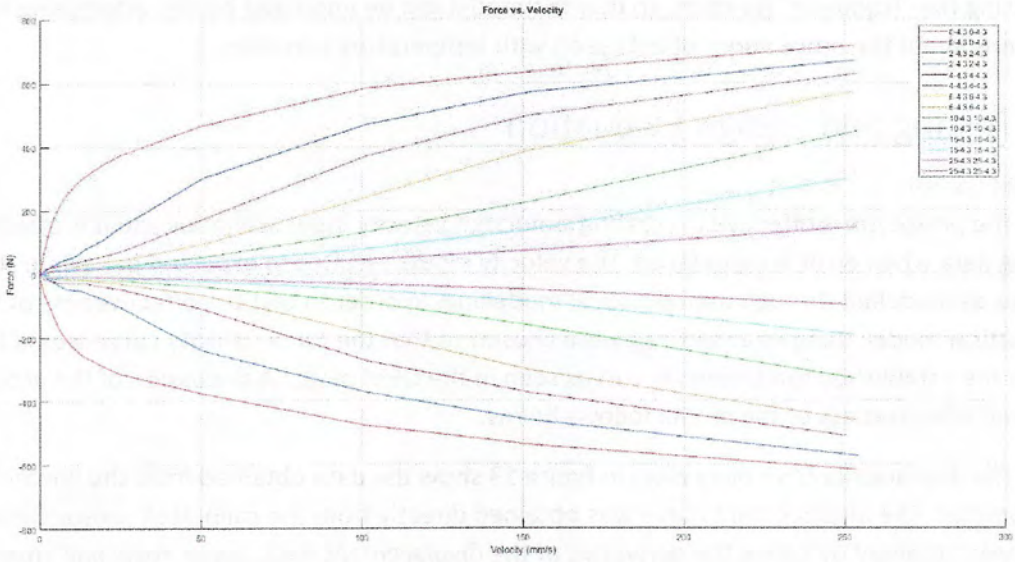

Figure 14: Reproduced OEM Plot – Low Speed Variation

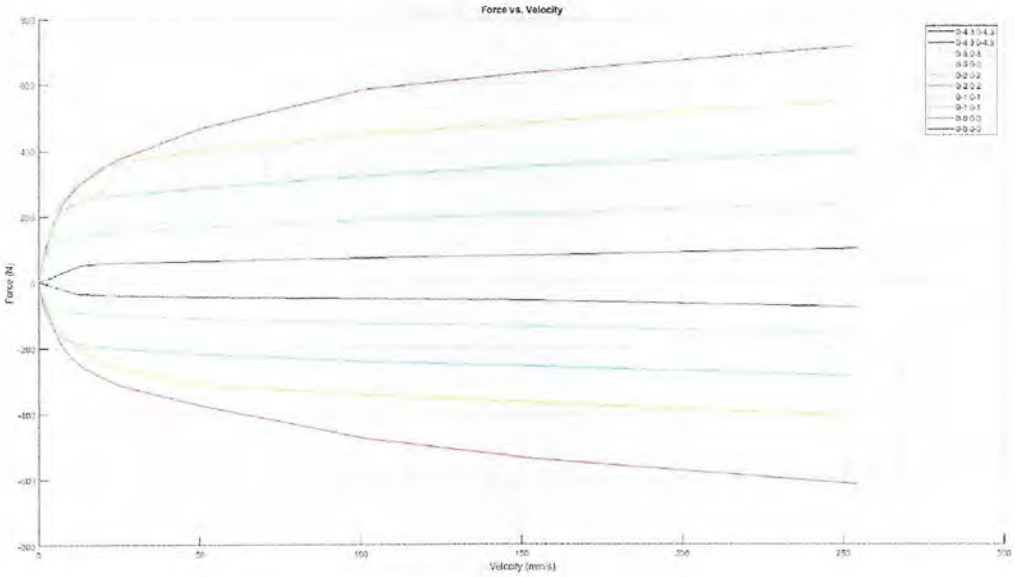

Figure 15: Reproduced OEM Plot – High Speed Variation

Throughout the program, some capability has also been written in to deal with temperature sensor data from the damper. Inferring relationships about how the viscosity and damping force change with temperature is however quite advanced for the current scope of the project, so this sensor was not ultimately implemented. More refining to the accuracy of the curve fitting should first be carried out, ideally using the "lsqnonlin" function, so that the model can be improved before attempting to make conclusions about the more minor effects seen with temperature variation.

4- Testing and Design Evaluation

4.1 - Discussion

The prototype is effective in creating simulated velocity input scenarios and it is effective in collecting data when error is considered. The velocity inputs resulted in expected behaviour from the apparatus as modelled through mathematical modelling. In order to test the effectiveness of the mathematical model, dampener settings were chosen so that the force-velocity curve would fall between the established force-velocity curves seen in the OEM plots. A discussion of the accuracy of results and effectiveness of the model follows below.

The displacement/ velocity plots in figure 13 show the data obtained from the linear potentiometer. The displacement curve was obtained directly from the calibrated sensor data and the velocity was obtained by taking the derivative of the displacement data. Some noise and small variations in the displacement plot can be seen at the peeks of the sinusoidal curve. These small variations can be attributed to various sources of error, discussed below. Any variations or disturbances in the displacement data are amplified by the derivative, thus showing greater noise in the velocity plot. When this noise is ignored, as it can be attributed to the mathematical processing, the velocity follows an oscillating, sinusoidal pattern which is to be expected as a scotch-yoke mechanism outputs a sinusoidal velocity pattern. This varying velocity was used to replicate the OEM plot by sampling various velocity

values at various points in time and matching them to points on the force data occurring at the came time.

The force plot seen in figure 13 was obtained directly from the calibrated strain gauge data. This force plot does not follow the shape of a sinusoidal function; however, it does show a repeating, oscillating pattern which it to be expected as the velocity input followed an oscillating pattern. The pattern does not follow is sinusoidal shape due to the non-linearity of the damper. When the velocity reaches its inflection point (the velocity vector changes direction) and it begins to speed up, the damper will exert its highest resistance in opposition to the change in velocity. The force rapidly increases until the maximum velocity is reached, and then the force slightly levels out before as the velocity begins to slow. This can be attributed to the dissipation of the force within the dampener due to the propertied of the fluid within the damper as well as the design of the dampener itself. The next rapid change in force occurs when the velocity begins to speed up again as the vector changes once more. This pattern continues at the oscillating velocity input repeats.

The theoretical OEM data was fit with an exponential function as this provided the most appropriate line of best fit. The top, red trend line represents the compression response of the dampener and the bottom, red trend line represents the rebound response. This exponential function provides an accurate representation of the OEM data at lower velocity inputs; however, the model loses accuracy at higher velocities. As see in figure 14, the experimental data (in black) follows the trend of the theoretical exponential curves (in red) up until a velocity of approximately 200 mm/second is reached. After this point the theoretical model loses accuracy. When compared to the OEM plots in figures 11 and 12, the experimental data does follow the high-speed trends exhibited in the OEM plots, therefore the data can be considered as a valid reflection of the behaviour of the system. The points that fall between the two dominant trend lines can be attributed to error within the data sampling. When the force-velocity pots were created, periodic sampling of the force and velocity data was obtained, and this sampling could have captured some of the noise present from the amplification due to the derivative being applied in the velocity plot. These points will then cause inaccurate reflections of the velocities at those points, thus causing outliers to occur within the force-velocity plot.

Some other sources of error can cause some of the irregularities present in the data. The data outliers present in the figure 14 can also be attributed to error within the strain gauge. There were consistent technical difficulties in calibrating the strain gauge as it consistently exhibited odd readings when the dampener was in the rebound state (the strain gauge experienced tensile force). Further mathematical calibration and "if statements" were applied in order to combat these irregularities. In addition, a small amount of testing was completed within the timeline of this project. In order to establish strong force-velocity correlation curves, extensive testing is required in order for definitive experimental trends to occur.

The displacement, velocity and force graphs do not exhibit completely smooth sinusoids. This can be attributed to slight movement of components of the apparatus. Some bolts could not be completely tightened due to the nature of the tolerancing within our manufacturing capabilities. In some cases, there were slight clearance fits between fasteners and holes to aid in ease of assembly and these clearance fits could have introduced unwanted vibrations in to the system. The scotch yoke pin also experienced some friction in the slot, and was not perfectly fitted, leaving some room for slight movement and stuttering perpendicular to the intended sliding direction. This slight shifting in the

apparatus is reflected in the graphs by the discrepancies in the smooth displacement, velocity and force curves in figure 13.

4.2 - Future Changes and Recommendations

~~Some improvements that that could be implemented during future testing to help mitigate some of the sources of error could be: potentially employing more complex numerical methods to create more sophisticated functions to better model the manufacturer provided damper plots in the high velocity regions, using tighter tolerances in the manufacturing all of the structural components, pins and fasteners used secure and transfer force between the motor, the shock, the strain gauge, and frame, to reduce vibrations and unintended motions which may introduce error into the strain gauge reading readings, and exploring alternate mechanisms for converting the rotational motion of the motor shaft into linear translation could be tested as a method of reducing unintended jerk movements in the damper system. The slot and pin components may not have been rigid and/or made to tight enough tolerances to effectively translate 100 percent of the rotational motion of the motor into linear translational motion without incurring losses and stuttering at the top and bottom of the motion cycle, where the apparatus transitioned between compression and tension. A different mechanism, such as a four-bar linkage, may provide a smoother linear translation motion cycle, without any sudden accelerations or jerks, producing a more consistent force curve.~~

- Would be good to add the hall effect sensor back in. Allows velocity to be measured directly by taking RPM rather than differentiating the displacement signal, which introduces noise/error.
- Make sure there is no slop in anything when running (shoulder bolt or spring pin on damper connections)
- See comments for modeling improvements in sec. 3.1 pg 13-14

-Orion

4.3 – Conclusion and Closing Comments

When accounting for mechanical errors, the model was able to provide an approximation of the force values expected in the test. The model was most accurate in the low-velocity tension, low-velocity compression, and high-velocity compression regions, but lost some accuracy in the high velocity-tension region. As seen in figure 14, test data falls to below 60 percent of the expected theoretical force value.

The apparatus itself was able to successfully perform all required tests on the damper, allowing sufficient data to be collected in order to analyze the model over a wide range of speed values, and compare it to the corresponding manufacturer data. The electrical components of the apparatus; the series of microcontrollers, the integrated circuitry, the electrical sensors, the user controls, the software, and the electrical motor were all successfully incorporated into the system, allowing for safe and consistent control of the testing device, and for accurate data collection. The mechanical components; the frame, linkages, fasteners and damper itself were all successful as well, as no mechanical parts experienced any failures, unexpected or otherwise. The only potential future mechanical modifications recommended to the system structure are to increase precision and reduce error.

Finally, the initial modifications made to the apparatus to address the issues faced by the previous student groups were all successful as well. The deflections in the baseplate were corrected in its replacement, and the new strain gauge that was used in the updated design was properly suited to

the ranges of forces encountered in the test and did not encounter any forces outside of its suitable range.

5- Appendices

5.1 – Appendix A – Drawings

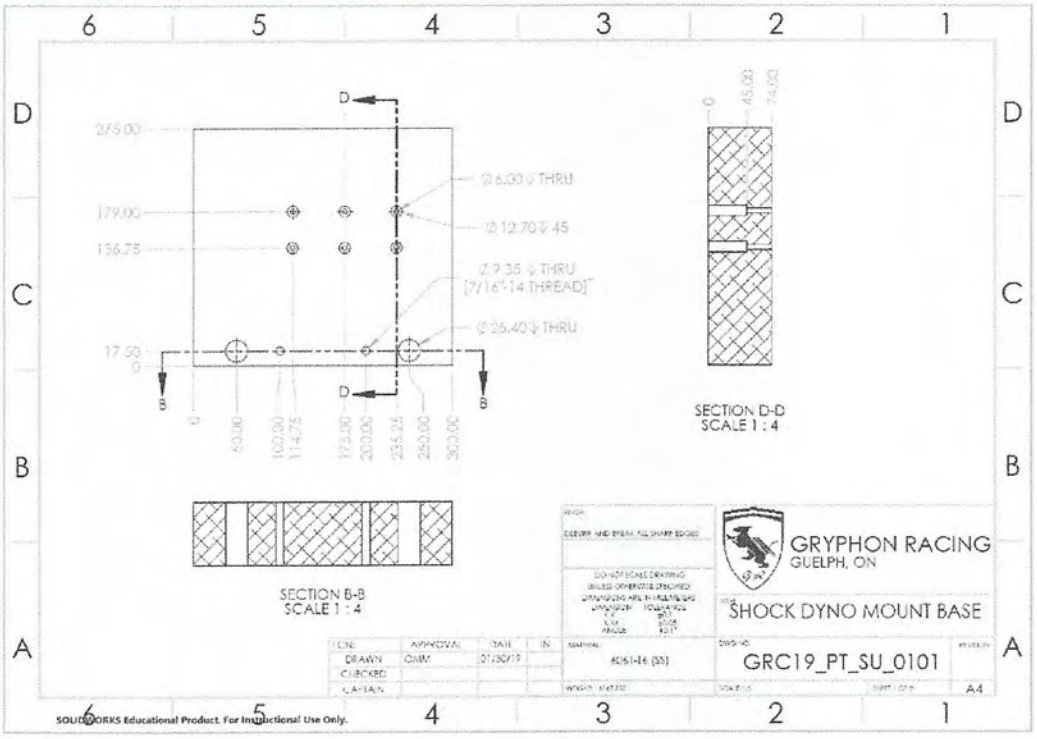

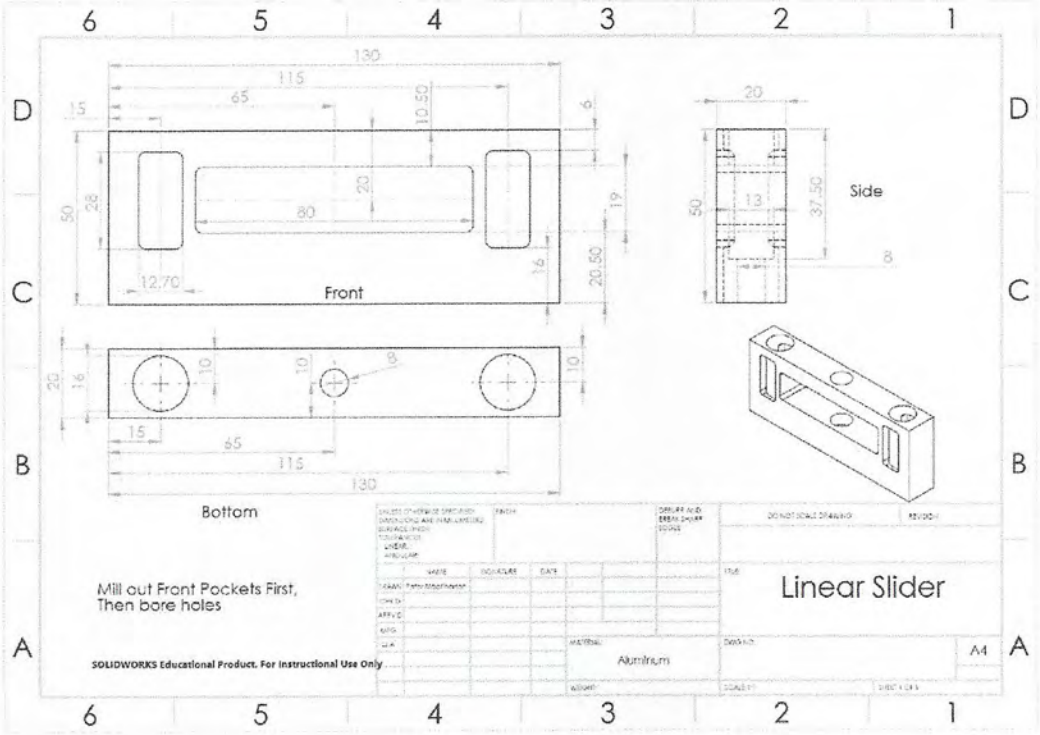

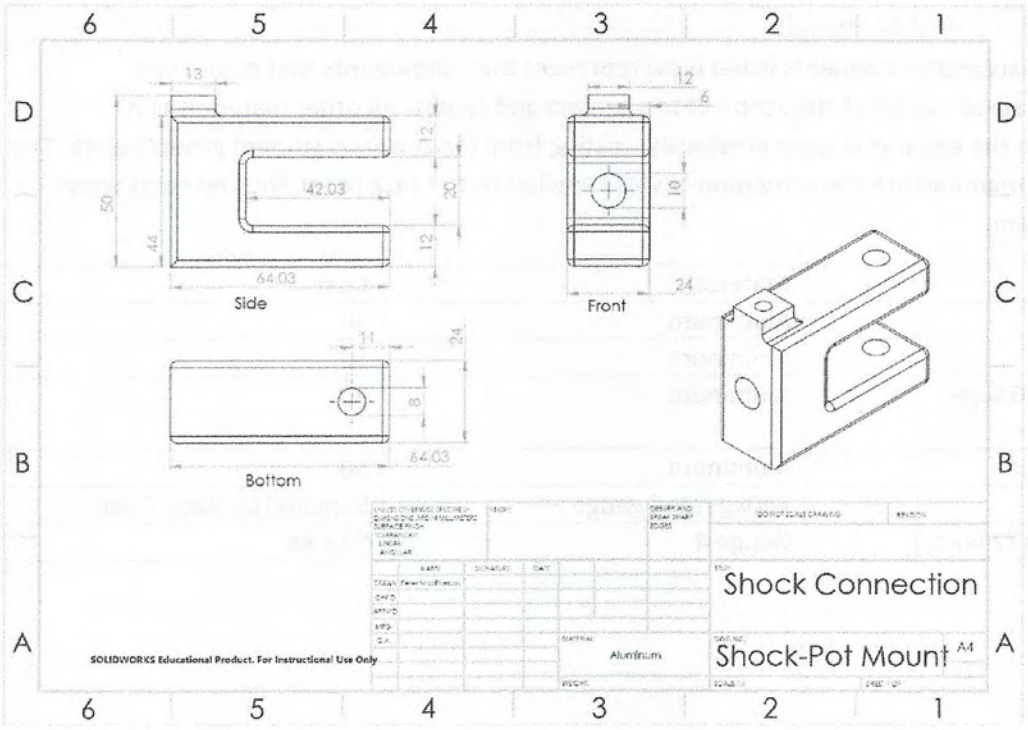
Side
Front
Bottom
Shock Connection
Shock-Pot Mount
Aluminum
A4
SOLIDWORKS Educational Product. For Instructional Use Only

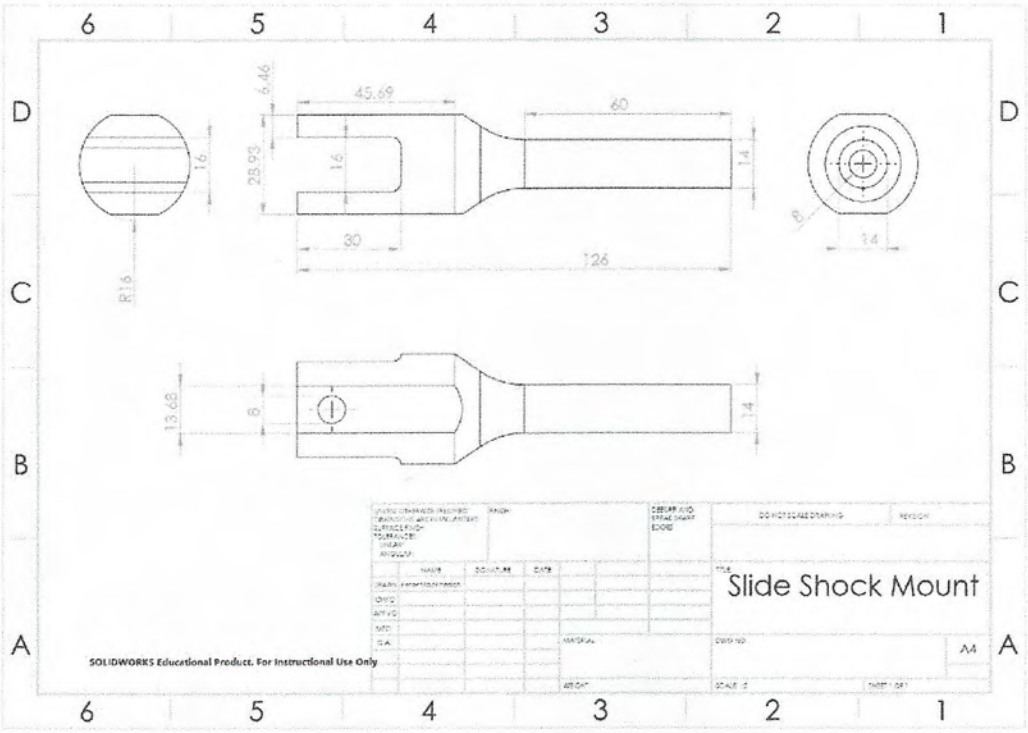
Slide Shock Mount
A4
SOLIDWORKS Educational Product. For Instructional Use Only

5.2 - Appendix B – Bill of Materials

The materials and components listed blow represent the components that have been manufactured/obtained as part of the scope of this project and report. All other materials and components within the apparatus were previously existing from the previous student group's work. The aluminum used to manufacture the components was supplied by the race team, thus no costs were incurred by this team.

Component	**Material**	**Cost**
Base	Aluminum	$0
Linear Slider	Aluminum	$0
Shock and Strain Gauge Connection	Aluminum	$0
Slide Shock Mount	Aluminum	$0
Strain Gauge	100kg rated gauge	Supplied by Race Team
12V Battery leads (2 leads)	Gauge 4	$33.88

5.3 - Appendix C – Matlab Code

```
%%%
```

```
index0_0_0_0 = OhlinsData0_0_0_0(:,2)>0; %Use logical indexing to split each into two files
%separate compression and rebound data
OhlinsData0_0_0_0Comp = OhlinsData0_0_0_0(index0_0_0_0,1:2);
OhlinsData0_0_0_0Reb = OhlinsData0_0_0_0(~index0_0_0_0,1:2);
%Order force vals from lowest to highest (fixes a quirk in the data)
OhlinsData0_0_0_0Comp = sort(OhlinsData0_0_0_0Comp);
OhlinsData0_0_0_0Reb = sort(abs(OhlinsData0_0_0_0Reb));
%Make the comp and rebound sets have equal lengths (some have a slight
%difference)
OhlinsData0_0_0_0Reb(:,2) = -OhlinsData0_0_0_0Reb(:,2);

%Repeat this procedure for all other data sets
index0_1_0_1 = OhlinsData0_1_0_1(:,2)>0;
OhlinsData0_1_0_1Comp = OhlinsData0_1_0_1(index0_1_0_1,1:2);
OhlinsData0_1_0_1Reb = OhlinsData0_1_0_1(~index0_1_0_1,1:2);
OhlinsData0_1_0_1Comp = sort(OhlinsData0_1_0_1Comp);
OhlinsData0_1_0_1Reb = sort(abs(OhlinsData0_1_0_1Reb));
OhlinsData0_1_0_1Reb(:,2) = -OhlinsData0_1_0_1Reb(:,2);
OhlinsData0_1_0_1Comp = OhlinsData0_1_0_1Comp(1:286,:);

index0_2_0_2 = OhlinsData0_2_0_2(:,2)>0;
OhlinsData0_2_0_2Comp = OhlinsData0_2_0_2(index0_2_0_2,1:2);
OhlinsData0_2_0_2Reb = OhlinsData0_2_0_2(~index0_2_0_2,1:2);
OhlinsData0_2_0_2Comp = sort(OhlinsData0_2_0_2Comp);
OhlinsData0_2_0_2Reb = sort(abs(OhlinsData0_2_0_2Reb));
OhlinsData0_2_0_2Reb(:,2) = -OhlinsData0_2_0_2Reb(:,2);
OhlinsData0_2_0_2Reb = OhlinsData0_2_0_2Reb(1:290,:);

index0_3_0_3 = OhlinsData0_3_0_3(:,2)>0;
OhlinsData0_3_0_3Comp = OhlinsData0_3_0_3(index0_3_0_3,1:2);
OhlinsData0_3_0_3Reb = OhlinsData0_3_0_3(~index0_3_0_3,1:2);
OhlinsData0_3_0_3Comp = sort(OhlinsData0_3_0_3Comp);
OhlinsData0_3_0_3Reb = sort(abs(OhlinsData0_3_0_3Reb));
OhlinsData0_3_0_3Reb(:,2) = -OhlinsData0_3_0_3Reb(:,2);
OhlinsData0_3_0_3Comp = OhlinsData0_3_0_3Comp(1:277,:);

index0_43_0_43 = OhlinsData0_43_0_43(:,2)>0;
OhlinsData0_43_0_43Comp = OhlinsData0_43_0_43(index0_43_0_43,1:2);
```

```
OhlinsData0_43_0_43Reb = OhlinsData0_43_0_43(~index0_43_0_43,1:2);
OhlinsData0_43_0_43Comp = sort(OhlinsData0_43_0_43Comp);
OhlinsData0_43_0_43Reb = sort(abs(OhlinsData0_43_0_43Reb));
OhlinsData0_43_0_43Reb(:,2) = -OhlinsData0_43_0_43Reb(:,2);
OhlinsData0_43_0_43Comp = OhlinsData0_43_0_43Comp(1:280,:);

index2_43_2_43 = OhlinsData2_43_2_43(:,2)>0;
OhlinsData2_43_2_43Comp = OhlinsData2_43_2_43(index2_43_2_43,1:2);
OhlinsData2_43_2_43Reb = OhlinsData2_43_2_43(~index2_43_2_43,1:2);
OhlinsData2_43_2_43Comp = sort(OhlinsData2_43_2_43Comp);
OhlinsData2_43_2_43Reb = sort(abs(OhlinsData2_43_2_43Reb));
OhlinsData2_43_2_43Reb(:,2) = -OhlinsData2_43_2_43Reb(:,2);

index4_43_4_43 = OhlinsData4_43_4_43(:,2)>0;
OhlinsData4_43_4_43Comp = OhlinsData4_43_4_43(index4_43_4_43,1:2);
OhlinsData4_43_4_43Reb = OhlinsData4_43_4_43(~index4_43_4_43,1:2);
OhlinsData4_43_4_43Comp = sort(OhlinsData4_43_4_43Comp);
OhlinsData4_43_4_43Reb = sort(abs(OhlinsData4_43_4_43Reb));
OhlinsData4_43_4_43Reb(:,2) = -OhlinsData4_43_4_43Reb(:,2);
OhlinsData4_43_4_43Reb = OhlinsData4_43_4_43Reb(1:266,:);

index6_43_6_43 = OhlinsData6_43_6_43(:,2)>0;
OhlinsData6_43_6_43Comp = OhlinsData6_43_6_43(index6_43_6_43,1:2);
OhlinsData6_43_6_43Reb = OhlinsData6_43_6_43(~index6_43_6_43,1:2);
OhlinsData6_43_6_43Comp = sort(OhlinsData6_43_6_43Comp);
OhlinsData6_43_6_43Reb = sort(abs(OhlinsData6_43_6_43Reb));
OhlinsData6_43_6_43Reb(:,2) = -OhlinsData6_43_6_43Reb(:,2);

index10_43_10_43 = OhlinsData10_43_10_43(:,2)>0;
OhlinsData10_43_10_43Comp = OhlinsData10_43_10_43(index10_43_10_43,1:2);
OhlinsData10_43_10_43Reb = OhlinsData10_43_10_43(~index10_43_10_43,1:2);
OhlinsData10_43_10_43Comp = sort(OhlinsData10_43_10_43Comp);
OhlinsData10_43_10_43Reb = sort(abs(OhlinsData10_43_10_43Reb));
OhlinsData10_43_10_43Reb(:,2) = -OhlinsData10_43_10_43Reb(:,2);

index15_43_15_43 = OhlinsData15_43_15_43(:,2)>0;
OhlinsData15_43_15_43Comp = OhlinsData15_43_15_43(index15_43_15_43,1:2);
OhlinsData15_43_15_43Reb = OhlinsData15_43_15_43(~index15_43_15_43,1:2);
```

```
OhlinsData15_43_15_43Comp = sort(OhlinsData15_43_15_43Comp);

OhlinsData15_43_15_43Reb = sort(abs(OhlinsData15_43_15_43Reb));

OhlinsData15_43_15_43Reb(:,2) = -OhlinsData15_43_15_43Reb(:,2);

OhlinsData15_43_15_43Comp = OhlinsData15_43_15_43Comp(1:277,:);


index25_43_25_43 = OhlinsData25_43_25_43(:,2)>0;

OhlinsData25_43_25_43Comp = OhlinsData25_43_25_43(index25_43_25_43,1:2);

OhlinsData25_43_25_43Reb = OhlinsData25_43_25_43(~index25_43_25_43,1:2);

OhlinsData25_43_25_43Comp = sort(OhlinsData25_43_25_43Comp);

OhlinsData25_43_25_43Reb = sort(abs(OhlinsData25_43_25_43Reb));

OhlinsData25_43_25_43Reb(:,2) = -OhlinsData25_43_25_43Reb(:,2);

OhlinsData25_43_25_43Reb = OhlinsData25_43_25_43Reb(1:271,:);


%Concatenate all these files into a single master data set so that analysis

%of the different conditions can be done with a loop

OhlinsDataMaster = vertcat(OhlinsData0_0_0_0Comp, OhlinsData0_0_0_0Reb, OhlinsData0_1_0_1Comp,...

OhlinsData0_1_0_1Reb, OhlinsData0_2_0_2Comp,OhlinsData0_2_0_2Reb, OhlinsData0_3_0_3Comp,...

OhlinsData0_3_0_3Reb, OhlinsData0_43_0_43Comp, OhlinsData0_43_0_43Reb,
OhlinsData2_43_2_43Comp,...

OhlinsData2_43_2_43Reb, OhlinsData4_43_4_43Comp, OhlinsData4_43_4_43Reb,
OhlinsData6_43_6_43Comp,...

OhlinsData6_43_6_43Reb, OhlinsData10_43_10_43Comp, OhlinsData10_43_10_43Reb,
OhlinsData15_43_15_43Comp,...

OhlinsData15_43_15_43Reb, OhlinsData25_43_25_43Comp, OhlinsData25_43_25_43Reb);


%Define the start and end points of each sweep so that these can be indexed

%through

SweepStarts = [1 282 563 849 1135 1425 1715 1992 2269 2549 2829 3102 ...

    3375 3641 3907 4176 4445 4713 4981 5258 5535 5806];


SweepEnds = [281 562 848 1134 1424 1714 1991 2268 2548 2828 3101 3374 ...

    3640 3906 4175 4444 4712 4980 5257 5534 5805 6076];


%Define number of different data sets within the master data set

SweepsNum = numel(SweepStarts);


%Define the adjustment conditions of the dampers through each of the sweeps

OhlinsDataLSC = [0 0 0 0 0 0 0 0 0 0 2 2 4 4 6 6 10 10 15 15 25 25];

OhlinsDataHSC = [0 0 1 1 2 2 3 3 4.3 4.3 4.3 4.3 4.3 4.3 4.3 4.3 ...
```

```
    4.3 4.3 4.3 4.3 4.3 4.3];

OhlinsDataLSR = OhlinsDataLSC;

OhlinsDataHSR = OhlinsDataHSC;


disp('Valve adjustment naming convention: LSC-HSC LSR-HSR (L=low, H=high, S=speed, C=compression,
R=rebound).');

disp('LS adjustments (3mm hex) are counted in clicks from fully closed (fully clockwise), HS
adjustments (12mm hex)');

disp('are counted in turns from fully open (fully counter-clockwise)');


TheoreticalFit = zeros(length(OhlinsDataMaster),1); %Initialize exponential fit


for i=1:SweepsNum

        %Create and exponential fit for each sweep:

        TheoreticalFit =
fit(OhlinsDataMaster(SweepStarts(i):SweepEnds(i),1),OhlinsDataMaster(SweepStarts(i):SweepEnds(i),
2),'exp1');


        %Store the equation coefficiencts as Cd (Initial Slope) and Lambda

        %(Non-linearity coefficient):

        Cd(i) = TheoreticalFit.a;

        Lambda(i) = TheoreticalFit.b;


end


Rce = zeros(SweepsNum); %Initialize ratio of compression over extension


for i=1:SweepsNum-1

    AvgCompForce(i) = mean(OhlinsDataMaster(SweepStarts(i):SweepEnds(i),2));

    AvgRebForce(i) = mean(abs(OhlinsDataMaster(SweepStarts(i+1):SweepEnds(i+1),2)));


    % Find the average ratio of compression over extension force for each

    % sweep:

    Rce(i) = AvgCompForce(i)./AvgRebForce(i);

end


Rce = Rce(1:2:SweepsNum); %Eliminates half the entries from the previous form of the matrix,
because only every other value is used


% FZ_CLASS(i) = interp1(FZ_LIST,FZ_LIST,FZ_AVG(i),'nearest');
```

```
%Load Test Data

TestData = load(uigetfile);


%Index Test by Variables

TestDataTime = TestData(:,1);

TestDataLinDisp = TestData(:,4);

TestDataLinVel = zeros(numel(TestDataTime),1);


for i=1:numel(TestDataTime)-1


    %Find linear velocity by differentiating displacement vs. time:

    TestDataLinVel(i) = abs(TestDataLinDisp(i+1)-TestDataLinDisp(i))./(TestDataTime(i+1)-
TestDataTime(i));


end


TestDataLinVel(numel(TestDataTime)) = TestDataLinVel(numel(TestDataTime)-1);


TestDataForce = TestData(:,2);

TestDataForce = TestDataForce*-0.009806; %Unit Conversion: Grams to Newtons

% TestDataTemp = TestData(:,4);


disp('Importing Test Data...')


while(1)

AdjustmentChoice = input('What kind of adjustment is being tested? Enter 1 for Low-Speed, enter 2
for High-Speed: ');


if AdjustmentChoice == 1

TestDataLSC = input('Enter Low Speed Compression: ');

TestDataLSR = input('Enter Low Speed Rebound: ');

TestDataHSC = 4.3;

TestDataHSR = 4.3;


break


else if AdjustmentChoice == 2

TestDataLSC = 0;
```

```
TestDataLSR = 0;
TestDataHSC = input('Enter High Speed Compression: ');
TestDataHSR = input('Enter High Speed Rebound: ');
break

    end
end
end

%Create a display of all measured variables vs. time
PlotTitle = sprintf('Test Data vs. Time, LSC: %s, LSR: %s, HSC: %s, HSR: %s', ...
    num2str(TestDataLSC), num2str(TestDataLSR), ...
    num2str(TestDataHSC), num2str(TestDataHSR));
f = figure('Name',PlotTitle,'NumberTitle','off','Position',[0 0 1300 670]);
figure(f)

subplot(3,1,1)
    plot(TestDataTime, TestDataLinDisp)
    title('Damper Displacement vs . Time');
    xlabel('Time (s)');
    ylabel('Displacement (mm)');
    grid on
  %  set(gca,'color',[0 0 0])

subplot(3,1,2)
    plot(TestDataTime, TestDataLinVel)
    title('Damper Velocity vs. Time');
    xlabel('Time (s)');
    ylabel('Velocity (mm/s)');
    grid on
 %   set(gca,'color',[0 0 0])

subplot(3,1,3)
    plot(TestDataTime, TestDataForce)
    title('Force vs. Time');
    xlabel('Time (s)');
    ylabel('Force (N)');
    grid on
```

```
  % set(gca,'color',[0 0 0])

%This code below is for if a temperature sensor were to be added
% to the apparatus in the future. Shows damper temperature during test.

% subplot(3,1,4
%     plot(TestDataTime, TestDataTemp)
%     title('Damper Temperature vs. Time');
%     xlabel('Time (s)');
%     ylabel('Temperature (C)');
%     grid on
%    % set(gca,'color',[0 0 0])

%Define model parameters for the given adjustment vals:

TestRce =(Rce(2)+Rce(3))./2; %Redundant, as the two curves are being defined by their different
initial Cd's
TestCdComp = (Cd(3)+Cd(5))./2;
TestCdReb = (Cd(4)+Cd(6))./2;
TestLambdaComp = (Lambda(3)+Lambda(5))./2;
TestLambdaReb = (Lambda(4)+Lambda(6))./2;

%I just defined the model parameters manually by checking what sweeps a high
%speed adjustment of 1.5 would match up with. It would be better to make a
%curve fit of Cd and Lambda (lsqnonlin?) which can be interpolated through for whatever
%adjustment is specified.

TheoreticalCompEqn = TestCdComp*exp(TestLambdaComp*TestDataLinVel); %Define modeled curve for
compression portion
TheoreticalRebEqn = TestCdReb*exp(TestLambdaReb*TestDataLinVel); % Define modeled curve for
rebound portion

f = figure('Name',PlotTitle, 'NumberTitle', 'off');
set(f,'units','normalized','outerposition',[0,0,1,1]);

        plot(TestDataLinVel, TestDataForce,'.k', 'DisplayName', 'Test Data', 'MarkerSize',20);
        hold on
%
plot(TestDataTime(SweepStarts(i):SweepEnds(i)),TestDataForce_Fit(SweepStarts(i):SweepEnds(i)),'k'
);
```

```
%       hold on

        plot(TestDataLinVel,TheoreticalCompEqn,'.r', 'DisplayName', 'Theoretical Fit',
'MarkerSize',20);

        plot(TestDataLinVel,TheoreticalRebEqn,'.r', 'DisplayName', 'Theoretical Fit',
'MarkerSize',20);


        grid on

        title('Force vs. Velocity')

        xlabel('Velocity (mm/s)')

        ylabel('Force (N)')

        legend


%   %This code is for if a temperature sensor were to be added to the apparatus in the future.
Produces a heat plot to show how the ...

%   %damper temperature changes throughout a test.

%

% f = figure('Name',sprintf('Test Data Heat Map: LSC = %s, LSR = %s, HSC = %s, HSR = %s',
TestDataLSC, TestDataLSR, TestDataHSC, TestDataHSR),'NumberTitle','off');

% set(f,'units','normalized','outerposition',[0,0,1,1]);

% dotsz = 25;

%
scatter(TestDataTime(SweepStarts(i):SweepEnds(i)),TestDataForce(SweepStarts(i):SweepEnds(i)),dots
z,TestDataTemp(SweepStarts(i):SweepEnds(i)));

% title('Force vs. Velocity, Temperature')

%


%The manufacturer data will now be graphed for each type of adjustment variation. These plots are
being added

%with the intention that as more tests are done with the apparatus in the

%future, their data can be plotted against each of these curves to

%see if they can be validated/reproduced.


f = figure('Name',sprintf('Manufacturer vs. Tested Damping Plots, Ohlins TTX25 Low-Speed
Adjustment Variation'),'NumberTitle','off');

set(f,'units','normalized','outerposition',[0,0,1,1]);



%         plot(,'.g'); %These commented out lines are for adding test data

        hold on

        plot(OhlinsData0_43_0_43Comp(:,1),OhlinsData0_43_0_43Comp(:,2),'r', 'DisplayName','0-4.3
0-4.3');

        plot(OhlinsData0_43_0_43Reb(:,1),OhlinsData0_43_0_43Reb(:,2),'r', 'DisplayName','0-4.3 0-
4.3');
```

```
%         plot(,'.r');

        hold on

        plot(OhlinsData2_43_2_43Comp(:,1),OhlinsData2_43_2_43Comp(:,2),'b', 'DisplayName','2-4.3
2-4.3');

        plot(OhlinsData2_43_2_43Reb(:,1),OhlinsData2_43_2_43Reb(:,2),'b', 'DisplayName','2-4.3 2-
4.3');

%         plot(,'.c');

        hold on

        plot(OhlinsData4_43_4_43Comp(:,1),OhlinsData4_43_4_43Comp(:,2), 'Color', [0.6350 0.0780
0.1840], 'DisplayName','4-4.3 4-4.3');

        plot(OhlinsData4_43_4_43Reb(:,1),OhlinsData4_43_4_43Reb(:,2), 'Color', [0.6350 0.0780
0.1840], 'DisplayName','4-4.3 4-4.3');

%         plot(,'.m');

        hold on

        plot(OhlinsData6_43_6_43Comp(:,1),OhlinsData6_43_6_43Comp(:,2), 'Color', [1 0.5 0],
'DisplayName','6-4.3 6-4.3');

        plot(OhlinsData6_43_6_43Reb(:,1),OhlinsData6_43_6_43Reb(:,2), 'Color', [1 0.5 0],
'DisplayName','6-4.3 6-4.3');

%         plot(,'.y');

        hold on

        plot(OhlinsData10_43_10_43Comp(:,1),OhlinsData10_43_10_43Comp(:,2), 'Color', [0 0.5 0],
'DisplayName','10-4.3 10-4.3');

        plot(OhlinsData10_43_10_43Reb(:,1),OhlinsData10_43_10_43Reb(:,2), 'Color', [0 0.5 0],
'DisplayName','10-4.3 10-4.3');

%         plot(,'.b');

        hold on

        plot(OhlinsData15_43_15_43Comp(:,1),OhlinsData15_43_15_43Comp(:,2),'c',
'DisplayName','15-4.3 15-4.3');

        plot(OhlinsData15_43_15_43Reb(:,1),OhlinsData15_43_15_43Reb(:,2),'c', 'DisplayName','15-
4.3 15-4.3');

%         plot(,'.k');

        hold on

        plot(OhlinsData25_43_25_43Comp(:,1),OhlinsData25_43_25_43Comp(:,2),'m',
'DisplayName','25-4.3 25-4.3');

        plot(OhlinsData25_43_25_43Reb(:,1),OhlinsData25_43_25_43Reb(:,2),'m', 'DisplayName','25-
4.3 25-4.3');

        grid on

        title('Force vs. Velocity')

        xlabel('Velocity (mm/s)');

        ylabel('Force (N)');

        legend

%         legend('0-4.3 0-4.3', '2-4.3 2-4.3', '4-4.3 4-4.3', '6-4.3 6-4.3', '10-4.3 10-4.3',
'15-4.3 15-4.3', '25-4.3 25-4.3')
```

```
f = figure('Name',sprintf('Manufacturer vs. Tested Damping Plots, Ohlins TTX25 High-Speed
Adjustment Variation'),'NumberTitle','off');

set(f,'units','normalized','outerposition',[0,0,1,1]);

%         plot(,'.g');

        hold on

        plot(OhlinsData0_43_0_43Comp(:,1),OhlinsData0_43_0_43Comp(:,2),'r', 'DisplayName', '0-4.3
0-4.3');

        plot(OhlinsData0_43_0_43Reb(:,1),OhlinsData0_43_0_43Reb(:,2),'r', 'DisplayName', '0-4.3
0-4.3');

%         plot(,'.r');

        hold on

        plot(OhlinsData0_3_0_3Comp(:,1),OhlinsData0_3_0_3Comp(:,2), 'Color', [0.75 0.75 0],
'DisplayName', '0-3 0-3');

        plot(OhlinsData0_3_0_3Reb(:,1),OhlinsData0_3_0_3Reb(:,2), 'Color', [0.75 0.75 0],
'DisplayName', '0-3 0-3');

%         plot(,'.c');

        hold on

        plot(OhlinsData0_2_0_2Comp(:,1),OhlinsData0_2_0_2Comp(:,2), 'Color', [0 0.75 0.75],
'DisplayName', '0-2 0-2');

        plot(OhlinsData0_2_0_2Reb(:,1),OhlinsData0_2_0_2Reb(:,2), 'Color', [0 0.75 0.75],
'DisplayName', '0-2 0-2');

%         plot(,'.m');

        hold on

        plot(OhlinsData0_1_0_1Comp(:,1),OhlinsData0_1_0_1Comp(:,2), 'Color', [0.3010 0.7450
0.9330], 'DisplayName', '0-1 0-1');

        plot(OhlinsData0_1_0_1Reb(:,1),OhlinsData0_1_0_1Reb(:,2), 'Color', [0.3010 0.7450
0.9330], 'DisplayName', '0-1 0-1');

%         plot(,'.y');

        hold on

        plot(OhlinsData0_0_0_0Comp(:,1),OhlinsData0_0_0_0Comp(:,2), 'Color', [0.2 0 0],
'DisplayName', '0-0 0-0');

        plot(OhlinsData0_0_0_0Reb(:,1),OhlinsData0_0_0_0Reb(:,2), 'Color', [0.2 0 0],
'DisplayName', '0-0 0-0');

        grid on

        title('Force vs. Velocity');

        xlabel('Velocity (mm/s)');

        ylabel('Force (N)');

        legend


toc
```

COMPONENT WEIGHTS

UNSPRUNG MASS

FRONT

TIRE - 3541 g
WHEEL SHELL - 1430 g
WHEEL CENTER - 389 g
HUB ASSEMBLY - 869 g
UPRIGHT - 680 g + 356 g
CALIPER - 550-600 g
ROTOR - 537 g
SUSP. LINKS - $\frac{1180 g}{2}$ = 590 g

TOTAL: 8672 g
8.67 kg (per corner)

REAR

HUB ASSEMBLY - 1336 g
UPRIGHT - 811 g
CALIPER - 457 g
ROTOR - 507 g
SUSP. LINKS - $\frac{1014 g}{2}$ = 507 g
HALF SHAFTS - $\frac{2340}{2}$ = 1170 g

TOTAL: 10145 g
10.14 kg (per corner)

SPRUNG MASS (SUSP. COMPONENTS ONLY)

FRONT

SUSP. LINKS - 590 g
SHOCKS - 655 g
BELLCRANK - 165 g
} x2
ARB - 271 g
STEERING RACK - 680 g
COLUMN ASSEMBLY - 610 g

TOTAL: 2971 g
2.97 kg

REAR

SUSP. LINKS - 507 g
SHOCKS - 655 g
BELLCRANK - 117 g
} x2
ARB - 308 g

TOTAL: 1587 g
1.58 kg

OVERALL TOTAL: ~~23.36 kg~~ ~~42.17 kg~~
47.55 kg

VEHICLE YAW INERTIA

$I_{zz} = 63.08 \ kg \cdot m^2$

→ Find difference between new and old wheels

Reduction in $I_{zz} = 4(3.180 \ kg)(0.98 \ m)^2 = 12.60 \ kg \cdot m^2$

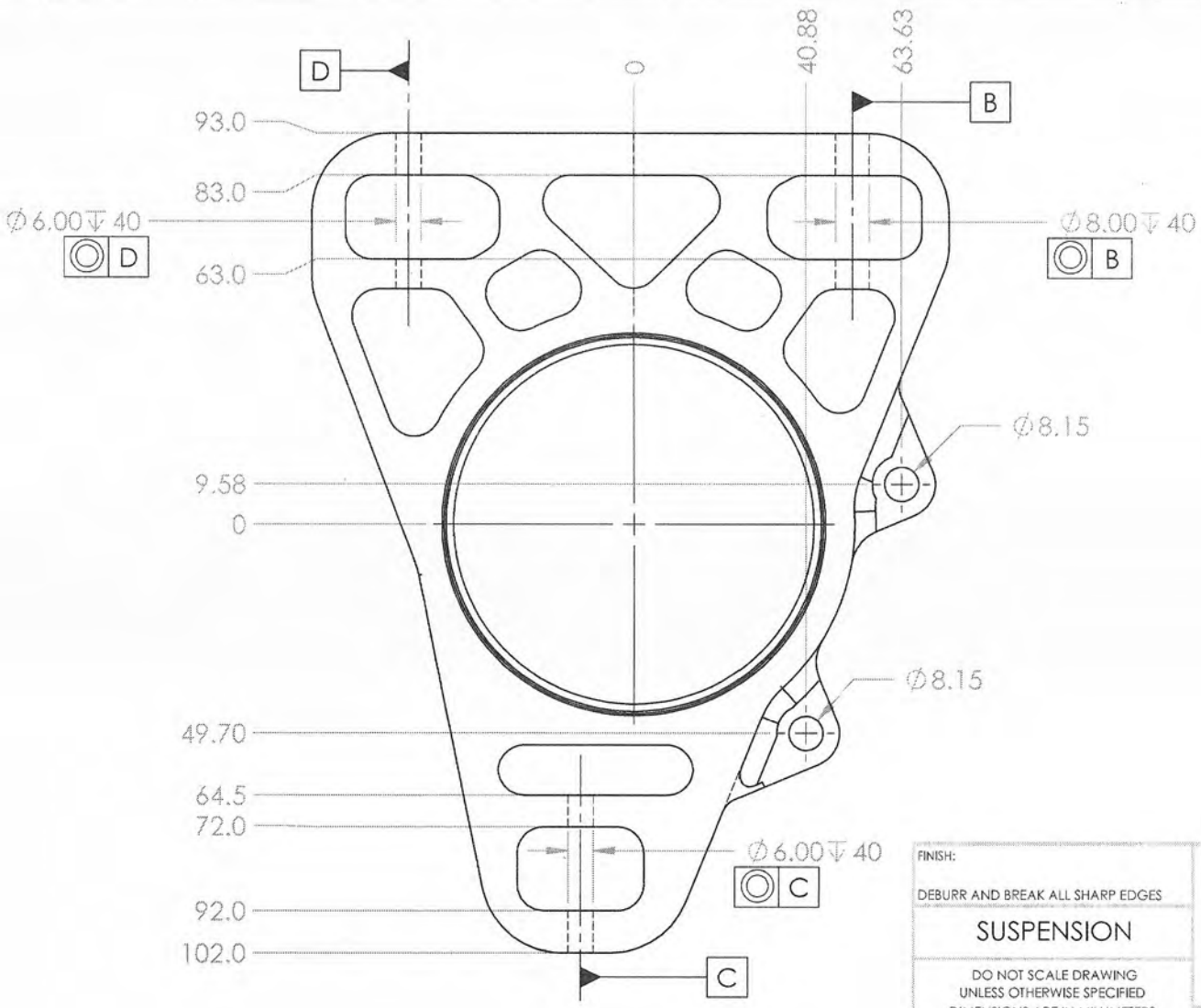

FINISH:

DEBURR AND BREAK ALL SHARP EDGES

SUSPENSION

DO NOT SCALE DRAWING
UNLESS OTHERWISE SPECIFIED
DIMENSIONS ARE IN MILLIMETERS

DIMENSION	TOLERANCE
X.X	±0.1
X.XX	±0.05
ANGLE	±0.1°

GRYPHON RACING
GUELPH, ON

TITLE:

REAR R-UPRIGHT

ECN:	APPROVAL	DATE	IN
DRAWN			
CHECKED			
CAPITAN			

MATERIAL: 6061 Alloy

WEIGHT: 810.831

DWG NO. GRC19_PT_SU_0036

REVISION

SCALE:1:5

SHEET 1 OF 3

A4

SOLIDWORKS Educational Product. For Instructional Use Only.

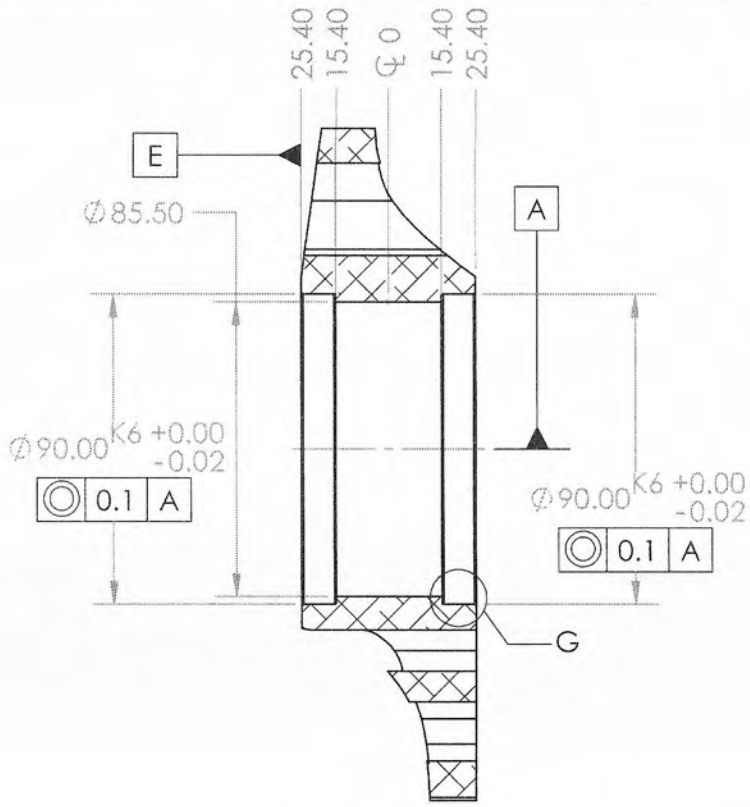

SECTION A-A
SCALE 1 : 2

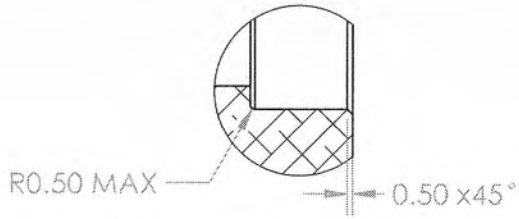

DETAIL G
SCALE 1.5 : 1

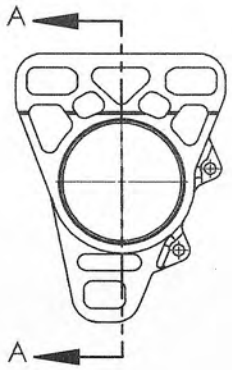

GRYPHON RACING
GUELPH, ON

TITLE:
REAR R-UPRIGHT

DWG NO.
GRC19_PT_SU_0036

REVISION

SCALE:1:5 | SHEET 2 OF 3 | A4

SOLIDWORKS Educational Product. For Instructional Use Only.

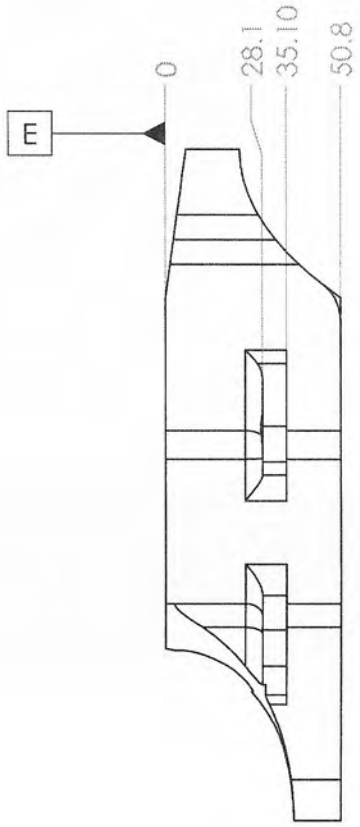

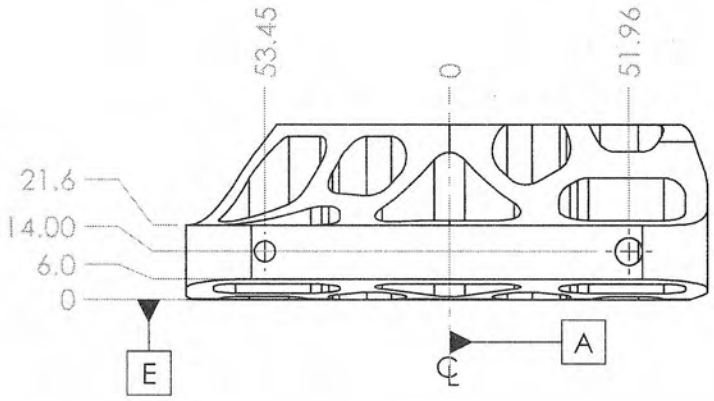

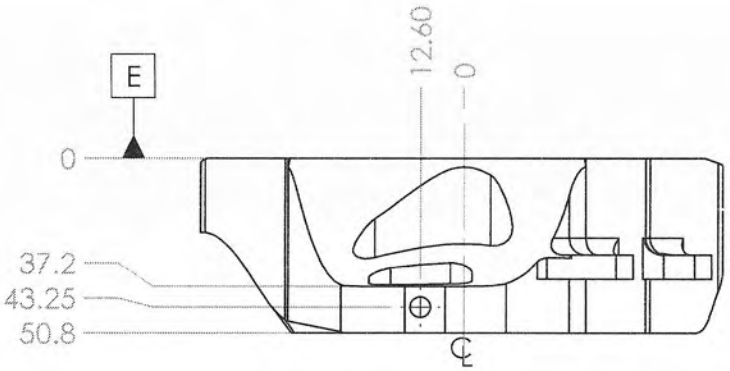

GRYPHON RACING
GUELPH, ON

TITLE:
REAR R-UPRIGHT

DWG NO.
GRC19_PT_SU_0036

REVISION

SCALE:1:5 | SHEET 3 OF 3 | A4

SOLIDWORKS Educational Product. For Instructional Use Only.

Rear Upright FEA

04/25/2019

Assumptions

- Part fixed at a-arm and toe link connections
- Case 1 (Fx) is applied as a torque on the caliper mount
- Case 2 (Fy) is applied on the main bearing face of the nearest bearing, separated into upper and lower halfs to represent the twisting that would occur from this force. (This is an understatement, setting this up like the front upright would be more accurate)
- Case 3 (Fz) is applied at the upper faces of the bearings

Material Properties

Model Reference	Properties
	Name: 6061-T6 (SS) **Model type:** Linear Elastic Isotropic **Default failure criterion:** Unknown **Yield strength:** 2.75e+008 N/m^2 **Tensile strength:** 3.1e+008 N/m^2 **Elastic modulus:** 6.9e+010 N/m^2 **Poisson's ratio:** 0.33 **Mass density:** 2700 kg/m^3 **Shear modulus:** 2.6e+010 N/m^2 **Thermal expansion coefficient:** 2.4e-005 /Kelvin

Mesh Details

- **Mesh Type: Hex Dominant**
- **Number of Cells: 9838**
- **Refinement: No**
- **Topology Criteria: NA**
- **Topology Percentage: NA**

Loads and Fixtures

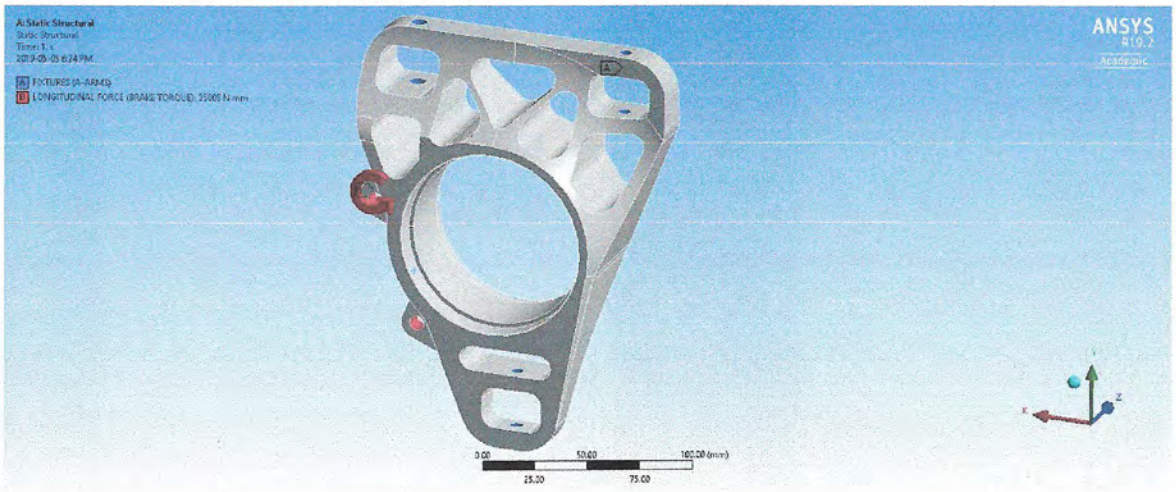

Case 1 Conditions

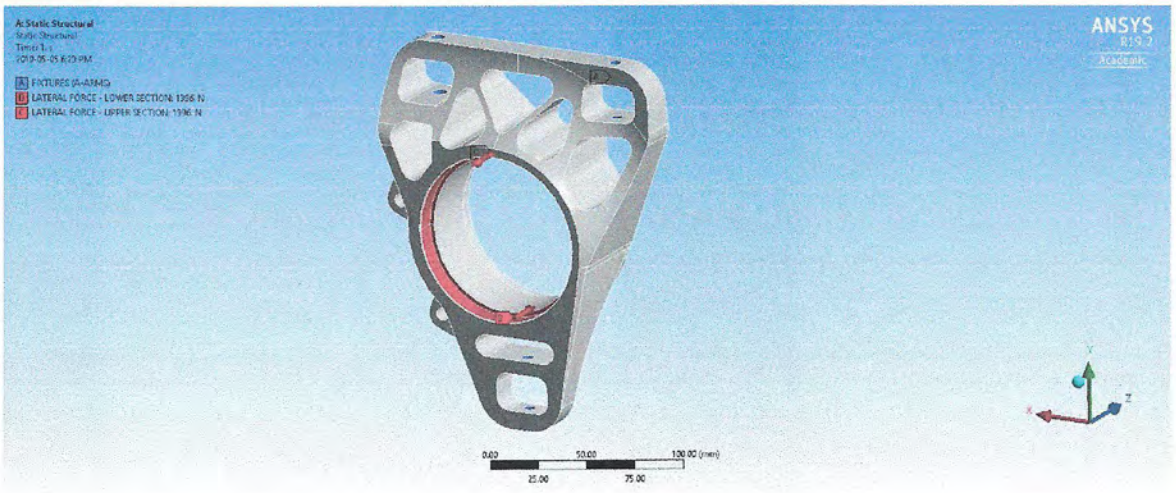

Case 2 Conditions

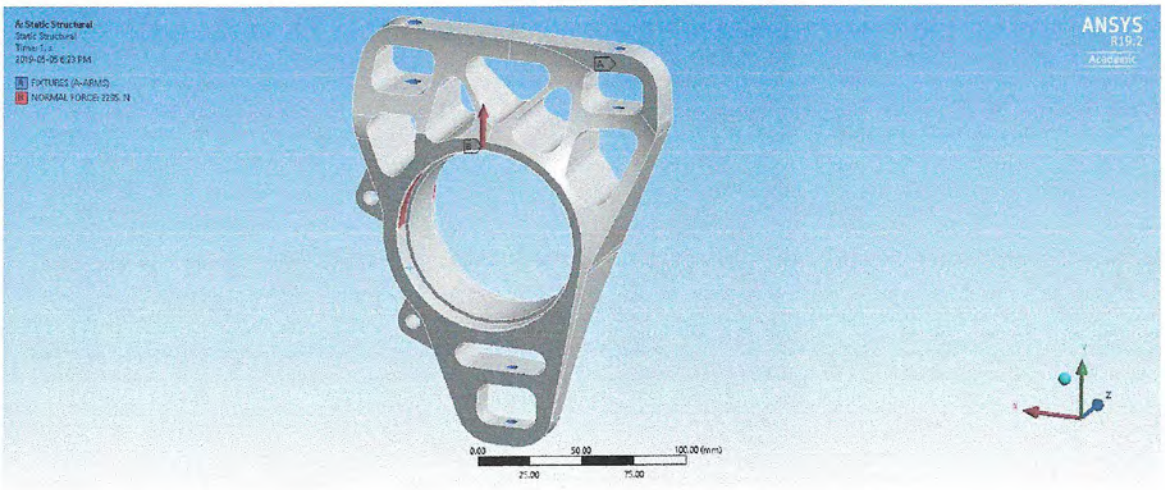

Case 3 Conditions

Study Results - Case 2

Name	Type	Max
Stress	VON: von Mises Stress	2.23e+008N/m^2

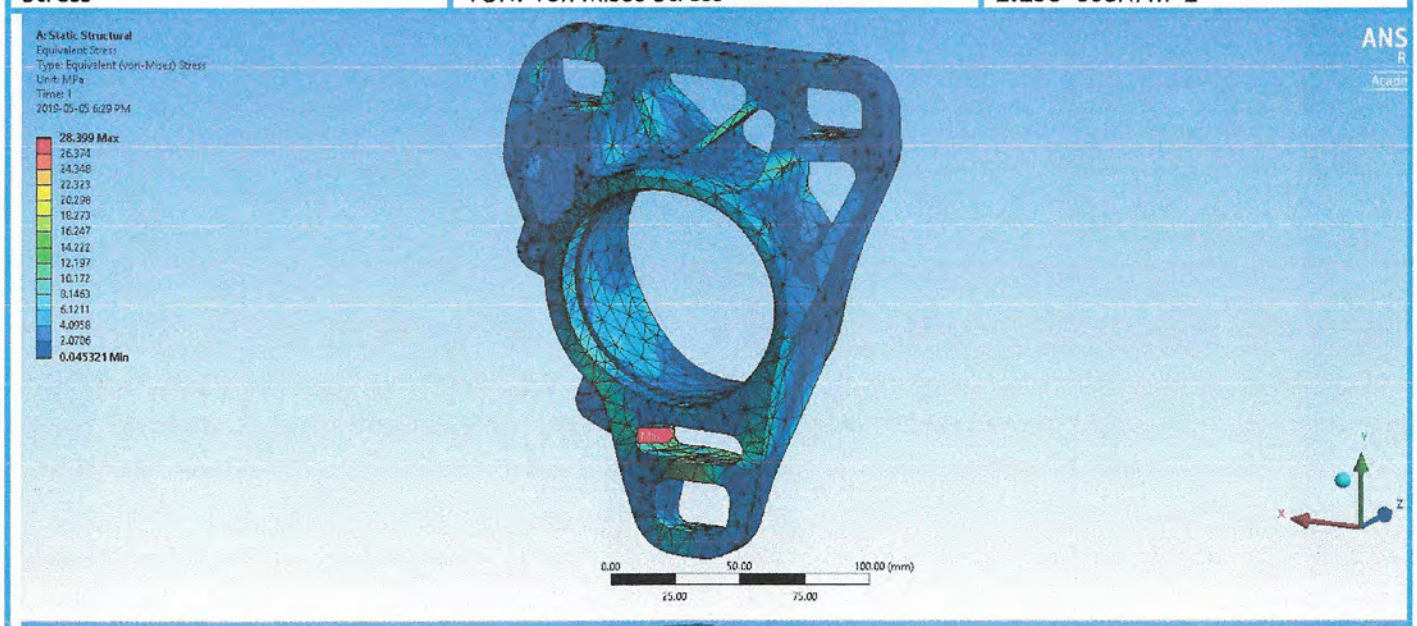

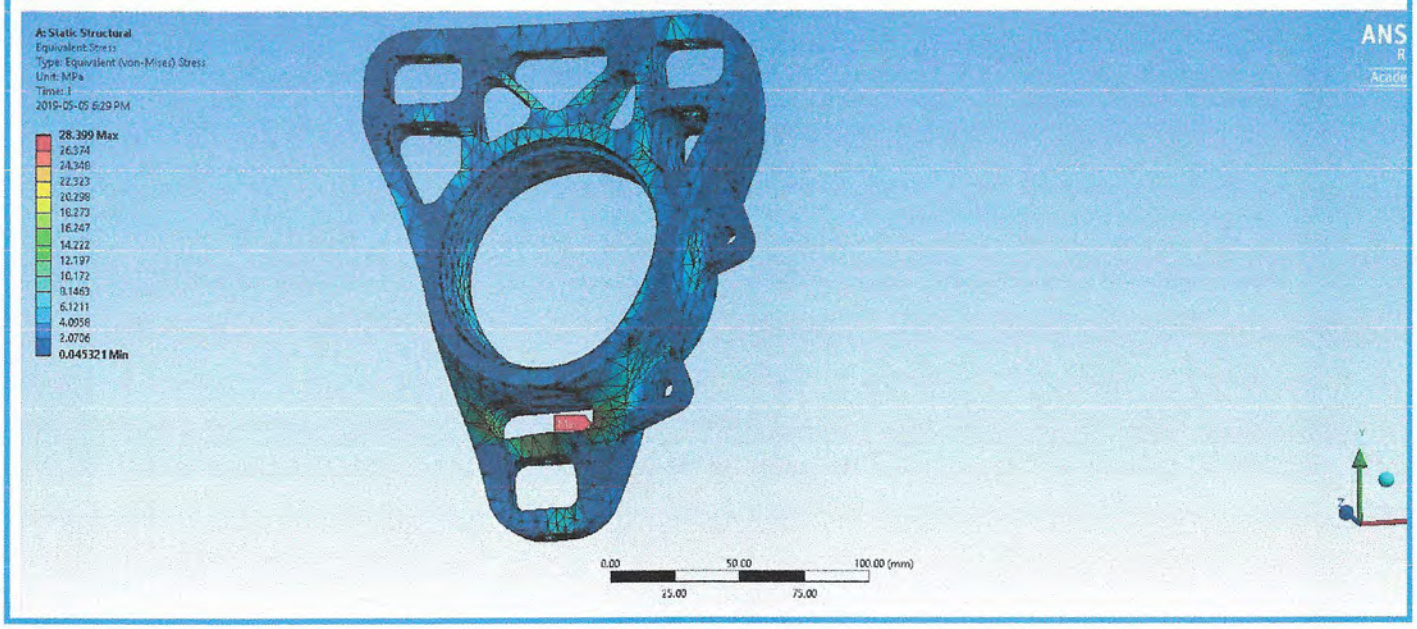

Name	Type	Max
Displacement	URES: Resultant Displacement	0.07mm

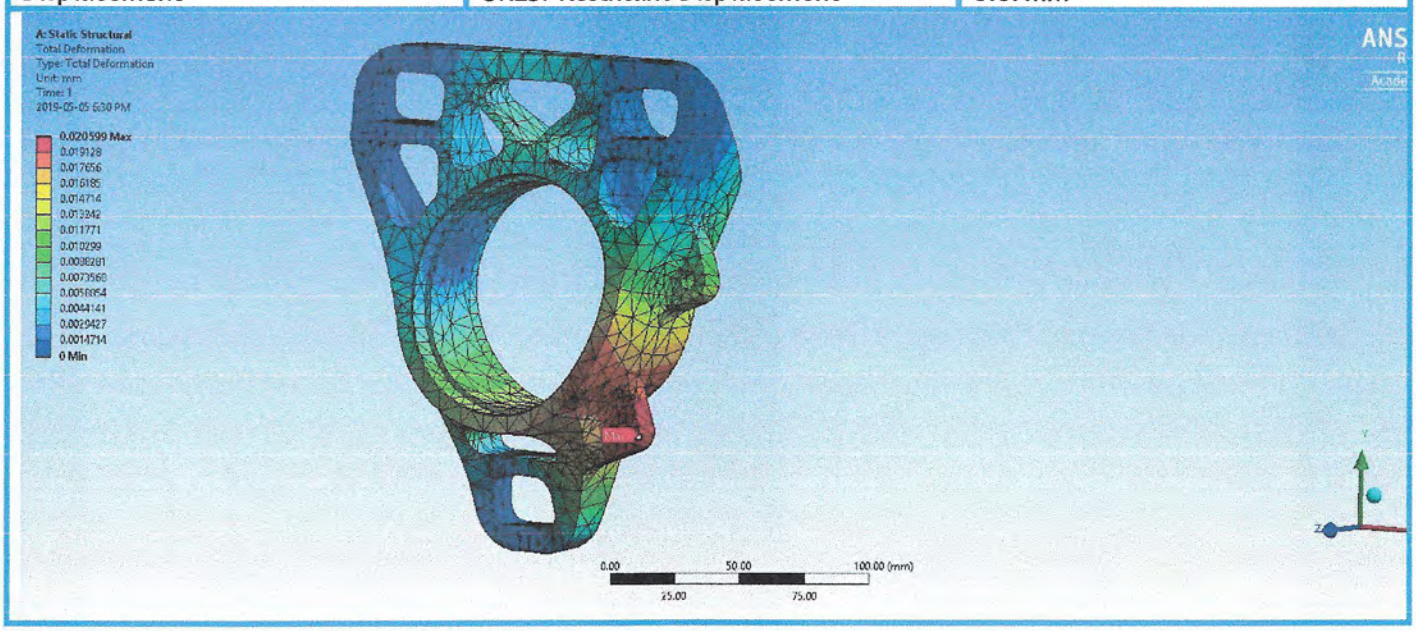

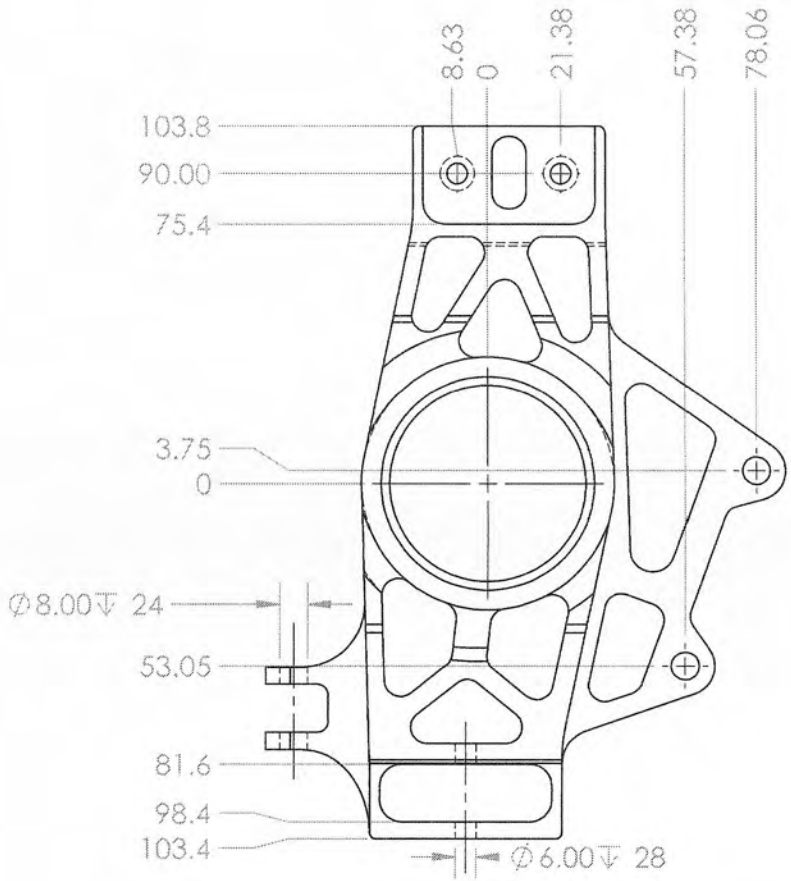

FINISH:

DEBURR AND BREAK ALL SHARP EDGES

SUSPENSION

DO NOT SCALE DRAWING
UNLESS OTHERWISE SPECIFIED
DIMENSIONS ARE IN MILLIMETERS

DIMENSION	TOLERANCE
X.X	±0.1
X.XX	±0.05
ANGLE	±0.1°

GRYPHON RACING
GUELPH, ON

TITLE:

FR UPRIGHT

ECN:	APPROVAL	DATE	IN
DRAWN			
CHECKED			
CAPITAN			

MATERIAL: 6061-T6 (SS)

WEIGHT: 645.62

DWG NO. GRC19_PT_SU_0053

REVISION 2

SCALE:1:5

SHEET 1 OF 2

A4

SOLIDWORKS Educational Product. For Instructional Use Only.

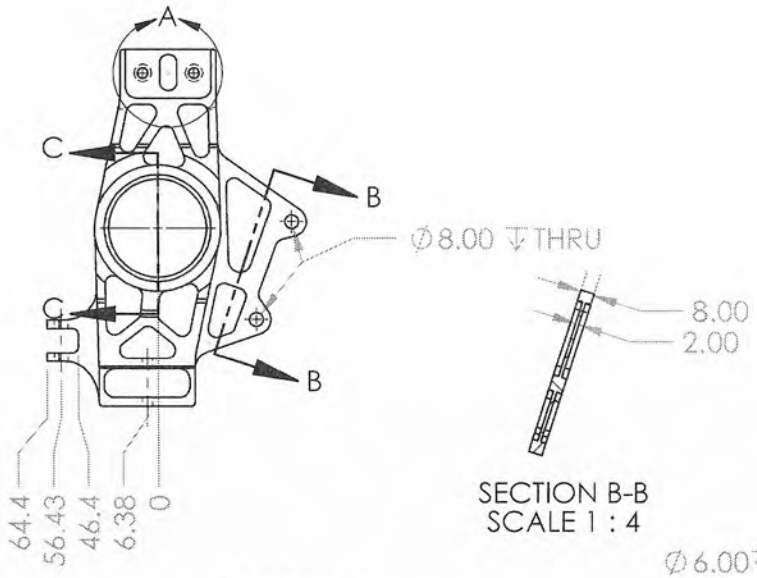

SECTION B-B
SCALE 1 : 4

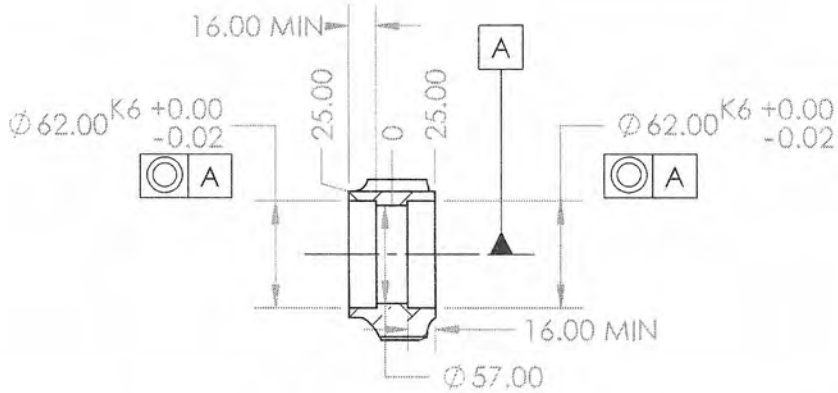

SECTION C-C
SCALE 1 : 4

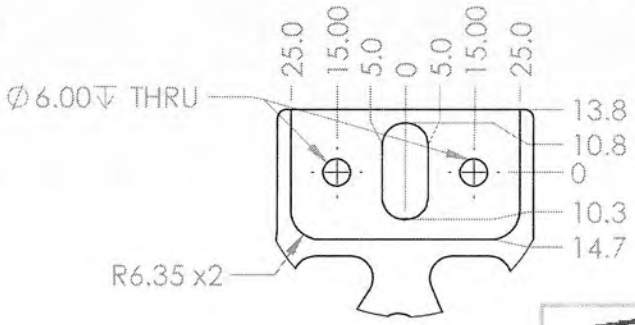

DETAIL A
SCALE 1 : 1.5

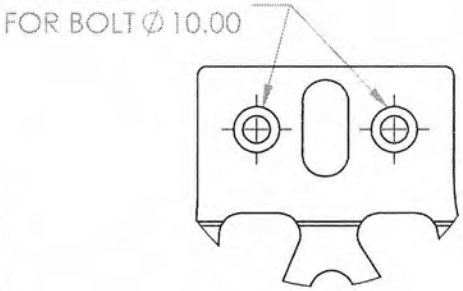

DETAIL D
SCALE 1 : 1.5

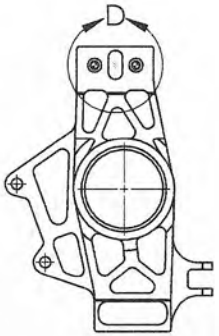

GRYPHON RACING
GUELPH, ON

TITLE:
FR UPRIGHT

DWG NO.
GRC19_PT_SU_0053

REVISION
2

SCALE:1:5

SHEET 2 OF 2

A4

SOLIDWORKS Educational Product. For Instructional Use Only.

Front Upright FEA

04/25/2019

Assumptions

- Part fixed at a-arm and tie rod connections
- Case 1 (Fx) is applied as a torque on the caliper mount
- Case 2 (Fy) is applied as a remote force at geometric center of contact patch to the opposing bearing seat feature
- Case 3 (Fz) is applied as a remote force at geometric center of contact patch to upper half of main bearing faces

Material Properties

Model Reference	Properties
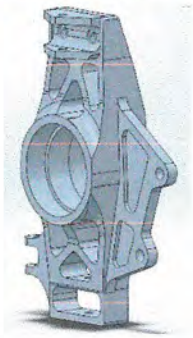	**Name:** 6061-T6 (SS) **Model type:** Linear Elastic Isotropic **Default failure criterion:** Unknown **Yield strength:** 2.75e+008 N/m^2 **Tensile strength:** 3.1e+008 N/m^2 **Elastic modulus:** 6.9e+010 N/m^2 **Poisson's ratio:** 0.33 **Mass density:** 2700 kg/m^3 **Shear modulus:** 2.6e+010 N/m^2 **Thermal expansion coefficient:** 2.4e-005 /Kelvin

Mesh Details

- **Mesh Type: Automatic**
- **Number of Cells: 61429**
- **Refinement: No**
- **Topology Criteria: NA**
- **Topology Percentage: NA**

Loads and Fixtures

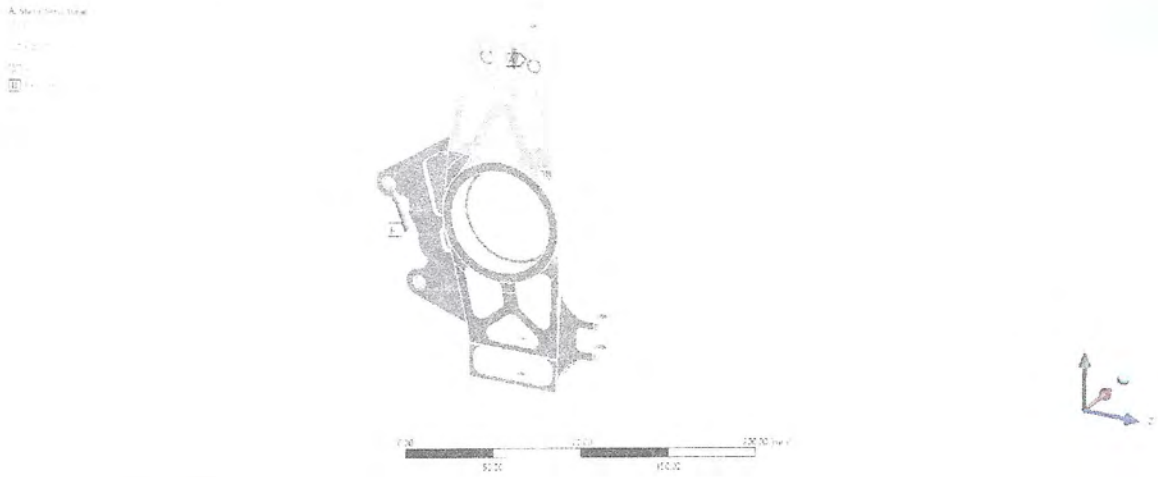

Case 1 Conditions

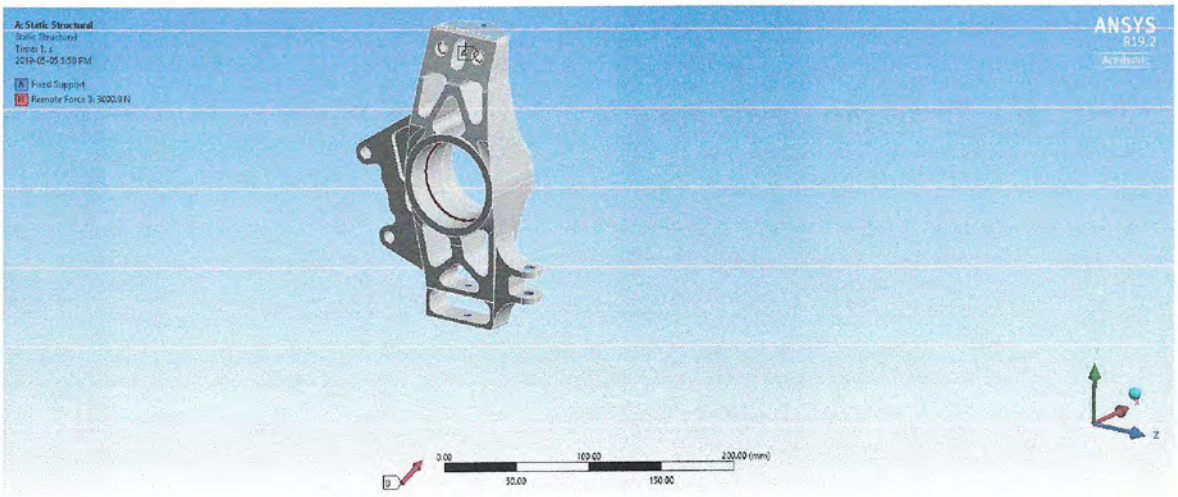

Case 2 Conditions

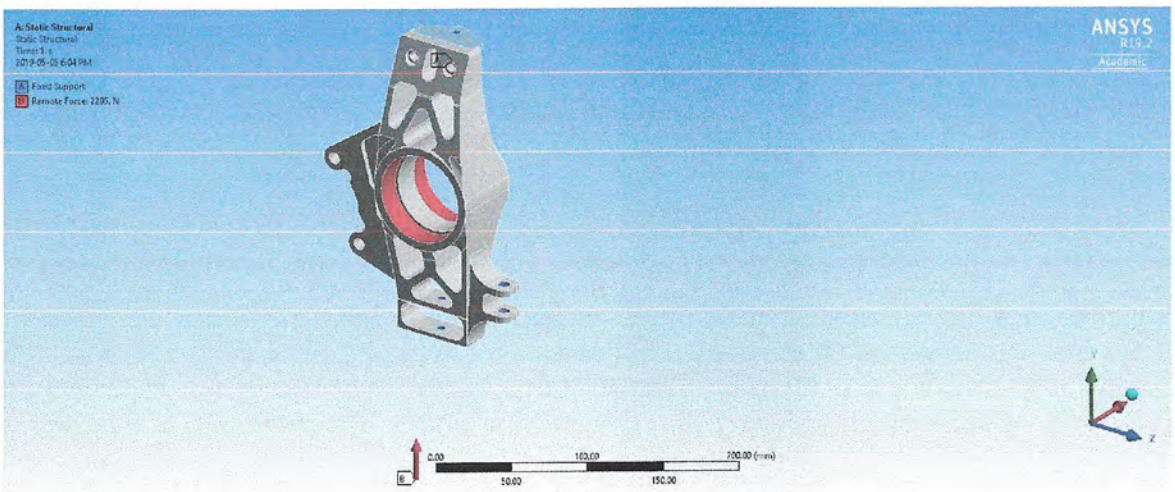

Case 3 Conditions

Study Results - Case 2

Name	Type	Max
Stress	VON: von Mises Stress	2.23e+008N/m^2

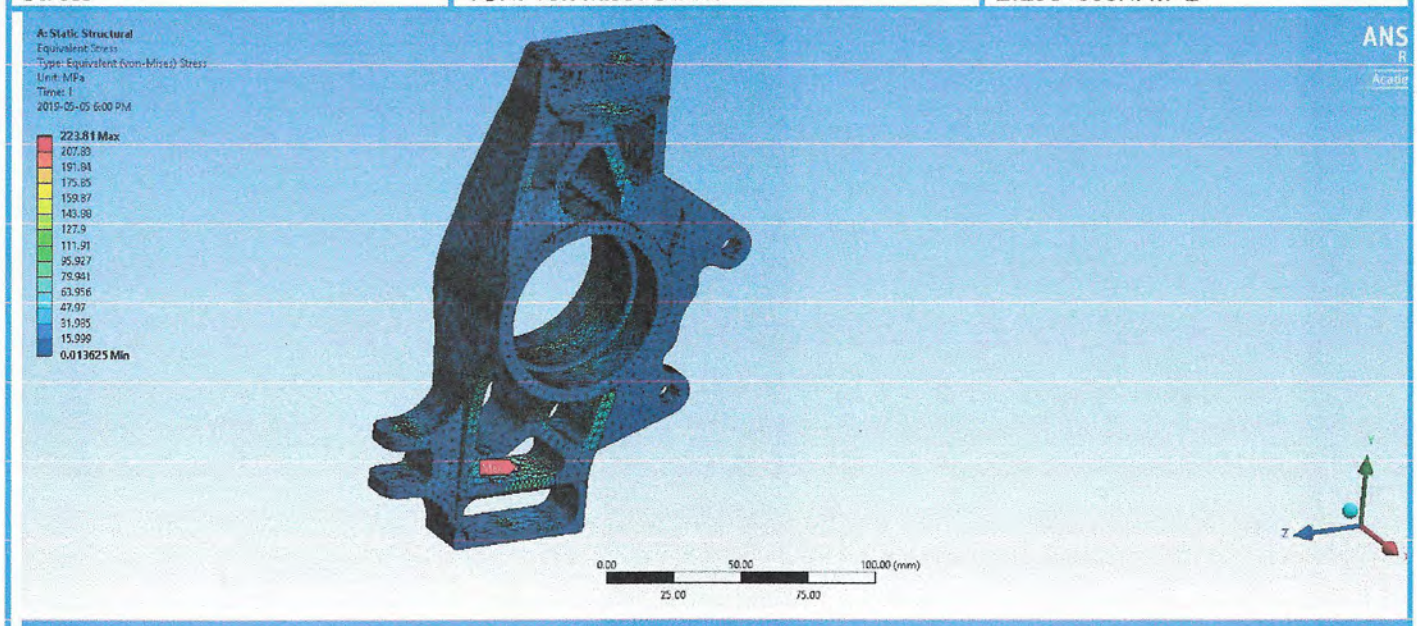

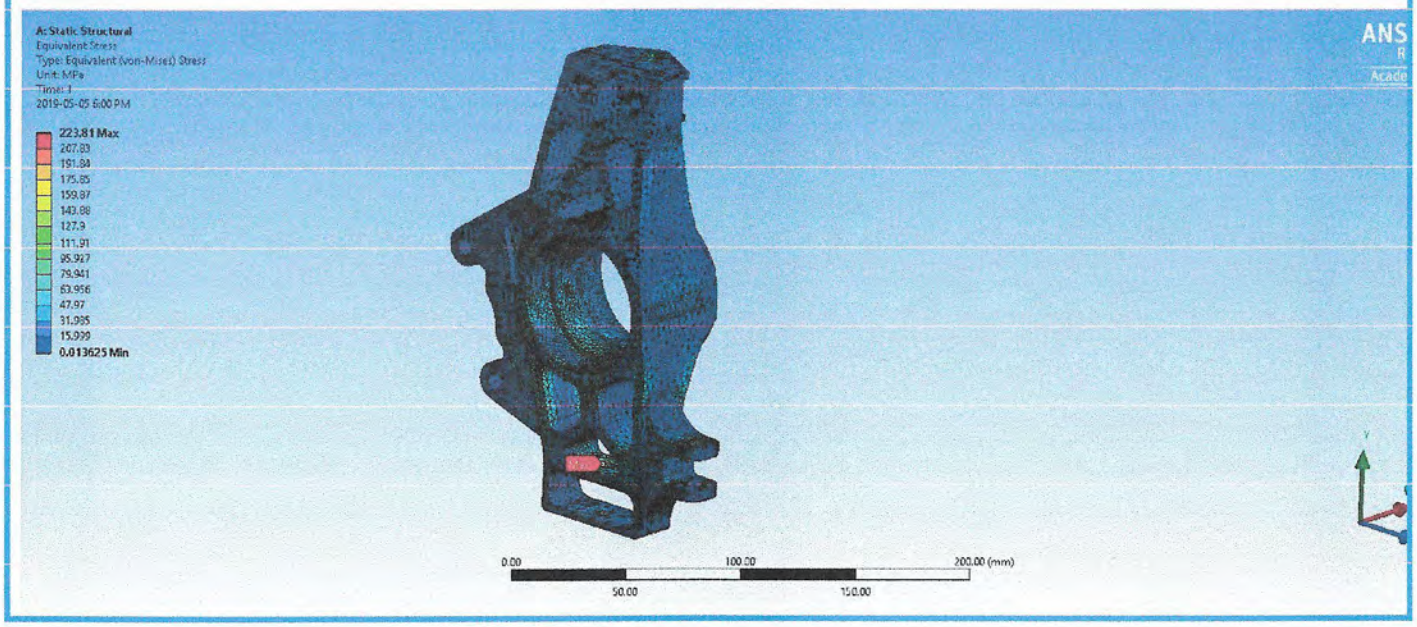

Name	Type	Max
Displacement	URES: Resultant Displacement	0.07mm

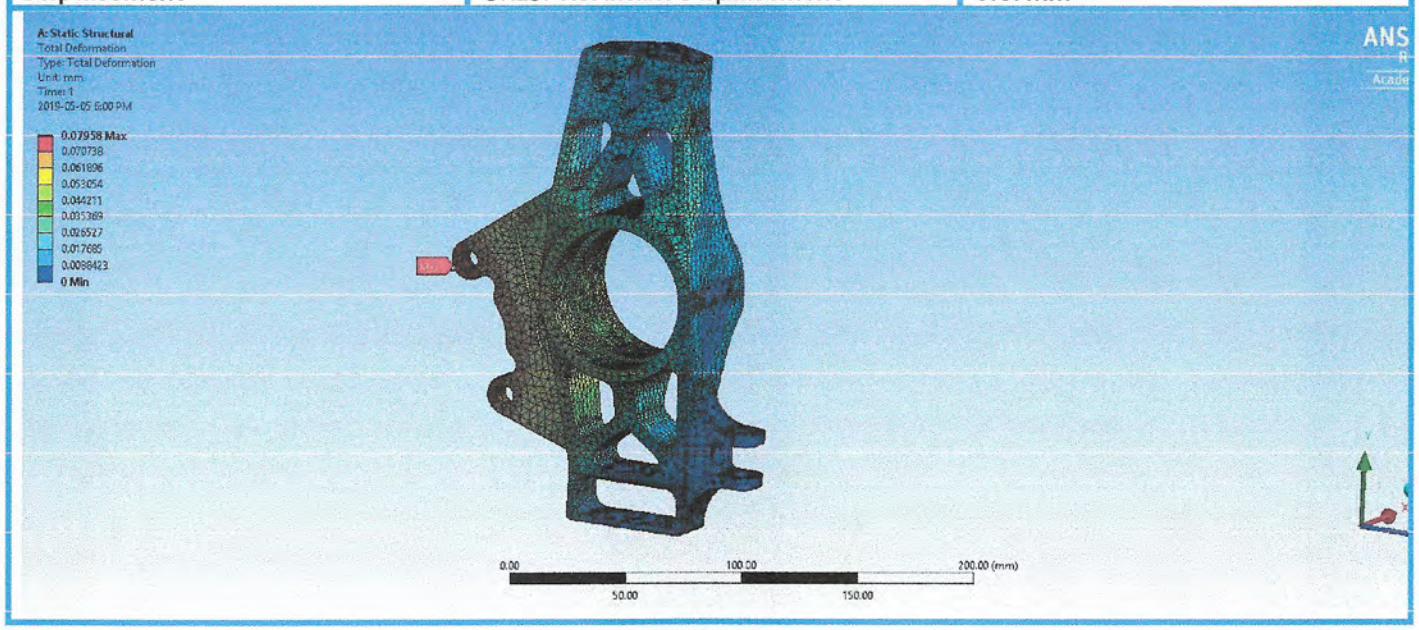

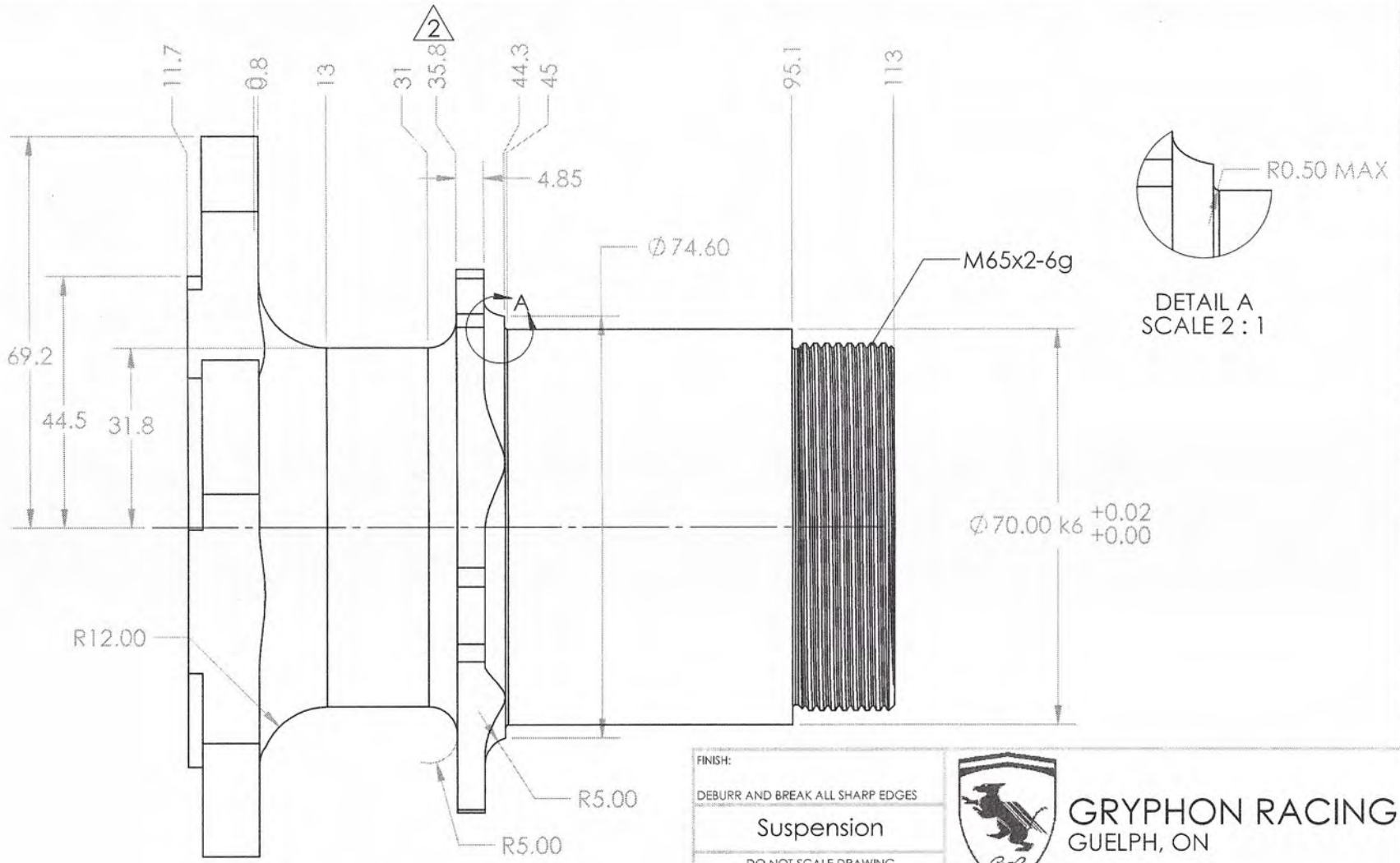

FINISH:

DEBURR AND BREAK ALL SHARP EDGES

Suspension

DO NOT SCALE DRAWING
UNLESS OTHERWISE SPECIFIED
DIMENSIONS ARE IN MILLIMETERS

DIMENSION	TOLERANCE
X.X	±0.1
X.XX	±0.05
ANGLE	±0.1°

GRYPHON RACING
GUELPH, ON

TITLE:

Rear Hub

ECN:	APPROVAL	DATE	IN
DRAWN			
CHECKED			
CAPITAN			

MATERIAL: 6061-T6

WEIGHT: 840.308

DWG NO. GRC19_PT_SU_0028

REVISION R2

SCALE:1:5

SHEET 1 OF 3

A4

SOLIDWORKS Educational Product. For Instructional Use Only.

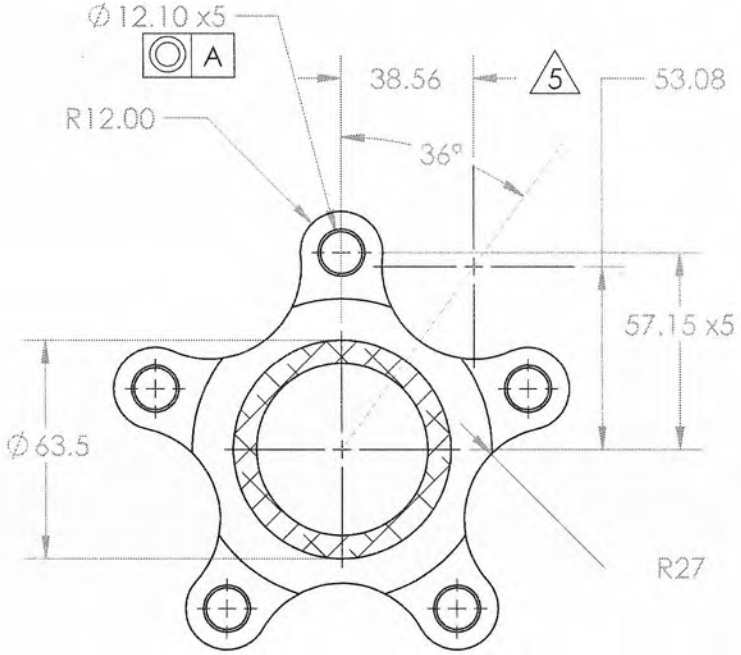

SECTION B-B
SCALE 1 : 2

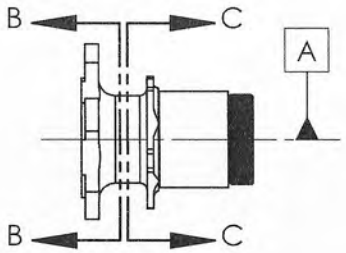

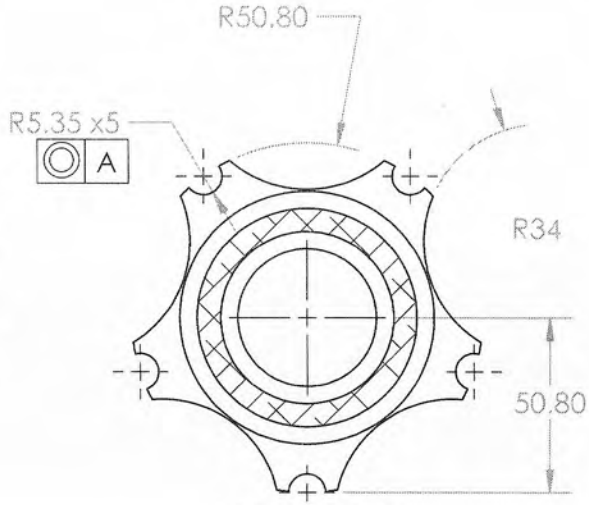

SECTION C-C
SCALE 1 : 2

GRYPHON RACING
GUELPH, ON

TITLE:
Rear Hub

DWG NO.
GRC19_PT_SU_0028

REVISION
R2

SCALE:1:5

SHEET 2 OF 3

A4

SOLIDWORKS Educational Product. For Instructional Use Only.

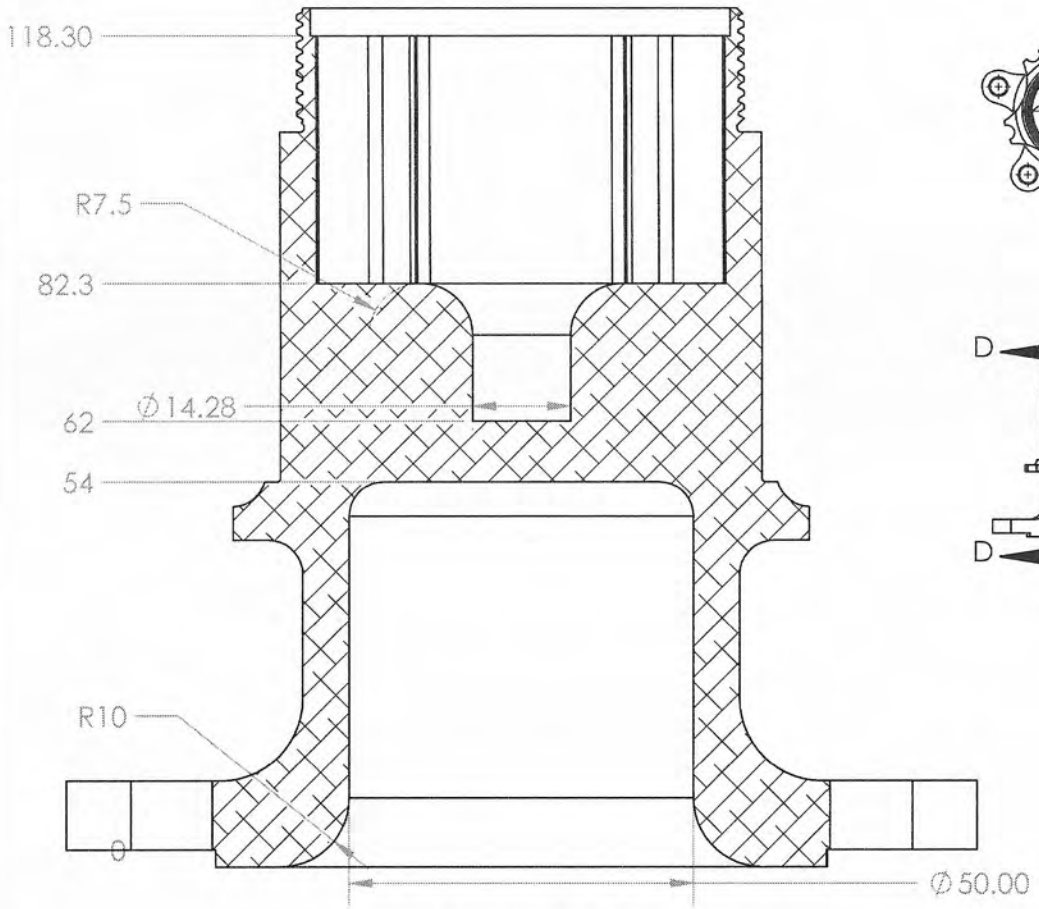

SECTION D-D
SCALE 1 : 1

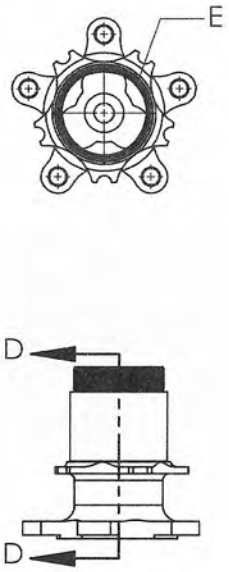

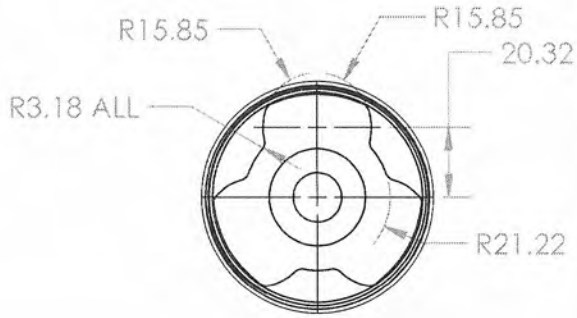

DETAIL E
SCALE 1 : 2

GRYPHON RACING
GUELPH, ON

TITLE:
Rear Hub

DWG NO.
GRC19_PT_SU_0028

REVISION
R2

SCALE:1:5

SHEET 3 OF 3

A4

SOLIDWORKS Educational Product. For Instructional Use Only.

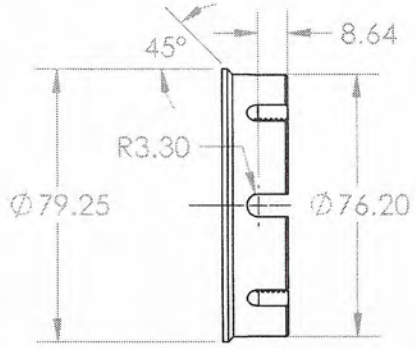

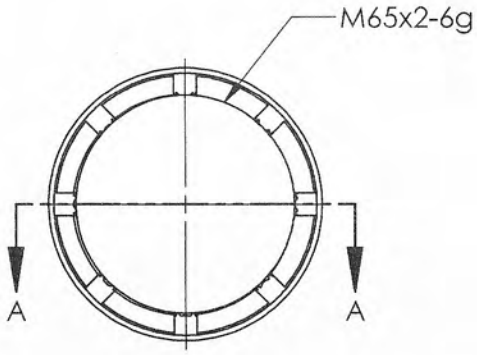

SECTION A-A

FINISH:

DEBURR AND BREAK ALL SHARP EDGES

DO NOT SCALE DRAWING
UNLESS OTHERWISE SPECIFIED
DIMENSIONS ARE IN MILLIMETERS

DIMENSION	TOLERANCE
X.X	±0.1
X.XX	±0.05
ANGLE	±0.1°

GRYPHON RACING
GUELPH, ON

TITLE:

Rear Hub Nut

ECN:	APPROVAL	DATE	IN
DRAWN			
CHECKED			
CAPITAN			

MATERIAL: 6061-T6

WEIGHT: 61.215

DWG NO. GRC19_PT_SU_0029

REVISION 2

SCALE:1:2

SHEET 1 OF 2

A4

SOLIDWORKS Educational Product. For Instructional Use Only.

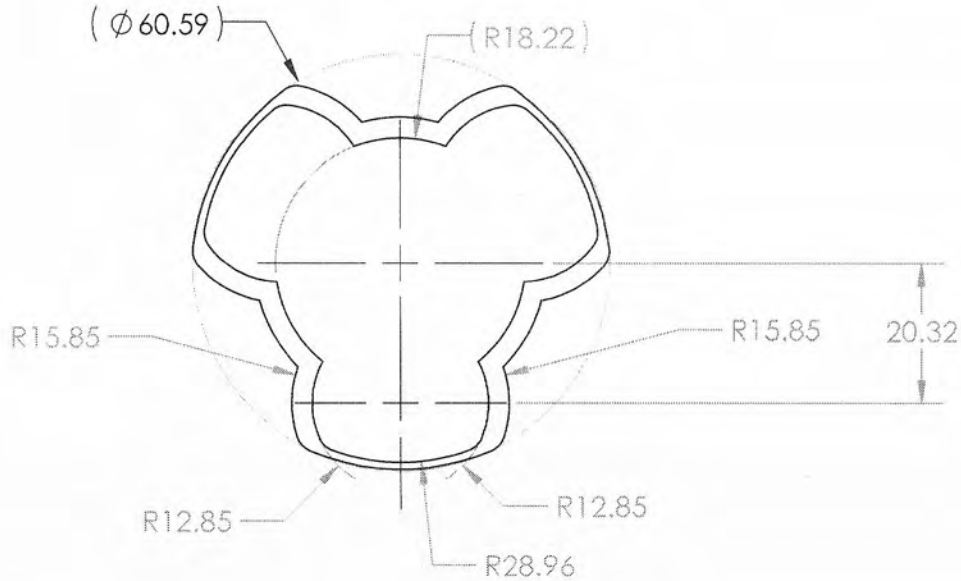

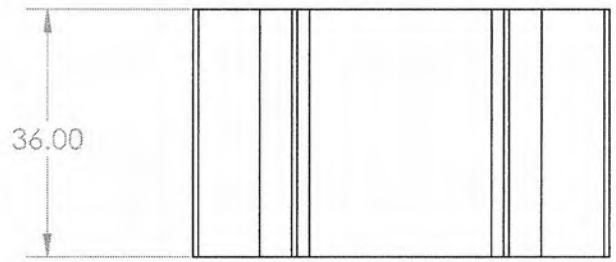

FINISH:

DEBURR AND BREAK ALL SHARP EDGES

SUSPENSION

DO NOT SCALE DRAWING
UNLESS OTHERWISE SPECIFIED
DIMENSIONS ARE IN MILLIMETERS

DIMENSION	TOLERANCE
X.X	±0.1
X.XX	±0.05
ANGLE	±0.1°

GRYPHON RACING
GUELPH, ON

TITLE:

TRIPOD SLEEVE

ECN:	APPROVAL	DATE	IN
DRAWN			
CHECKED			
CAPITAN			

MATERIAL:

AISI 4340 Steel, normalized

WEIGHT: 120.064

DWG NO.

GRC19_PT_SU_0032

REVISION 2

SCALE:1:1

SHEET 1 OF 1

A4

SOLIDWORKS Educational Product. For Instructional Use Only.

Rear Hub FEA

04/25/2019

Assumptions

- Part fixed with cylindrical and frictionless support at bearing contact areas, no axial displacement condition, and inboard face fixed.
- All loads applied as remote forces in contact patch center
- Case 1 (Fx) also fixes the bobbin contact areas
- Rotational inertia of 140 km/hr applied in all cases

Material Properties

Model Reference	Properties
	Name: 6061-T6 (SS) **Model type:** Linear Elastic Isotropic **Default failure criterion:** Unknown **Yield strength:** 2.75e+008 N/m^2 **Tensile strength:** 3.1e+008 N/m^2 **Elastic modulus:** 6.9e+010 N/m^2 **Poisson's ratio:** 0.33 **Mass density:** 2700 kg/m^3 **Shear modulus:** 2.6e+010 N/m^2 **Thermal expansion coefficient:** 2.4e-005 /Kelvin

Mesh Details

- **Mesh Type: Automatic**
- **Number of Cells: 104588**
- **Refinement: @ Outside bearing radius, value of 2**
- **Topology Criteria: NA**
- **Topology Percentage: NA**

Loads and Fixtures

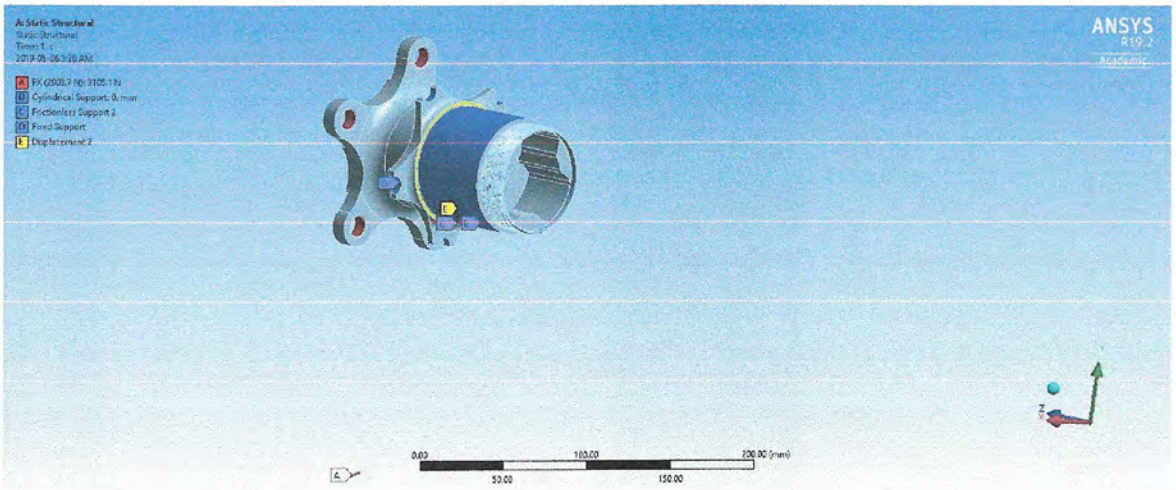

Case 1 Conditions

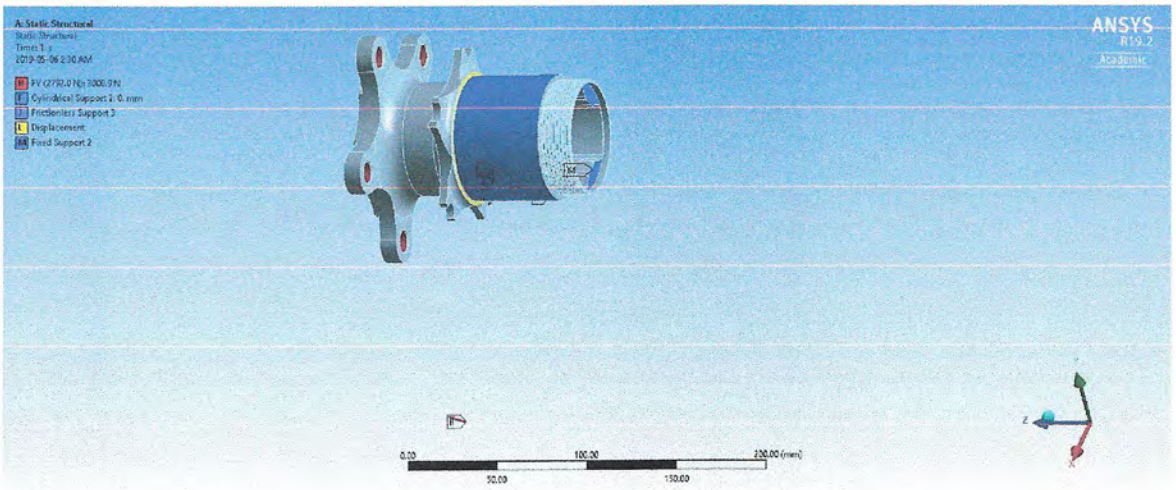

Case 2 Conditions

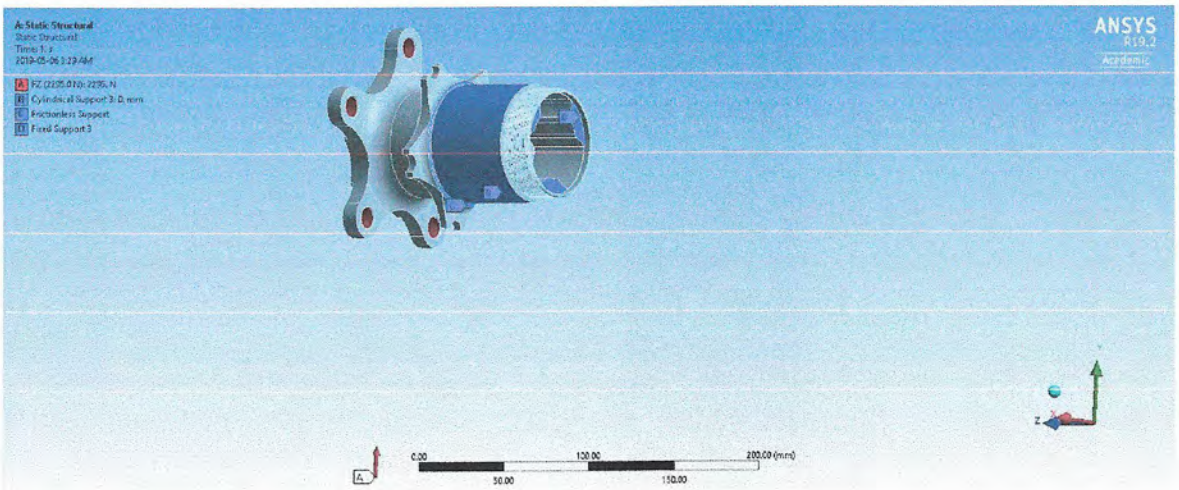

Case 3 Conditions

Study Results - Case 2

Name	Type	Max
Stress	VON: von Mises Stress	1.59e+008N/m^2

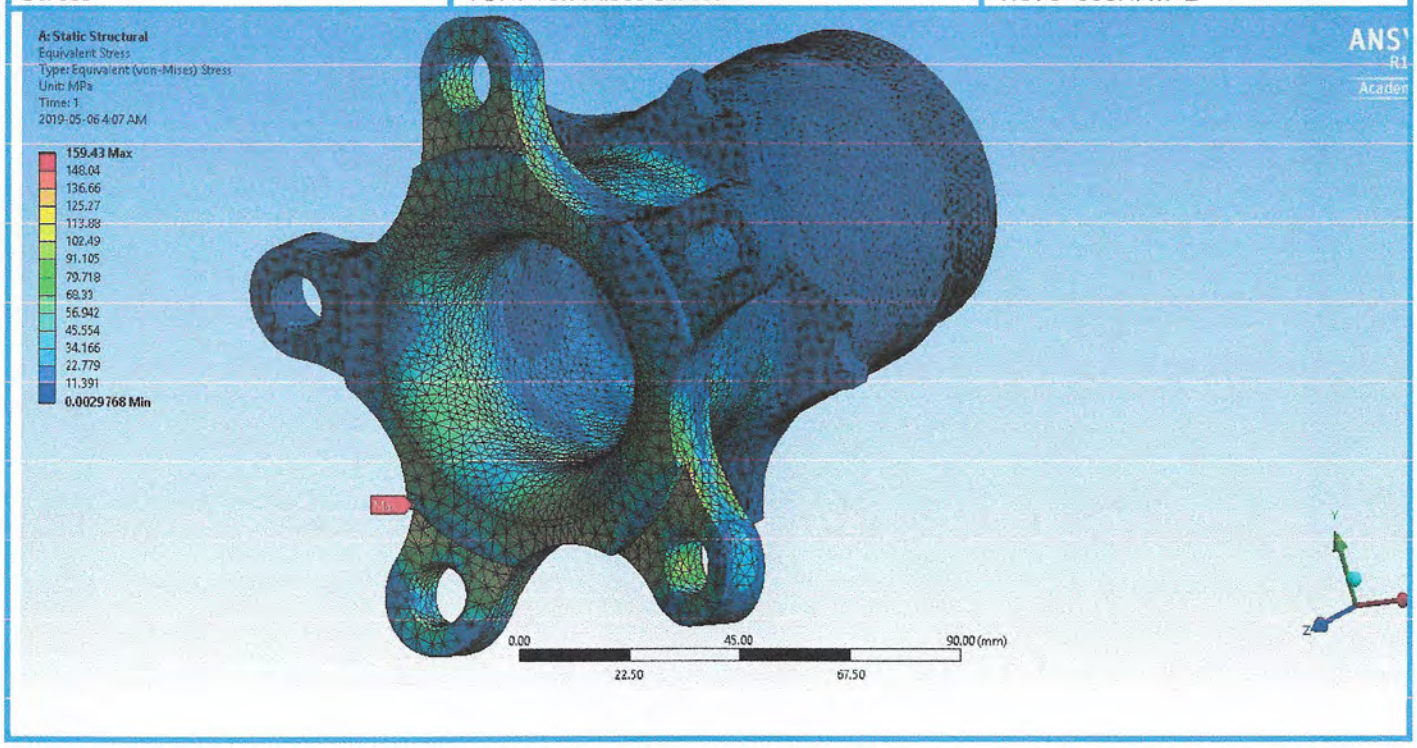

Name	Type	Max
Displacement	URES: Resultant Displacement	0.29mm

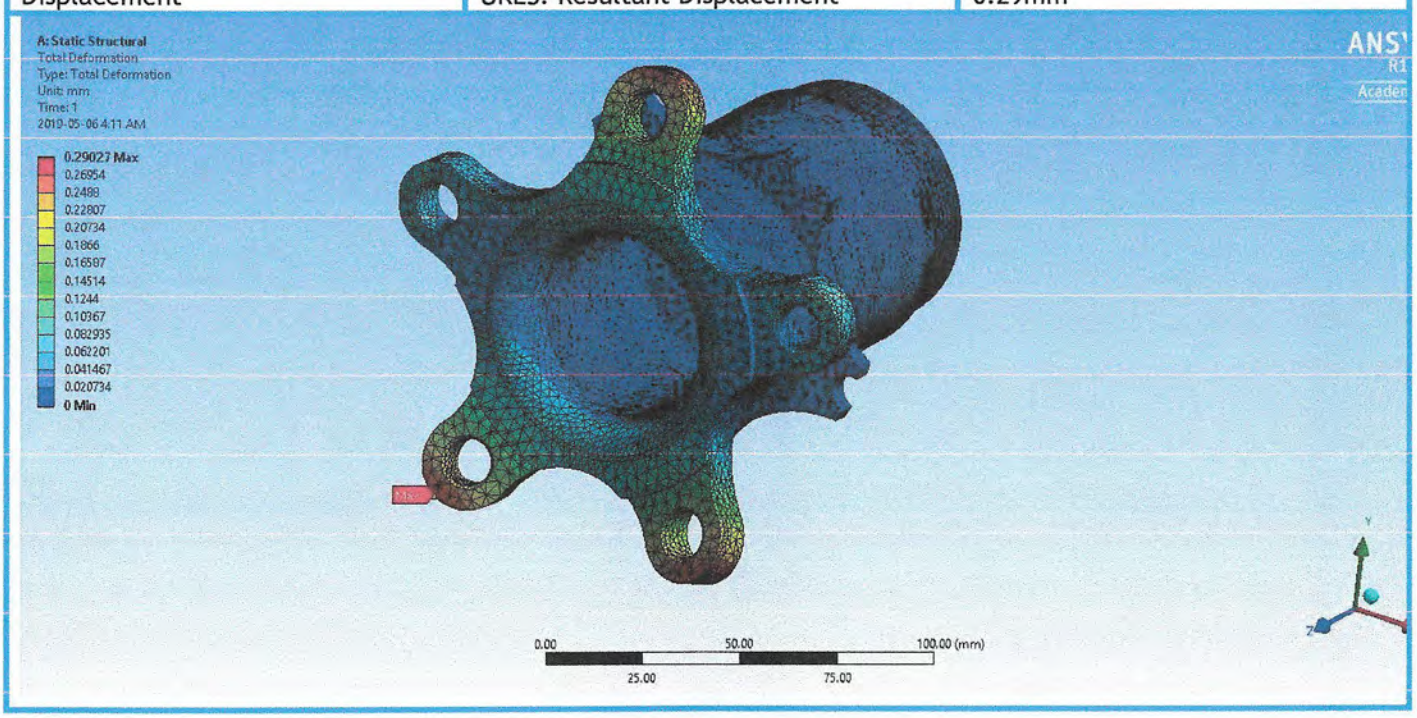

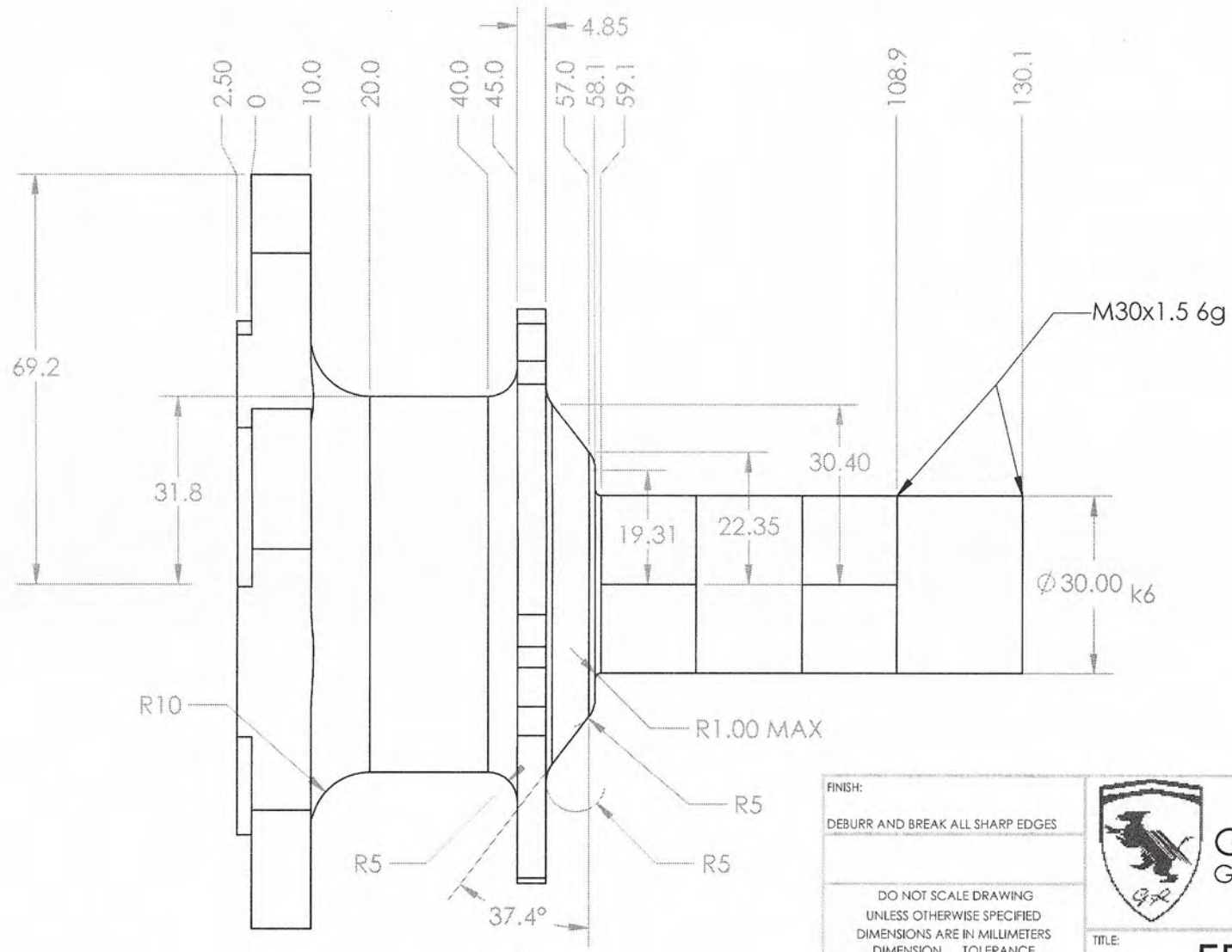

FINISH:

DEBURR AND BREAK ALL SHARP EDGES

DO NOT SCALE DRAWING
UNLESS OTHERWISE SPECIFIED
DIMENSIONS ARE IN MILLIMETERS

DIMENSION	TOLERANCE
X.X	±0.1
X.XX	±0.05
ANGLE	±0.1°

GRYPHON RACING
GUELPH, ON

TITLE:

FRONT HUB

ECN:	APPROVAL	DATE	IN
DRAWN	OMM	01/21/19	
CHECKED			
CAPITAN			

MATERIAL: 6061-T6
6061-T6 (SS)

WEIGHT: 523.6 g

DWG NO.
GRC19_PT_SU_0050

REVISION

SCALE:1:5

SHEET 1 OF 3

A4

SOLIDWORKS Educational Product. For Instructional Use Only.

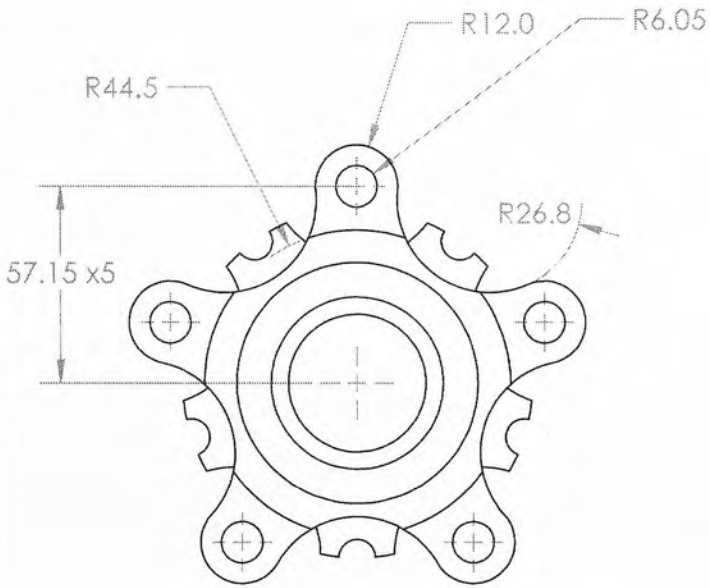

SECTION A-A
SCALE 1 : 2

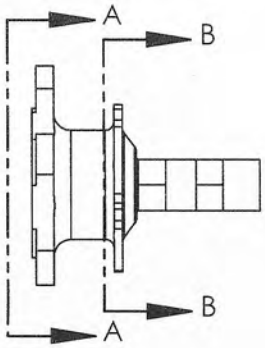

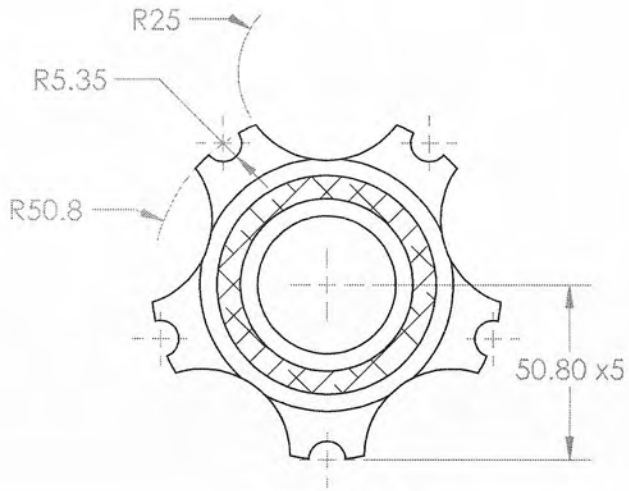

SECTION B-B
SCALE 1 : 2

GRYPHON RACING
GUELPH, ON

TITLE:
FRONT HUB

DWG NO.
GRC19_PT_SU_0050

REVISION

SCALE:1:5 | SHEET 2 OF 3 | A4

SOLIDWORKS Educational Product. For Instructional Use Only.

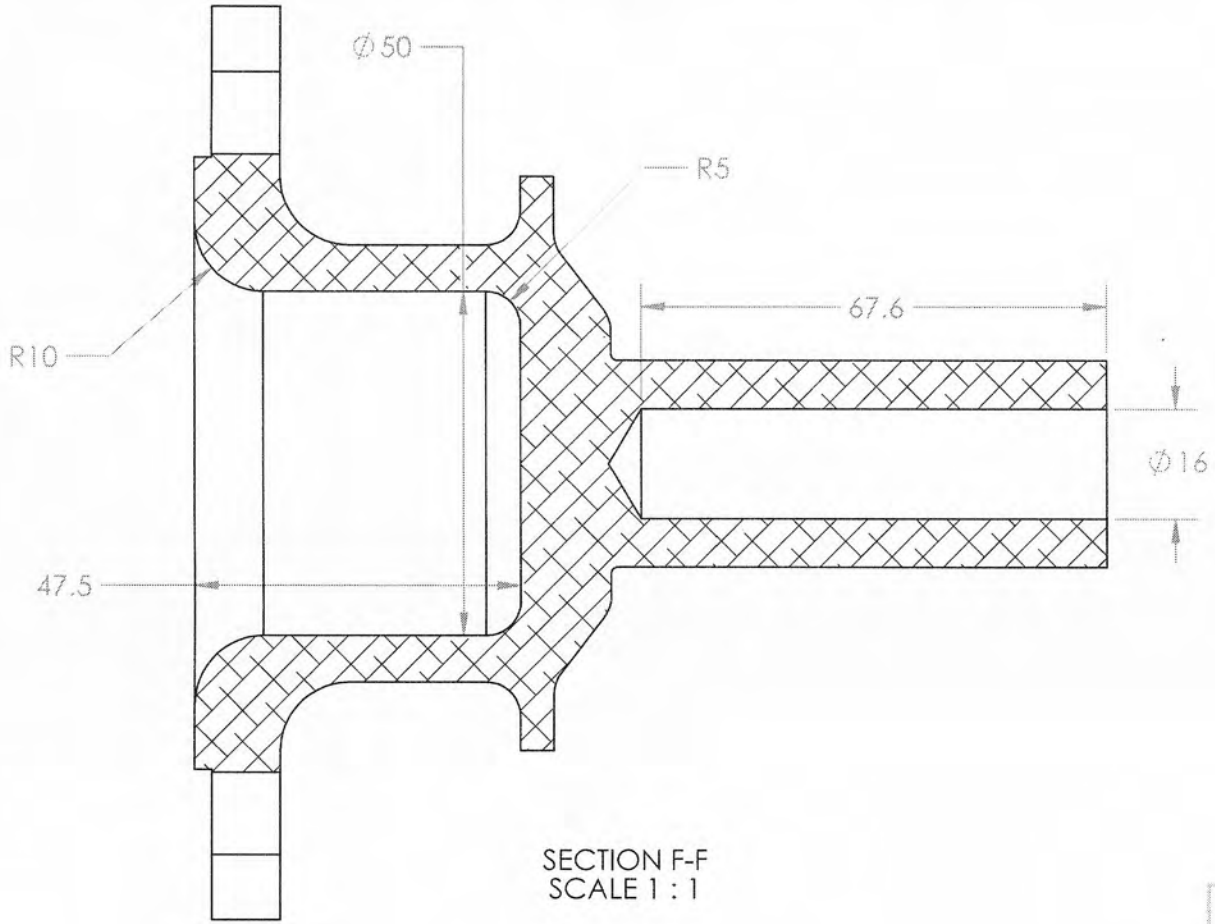

SECTION F-F
SCALE 1 : 1

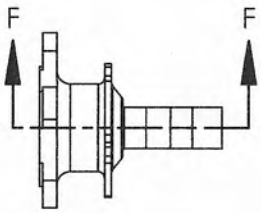

GRYPHON RACING
GUELPH, ON

TITLE:
FRONT HUB

DWG NO.
GRC19_PT_SU_0050

REVISION

SCALE: 1:5 | SHEET 3 OF 3 | A4

SOLIDWORKS Educational Product. For Instructional Use Only.

Front Hub FEA

04/25/2019

Assumptions

- Part fixed with cylindrical and frictionless support at bearing contact areas, no axial displacement condition, and inboard face fixed.
- All loads applied as remote forces in contact patch center
- Case 1 (Fx) also fixes the bobbin contact areas
- Rotational inertia of 140 km/hr applied in all cases

Material Properties

Model Reference	Properties
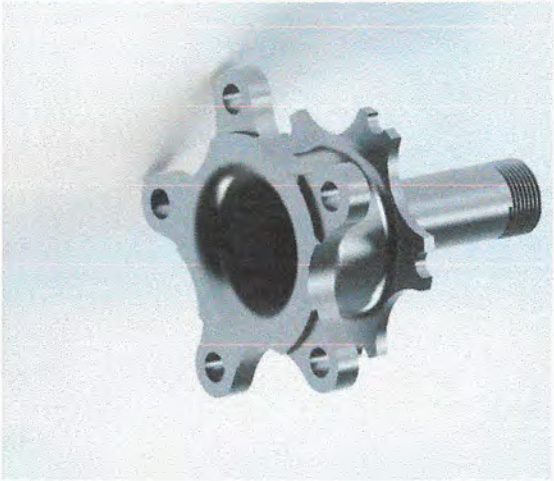	**Name:** 6061-T6 (SS) **Model type:** Linear Elastic Isotropic **Default failure criterion:** Unknown **Yield strength:** 2.75e+008 N/m^2 **Tensile strength:** 3.1e+008 N/m^2 **Elastic modulus:** 6.9e+010 N/m^2 **Poisson's ratio:** 0.33 **Mass density:** 2700 kg/m^3 **Shear modulus:** 2.6e+010 N/m^2 **Thermal expansion coefficient:** 2.4e-005 /Kelvin

Mesh Details

- **Mesh Type: Hex Dominant**
- **Number of Cells: 80190**
- **Refinement: No**
- **Topology Criteria: NA**
- **Topology Percentage: NA**

Loads and Fixtures

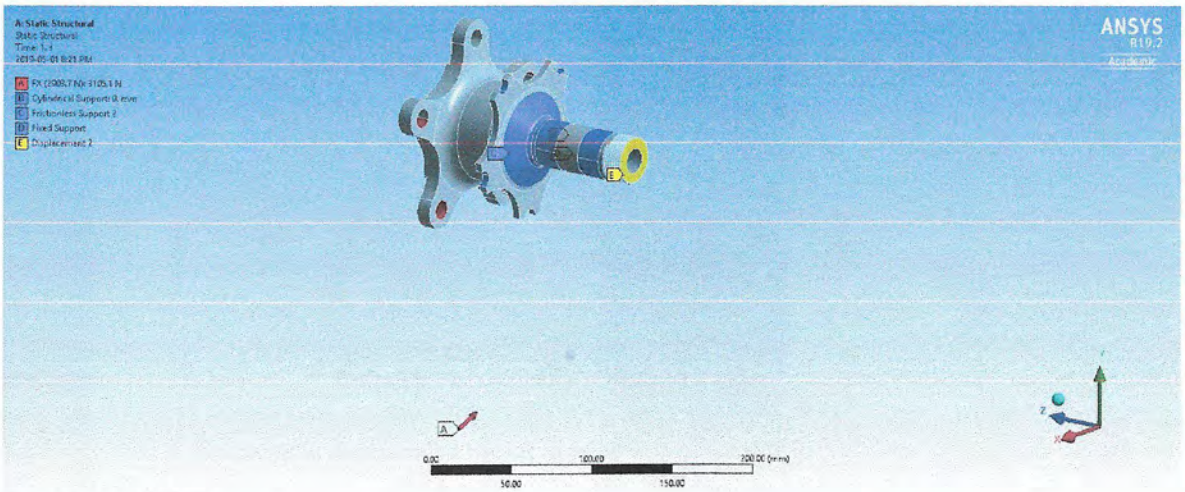

Case 1 Conditions

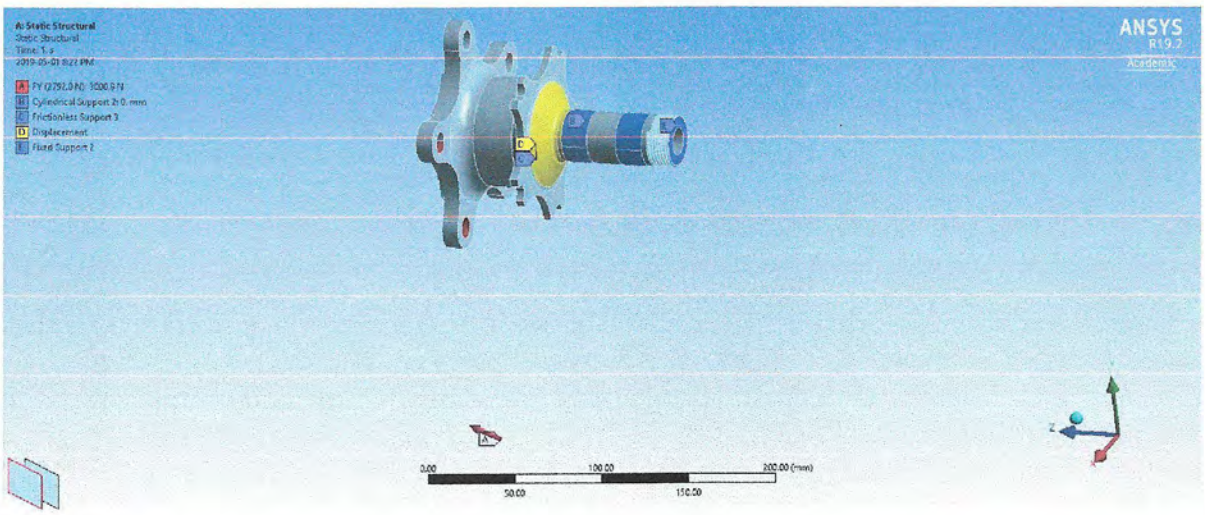

Case 2 Conditions

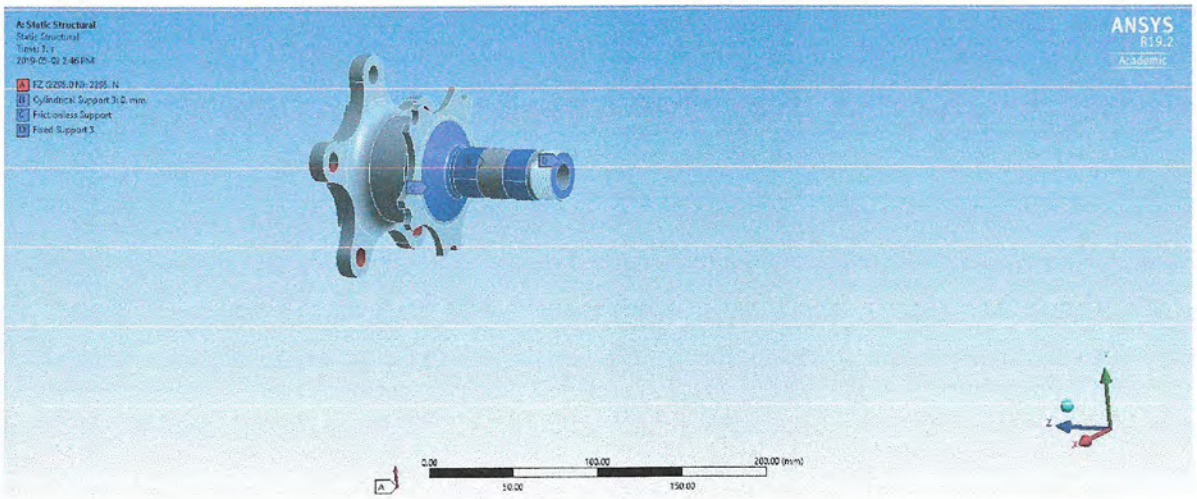

Case 3 Conditions

Study Results

Name	Type	Max
Stress	VON: von Mises Stress	0.94e+008N/m^2

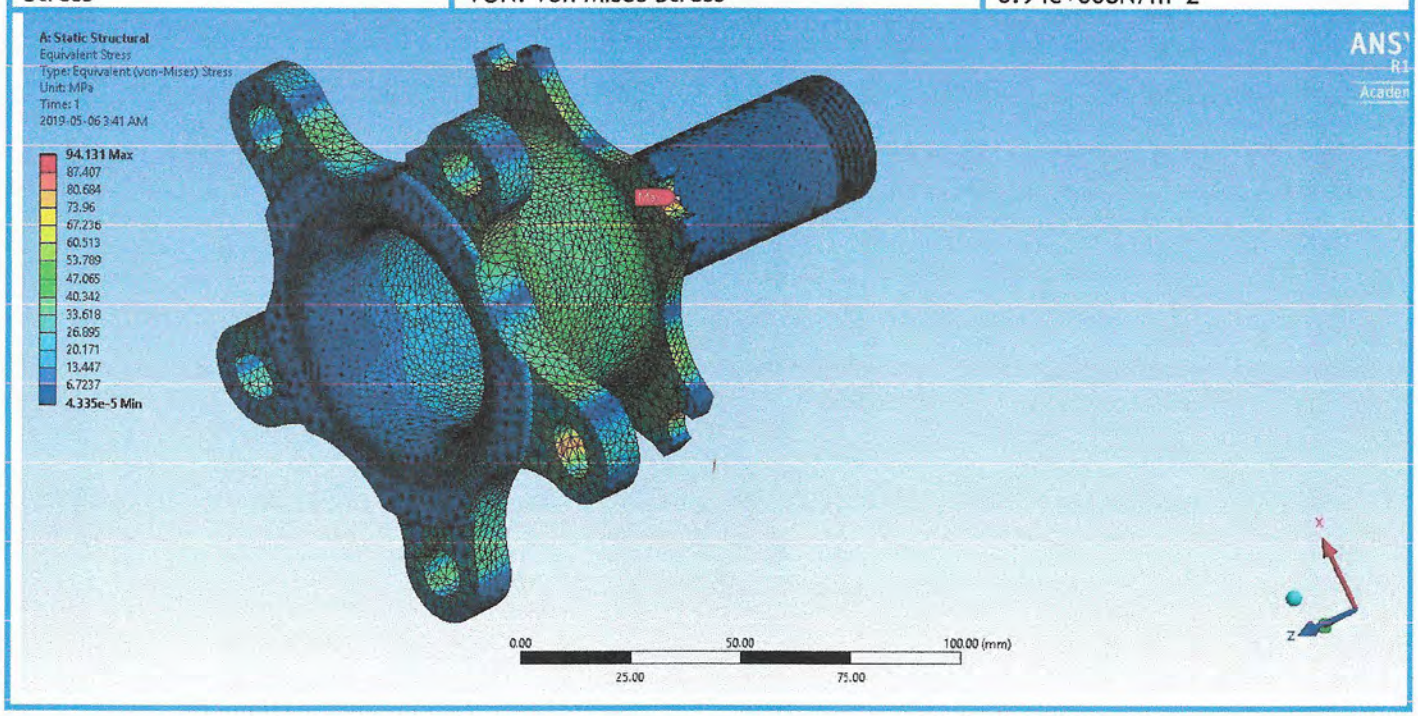

Name	Type	Max
Displacement	URES: Resultant Displacement	0.13mm

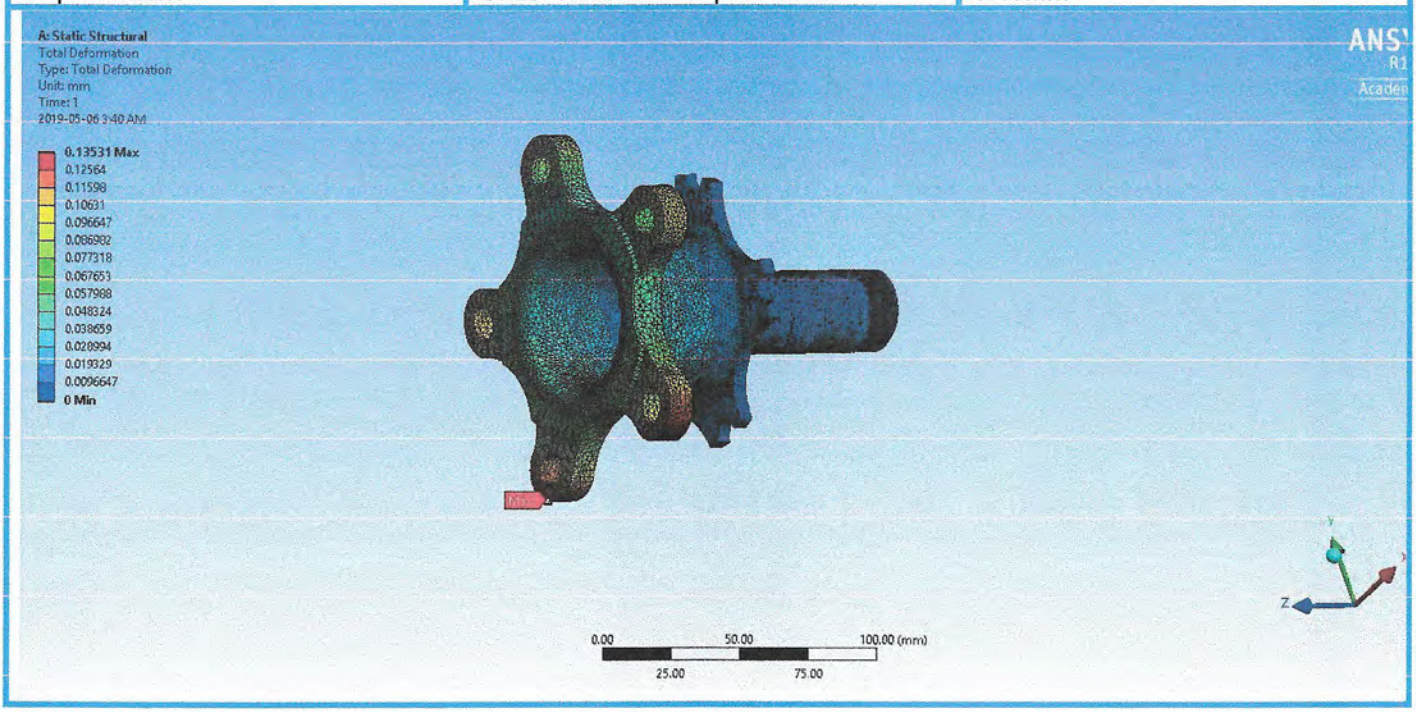

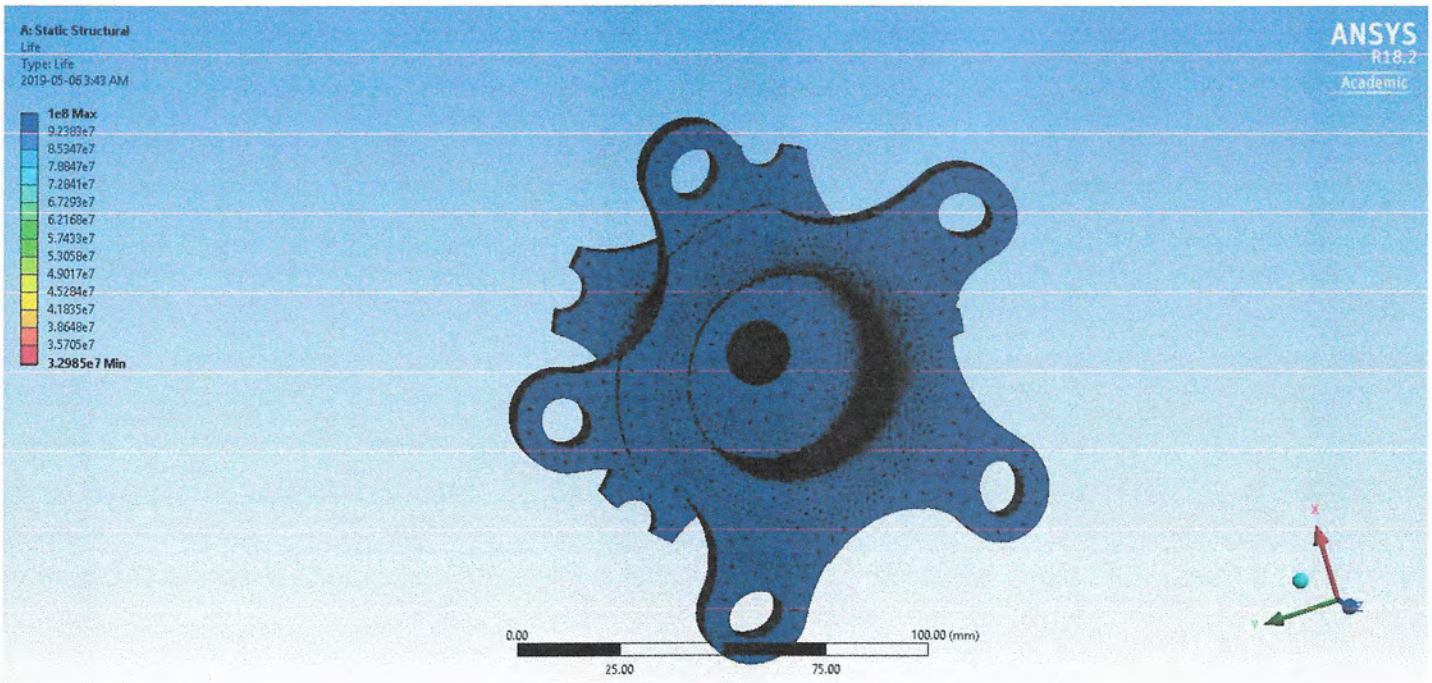

Fatigue Results

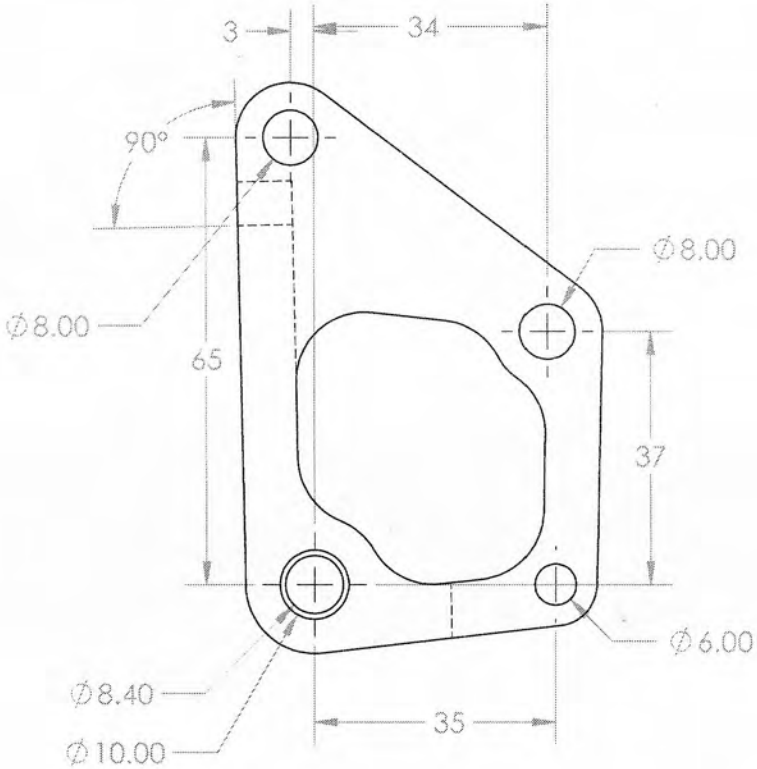

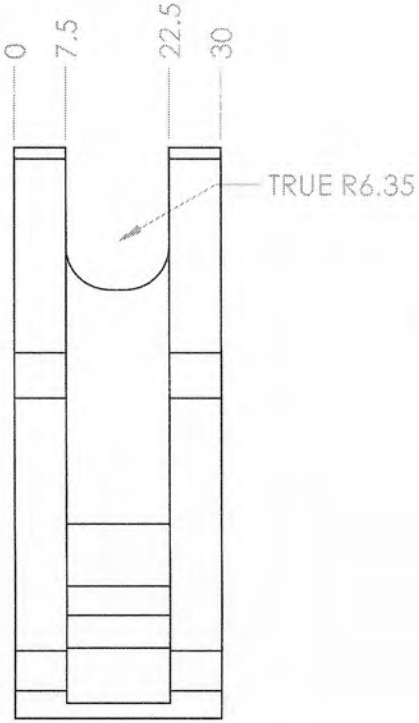

FINISH:

DEBURR AND BREAK ALL SHARP EDGES

DO NOT SCALE DRAWING
UNLESS OTHERWISE SPECIFIED
DIMENSIONS ARE IN MILLIMETERS

DIMENSION	TOLERANCE
X.X	±0.1
X.XX	±0.05
ANGLE	±0.1°

GRYPHON RACING
GUELPH, ON

TITLE:
REAR BELLCRANK

ECN:	APPROVAL	DATE	IN
DRAWN	OMM	01/18/19	
CHECKED			
CAPITAN			

MATERIAL: 6061 T6

WEIGHT: 117.254

DWG NO. GRC19_PT_SU_0079

SCALE:1:1

SHEET 1 OF 2

REVISION A4

SOLIDWORKS Educational Product. For Instructional Use Only.

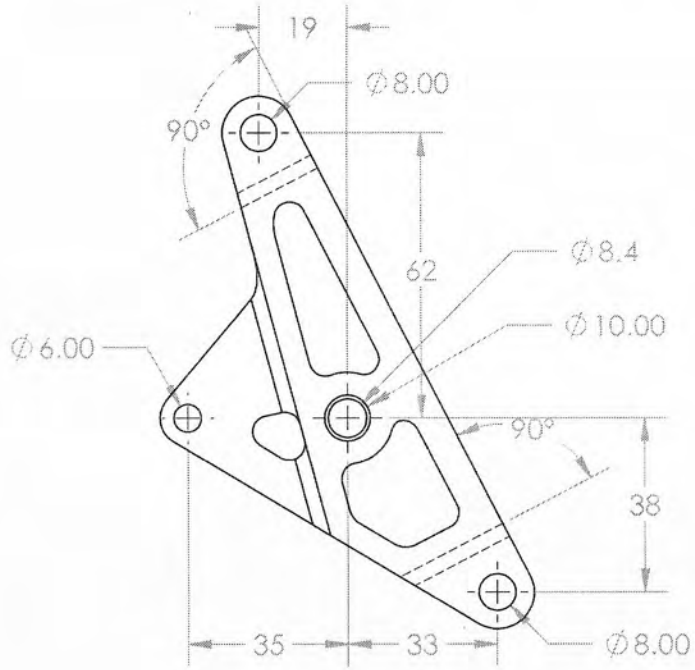

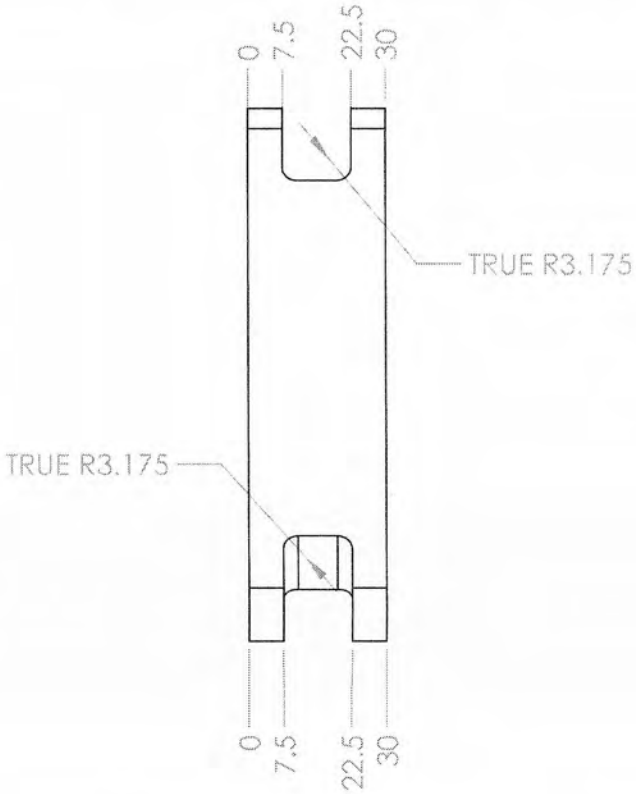

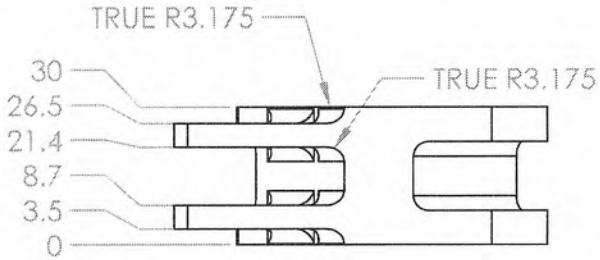

FINISH:

DEBURR AND BREAK ALL SHARP EDGES

DO NOT SCALE DRAWING
UNLESS OTHERWISE SPECIFIED
DIMENSIONS ARE IN MILLIMETERS

DIMENSION	TOLERANCE
X.X	±0.1
X.XX	±0.05
ANGLE	±0.1°

GRYPHON RACING
GUELPH, ON

TITLE:

Front Bellcrank

ECN:	APPROVAL	DATE	IN
DRAWN	OMM	01/18/19	
CHECKED			
CAPITAN			

MATERIAL: 6061-T6 (SS)

WEIGHT: 164.794

DWG NO. GRC19_PT_SU_0078

REVISION

SCALE:1:2

SHEET 1 OF 2

A4

SOLIDWORKS Educational Product. For Instructional Use Only.

Front Bellcrank FEA

04/25/2019

Assumptions

- Different loading cases used to reflect whether the pullrod or shock are "driving" the system. Stress results vary significantly depending on how the model is constrained.
- Pullrod max force of 4500N used for one case, an equivalent amount of force applied at the shock and ARB for the other (enough force as to cause a 4500N support reaction at pullrod fixture)
- Shock and ARB input forces are determined by comparing their relative stiffnesses.
- Forces are applied at 10 degrees out of plane to reflect the possibility of out of plane forces, because out of plane forces are generated at the extreme ends of the suspension travel. Also allows for build inaccuracy.

Material Properties

Model Reference	Properties
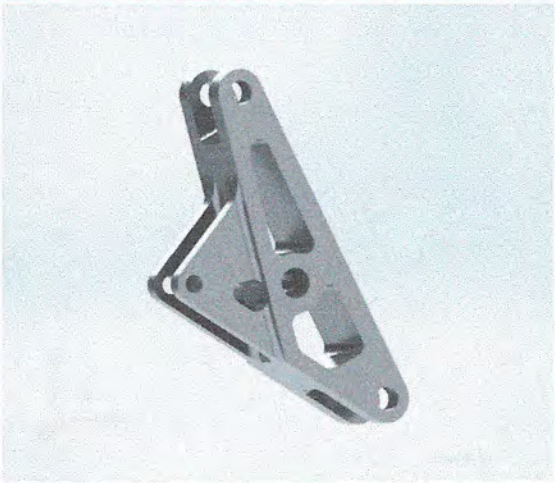	**Name:** 6061-T6 (SS) **Model type:** Linear Elastic Isotropic **Default failure criterion:** Unknown **Yield strength:** 2.75e+008 N/m^2 **Tensile strength:** 3.1e+008 N/m^2 **Elastic modulus:** 6.9e+010 N/m^2 **Poisson's ratio:** 0.33 **Mass density:** 2700 kg/m^3 **Shear modulus:** 2.6e+010 N/m^2 **Thermal expansion coefficient:** 2.4e-005 /Kelvin

Mesh Details

- **Mesh Type: Hex Dominant**
- **Number of Cells: 32369**
- **Refinement: No**
- **Topology Criteria: Mass**
- **Topology Percentage: Retaining 50% mass for early revisions, 80% for final revisions**

Loads and Fixtures

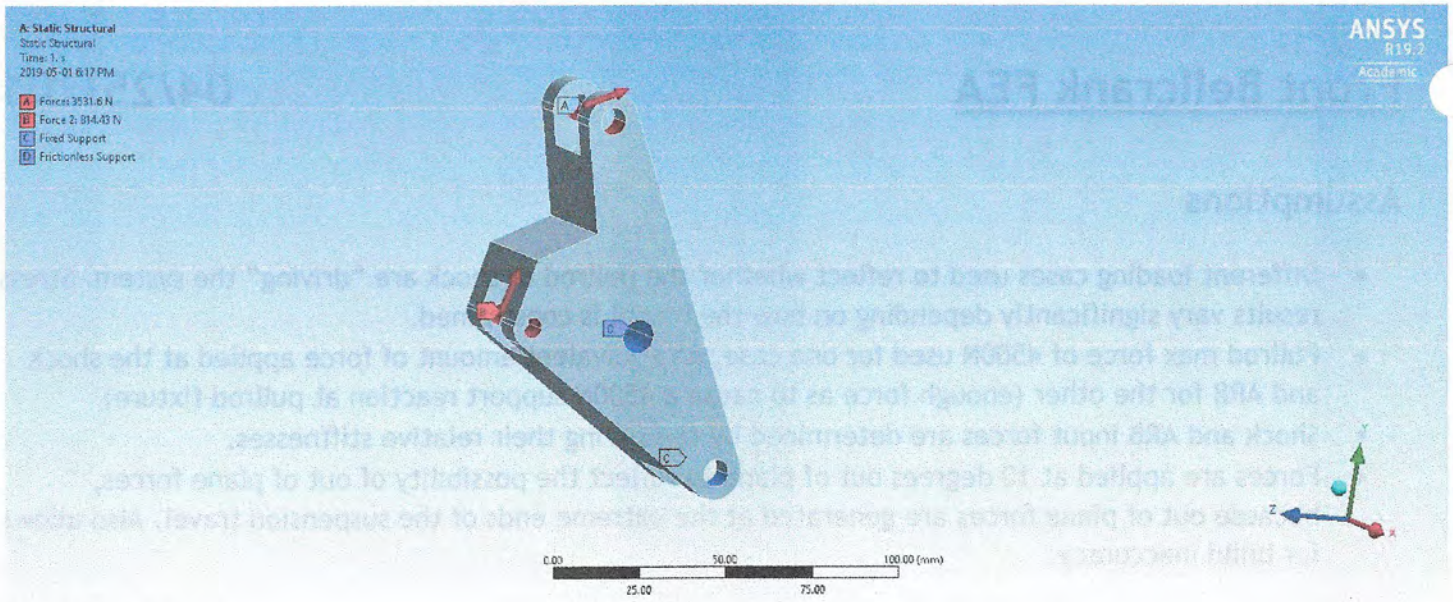

Case 1 Conditions

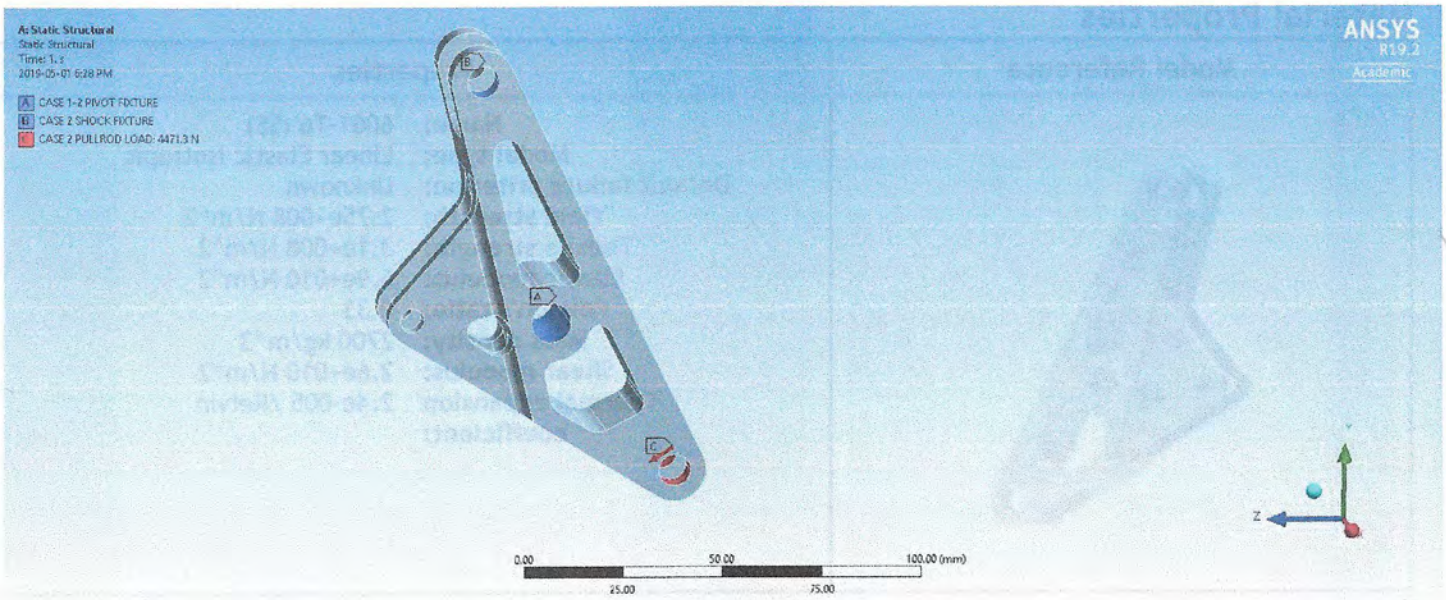

Case 2 Conditions

Study Results

Name	Type	Max
Topology Density - Preliminary Model	Retain 50% mass	

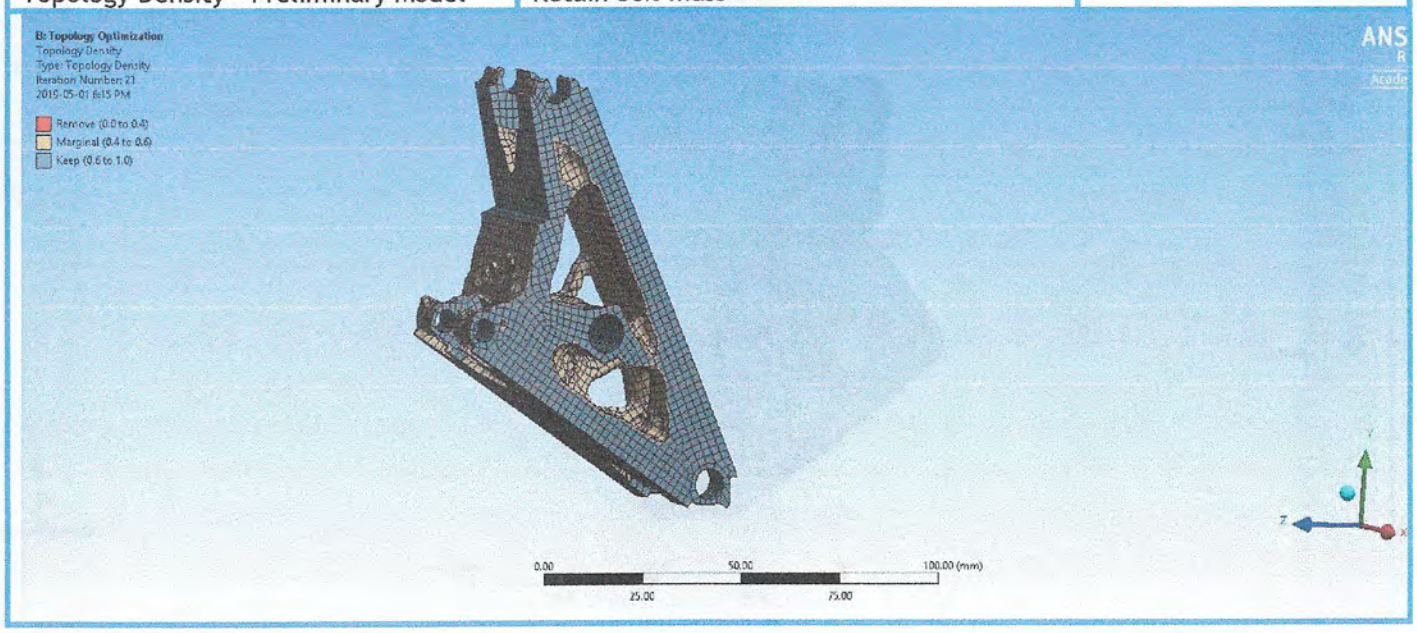

Name	Type	Max
Topology Density - Final Revision	Retain 80% Mass	

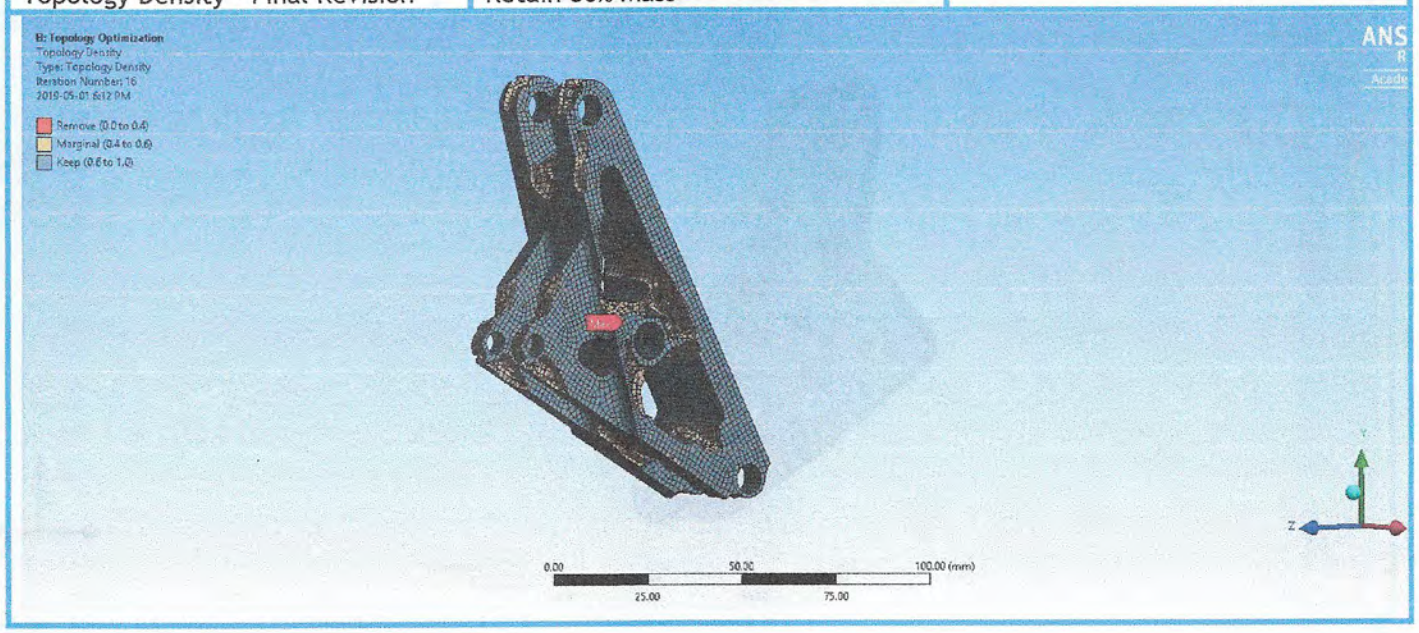

Study Results

Name	Type	Max
Stress	VON: von Mises Stress	1.47e+008N/m^2

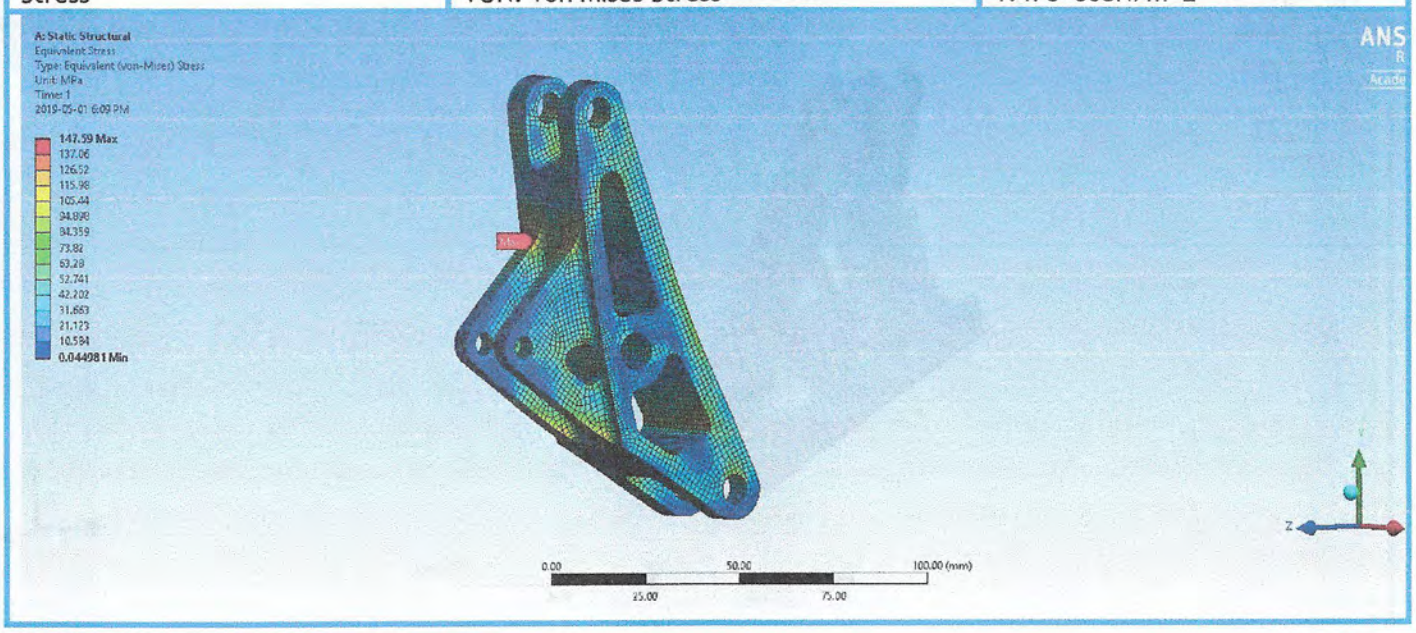

Name	Type	Max
Displacement	URES: Resultant Displacement	0.1mm

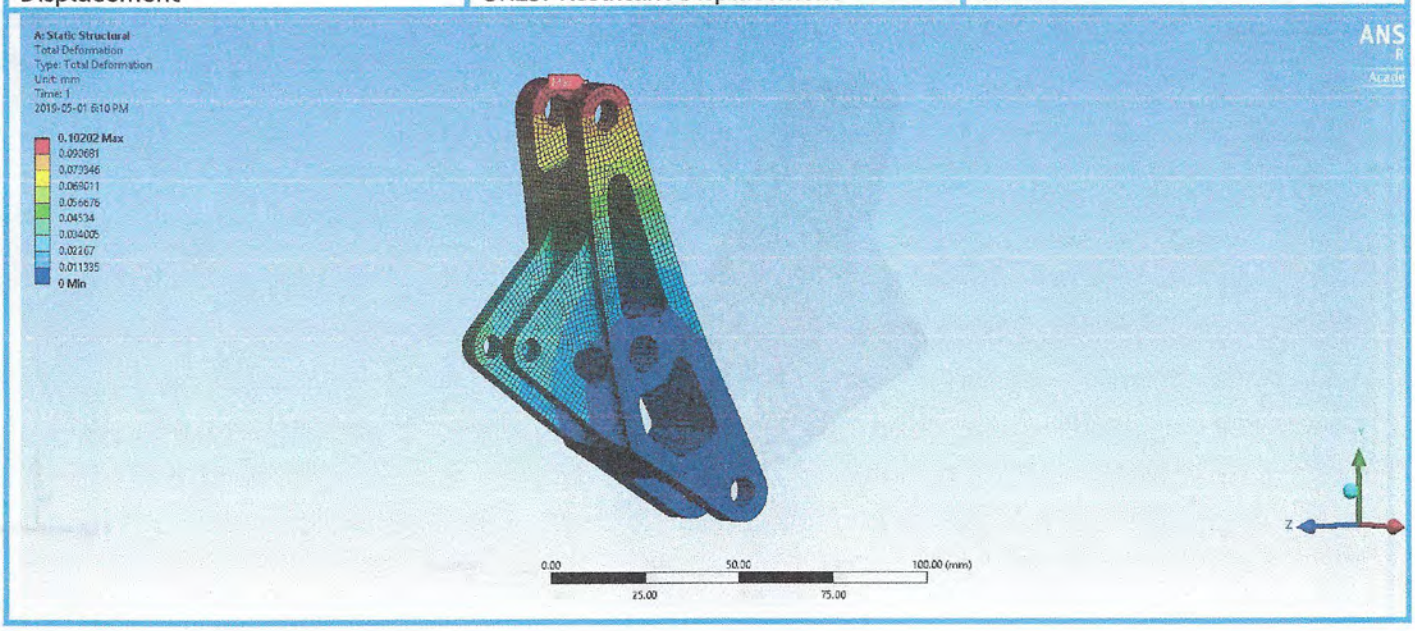

UNIVERSITY of GUELPH

FSAE Rim Design

Advisor: Dr. John Runciman Ph.D., P.Eng

Group# 26:

Nicolas Bessay-Torfs

Orion Miller

Andrew Roberts

Nicole Smith

April 8th, 2019.

UNIVERSITY of GUELPH

Dr. John Runciman Ph.D., P.Eng
Associate Director of Undergraduate Studies
50 Stone Rd E,
Guelph, ON
N1G 2W1
THRN 2408

Dear Dr. Runciman,

Please find attached the final report "FSAE Rim Design". This report outlines the design and fabrication of carbon fibre rims for the Gryphon Racing FSAE team. Should you have any questions regarding this report, please contact us by email at millero@uoguelph.ca.

Sincerely,

Nicolas Bessay-Torfs

Orion Miller

Andrew Roberts

Nicole Smith

In signing this report and providing my PEO SMP (Student Membership Program) number, I certify that I have been an active member of the team and provided approximately equal contribution to the work. I take shared credit and responsibility for the content of this report. I understand that taking credit for work that is not my own is a form of academic misconduct and will be treated as such.

Nicolas Bessay-Torfs		**054284**
Team Member One Name	Team Member One Signature	Team Member One SMP#
Orion Miller		**063296**
Team Member Two Name	Team Member Two Signature	Team Member Two SMP#
Andrew Roberts		**059029**
Team Member Three Name	Team Member Three Signature	Team Member Three SMP#
Nicole Smith		**054671**
Team Member Four Name	Team Member Four Signature	Team Member Four SMP#

EXECUTIVE SUMMARY

This report outlines efforts to develop a prototype carbon fibre rim design for FSAE racing. This design has been pursued with the goal of improving vehicle performance through reduction in rim mass. The project aims to lay all relevant design groundwork for implementing this change, as well as establish and document suitable manufacturing processes.

The first section reintroduces the problem description and background which has been revised and expanded upon since the interim report. The potential benefits of reducing the mass of the FSAE car's rims are discussed; this includes reduced overall mass and unsprung mass, reduced rotational inertia, and reduced yaw inertia. The combination of these reductions improves acceleration and cornering responsiveness, as well as decreasing weight transfer, all of which are very desirable results for an FSAE car. In this section the forces encountered by the rim under racing conditions are specified. A review of the state of current racing rim technology is conducted. The benefits of carbon fibre compared to magnesium and aluminum rims are discussed. Carbon fibre is a desirable material for a racing rim because it is lighter than magnesium and aluminum alloys while providing much more stiffness and strength (Young's modulus of 228 GPa compared to 45 GPa for magnesium and 70 GPa for aluminum, ultimate tensile strength of 560MPa). An overview of available fibre weaves is conducted. For this project, 2x2 twill weave has been selected in the interest of cost saving, as its properties are suitable and it is already used in other sections of the 2019 car.

The design of the rim, its structural analysis using ANSYS, the design of the mold, and progress developing the layup process are detailed in Section 2. Material testing was done to ensure that ANSYS material properties were reasonable. By finding ultimate tensile strength using an Instron machine, it was possible to verify the quality of materials being used and the potential validity of the designed layup procedure. A 2-degree draft angle was added to the design of the inside shell's profile in order to ensure release from the mold. A female mold was selected as this would ensure that tire bead geometry and other critical surfaces are accurate. The final mold design and the process of manufacturing it is detailed. It was machined in eight parts which assembled to form the complete mold. ANSYS simulations were performed and the resulting deflections and stresses for an aluminum rim and a 10-layer CF rim are compared when subjected to four loading cases: maximum lateral force, maximum longitudinal, maximum normal, and high pressure. The finite element analysis of the designed carbon fibre rim shows that its strength is an improvement over the aluminum rim. The increased wheel offset reduced the benefit of the carbon fibre's higher stiffness and increased deflection at the tire bead. A 10-layer CF rim with this design is estimated to have 50% of the stiffness of the aluminum rim with 17% reduction in mass. This estimate is conservative, and the stiffness to weight ratio may be improved in the future with better CF layups.

The success of this project has been measured by the ability to carry out a comprehensive rim design process, as well as manufacture a full mold assembly and prototype rim to prove the feasibility of the design. During the period of this project, skills such as vehicle dynamics and MATLAB, materials testing, structural analysis and ANSYS, solid modeling, and manufacturing were applied to cover all relevant aspects of this engineering problem. With the successful execution of the intended goals, this project is now considered complete.

ACKNOWLEDGEMENTS:

Special thanks to Dr. Runciman Ph.D., P.Eng, Barry Verspagen, Ken Graham, Dave Wright, Gryphon Racing, Anthony Meola, and Musashi Auto Parts.

TABLE OF CONTENTS

Executive Summary 4
Acknowledgements: 5
List of Tables 5
List of Figures 6
List of Acronyms and Terms 7
1.0 Introduction 7
1.1 Problem Description 8
1.2 Background Information 10
1.3 Literature Review 15
1.4 Scope and Objectives 17
1.5 Constraints and Criteria 18
1.6 Project Management 19
2.0 Design Methodology 21
2.1 Rim Design 21
2.2 Mold Design 29
2.3 Carbon Layup Process and Prototype 34
3.0 Uncertainties and Risk 39
4.0 Conclusions and Recommendations 40
5.0 References 42
6.0 Appendices 43
7.0 Resources 59
7.1 Bill of Materials and Equipment 59

LIST OF TABLES

Table 1: Sensitivity Analysis 30

LIST OF FIGURES

Figure 1: Suspension Geometry of GRC19 9
Figure 2: Example of Positive Camber in Cornering Due to Suspension Compliance 10
Figure 3: Standard Convention for Forces Acting on a Wheel 11
Figure 4: Normal Load due to Lateral Forces and Slip Angle (Tire Deformation) at 10psi 12
Figure 5: Maximum Normal Force on One Wheel 13
Figure 6: Traction Circle for 1100N Vertical Force 14
Figure 7: Tire Temperatures during Lateral Test 14
Figure 8: Updated Gantt Chart 20
Figure 9: Stress Strain Curves 5- and 10-layer Carbon Fibre Samples 21
Figure 10: Machined ASTM 370 Tensile Test Sample 22
Figure 11: Comparison of Finalized Rim Profile (Blue) vs. Aluminum Original (Gray) 23
Figure 12: Thickness (m) of Inner Shell with 10 layers and 10 Reinforcing Layers (Red Areas) 24
Figure 13: Thickness (m) of Outer Shell with 10 layers and 10 Reinforcing Layers (Red Areas) 25
Figure 14: Loads and Fixtures. 26
Figure 15: Deformation Comparison 27
Figure 16: Stress Comparison. 28
Figure 17: Isometric Views of Final Mold Design 29
Figure 18: Exploded Final Mold Design 30
Figure 19: Mold Assembly Cross Section 31
Figure 20: Mold Assembly Isometric View (Displayed Translucent for Detail) 32
Figure 21: Carbon Fibre Layup Schematic 34
Figure 22: Carbon Fibre Test Piece Using a Safety Hat as a Mold 35
Figure 23: Banded-style layup shapes. 36
Figure 24: Banded-Style Layup in Progress on the Mold 36
Figure 25: Radial Slice-Style Layup Shapes. 37
Figure 26: Radial-Style Layup in Progress on the Mold. 37
Figure 27: Features to be Machined 38
Figure 28: Final Prototype 39
Figure 29: Rim Profile of Final Design 43
Figure 30: Rim Profile of Original Aluminum Design 43
Figure 31: Section View of Mold Version 1 44
Figure 32: Section View of Mold Version 2 44
Figure 33: Sketched Layout of Fastening Features (Version 2) 45
Figure 34: CAD Layout of Fastening Features (Version 2) 45
Figure 35: Diagram of Mold Removal Using a Hydraulic Press 46
Figure 36: Diagram of Section Separation 46
Figure 37: Band Saw Cuts to be made in Aluminum Block 47
Figure 38: Machining Setup for Machining of Block Side Faces 47
Figure 39: Machining of Block Side Faces 48
Figure 40: Main Sections after Facing 48
Figure 41: Roughing Tool Path for Section 2 49
Figure 42: Finishing Tool Path for Section 2 49

Figure 43: Section 2 after CNC Machining 50
Figure 44: Section 4 before CNC Machining, with Section 3 and Section 2 Below. 50
Figure 45: Mold Sections after CNC Machining 51
Figure 46: Mold Release of Finished Outer Shell 51
Figure 47: Fully Assembled Mold in 3D 52
Figure 48: Fully Assembly Mold in 2D 53
Figure 49: Schematic of Mold Section 1 54
Figure 50: Schematic of Mold Section 2 55
Figure 51: Schematic of Mold Section 3 56
Figure 52: Schematic of Mold Section 4 57
Figure 53: Schematic of Side Handles 58

LIST OF ACRONYMS AND TERMS

FOS – Factor of Safety
SOE – School of Engineering (University of Guelph)
FSAE - Formula Society of Automotive Engineers
GRCxx – Gryphon Race Car (Naming Convention for Gryphon Racing Vehicles)
CNC - Computer Numerical Control
AML – Advanced Manufacturing Laboratory
FEA – Finite Element Analysis
ACP - ANSYS Composite Prep/Post
PVA – Poly Vinyl Alcohol
HSS – High-Speed Steel
BOM – Bill of Materials
CF – Carbon Fibre

1.0 INTRODUCTION

41XX design projects are completed by all University of Guelph undergraduate engineering students throughout their final academic year. These projects are meant to challenge students with open-ended design problems and expose them to the types of project planning and management situations that will be encountered during their careers. Students are required to cap their undergraduate degree by bringing together and applying a wide variety of skills, techniques, and tools learned throughout their studies. The 41XX design project is also an opportunity for students to look forward to the types of careers they wish to pursue. This is a chance to gear studies towards fields of interest and learn from working engineers prior to graduation.

This design project focuses on the design and manufacturing of carbon fibre racing rims, in cooperation with the Gryphon Racing Formula SAE team. Formula SAE is an intercollegiate engineering design competition in which teams design, build, and race open-wheel race cars. As the team's size and available resources have increased in recent years, it has become possible for more comprehensive design solutions to be implemented in favor of simple or off-the-shelf parts. However, as time is the

most critical resource to the success of the team, the resulting functional improvements must be quantitatively proven as worthwhile.

Creating carbon fibre components is a highly specialized, time intensive process that is being used with increasing prevalence in automotive applications requiring high performance. When well executed, carbon fibre parts have an unmatched combination of high specific strength and stiffness. It is expected that a significant reduction in mass of the rims can be achieved through this approach, yielding major performance benefits to the Gryphon Racing car. The project therefore aims to lay all the relevant design groundwork for this change, as well as establish and document the required manufacturing processes.

This project has involved the application of skills in vehicle dynamics and MATLAB, materials science, structural analysis and ANSYS, solid modeling, and manufacturing to the problem of developing race-worthy carbon fibre rims. The team has relevant background in these areas, and has also been able to learn new skills, such as carbon fibre layup and vacuum bagging.

1.1 Problem Description

Before beginning the design process, the specific problems to be addressed by this project should first be examined. The motivation for developing carbon fibre rims to replace the current aluminum rims, which are both affordable and readily available, must have clear justification. The benefits of reduced mass and increased stiffness, the two main improvements possible with this new design, are now explored.

Impact of Rim Mass on Vehicle Performance

In a racecar, the performance of the vehicle is limited by the mass of the rims for a number of reasons. Firstly, heavier rims have higher rotational inertia, making them more difficult to accelerate about the spindle axis and steering axis (see Figure 1 below). Secondly, the rims are part of the vehicle's unsprung mass; higher unsprung mass is harder for the suspension to control. Thirdly, the rim mass contributes to the vehicle's yaw inertia, an important factor impacting the cornering responsiveness of the car. Yaw inertia is calculated using the following relationship:

$$I = \sum md^2$$

The rims, which lie at the far extremities of the vehicle, are very influential in this calculation because the distance term is exponential. Therefore, reduction of rim mass is a particularly effective way to improve cornering response.

Figure 1: Suspension Geometry of GRC19

A major weight reduction would improve these characteristics, and also result in a significant reduction in total vehicle weight (on GRC18 the rims constitute around eight percent of the car's total curb weight). The use of smaller diameter wheels this season lowers the centre of gravity of the car; the centre of gravity of the rims and tires as well as all other unsprung components can be lowered by approximately 2.25 inches with the smaller 16" tires. This mass constitutes around 20 percent of the car, leading to a total CG reduction of around 0.4" in the vehicle.

Impact of Stiffness on Vehicle Performance

As the part which transfers all forces between the car and the road, the high loading in the rims makes them a major source of suspension compliance. Other sources of compliance include the stiffnesses of the hubs, uprights, a-arms, and frame mounts, as well as free play in all connecting spherical joints, rod ends, and bolts. When designing a car, suspension compliance is to be minimized as it causes the tires to deviate from their intended orientation and range of motion, undermining the suspension's kinematic properties. One such example of this is positive wheel camber during roll. Positive camber is very detrimental to tire dynamics during cornering; it is often the case that designers set up their kinematics in a manner they believe will make this theoretically possible, yet have it occur once the car is built due to compliance.

Figure 2: Example of Positive Camber in Cornering Due to Suspension Compliance

Increased rim stiffness can help to reduce compliance in suspension, therefore making the system more predictable and controllable.

Summary

Implementation of rims that are lighter or stiffer can result in major performance improvements to the FSAE car. At first glance, it appears that pursuing mass reduction during design will yield a greater overall improvement to the car. However, the most appropriate balance of strength and stiffness for the design will not be determined until structural analysis can provide further information.

1.2 Background Information

Load Case Determination

In order to carry out the structural analysis, which will be used to choose the quantities and orientations of carbon laminae used, suitable loading cases to apply in the FEA simulations must first be determined. These simulations are to be done comparatively to the current aluminum wheels, with the success of the new design judged on the relative improvements it offers towards achieving the performance requirements.

To determine the loading cases, the most strenuous situations encountered by the wheels are investigated. Vehicle dynamics analysis is required to determine the maximum forces on a wheel in each of the coordinate directions, reflective of the different types of loads seen in driving situations. There must also be consideration for other stresses acting simultaneously due to tire pressure and inertial loading. The coordinate axes defining the forces on a rim are shown below in Figure 3.

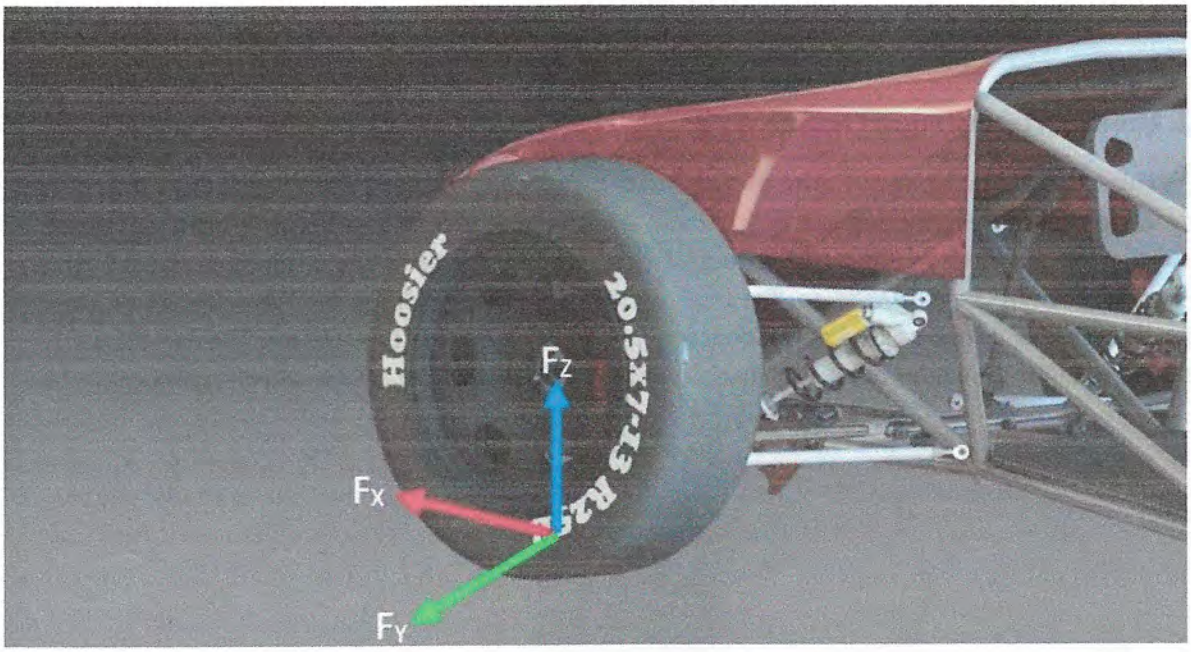

Figure 3: Standard Convention for Forces Acting on a Wheel

Case 1: Maximum Longitudinal Force Conditions

This case is to be representative of straight-line acceleration and braking. Longitudinal forces (x-direction) are caused by the driving and braking torques. They put a torsional load on the rim about the centre axis of the spindle. This information is typically determined by tire test data, however there is no longitudinal data available for the tires being used as they were only recently released. A reasonable approximation can be made by examining the ratio of maximum longitudinal force to lateral force in the data of similar tires and multiplying the maximum lateral force, which is known, by this proportion.

$$F_{X(Max.)} = 1.05 F_{Y(Max.)}$$

$$F_{X(Max.)} = 1.05(2792.0N)$$

$$F_{X(Max.)} = 2903.7\ N$$

To be applied in conjunction for this load case are:

- Normal force (Fz) of 1100N: This force represents a longitudinal weight transfer of approximately 80-20 %, which suspension analysis has found to be a reasonable expected amount for maximum longitudinal acceleration.
- Tire pressure force of 101 kPa (14 psi). This pressure represents the maximum upper range of pressure that could be expected for use in an FSAE tire. Note that the maximum longitudinal and lateral forces are taken at 10 psi however, because force is highest at this pressure. Although these are not capable of being true at the same time, this approach keeps the load case conservative.

- Inertial loading of 140 km/hr: This is the theoretical top speed experienced by the vehicle during a race.

Case 2: Maximum Lateral Force Conditions

This case is to be representative of maximum lateral g's in a steady state turn. Lateral forces (y-direction) are caused by cornering and put a bending load on the rim. Shown below is a plot of lateral force on the selected tires vs. slip angle, a quantification of how the tire's line of travel deviates from its heading as a result of tire deformation. The plot used is for a value of 10 psi, the lower bound of possible operating pressures, as maximum lateral force is inversely proportional to pressure. The five colors correspond to different values of normal load. The curve of interest is in yellow, which represents 1100 N.

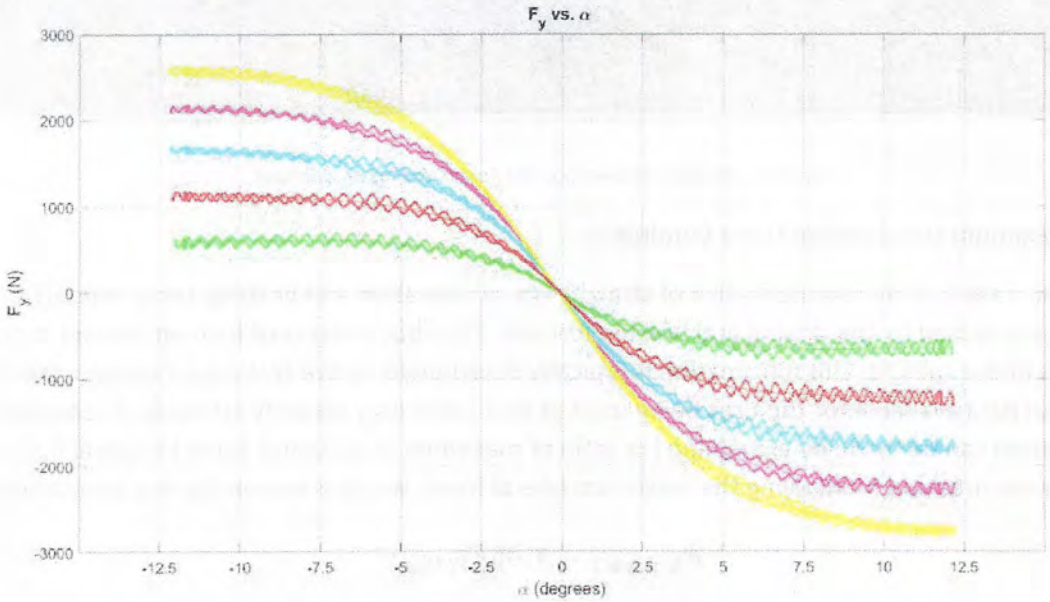

Figure 4: Normal Load due to Lateral Forces and Slip Angle (Tire Deformation) at 10psi

From the plot,

$$F_{Y(Max.)} = 2792.0\ N$$

Again, 1100 N was selected as the value of normal force, using lateral weight transfer of around 80-20 % as a realistic upper estimate. The other forces to be applied in conjunction with this lateral force are:

- Normal force (Fz) of 1100N.
- Tire pressure force of 101 kPa (14 psi).
- Inertial loading of 140 km/hr.

Case 3: Maximum Normal Force Conditions

This case is to be representative of hitting a large pothole or bump. Although the car typically drives on quite smooth tracks, it is sensible to test this separately to ensure that the car can handle this situation. Normal forces (z-direction) are determined by the weight distribution in the vehicle at a given instant as well as bumps from road irregularities. This force puts a radial load on the tire. Because much of the tire's stiffness comes from the pressure of the air inside, a large proportion of these loads are transferred to the rim as a uniform compression on the entire outside face of the rim shell. The remainder of the force is transferred to the underside of the rim's tire bead surface through the tire sidewalls. The proportioning of how these loads are resolved between these two mechanisms is not known; the normal force is therefore be assumed to act 100% through the sidewalls, as the other means (through air pressure) essentially causes a hydrostatic stress on the rim and is therefore a less severe load.

The maximum normal force was taken to be that applied during a 3g bump to one of the wheels. This is a realistic magnitude to represent a large pothole or bump.

Bump Condition				
		Front	Rear	Units
Dim.	Bump G's	3.0		Accel.
	Vertical Load (One Wheel Z)	2118.960	2295.540	N

Figure 5: Maximum Normal Force on One Wheel

The difference in front and rear forces is driven by the static weight distribution of the car. Maximum normal force is the higher number of the two:

$$F_{Z(Max.)} = 2295.5\ N$$

The other forces applied in this case are:

- Tire pressure force of 101 kPa (14 psi).
- Inertial loading of 140 km/hr.

Case 4: Maximum Inflation Pressure

The maximum possible inflation pressure is the last loading case that needs to be considered. No vehicle dynamics analysis is needed for this case, as the value of failure is determined using FEA. Maximum inflation pressure is relevant when mounting tires as the machine applies bursts of pressure to seat the tire bead onto the rim. A maximum psi rating should therefore be determined.

Loading Case Limitations and Sources of Inaccuracy

Although the maximum force situations in each of the coordinate directions are an intuitive way of organizing the design approach, it should be kept in perspective that other force combinations on the tire are possible. Shown below is a traction circle for the selected tires written in Matlab. The ellipse represents the maximum limit of the tire's traction capacity at different proportions of longitudinal and lateral force. The ellipse is asymmetrical about the abscissa because more acceleration is available in

braking than from the two driven wheels. This figure illustrates that there are other combinations of longitudinal and lateral force along the curve which could potentially stress the rim more. However, this traction circle is only an idealized version, real traction circles are less uniformly shaped and require track test data which is not available.

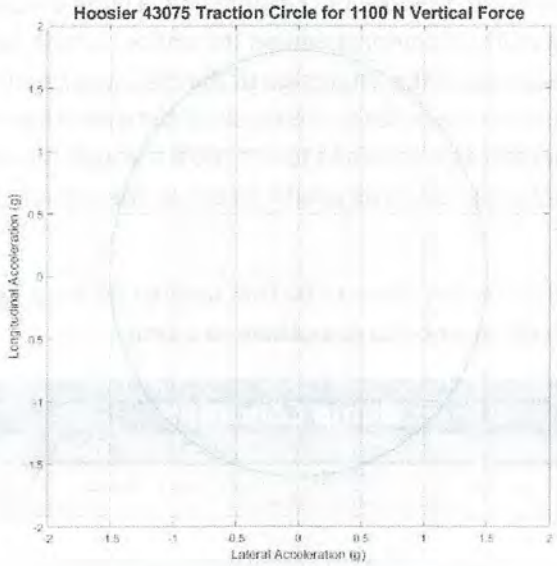

Figure 6: Traction Circle for 1100N Vertical Force

Another source of limitation is how the tire test data used was collected. All forces in the test are essentially "too perfect", as they are done on a very uniform sandpaper-like test belt, with the tire within perfect operating temperatures. Tire test data is supposed to be adjusted with correction factors that are determined from driving test data, so that a more accurate model can be converged upon. This means that forces assumed for longitudinal and lateral force are likely conservative.

Upon implementation of a sufficiently sophisticated range of sensors in the Gryphon Racing vehicles, these loading cases should be revisited and further refined.

Tire Heat Generation

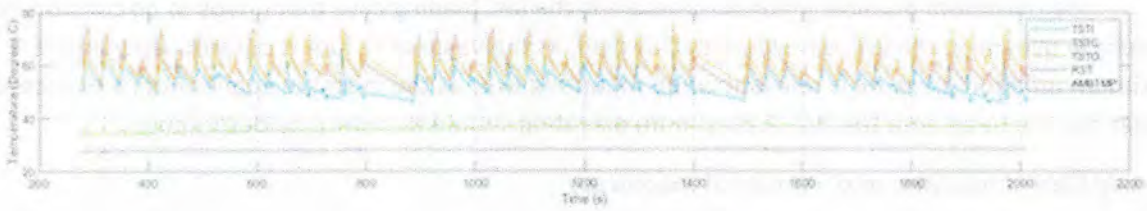

Figure 7: Tire Temperatures during Lateral Test

Heat generation from the tire tests is now observed to verify to what degree the tire will heat the rim. This is of interest because the epoxy used for carbon generally softens at excessive temperatures. Shown above is a plot of the tire temperatures recorded during the lateral test. It is seen

that tire tread temperatures reach a range of about 75 degrees Celsius at maximum. This amount of heat generated by the tires is not serious enough to cause issues with the epoxy selected. The epoxy is stated to be safe under temperatures of around 140 Celsius.

1.3 Literature Review

Deciding on materials and processes for high performance rim design is difficult and research into the current racing market is important before a final decision can be made.

Rims are a key component in decreasing a race car's unsprung mass (the mass of the car that is not supported by the suspension system). Decreasing this mass will improve vehicle acceleration and control [5]. For this reason, the materials chosen for these applications are the ones that can reduce weight most effectively.

In the current market there are three main options for lightweight rim manufacturing. These options are magnesium alloys, aluminum alloys, or composites such as carbon fibre [6]. Aluminum is the most common rim material for most applications. It has a good weight to stiffness ratio and corrosion resistance. It is also much easier to machine and less costly than other alternatives, making it a more easily accessible option for smaller racing teams.

Magnesium rims have had a long history with the racing community. Their stiffness is comparable to that of aluminum with a 50% lower density as it is the lightest of all the metals [3]. Unfortunately, pure magnesium rims used early on in racing were susceptible to both corrosion and fire elements [10]. When exposed to heat from a burning tire or even prolonged contact with the road, these rims would combust violently due to the reactive nature of this metal. These rims were also known to corrode quickly, leading to pitting and failure. These factors led to their unpopularity in the following years. Now as technology has improved, it has been found that alloying magnesium (particularly with Yttrium and rare earth elements) can create good fire resistance [12]. This leaves a rim that is very light and stiff without the unfortunate combustible side-effects.

The third main option for rim design is carbon fibre. Unlike the other two discussed earlier, this is a composite, in that it is composed of 2 distinct parts. The first is fibres of carbon, which give strength and act as the reinforcement. The second is a resin which permeates the sheets and creates cohesion, this combination is known as the matrix [9]. The result of this mixture is a material which is marginally lighter than magnesium alloys with much more stiffness (exhibiting a modulus of 228 GPa compared to 45 GPa for magnesium and 70 GPa for aluminum) and an ultimate tensile strength of 560MPa. These properties are ideal for modern racing rims, but they are also very expensive [4]. Machining CF is difficult as it can produce aerosolized particles which are known to be irritant and carcinogenic. It is also very abrasive, leading to rapid wear on machining tools [1]. For these reasons, it is difficult and very costly to find shops which are specialized enough to create high quality rims. Despite these drawbacks, carbon fibre is still the lightest material that can fill this role, making it the material of choice for high-end rims.

While CF has very good material properties for this application, it is an anisotropic material. This means that its properties are not uniform and will respond differently to loads in different directions. Within the material, individual carbon fibres are all oriented in particular directions (with some exceptions). For this reason, the material will be very strong when loaded along fibre lengths but will rely almost entirely on the strength of the resin when loaded perpendicular to fibres. The result of this in the context of rim design is that one must take the various load cases into account when deciding how to orient the various sheets of CF [9]. In this way it can be ensured that the material will be strong

enough in both the strong and weak axes. Unlike alloy rims, which will warp and stretch before they fail; CF will reach its failure point and fracture (brittle failure).

Once CF is selected as the material of choice, the next decision is the type of woven sheet that will be used. The simplest type of CF sheet is unidirectional. In this configuration, all the carbon filaments are oriented in the same direction. This is advantageous because this means that layers can be rotated in order to ensure a particular strength in each direction, to match the expected loading very specifically. Unidirectional is very flexible and can easily drape over complex geometries and contours.

The next CF configuration is known as a plain weave. It features a 1 by 1 weave of CF strips. Weave has equal strength against planes stress in two directions, making it more suited to applications were forces are relatively equal in each coordinate. This has been found to be the case during load case analysis of the rims. It also allows less severe rotation of the adjacent layers during layup which will lead to more uniform properties throughout this material. This variety of weave has the poorest drapability, due to the tendency of the 1x1 weave to hold itself tightly together.

The final CF sheet layout is a 2x2 twill weave. The double parallel strands reduce the strength of the final material slightly but make it far easier to drape around the complex geometry required to make a rim. The twill pattern increases strength and density, which will raise weight slightly, but keep the properties of the material within the target values [8]. The 2019 FSAE car makes use of 2x2 twill weave in other sections, and it has been selected for use in this project. This choice has been made because of the drapability, the relatively even loading in each direction, and the cost savings, as this material is already available to the group. Potentially, some sections of a CF rim could be reinforced with unidirectional CF, but performance gains would likely be marginal and this was too costly for the 2019 season.

Having chosen a weave type, the next decision one must make is between a wet layup or a prepreg autoclave procedure. Both of these involve CF sheets cut into the proper shapes for the application and epoxy, but they are very different in their implementation. Prepreg features sheets with a premixed epoxy solution applied to the carbon in a thin layer by a machine. These sheets are then laid up onto the mold and cured with constant temperature and pressure in an autoclave. In a wet layup, epoxy is mixed and layered onto dry carbon sheets manually, layer by layer. After this it is vacuum bagged and allowed to cure at room (or slightly elevated) temperatures. The difference between these two methods is in the precision with which variables are controlled. Manual layering generally has greater thickness and can be uneven or poorly mixed in places. For this reason, the true golden standard of composites is prepreg cured in an autoclave, where layers are far more likely to be uniform and imperfections are minimized.

Unfortunately, an autoclave is a very large, expensive, and energy-consuming machine to which access is often limited. A wet-layup will be available at a fraction of the cost and can be assembled using relatively inexpensive materials. By exercising extreme care in the mixing and application of the epoxy on the wet layup, one can achieve strengths and thicknesses very similar to the prepreg method [7].

After selecting a layup method, the final step in a CF process is epoxy and hardener selection. This combination of materials will be responsible for out of plane stresses and adhesion in a CF part and is therefore very important in achieving success. Although there are many different types of epoxies with various properties, there are 3 main things that must be kept in mind during selection. These are temperature resistance, strength, and cure-time. Temperature resistance is important because many epoxies will begin to lose hardness and fail at certain temperatures. To produce rims, tire heat data was found to have temperatures up to 75 degrees Celsius. This temperature must be withstood by whichever resin is chosen. Strength is a straightforward property for these purposes, it should match the necessary strengths for the various loading cases expected for the tire. The final factor for resin and hardener selection is hardening time. It is crucial that the layup does not harden before the vacuum

pressure has been established. This means that as the number of layers increases, a hardener with a longer hardening time must be selected to prevent inconsistent curing [2].

The current methods and materials for rim manufacturing are widely variable and there are many factors that must be taken into consideration. Each process must be tailored to the needs and particular goals of the process. By taking time to select optimal components, the best possible outcome can be achieved.

1.4 Scope and Objectives

Objectives:

- Determine realistic design load cases through vehicle dynamics analysis.
- Perform materials research to select appropriate fabric and epoxy types.
- Develop a carbon fibre rim design to meet the performance targets.
- Design and manufacture the required aluminum molds.
- Build a completed prototype rim.

The summarized objectives of the project are seen above. The project focused on the design and fabrication of carbon fibre rims. It began with tire and vehicle analysis to determine suitable loading criteria upon which to base a rim design. Force analyses using ANSYS to determine the stiffness of the previous aluminum rims were also completed. An ANSYS analysis of composite carbon fibre rims was performed in order to estimate the number and placement of layers of carbon fibre weave that would achieve a stiffness comparable to the aluminum rim. A custom rim profile has been developed for this new design, with consideration of suspension design criteria, ease of mold release, and minimization of stress concentrations. The final design iteration included 11 layers and approximately matched the stiffness of the original aluminum rims while minimizing the amount of carbon fibre used in order to reduce weight, all while maintaining a thickness of the rim less than 1/8". The performance targets set for the rim design follow below.

Performance Targets

- **Strength:** Because of the possibility that the produced rims will not be as strong as predicted due to manufacturing imperfections or other sources of error, the rims were designed to have a higher factor of safety than the aluminum rim.
- **Durability:** The rims should have infinite expected life under fatigue analysis.
- **Stiffness:** Stiffness comparable to the original aluminum rims will be considered successful. Stiffness greater than the original aluminum rims while reducing weight would be preferred.
- **Weight:** A weight reduction of more than 10% (while maintaining comparable performance) would be successful, 25% or more would be considered very successful.

A full mold assembly has been designed, it is made up of four separate main sections and four smaller additional pieces which are added to the sides. The four main pieces that make up the mold were designed so that they could be fastened together accurately for layup, then easily disassembled to remove cured parts. To manufacture the mold, blocks of aluminum were first faced manually to the

required dimensions, and all required fastening features machined. Following this, the mold was machined using the Advanced Manufacturing Lab CNC mill to provide high accuracy machining of the rim profile.

Once the mold was completed, prototyping of the carbon fibre rim was carried out. Throughout the prototyping process, small test parts were made in order to practice the process of laying up and vacuum bagging carbon fibre. These test parts were also used in material testing to determine the actual physical properties of parts manufactured by the team. ANSYS models of the carbon fibre rims were verified using measurements of ultimate tensile strength, density, and layer thickness for the carbon fibre parts.

The layup process then followed, and a rim was manufactured by hand. A carbon fibre weave was laid onto the mold and using a vacuum bag to apply pressure, the laminated layers were set (this process is explained further in Section 2.3). The rim was then machined, and a clear coat was applied. This prototype was proof that a carbon fibre piece could successfully be created using the mold and layup technique.

The overall success of this project was measured by the progress towards establishing and documenting a reliable in-house process for manufacturing carbon fibre rims using the facilities and knowledge available to the Gryphon race team. The project team recognized that the production of a complete set of suitable racing rims is a lofty goal and will require the efforts of future students to complete the work. For this reason, attention was paid to documentation and reproducibility of manufacturing methods so that the project may continue and carbon fibre rims for a future Guelph racing team will still be produced. Therefore, the ultimate goal of this project has been to leave future students with the documentation, molds, and tools necessary so that the designs can be refined and carbon fibre rims can be regularly manufactured for the Gryphon race team.

1.5 Constraints and Criteria

The various restrictions which will play a role in developing a suitable rim and mold design are outlined below. The manner in which these factors limit and influence design decisions will be further discussed throughout the design explanations as relevant.

Constraints

- Reduce the weight of the rim by at least 10% (preferably 25%).
- The rim profile must have suitable geometry such that the tire can be mounted.
- The mold must be physically possible to machine. There cannot be any negative angles to mill, and milling cannot be done deeper than the length of the available tooling.
- The mold must be able to facilitate mold release by some means.
- Geometry of the rim shells cannot be such that they are mechanically locked into the mold after layup.
- The width of the rim must fall within the specified acceptable range (5.5-7.0") for the selected tires.
- The rim offset must fall within the range of +10 to +30 mm as dictated by vehicle suspension design requirements.

- The rim must use a 12-hole bolt circle of diameter 6.75 inches, with each hole of ¼ inch diameter, for the mounting of the available rim centres.
- The rim must be entirely airtight up to a value of 100 psi.
- There must be some means of tire inflation/deflation incorporated into the rim.
- The rim must be designed such that the tire will not de-bead during operation.
- Inside diameter of the inner rim section must be equal to or greater than 9.35" to accommodate suspension packaging requirements.
- Any machining, sanding, polishing, or other post-processing of the carbon rims must be performed with air extraction available to reduce the risk of adverse health effects which are associated with carbon fibre dust.

Criteria

- All mentioned performance targets should be satisfied.
- The carbon weave used should have as high drapability properties as possible to facilitate proper layup on complex surfaces.
- The directions of the carbon lamina should be oriented proportionately to the applied loads.
- Any machining, sanding, polishing, or other post-processing of the carbon rims should be minimized to reduce the risk of adverse health effects which are associated with carbon fibre dust.
- The molds should be made from material that is available to the group at minimal cost.
- The molds should be designed such that critical tolerances for the rim geometry (critical dimensions and surface finishes) are followed as closely as possible.
- The molds should be designed such that the cutting depth required for milling operations is kept within reasonable limits. Chattering can be encountered when using long tools at high speed.

1.6 Project Management

Budget

The budget of the project was constrained to the funding received through LabFund. Careful planning had to be conducted to ensure any additional costs could be kept to a minimum. For example, the team initially considered the use of a third party to water cut the plates for the mold. By taking advantage of the CNC in the Advanced Manufacturing Lab, this cost was avoided. The team also initially believed that a new vacuum pump would have to be purchased as the one available would overheat and leak oil. By repairing the old one, this cost was also mitigated. Mold constraints led to a significantly increased number of fasteners, but this had a relatively small impact on the budget of the project.

Schedule

Task	Task Description	Star Date	End Date	2-Nov	9-Nov	16-Nov	23-Nov	30-Nov	7-Dec	14-Dec	21-Dec	28-Dec	4-Jan	11-Jan	18-Jan	25-Jan	1-Feb	8-Feb	15-Feb	22-Feb	1-Mar	8-Mar	15-Mar	22-Mar	29-Mar	5-Apr
1	Modelling and Research	02 Nov	28 Dec																							
2	ANSYS Force Evaluation	02 Nov	04 Jan																							
3	Carbon Fibre rim design	05 Jan	31 Jan																							
4	Mold manufacturing	01 Feb	Mar 19																							
6	Material Testing	01 Mar	08 Mar																							
7	Carbon Fibre Rim Manufacturing	24 Mar	30 Mar																							
9	Final Report	01 Apr	07 Apr																							

Figure 8: Updated Gantt Chart

An updated Gantt chart detailing the team's schedule is shown above. Every task necessary for the completion of this project has been performed. Modelling and research took place for two months to make sure all information needed to pursue this project was acquired. FEA using ANSYS also took two months as the team had to wait for CAD of the aluminum rims to arrive before any analysis could take place. Rim design only took one month as very few changes had to be made to the CAD of the aluminum rims in order to create the carbon fibre ones. Some changes included a draft angle added to the larger half of the rim and a curve that was added to the smaller half. Mold manufacturing occurred after a rim design had been finalized. For a month and a half, the team created and revised their design for the rim to ensure the best product would come from their work. Material testing also took place during this time to confirm that the carbon fibre rim would be stronger and lighter than the aluminum one. After testing took place, the rim was finally created. The last task for the team was the final report, which the team allotted one week for.

The resources required for this project included: tools and space to work safely with carbon fibre, access to large amounts of time in the machine shop, and the acquisition of the raw materials purchased with the lab fund. The tools needed to work with carbon fibre were borrowed from the race team. Cutting carbon fibre results in the release of potentially hazardous particles into the air, which is dangerous when breathed into the lungs. The race team shop was the best option for the team, but it was decided that in order to use this shop, an extraction system would be needed to dispose of the airborne carbon fibre filaments.

Some challenges that were anticipated were related to the molding of carbon fibre parts. Working with carbon fibre was difficult and there were several potential errors that could have compromised the quality (and therefore the performance) of the rims or even the molds themselves. Poor installation could have led to poor appearance, performance of the rims, or the inability to separate part from mold, which would mean the destruction of all physical products of this project. In order to minimize these risks and familiarize group members with the intricacies of composite molding, several test parts had been created. Using knowledge gained from these trials, more test pieces were made with specific attention on the maintenance of complex geometry.

Several challenges were encountered and had to be overcome in order to progress in this project. One such issue was the early misconception that the provided aluminum plates were large enough to accommodate the rim geometry. While this proved to be false, some modifications to the mold quickly solved this issue. Another problem discovered was the rigidity of the carbon fibre sheets that were in the FSAE shop. During testing, the team discovered that sheets of this rigidity would not be

able to cover the particular geometry of a rim. Far more flexible weave was found, which were more difficult to cut cleanly, but easily formed to the curves of the design. Some of the early test pieces had proven to be unsuccessful, but the team was able to form a hard hat with a fair degree of strength and dimensional accuracy. Before an attempt to make rims was made, the team continued to learn as much as possible about the carbon fibre manufacturing process through trial and error with simpler geometries. This way, many problems that related to material properties were solved so that the team could focus efforts on meeting geometry related difficulties when the rim layup stage of production began.

2.0 Design Methodology

2.1 Rim Design

Material Selection

The 2x2 twill weave carbon fibre available in the FSAE race shop is the primary material used to make the rims, due to its ability to easily distort and drape around the rim geometry during the layup process. Using material that is already available also allows the cost of the project to be minimized. The epoxy chosen is Aeropoxy PR 2032 resin which is often used in high performance structural applications of composites. Because the rims are not merely an aesthetic part and will be experiencing strenuous loading during use, a strong epoxy must be used. The hardener paired with this epoxy is Aeropoxy PH 3663, which is a common hardener for fabricating carbon fibre parts and has an intermediate working time of 90 minutes. This provides ample time to successfully run through an entire layup process. The peel ply chosen for this project is Airtech Bleederlease B peel ply. This material is infused with silicon to ensure efficient release from the composite and epoxy. The cotton, vacuum bagging, and other intermediate plastic layers used in the layup process were also found in the FSAE race shop, allowing further reduction of costs.

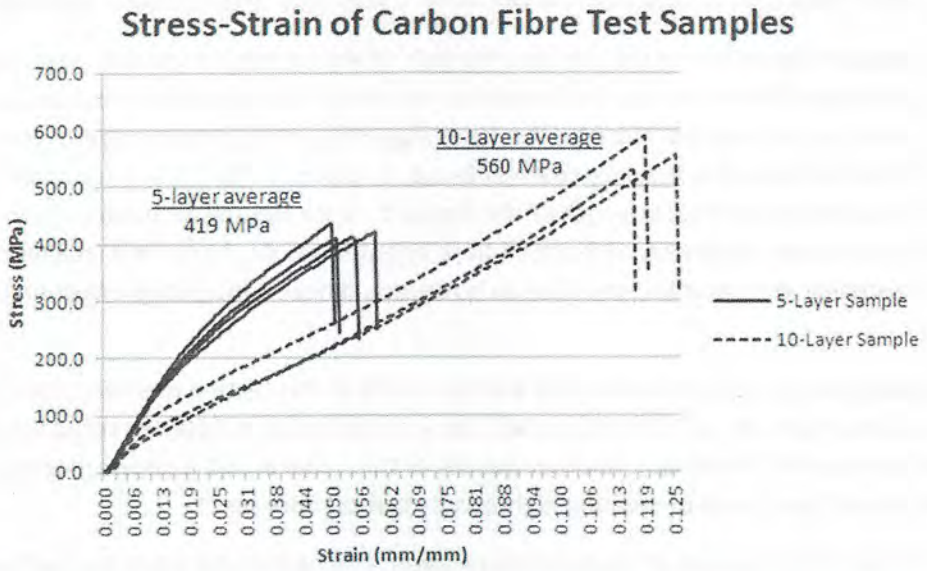

Figure 9: Resulting Stress Strain Curves from Ultimate Tensile Strength Tests on 5- and 10-layer Carbon Fibre Samples

In order to confirm that these materials met the requirements for this project, destructive testing was done on several samples. These tests were done on the universal testing machine (Instron) in the university of Guelph materials testing lab. This machine has a 100 kN capacity and is used to perform ultimate tensile tests. By performing this testing, a designer can ensure that the material properties used for analysis will most closely match the actual materials used. For this reason, all test sample strips were created using the same epoxy, carbon fibre, and layup methods that would be used in the final product.

Figure 10: Machined ASTM 370 Tensile Test Sample

For many materials, ductile failure occurs, producing a stress strain curve with 3 main sections. The first is the elastic region, a linear portion at the beginning of deformation from which the material would return to original dimensions if released. After this the material begins to deform plastically, meaning that it would be permanently deformed but unbroken if released. This section generally shows a stress continuing to increase with a decreasing slope. Finally, the stress reaches the yield point, after which it will decrease until the part fails.

As expected, the results for this test on the carbon fibre indicate a much more brittle material in that almost all deformation is in the elastic region, followed by yield and immediate failure. This is because carbon fibre is incredibly stiff and will deform very little before failure. The high modulus.

Looking at Figure 9, one can see that the yield stress on the 5-layer test strips is lower than the yield strength of the 10-layer strips. This is strange as stress varies with cross sectional area where failure occurred and should therefore be the same regardless of test sample size. This inconsistency is likely due to the human error involved in a wet layup. As stated earlier, there are many factors in a wet layup that could affect the final strength of the product. These include air bubbles in the resin, inconsistent resin layer thickness, and carbon fibre orientation. As there are a smaller total number of layers in the smaller test samples, any error in layup would have a magnified effect on the overall strength.

Despite minor inconsistencies, the average result of this testing was very close to the suggested values for carbon fibre. By performing this test, an accurate value of 560MPa could be used for all further FEA analysis of this design. Another benefit of this value is that it shows planned team layup procedure would be capable of creating high-quality carbon fibre parts.

With a strong baseline of material information, a design can be made that will realistically satisfy both strength and geometric criteria.

Rim Geometry

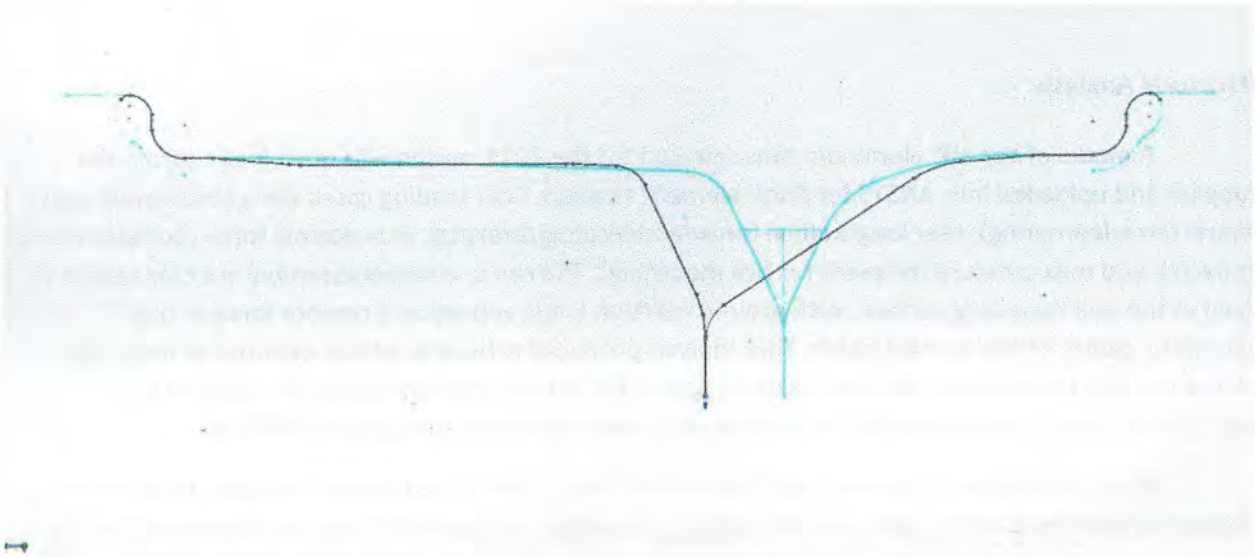

Figure 11: Comparison of Finalized Rim Profile (Blue) vs. Aluminum Original (Gray)

Seen above is a sketch of the finalized carbon rim profile overlain with the original profile of the aluminum rim (Individual sketches available in Appendix Figures 29 & 30). The inner rim shell is seen on the left, and the outer shell on the right.

The revised rim incorporates a 2-degree draft angle into the inside rim section to facilitate mold release. 0-degree angles are not desirable because this places the part entirely in shear, in which the mold-part interface is strongest. An angle of only 2 degrees is used because of the limitations imposed on minimum rim diameter by suspension design requirements in that section. The revised rim features an increase in rim offset as well, from 12.7 mm to 27.7 mm. This decision was also made for suspension design considerations; the manufactured rims are made available in offsets of discrete 1-inch increments, however a value between two of these was determined as most desirable. This has the beneficial side effect of decreasing the mold's thickness in the outer rim's section, decreasing the depth of milling required in the thickest section. The sections where the rim profile curves out from the centre mounting surface has also been made the same for each section, and the adjacent curvature in the outer shell has been smoothed out. Because this design is not restricted to using a limited number of discrete radius tools like the spun-forged aluminum parts, this revised profile can reduce the stress concentration in this region.

The rims share the same tire bead geometry. For some rim designs, an additional "hump" is added inward of the tire bead area as an added means of keeping the tire securely seated during operation. In the absence of this feature, the tire bead relies on the friction at the tire-rim interface in combination with the outward air pressure to keep it properly seated. It would not be possible to add a feature like this into the mold because it would not be feasible to machine with a 3-axis vertical mill and it would also result in the rim being mechanically locked into the mold after layup. Extra thin strips of carbon could in theory be added on after the main layup process, when the part has been removed from the mold. However, this feature is not commonly used so it is assumed to be unnecessary to keep the

tire properly seated. In the future, if issues are encountered with tire de-beading, this idea will be revisited as modifications of this nature can be easily made.

Structural Analysis

A model of the 10" aluminum rims selected for the 2019 season was downloaded from the supplier and uploaded into ANSYS for finite element analysis. Four loading cases were considered: max lateral force (cornering), max longitudinal force (accelerating/braking), max normal force (bump/pothole impacts), and max pressure (relevant for tire mounting). The rim and wheel assembly are considered as fixed at the hub mounting surface, with ground reaction loads applied as a remote force at the geometric centre of the contact patch. This analysis produced estimates of the locations of deflections on the rim and their magnitudes and it can be seen later in this report in figures 15 and 16. The deflections in each case were then the benchmarks when designing the carbon fibre rim.

After the design of the mold and the profile of the carbon fibre rim was finalized, further finite element analysis was conducted using the ANSYS composites package (ACP-pre) to model a carbon fibre rim. Tensile testing with 5-layer and 10-layer tensile test samples indicated a UTS of 450-560 MPa in X and Y. In the ANSYS project section "Engineering Data" the properties of CF layers were modified with the 560 MPa value found in testing. A shell of the mold geometry was uploaded to ANSYS and the rim was separated into an inner and outer hemisphere that were modelled separately and joined later for the structural analysis. The faces that carbon mats would be laid-up onto were added to "named selections"; these locations included two rings to reinforce where the profile of the rim changes quickly and at the tire bead. The number of layers, the location of reinforcements, and the orientation of the layers were changed iteratively, while comparing the resulting stiffness and strength of the CF rim to the aluminum rim.

It was found that the stiffness of the CF rim was greatly improved with strategic placement of areas of reinforcement where stress is concentrated (see Figures 12 and 13 below). Overlapping areas of carbon fibre are also inherent to the design since the curved geometry of the part can only be achieved by sectioning each layer into multiple carbon pieces, and these naturally must overlap in order to achieve 100% coverage of the curved faces in the mold. The tire bead area is reinforced as this section will be trimmed after molding and therefore is particularly vulnerable to fraying.

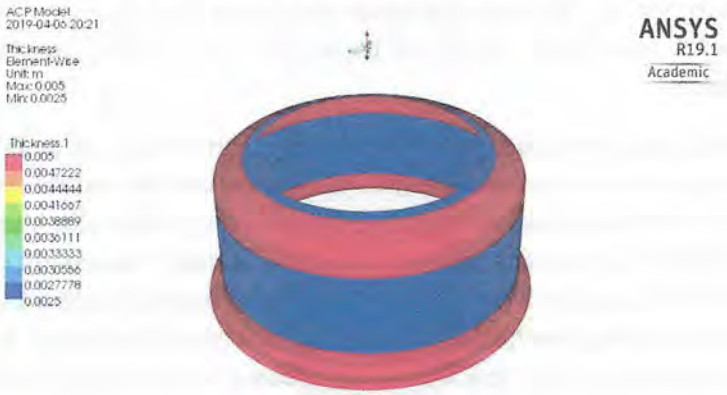

Figure 12: Thickness (m) of Inner Shell with 10 layers and 10 Reinforcing Layers (Red Areas)

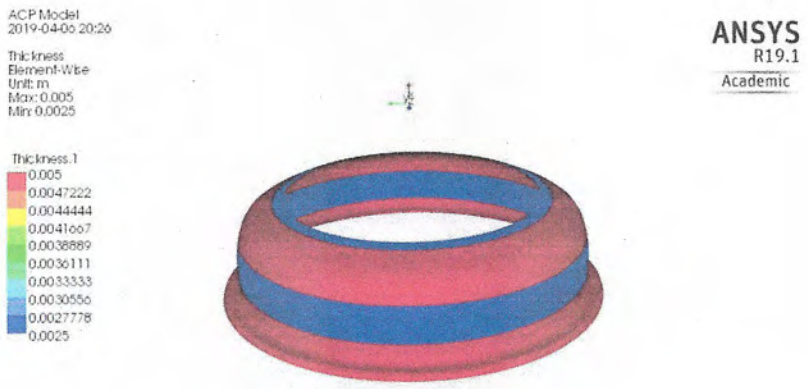

Figure 13: Thickness (m) of Outer Shell with 10 layers and 10 Reinforcing Layers (Red Areas)

The loads and fixtures that were used for ANSYS simulation are shown below in Figure 14. In Figures 15 and 16, the performance of a 10-layer CF rim with the layup outlined above is compared to that of the original aluminum rim. The 10-layer CF rim has a higher factor of safety in each case than the aluminum rim. The new design geometry lengthens the flattened barrel region and adds a draft angle. An unanticipated consequence of this is lengthening the moment arm of forces applied at the tire bead, which results in increased deformation at the inner shell's tire bead. The increased deflection is small, less than 0.6mm in the most extreme case.

The mass of a 10-layer rim is estimated at 1.18kg, which is 10/6 x 0.710kg (the mass of the prototype 6-layer CF rim).

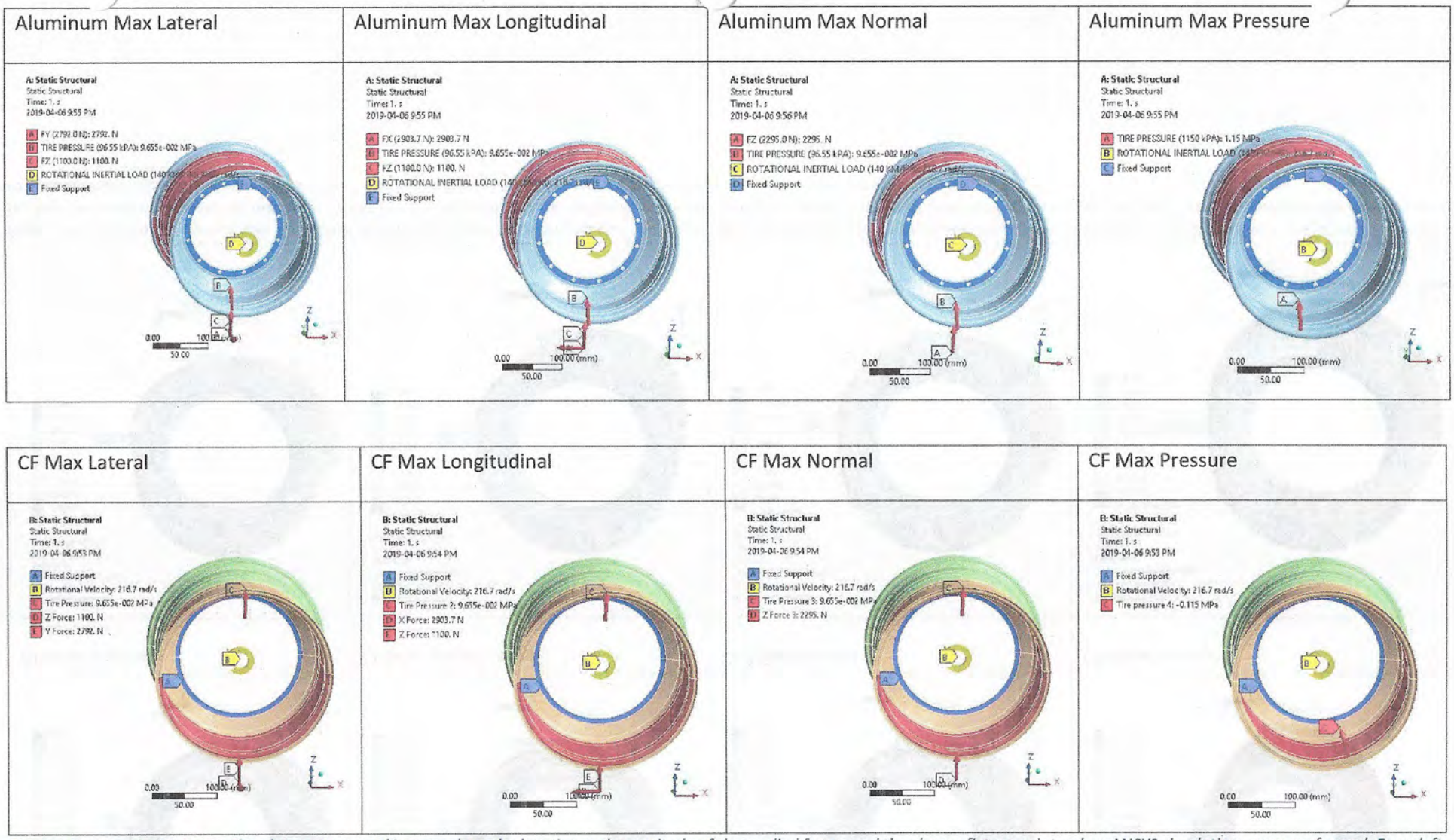

Figure 14: Loads and Fixtures. The above two sets of images show the location and magnitude of the applied forces and the chosen fixture points when ANSYS simulations were performed. From left to right, the cases correspond to: maximum lateral force, maximum longitudinal force, maximum normal or bump force, and maximum pressure. The first row of images represents the cases applied to the aluminum rim and the second row is the CF rim. In each case, the rims were subject to the same forces in the same locations.

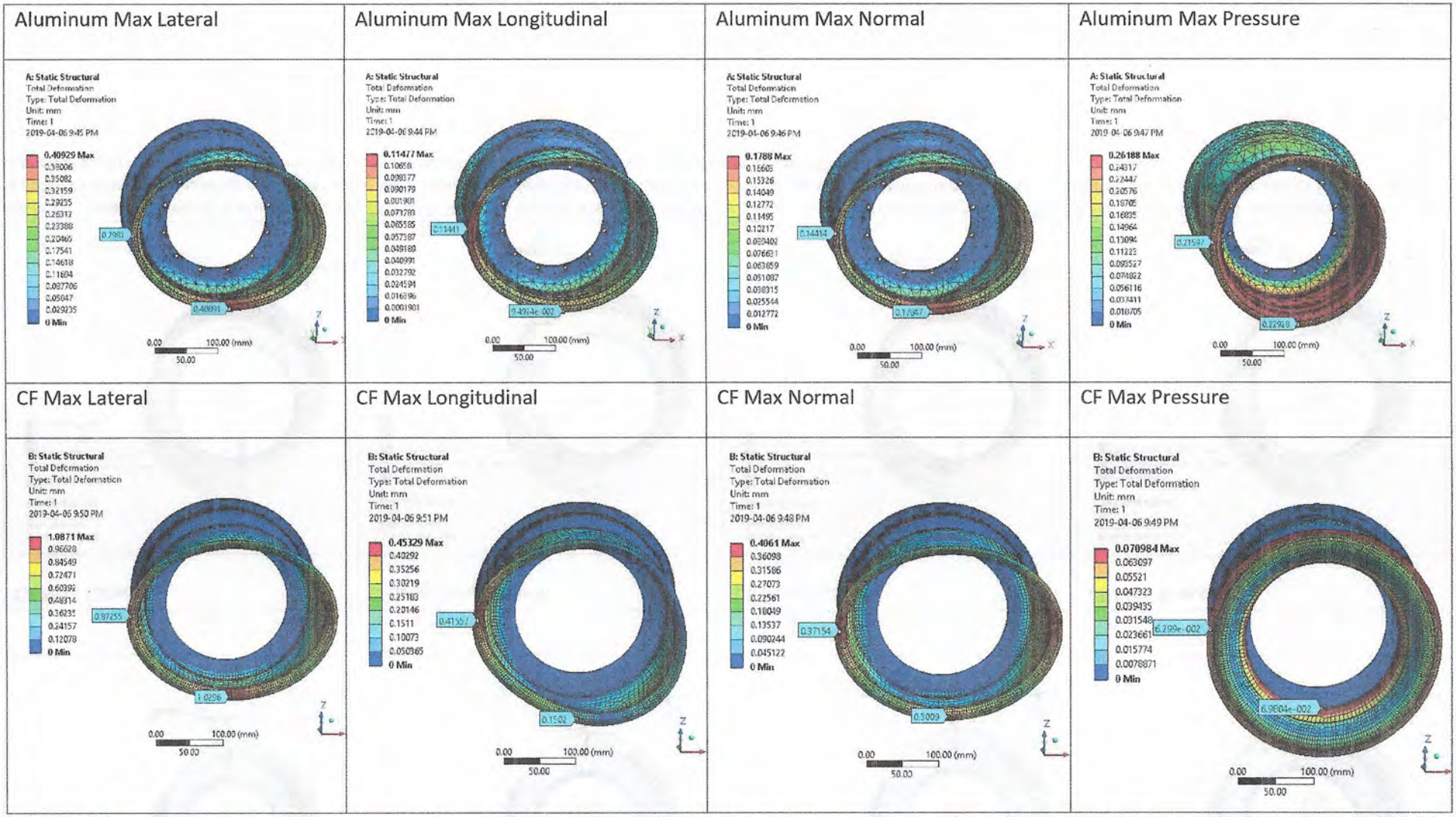

Figure 15: Deformation Comparison. The above two sets of images show the location and magnitude of deflections for the aluminum and CF rim when ANSYS simulations were performed. From left to right, the cases correspond to: maximum lateral force, maximum longitudinal force, maximum normal or bump force, and maximum pressure. The first row of images represents the cases applied to the aluminum rim and the second row is the CF rim. In each case the rims were subject to the same forces in the same locations.

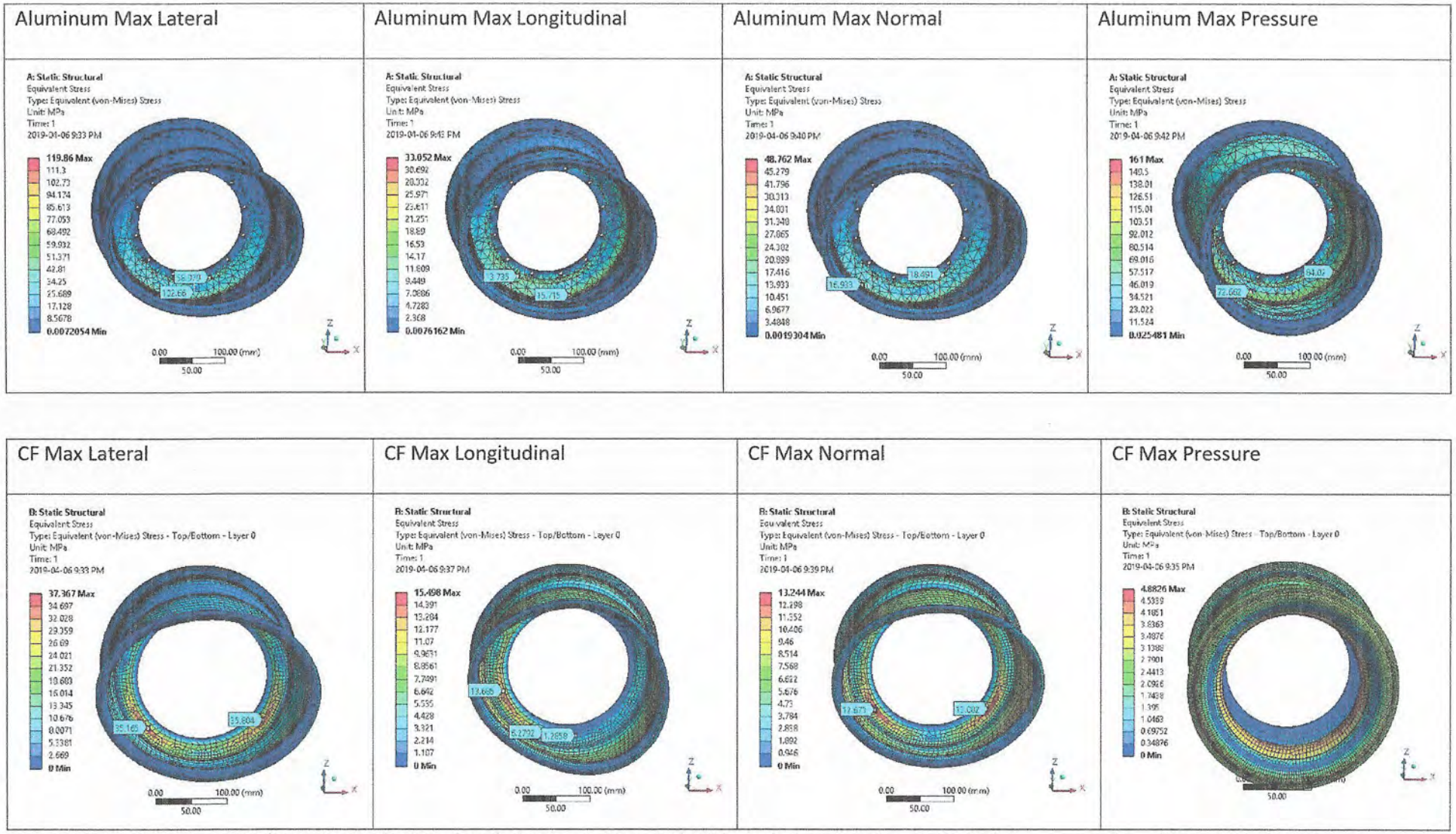

Figure 16: Stress Comparison. The above two sets of images show the location and magnitude of the applied stresses when ANSYS simulations were performed. From left to right, the cases correspond to: maximum lateral force, maximum longitudinal force, maximum normal or bump force, and maximum pressure. The first row of images represents the cases applied to the aluminum rim and the second row is the CF rim. In each case the rims were subject to the same forces in the same locations.

Based on the stiffness and mass of the prototype rim produced, as well as the above ANSYS simulations and the results of tensile testing, the following sensitivity analysis was performed in order to determine the optimum number of layers for an FSAE CF rim. The sensitivity analysis favours keeping the weight of the rim below 1.42 kg which is the weight of the aluminum rim. The term related to deflection percentage is squared to weight it heavily against rims that are low stiffness. The factor of safety term is weighted less than the other two terms as it is high even with few layers. With this weighting the optimum number of layers is shown to be 10 or 11 layers. With 12 layers the rim's mass would be nearly the same as the aluminum rim without an improvement to stiffness, though the factor of safety would be improved.

Table 1: Sensitivity analysis was performed with the following equation: (1.42 - Mass) x 30 - (Def %)^2 / 300 + FOS / 1.8. With this weighting the optimum number of CF layers is 11.

CF Layers	Mass (kg)	Deflection (%)	Factor of Safety	Sensitivity Analysis
5	0.59	87.5	0.5	-0.39
6	0.71	80	1	0.52
7	0.83	72.5	3.25	2.03
8	0.95	65	5.5	3.17
9	1.07	57.5	7.75	3.93
10	1.18	50	10	4.32
11	1.30	42.5	12.25	4.33
12	1.42	35	14.5	3.97
13	1.54	27.5	16.75	3.23
14	1.66	20	19	2.12
15	1.78	12.5	21.25	0.63

2.2 Mold Design

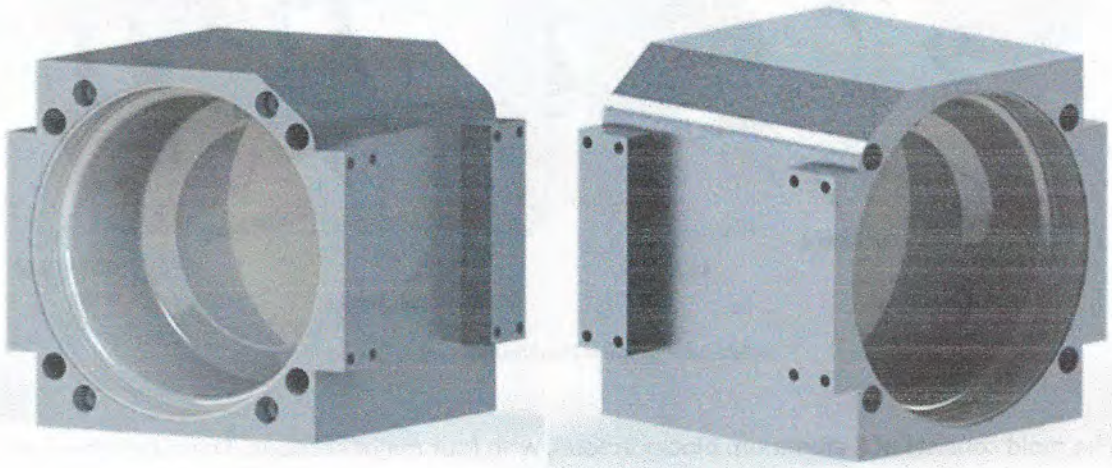

Figure 17: Isometric Views of Final Mold Design

Type of Mold

A major decision to be made is whether to use an internal or external mold for the rims. A male mold would be made on a lathe or mill and would use the least amount of stock material. It also allows the possibility of mounting the assembly on a spindle to be rotated during the layup process. A female mold would require more material and would be made in a mill. It would require more vacuum bagging as the material must curve around and into the cavity.

A key consideration in this decision is which surfaces of the rim geometry are most important. The surface lain up on will be perfectly accurate to the mold and have superior surface finish. From this perspective, a female mold has a noticeable advantage. The tire bead geometry is of critical importance as there are tightly defined requirements for the rim-tire interface. Additionally, the rest of the outer rim surface must have a smooth surface finish so that seating the tires will be feasible. Lastly, the surfaces where the inner and outer shells attach to each other (the rim centre mounting feature) should be as smooth and flat as possible; this surface would also be covered with a female mold.

For these reasons, a female mold is best suited to meet the design requirements. The mold will be created out of 4.5" 6061-T6 aluminum slabs that are available to the group through the Gryphon Racing team. Aluminum is an ideal material for this detailed section due to its machinability. Also, as a high-density material, aluminum does not require any gel coat on the mold surface.

Sectioning

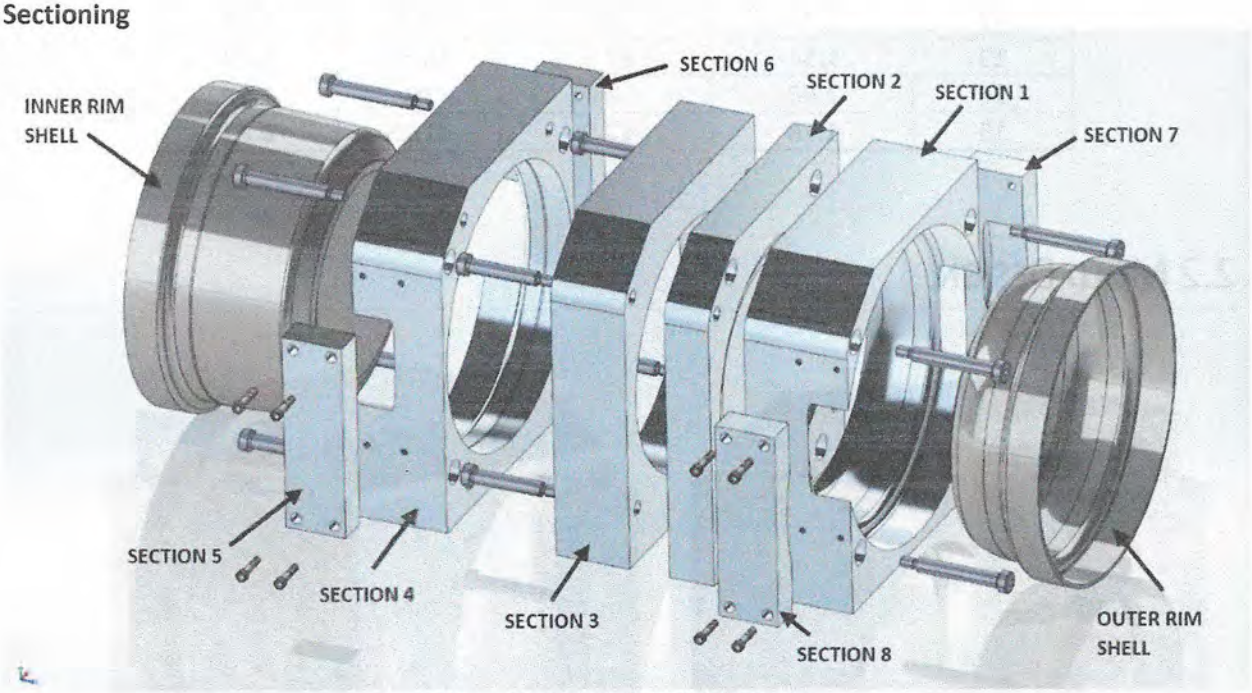

Figure 18: Exploded Final Mold Design

The mold consists of 8 aluminum blocks in total, with four major sections. The outer rim shell geometry is contained within Sections 1, 2, 7, and 8. The inner rim geometry is contained within sections 2, 3, 4, 5, and 6. Sections 5-8 are small blocks added on to the edge of the inner and outer rims because the available material is slightly too small to incorporate the geometry entirely. The major sections are

also rounded in one of the corners because of the shape of the available material (Appendix Figure 37). Note that only one rim shell will be created at a time, working exclusively with an assembly of their associated blocks. The designs are only shown as a full assembly as a convenient means of displaying all parts to be used. This would also be a convenient configuration for storage.

Section 2 is designed to be reversible so that it may be used for both laying up and drilling for either of the two rim shells. The sides used for laying up and drilling will be kept consistent such that one side is marked up from being used for all machining operations whereas the other is always used for layup and remains clean.

The edges of both the inner and outer rim shell geometry feature a continuation of the mold at the tire bead diameter. For carbon layup, it is good practice to create a bigger part than required because the edges often have issues with fraying and not saturating entirely. An additional 35 mm of length is provided so that this material may be trimmed away as excess.

With the goal of minimizing the number of sections required, mold development began from a version using three major sections (Appendix Figure 31). However, it was decided that it would be better to use four so that three of the sections would feature a "through hole" which could be waterjet cut out to expedite material removal and the fourth section would allow for the previously mentioned functionality of Section 2. Although it was decided that waterjet cutting would not be necessary, this through hole is still incorporated in the design to facilitate the layup process. The design was then changed to include a fourth section as a flat plate to incorporate these considerations. As the details of this configuration were further evaluated, concerns arose with this design as well. The flat plate connected with Section 1 caused a knife edge geometry in that section. This is not desirable because this feature could break, would be very sharp, and may not machine accurately. Also, in Section 1, the thickness of the part was very close to the upper limit of what depth can be machined. To resolve these issues, it was determined that it would be more appropriate to place the seams on either side of Section 2 as slightly inward on the rim curvatures rather than at their mounting surfaces. A cross sectional view of the final sectioning layout is shown below.

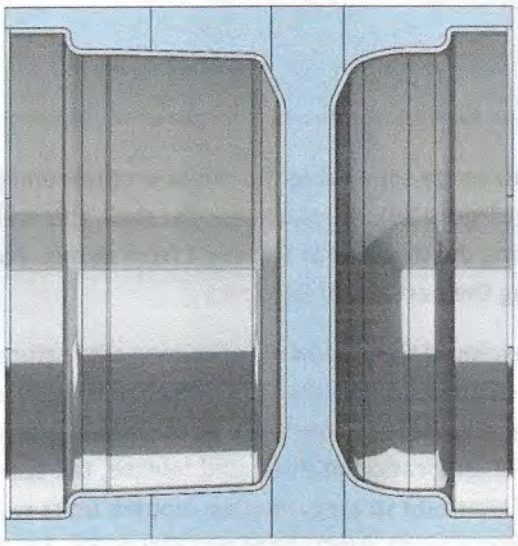

Figure 19: Mold Assembly Cross Section

Fastening and Mold Release

The sections are attached and detached using a combination of socket head shoulder bolts and standard socket head bolts. Shoulder bolts are desirable because they allow the part to be both properly located and attached with one piece of hardware. A previous design consideration was to use standard bolts in combination with dowel pins to ensure proper location, however this adds additional room for error in the manufacturing process as it requires each section to be flipped (Appendix Figures 33-34). Using shoulder bolts allows the same functionality to be accomplished with less complexity.

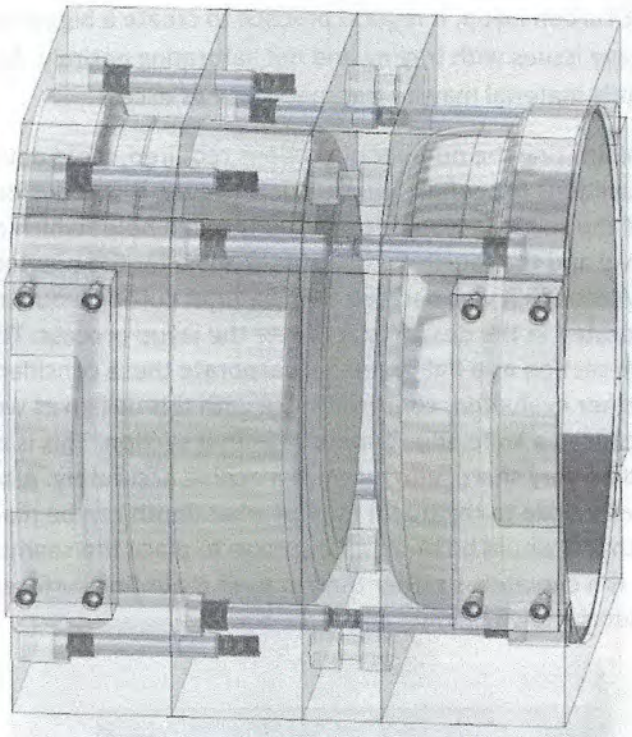

Figure 20: Mold Assembly Isometric View (Displayed Translucent for Detail)

Mold release is accomplished by separating the major sections and pressing the finished rim out using a hydraulic press (Appendix Figure 35). For the inner rim shell, this will mean removing Section 2, then Section 3, afterwards pressing the part out of Section 4 from above. For the outer rim shell, Section 2 will be removed before pressing the part out of Section 1.

The preliminary design explored the option of machining slit features between each of the major sections, such that wedge-shaped objects could be driven in to separate the parts (Appendix Figure 36). However, because the rims have a large amount of surface area and may require significant force to remove, even with proper application of PVA mold release, the team was unsure of the effectiveness of this method. An alternate strategy was developed; bolts were to be threaded in to the existing fastener holes to drive the sections apart (Appendix Figure 33, 34). Standard 5/8" bolts could be

adapted for this purpose by making some simple step-down modifications in diameter along their length.

Manufacturing Procedure

The manufacturing processes of the molds are outlined below (relevant images available in Appendix Figures 31-45):

1. Bandsaw cutting of aluminum blocks for Section 1-8. The aluminum slabs used came in an unusual shape; cuts were first done to remove excess material, leaving a square block of rough oversized dimensions. In one case, a bandsaw cut was also done to trim a block to thickness to avoid excessive facing operations.
2. Manual milling of blocks to square them to the correct length, width, and height. The blocks were first faced to the correct thickness, machining both sides to ensure smooth surfaces. The side faces of the blocks were then faced to square the blocks and make their lengths and widths equal. For the four main sections, a double vice setup including an angle plate and clamps was used to ensure adequate rigidity (see Appendix). The side features to secure Sections 5-8 were also drilled as this time.
3. Drilling/boring of fastener holes using manual mill. All ½" holes for the shoulder bolts were first drilled to a lower diameter and then reamed to ensure tight tolerances. All countersink features for bolt heads were done by plunging with end mills. Slits were machined into section edges for mold release. Because this method is much easier than machining custom bolts, it was tried first, and ultimately turned out to be sufficient.
4. Tapping of required ¼", 3/8", and 5/8" threads.
5. CNC machining of Section 2, side 1. Done using a 5/8" bullnose end mill with a 0.09" corner radius, 5" overall length. Block was dialed in square to the table and zeroed, with toolpaths for roughing, rest roughing and finishing. The rest roughing toolpath was done because roughing leaves a "staircase" like pattern on the outside contours; these should be smoothed out so that the finishing passes remove a relatively consistent amount of material.
6. CNC machining of Section 3. This was done by bolting on to Section 2 while still on the table. It was important that the CNC machining was done sequentially with each block bolted on top of the other in the machine. This allowed the same original datum from zeroing on Section 2 to be maintained so that each profile was machined entirely with respect to it. If each piece were to be machined separately, there would be an increased likelihood that the seams at the profile would not match up perfectly when sections were joined because of small errors re-zeroing and dialing the parts. A 2" face mill was used for roughing, ramping in to each stepdown helically. Rest roughing and finishing were once again done with the 5/8" end mill.
7. CNC machining of Section 4, by attaching to Section 3. Because of the thickness of this part, the face mill could not reach down to the full depth of the part. After this point, the 5/8" mill carried on the remainder of the roughing, as well as the rest roughing and finishing.
8. CNC machining of Section 2, side 2. The same operations used in Step 5 were repeated on the opposite side of Section 2.
9. CNC machining of Section 4, by attaching to Section 2. Like Section 3, the thickness did not allow the face mill to be used for all roughing. Also, the 5/8" end mill was extended to reach down a full 4" from the collet. Step downs and step overs were slightly reduced in case of chattering with this reduced rigidity.

10. Sanding and polishing of rim surfaces. Sanding was done with sandpaper of 150, 220, 400, and 600 grits. Relatively good finish was obtained from machining such that excessive sanding was not required except where rougher "staircase" shaped contours occurred, which required 40 and 100 grit sandpapers. The parts were then cleaned using a polishing attachment and compound.

2.3 Carbon Layup Process and Prototype

Layup procedure

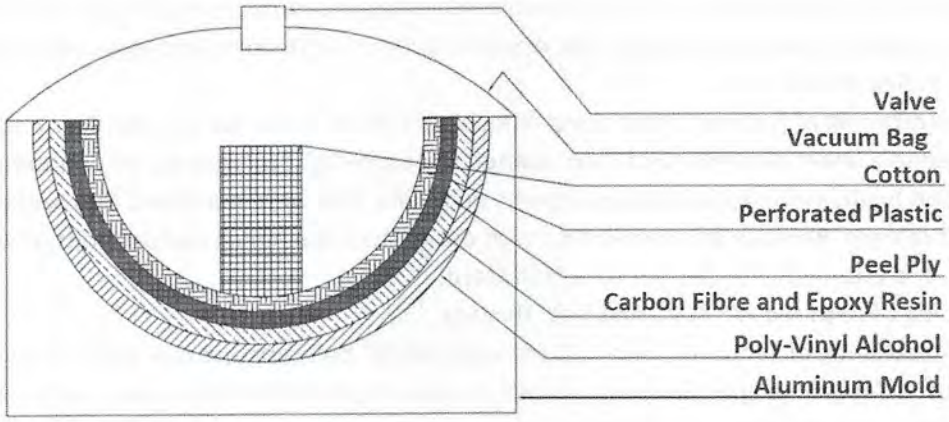

Figure 21: Carbon Fibre Layup Schematic

The physical creation of the rim begins with the layup process. First, the surface of the mold is degreased with isopropyl alcohol. A layer of PVA mold release must be applied to the mold using a brush or cloth. After the PVA has dried for at least 15 minutes, a thin layer of epoxy is applied to the surface and the first layer of carbon fibre is laid down. After the carbon fibre is secure, a layer of epoxy is applied using a dabbing motion to the carbon fibre. This process is repeated until the required number of composite layers is achieved. Peel ply is set on top of the carbon fibre-epoxy stack. The peel ply layer performs multiple functions: it absorbs and disperses epoxy and separates the above layers from the CF part. Above the peel ply comes a layer of perforated plastic. The holes in the plastic allow the epoxy to disperse at a controlled rate when the vacuum pump is running. Any extra epoxy is well dispersed and is absorbed by the cotton layer. This cotton layer prevents any extra epoxy from pooling in one area of the piece and prevents epoxy from reaching and destroying the valve. The last layer is the vacuum bag which is secured to the mold base using double sided tape. This bag has a small hole cut into the top of it to insert the valve for the vacuum pump hose.

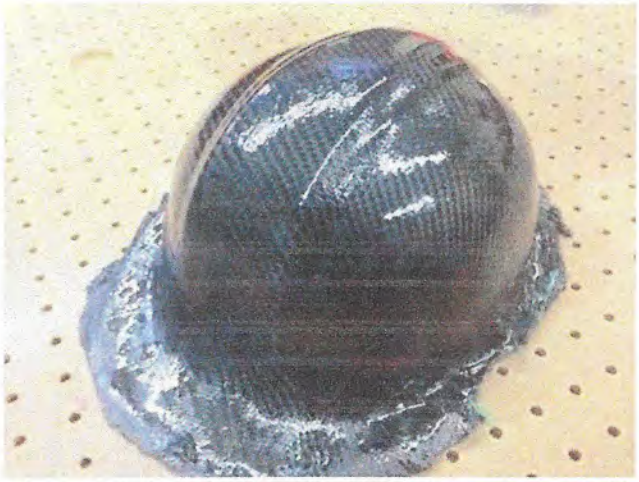

Figure 22: Carbon Fibre Test Piece Using a Safety Hat as a Mold

To practice this detailed process, test pieces were made using a 1x1 weave carbon fibre found in the race shop. Using a bump cap as a mold, the layup process was practiced. The CF bump cap was made using only two layers of carbon fibre and could withstand a large amount of force. Four pleats were cut into the pieces of carbon fibre to allow proper draping of the composite. The same method was used when creating the carbon fibre pieces for the rim. Additional strips of carbon fibre can be used to create an appropriately thick tire bead for the rim. These extra layers also ensure the bead will not fray and fail when in use. At the edge of the tire bead, the layers end slightly below the edge of the mold surface so that the vacuum bag does not catch the carbon and peel it downward off the mold.

When the time came to make a prototype carbon fibre rim with the aluminum mold, templates were created using the flatten tool in SolidWorks and these were printed at a 1:1 scale onto poster board. Carbon fibre shapes were cut out by taping around these templates, then cutting through the centre of the tape. Cutting through the centre of the tape ensures a slightly oversized part that will overlap with the parts around it, and the tape also keeps CF fibres from being pulled out of the correct orientation.

The outer shell of the prototype rim was made with bands of CF that built up from the bottom of the mold (see Figures 23 and 24 below). Using bands of carbon fibre was an acceptable option but was very time consuming and required extreme care when applying the strips of carbon to the mold, since the first layers tended to slip down to the bottom of the mold as more layers were applied on top.

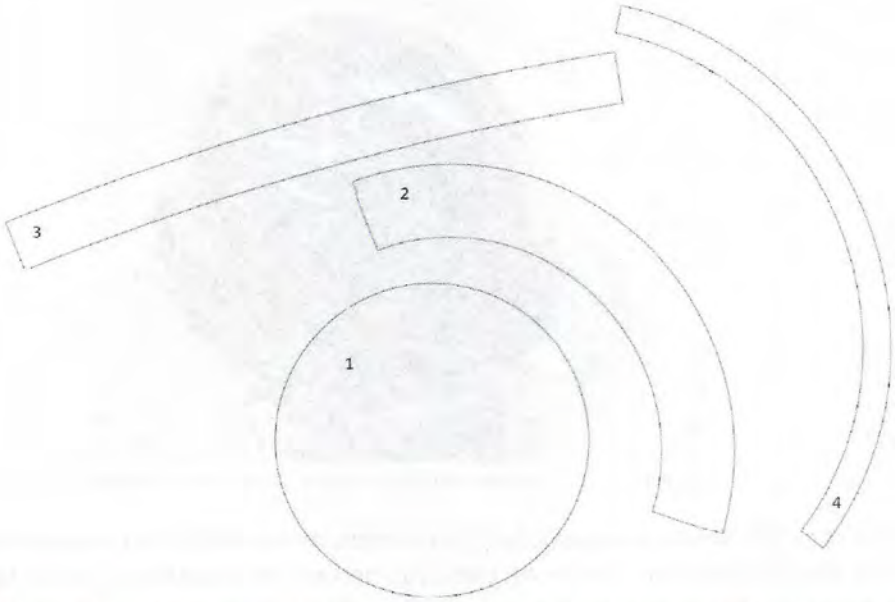

Figure 23: Banded-style layup shapes. Shapes Were Applied in the Numbered Order Which Built up the CF Part from the Bottom to the Top. The Arcs 2, 3, and 4 are Half-Length in Order to Fit on 18" x 22" Sheets of Paper

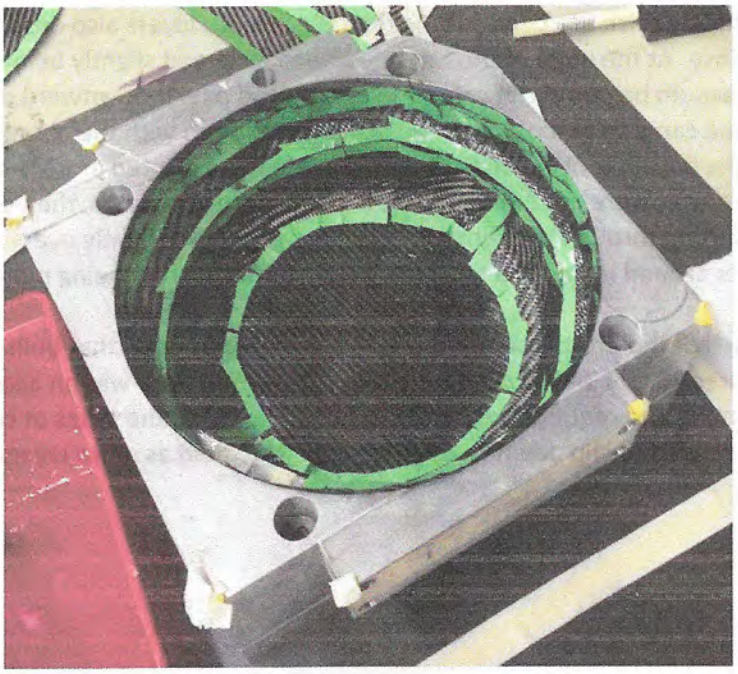

Figure 24: Banded-Style Layup in Progress on the Mold

The inner half of the rim was created with a central circle and radial slices (see figures 25 and 26 below). In order to ensure that the overlapping areas of the slices would not be a weak point, each layer of this template was oriented 45 degrees from the previous. Laying up the carbon in a radial pattern proved easier than the bands used for the previous section. The half of the rim created using radial slices had an improved surface finish compared to the half of the rim created with the vertical bands. Building up the carbon using these radial slices is the recommended method for future layups performed by the Guelph FSAE team. It is preferable to use as few individual pieces with as few relief cuts as possible, as

the strength of the composite relies on the continuity of the carbon. With each layup style, relief cuts were made into the cut-outs where they were required to lay flat over a curved surface, as discussed above with the bump cap.

Note that only six layers of carbon were used in the creation of the prototype rim, as this part is intended only as a proof of concept.

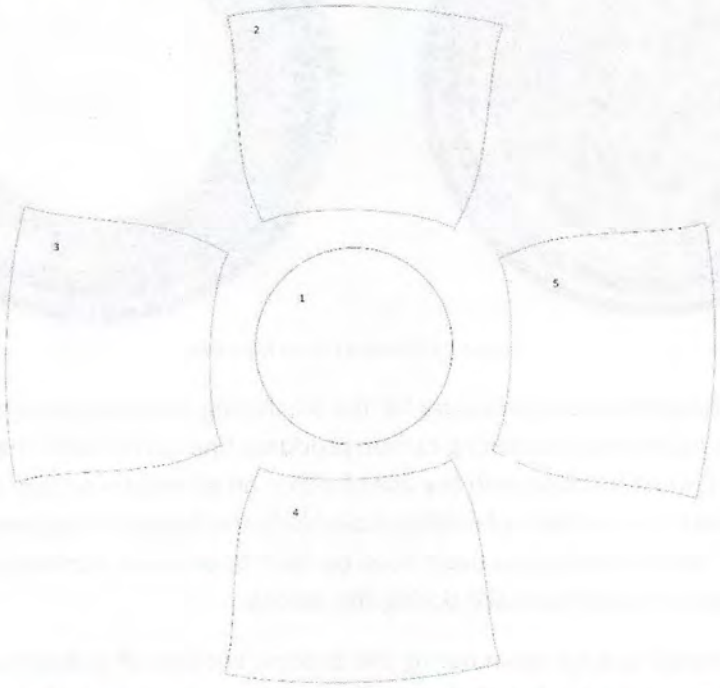

Figure 25: Radial Slice-Style Layup Shapes. Shapes Were Applied in the Numbered Order Which Built out the CF Part Radially. Shapes 2, 3, 4, and 5 Were Offset by 45 Degrees from the Layer Above and Below in Order to Ensure No Weak Points

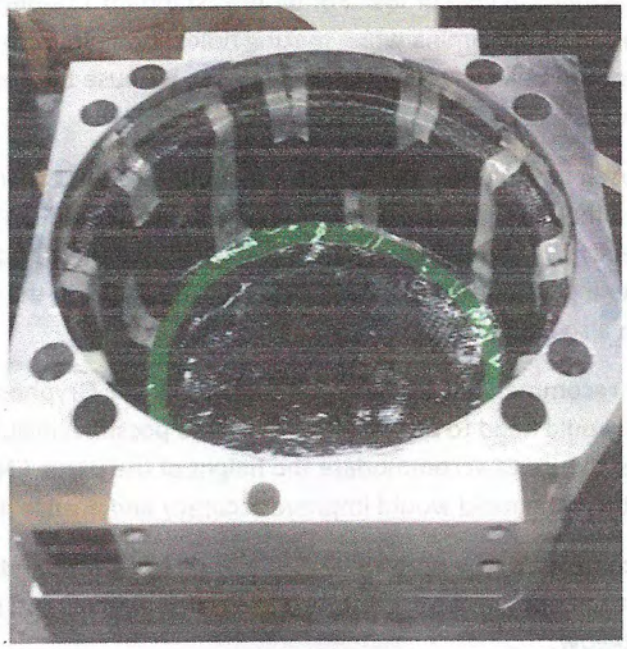

Figure 26: Radial-Style Layup in Progress on the Mold.

Post-Machining and Finishing

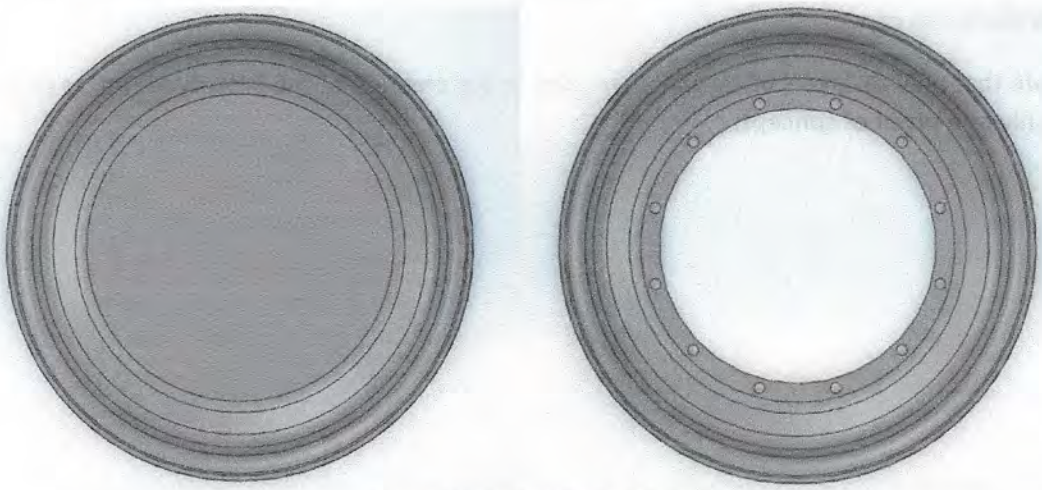

Figure 27: Features to be Machined

There are some precautions necessary for the machining of carbon fibre in terms of both safety and the quality of the machining. Machining carbon produces fine particulates that are hazardous to breathe in, therefore it must be done with the use of either an extraction system or dust binding coolant. This means that the machining facilities available in the School of Engineering, such as the CNC mill, are not suitable. The machining has been done by hand to produce a prototype part, with the extractor in the Gryphon Racing shop used during the process.

Special care should also be taken during this process because of carbon's abrasiveness and sensitivity to machining conditions. In industry, typically diamond coated carbide tooling is used because high speed steel (HSS) or uncoated carbide will wear at an accelerated rate. Wear is further increased if the feeds and speeds are either too high or low. For drilling, standard 118-degree angle drill bits are known to cause delamination of the lamina when making holes. Drill bits with elliptical profiles and other specialized geometry can be used to avoid delamination because they apply less downward pressure in the drilling process. [11]

The team has chosen not to make the extra investment into this tooling as it was determined to be cost prohibitive. Also, although this equipment is most suitable, regardless it can still be quickly ruined when used incorrectly by inexperienced operators. Drilling of the 12 bolt holes has been carried out successfully by sharpening a standard drill bit to a 60-degree angle. In the future, an additional hole for the pressure valve can also be drilled in this manner.

In the future, it is recommended to use the CNC router in the Gryphon Racing shop for carbon machining. Modifications would need to be made for this to be possible, including removal of the table or a redesign of the router fixture to accommodate the height of the parts. CNC machining these features with each part still in the mold would improve accuracy and ensure proper concentricity.

With machining completed, the parts are then finished by lightly sanding with fine sandpaper, applying a gloss clear coat to improve the appearance of visible surfaces, and sealing them together. The final prototype is shown below.

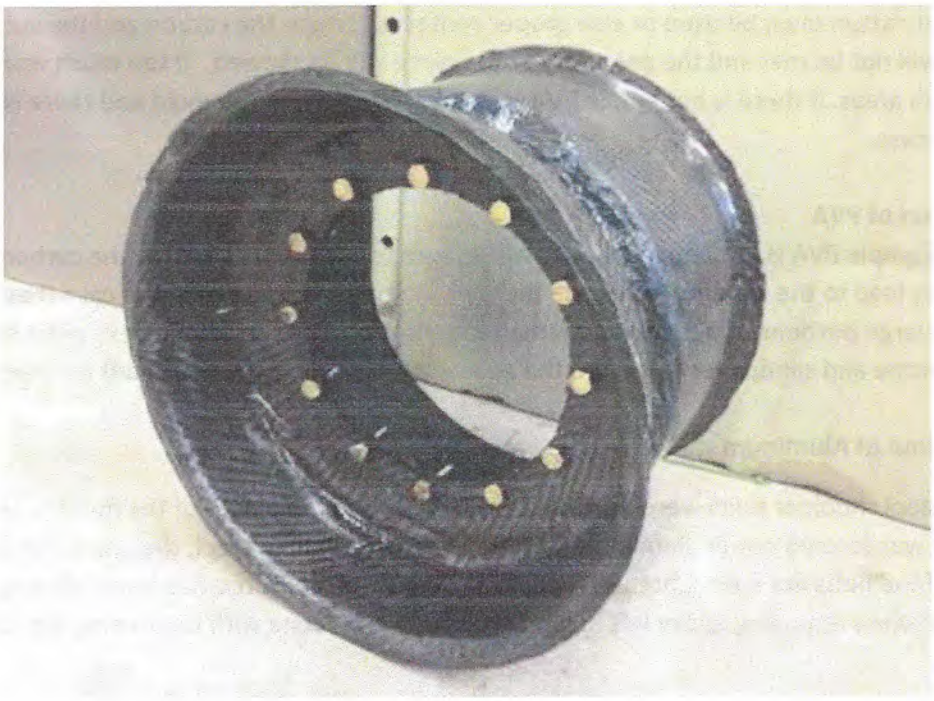

Figure 28: Final Prototype

3.0 Uncertainties and Risks

There are several risks associated with this project. They are all dependent on the preparation and care taken both before and during the process. With proper research, safety equipment, and being attentive to the process, most of these risks can be removed.

Carbon Fibre Research

Research must be conducted long before the layup process occurs to ensure the correct type of carbon fibre is used. If an incorrect weave is used (i.e. using unidirectional when twill should be used) the carbon fibre will not behave as intended, leading to difficulty in adhering to contours during layup or incorrect strength properties due to orientation. The physical properties of the cured carbon fibre are highly dependent on the type of weave used.

Quality of Epoxy

The quality of the epoxy resin and hardener must also be considered before the layup process begins. If a low-quality epoxy is utilized, the carbon fibre part will not offer the anticipated strength and stiffness properties and will delaminate sooner than expected. The epoxy and hardener must also be mixed for an ample amount of time before it can be applied to the carbon fibre. If insufficient mixing occurs, there will be a lack of bonding between the two fluids and once again, the expected properties will not be achieved.

Caution During Layup

Extra care must be taken when completing the layup process. The pieces must not overlap too much or else the thickness will be uneven, and the strength of the overall piece may change. The correct

amount of cotton must be used or else proper contact between the carbon and the suction of the vacuum will not be met and the geometry of the piece will be skewed. If too much epoxy is added, it will pool in areas. If there is not ample PVA, epoxy may adhere to the mold and there is an increased risk of air bubbles.

Application of PVA

If ample PVA is not applied, epoxy will adhere to the mold as well as the carbon fibre and could potentially lead to the inability to release the part form the mold. Even in the case that the part was released, large portions of epoxy could remain on the mold. This residual epoxy must be fully cleaned using acetone and sandpaper to ensure the geometry (especially the tire bead) is consistent between uses.

Degradation of Aluminum

Steel shoulder bolts were used to connect the separate pieces of the mold together. Because the mold was formed out of aluminum, which is much softer than steel, there is a risk of stripping threads if the bolts are overtightened repeatedly. Also, the molds require some sanding after making each part when removing epoxy left behind. This should be done with care, using acetone to ease the process.

Carbon Fibre Strength Post-Machining

Carbon fibre gets its strength from the entwinement of long carbon chains. When the carbon is machined, these long carbon chains are disrupted and the physical properties of the carbon changes at the location of machining. The epoxy generally adds enough strength to the fibre matrix to overcome this strength difference.

Hazards of Carbon Fibre

Carbon fibre releases small particles into the air when it is cut or machined. There is a risk of these particles entering the lungs and causing tissue damage. There is also a risk of the fibres embedding themselves into skin causing itchiness, splinters, or both. For these reasons it is important to wear proper personal protective equipment and take proper precautions before working with the carbon fibre. Proper equipment includes respirators and gloves to prevent inhalation and splintering. Before working with carbon fibre ensure that any carbon fibre particulates will be extracted by either a ventilation system or a specialized coolant.

4.0 Conclusions and Recommendations

A reduction of mass in the rims was necessary to improve vehicle performance of the Gryphon Racing FSAE car as it reduced rotational inertia, unsprung mass, yaw inertia, and overall vehicle mass. 2x2 twill weave carbon fibre in combination with high quality structural resin has been deemed the best material choice due to the high strength to weight ratio and ease of draping on complex surfaces.

A custom rim profile has been designed with consideration of suspension design criteria, ease of mold release, and minimization of stress concentrations. Detailed structural analysis of the composite rim was completed to determine the required layering and orientations of the carbon laminae. Load cases for cornering, longitudinal acceleration, road bumps, and over-pressurized tires were considered.

A modular female aluminum mold has been designed. This type of mold was specified because it provides high dimensional accuracy on critical surfaces and could be feasibly machined using SOE facilities. This design was successful executed, and the finished mold assembly is fully functional. A complete prototype rim was created, including the necessary post machining features.

The success of this project has been measured by the ability to carry out a comprehensive rim design process, as well as manufacture a full mold assembly and prototype rim to prove the feasibility of the design. During the period of this project, skills such as vehicle dynamics and MATLAB, materials testing, structural analysis and ANSYS, solid modeling, and manufacturing were applied to cover all relevant aspects of this engineering problem. With the successful execution of the intended goals, this project is now considered complete.

Recommendations for the future advancement and implementation of this design are as follows. The carbon fibre layup process of the rim should be further refined to ensure proper and uniform adherence to the mold surfaces throughout the entirety of the part. One approach to this would be to change the shape of the excess cotton layers added underneath the vacuum valve, such that this material does not prevent the vacuum bag from being drawn into the part's corners. It would also be sensible to perform destructive testing on the prototype rim, to provide a final verification of the ANSYS model. This would shed much more light on the accuracy of the modeling conditions than the previously done tensile tests, which can verify material properties but not give any information regarding the possible effects of layer interruption and overlap throughout the part, and the addition of tape to layer edges. The FEA model can be modified to have six layers like the prototype part relatively easily. It is also recommended to find a method of post machining the rim features more accurately on a CNC mill or router as discussed in the post-machining section. When a tire is added to the rim, it should be checked that it is airtight, and not out of round or bent.

5.0 REFERENCES

[1] Adam, H. "Carbon Fibre in Automotive Applications". *Materials and Design.* Vol 13. Iss 4-6. PP 349-355. December 1997. DOI: https://doi.org/10.1016/S0261-3069(97)00076-9

[2] "Aeropoxy PR2032 + PH3663 (Gallon kit)". Composites Canada. March 28, 2019. URL: https://shop.compositescanada.com/#/product/AE2032-63-X

[3] "Aluminum Wheels vs. Magnesium Wheels". CarsDirect. February 21, 2012. URL: https://www.carsdirect.com/aftermarket-parts/pros-and-cons-of-magnesium-wheels

[4] "Aluminium vs. Carbon Fiber - Comparison of Materials." DexCraft. October 7, 2015. URL: http://www.dexcraft.com/articles/carbon-fiber-composites/aluminium-vs-carbon-fiber-comparison-of-materials/

[5] Bastow, D., Howard, G., Whitehead, J. "Car Suspension and Handling". Feb 2004. Available: http://sutlib2.sut.ac.th/sut_contents/H96323.pdf

[6] Chapman, Matthew K. "Development of a Composite Wheel Rim for an FSAE Car". University of New South Wales. 2011. Print.

[7] Drakonakis, V., Seferis, J., Doumanidis, C. "Curing Pressure Influence of Out or Enclave Processing on Structural Composites for Commercial Aviation". *Advances in Material Science and Engineering.* Vol 13. Sept 2012. Available: https://www.hindawi.com/journals/amse/2013/356824/

[8] "Fabric Styles". Advanced Composite Materials inc. 2016. URL: http://www.a-c-m.com/fabric_styles/default.html

[9] Hyer, Michael. "Stress Analysis of Fiber Reinforced Composite Materials". Boston: McGraw-Hill. 1998. Print.

[10] Luo, M. "Magnesium: Current and Potential Automotive Applications". *Journal of Minerals, Metals, and Materials Society.* 54:42. Feb 2002. Available: https://doi.org/10.1007/BF02701073

[11] MacArthur, Mike. "How to Machine Carbon Fibre and Today's Difficult Composites". Youtube. Feb 10, 2012. URL: https://www.youtube.com/watch?v=OIaL_epxjoA.

[12] Marker, T. "Evaluating the Flammability of Various Magnesium Alloys During Laboratory- and Full-Scale Aircraft Fire Tests" *US DOT FAA*. January 2013. Available: https://www.fire.tc.faa.gov/pdf/ar11-13.pdf